



Aluminium Foams For Heat Transfer Applications

Gael Yazen Zaragoza Reyes

Submitted for the degree of PhD

Department of Materials Science and Engineering

November 2012

Supervisor: Dr. Russell Goodall

University of Sheffield

Acknowledgements

I gratefully acknowledge the provision of the CONACyT scholarship by the Mexican Government for the research described in this dissertation.

I would like to thank my supervisor, Dr. Russell Goodall for his advice, support and encouragement throughout my time here. I have very fortunate to work with a supervisor who is knowledgeable and approachable is making the SMaSh (Sponge Metals at Sheffield) group a very pleasant environment to work in. Thanks to the technical staff Mr. Ian Watts, Ms. B. Lane, Mr. S. Batter and Mr. P. Staton. A special mention goes to Ian Lyne whom his very great expertise placed on the rig design was very helpful.

To my friends in Sheffield (hopefully who will not be reading this) who made more pleasant and kept me sane in my time here, and specially thanks for their guidance and support on football games, parties and Sheffield's pub, they know that without them I would have finished sooner, and they are the only ones (specially the Mexicans) who know and agree with me that "Tacos al pastor" is "exquisite". Of course a very special thanks also for the guys in the office who tried their best to not make any noise (Andy, Zi Fu, Shuang Shuang, Paul, Everth, Jusien and David).

Thanks to my brothers and sisters and last but by no means least thanks to my parents (Abel and Nena) for all their support and encouragement over the last four years.

ABSTRACT

Open cell metal foams show great potential as a heat exchangers, due to their permeability to fluids and the high conductivity of the metallic network. In this study, aluminium foams were produced using the replication technique with NaCl, flour and water used to create the preform. The samples produced included both uniform pore sizes and examples where different pore sizes were created in different parts of the sample as well as these, samples made commercially by a similar technique (Corevo foams) and by an investment casting process (Duocel foams) were examined. A bespoke rig was designed, built and used to measure the thermal and fluid flow performance of all foams being investigated under forced convection conditions. Results for heat transfer coefficient and pressure drop across the sample with the comparison between each type of sample are presented. It was found that all the foams tested can have favourable heat transfer behaviour under certain conditions asymmetric behaviour can be obtained when non-uniform pore sizes are present; a factor that could be exploited in heat exchanger design.

Contents

1	Introduction	1
2	The Nature and Processing of Metal Foams	3
2.1	Foams from metal ions in solution	4
2.2	Foams from gaseous metallic compounds	6
2.3	Foams from solid-state metal	7
2.4	Foams from liquid metal	10
2.4.1	Direct foaming of liquid metal	10
2.4.2	In-situ gas generation	12
2.4.3	Powder-compact foaming technique	15
2.4.4	Gas-metal eutectic solidification (“gasars”)	19
2.4.5	Casting methods	20
3	Applications of Metal Foams	26
3.1	Structural applications	27
3.2	Sound absorbers	31
3.3	Vibration suppression	32

<i>CONTENTS</i>	v
3.4 Filters	33
3.5 Heat Exchangers	34
4 Thermal and Fluid Flow Properties	39
4.1 Foam conductivity	40
4.2 Foam permeability	49
4.3 Key elements of heat transfer	57
4.4 Heat transfer in foams	62
4.4.1 Buoyancy-Induced flow conditions	62
4.4.2 Forced convection	65
4.4.3 Oscillatory flow	74
4.4.4 Theoretical approaches	76
4.5 Summary of trends in heat transfer and permeability	79
5 Experimental Procedure	81
5.1 Replication technique	81
5.1.1 Fabrication of the open pore pattern (preform)	82
5.1.2 Infiltration of the liquid metal into the preform	83
5.1.3 Removal of the preform	83
5.2 Machining (Electro Discharge Machining)	84
5.3 Heat transfer measurements	85
5.3.1 Data acquisition system	86
5.4 Test procedure	87
5.5 Heat transfer coefficient calculation	88

5.6	Structural characterization	89
5.6.1	Density measurement	90
5.6.2	Pore size characterization	90
5.7	Scanning Electron Microscopy (SEM/EDS)	91
5.7.1	Energy-Dispersive X-Ray Spectroscopy (EDS)	91
6	Development of Foam Fabrication Method	92
6.1	Fabrication of the open pore pattern (preform)	92
6.1.1	Mix composition	92
6.1.2	Manufacture of the preform	95
6.1.3	Heat treatment of the preform	96
6.1.4	Dissolution in water of the preform	99
6.2	Infiltration of the preform with aluminium	100
6.3	Removal of the preform	102
6.4	Density measurement	103
6.5	Chemical analysis of fabricated samples (SEM/EDX)	104
6.6	Structural characterization	106
7	Test Method Development	108
7.1	Final rig design	108
7.1.1	Steel chambers	109
7.1.2	Copper cylinder (test section)	109
7.1.3	Ceramic discs	114
7.1.4	Plastic O-rings	114

7.2	Verification of the temperature homogeneity	116
7.2.1	Front face results	116
7.2.2	Lateral results	119
7.3	Blank test	121
7.4	Dummy sample tests	122
7.5	Testing Aluminium Foam	124
7.6	Long Duration test on Aluminium Foam	125
7.7	Contact between foam and copper cylinder	127
7.7.1	Clamped sample	128
7.7.2	Brazed Sample	128
7.7.3	Thermal paste sample	129
7.7.4	Test comparison	129
7.8	Error analysis	131
8	Heat Transfer of Single Pore Size Foams	132
8.1	Heat transfer coefficient of Duocel foams	133
8.1.1	Influence of density on the heat transfer in Duocel foams	135
8.1.2	Influence of pore size on heat transfer in Duocel foams	138
8.2	Duocel foams pressure drop	144
8.2.1	Influence of density on pressure drop in Duocel samples	144
8.2.2	Influence of the pore size on the pressure drop in Duocel foams	145
8.3	Corevo foams heat transfer coefficient	149
8.3.1	Influence of density on the heat transfer in Corevo foams	149

8.4	Corevo foams pressure drop	152
8.4.1	Influence of density on the pressure drop in Corevo foams	152
8.5	Heat transfer of laboratory made replicated foams	154
8.6	Pressure drop of laboratory made replicated foams	156
8.7	Heat transfer coefficient as a function of the pore size	157
8.7.1	Duocel samples	157
8.7.2	Corevo samples	159
8.7.3	Replicated samples	160
8.8	Comparison between single all pore size samples	164
9	Heat Transfer of Multiple Pore Size Foams	166
9.1	Fabrication and characterization of integrated samples	168
9.2	Testing integrated samples	169
9.2.1	Heat transfer coefficient of integrated samples	169
9.2.2	Integrated samples pressure drop	171
9.2.3	Pressure drop "bow wave" effect in integrated samples	172
9.3	Fabrication of segmented samples	181
9.4	Testing segmented samples	181
9.4.1	Heat transfer coefficient of segmented samples	182
9.4.2	Pressure drop across segmented samples	183
9.4.3	Pressure drop "bow wave" effect in segmented samples	184
10	Heat Exchangers Analysis and Comparisons	193
10.1	Nusselt number	193

<i>CONTENTS</i>	ix
10.2 Comparison of experimental data with modelling	200
10.3 Performance comparison and suggestions	203
11 Conclusions and Further Work	210
11.1 Conclusions	210
11.1.1 Replication technique for foam manufacture	210
11.1.2 Test method development	211
11.1.3 Heat transfer and pressure drop	212
11.2 Further work	214
References	216
Appendix	234

Chapter 1

Introduction

The low density of porous metals and the functional properties (e.g. thermal conduction, permeability to fluid flow, etc.) unachievable in other materials has made them attractive for many industrial and scientific applications. Frequently due to the need to cool systems such as power electronics and the desire to recapture waste energy, heat exchangers are increasingly important in engineering. The permeability to fluid of an open cell foam, coupled with the high conductivity of a metal immediately suggests applications in heat exchange.

Several processes to obtain metal foams have been developed and frequently are classified according to the physical state of the metal when they are fabricated. In this work aluminium open-cell foams with single and graded pore sizes were obtained through a version of the replication technique developed in the laboratory.

The single and multi-pore graded samples obtained in-house were thermally, hydraulically and physically characterized and compared with Duocel samples supplied by the ERG Aerospace Corporation and Corevo samples provided by Constellium. To characterize the thermal and fluid behaviour a new and unique experimental apparatus was created.

The heat transfer coefficients have been determined for single pore size samples and

are compared with the literature. Novel thermal and fluid flow properties for graded pores aluminium foams were obtained.

This work reports the properties found and suggests, based on the results obtained the best suitable aluminium foam among the samples studied to be used as a heat exchanger for several applications and the thermal and hydraulic advantage of having two different pore sizes in the same sample.

Chapter 2

The Nature and Processing of Metal Foams

Metallic foams are solid structures with a certain volume fraction of pores filled by gas, where these pores could be what is described as open-cell or closed-cell, Figs. 2.1(a) and 2.1(b). These materials can present a very attractive combination of physical and mechanical properties. These metal foams can be manufactured from a wide range of pure metals or alloys, with typical densities between 75 to 95 % and pore sizes around 5 mm to microns; these two characteristics, density and pore size, can be manipulated with the manufacturing processes that currently exist, increasing the potential for metal foams in state of the art technology and in everyday human life. For example the high temperature resistance of some porous metals makes them interesting candidates for use as either a thermal barrier or as heat exchangers where having good control over the size and connectivity of the pores is of central importance.

The processes for manufacturing metal foams may be classified according to the state of matter in which the metal is processed, which can be solid, liquid, gaseous or ionized (i.e. in solution or in a compound). Some of these methods take advantage of electrical or sintering characteristics of metals, whereas others are similar to techniques

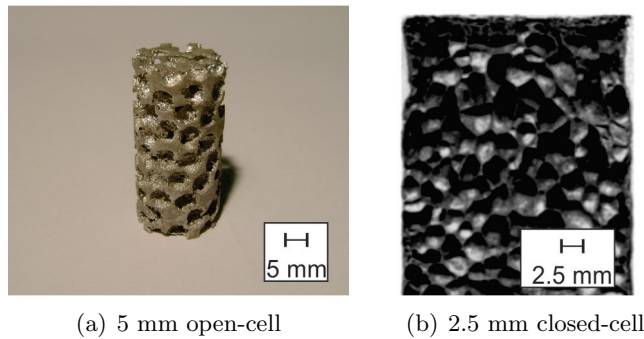


Figure 2.1: Aluminium metal foams. (a) Aluminium foam obtained by the replication technique with 5 mm open-cell pores and (b) 2.5 mm closed-cell aluminium foam obtained by the FORMGRIP process [1].

used for polymer liquids or foaming aqueous solutions. Melt route processes often use aluminium, such metals as titanium may be processed as powders in the solid state and nickel is frequently deposited from a gas or solution. The porosity, pore size, pore surface, interpore wall and strut size depend on the production process from which the metal foam is obtained. The production methods are frequently classified in four broad classes [2–4]:

2.1 From metal ions in solution.

2.2 From gaseous metallic compounds.

2.3 From solid-state metal

2.4 From liquid metal.

Table 3.1 reports productions methods, applications and references for metal foams, principally those made from aluminium. These methods will be explained in the following sections.

2.1 Foams from metal ions in solution

Very porous metallic foams with high specific surface area can be obtained by electro-deposition, requiring a foamed structure (typically polyurethane) to deposit the metal

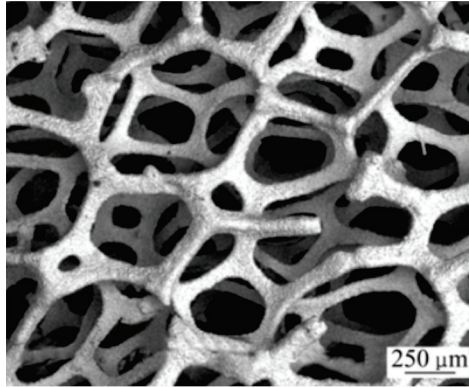


Figure 2.2: Zinc foam obtained from the plating of metal ions in solution onto a template [5].

onto. As electrodeposition requires the flow of electrons, the polyurethane foam requires some initial electrical conductivity before electrodeposition can start. The quality of the final foam is highly influenced by the treatment used to make the polyurethane precursor conductive; this is often surface metallization [3, 5], although alternative processes include electroless plating, vacuum evaporation, arc ion plating and coating with a slurry of a conductive material, due to low cost and easy formation of continuous and uniform coating on the substrate surface [3]. After deposition, the polyurethane foam (the parent structure) is removed chemically or thermally. Cellular structures with pore sizes of 6 to 70 PPI (PPI= pores per linear inch) and pore densities over 90% [3, 5] can be obtained. Fig. 2.2 shows a Scanning Electron Microscope (SEM) image of zinc foam with an average pore size of 0.3-0.4 mm obtained from the planting of metal ions in solution onto a template [5].

The foams produced by this method have very open structures, and frequently hollow struts [3]. The open structure with little metal means that the resistance to fluid flow will be low, but this same low quantity of metal means that the transport of heat through a foam of this type will be limited, and these foams are not commonly explored for heat exchange.

2.2 Foams from gaseous metallic compounds

The vapour deposition process (as for the electro-deposition technique 2.1), requires a porous structure to deposit the metal on. This structure is once again normally an open cell polyurethane (PU) foam [6, 7]. In the process the open cell template is fed through a plating device, in which metal carbonyl gas is supplied and heated up in the presence of a catalyst. This compound thermally decomposes and the metal is deposited onto the polymer foam substrate and the 'as-plated metal foam' is formed [6, 7]. To remove the polymer, and also densify the ligaments, the as-plated metal foam is sintered (or annealed) in a reducing atmosphere. After sintering a cellular structure is obtained with hollow ligaments. These Chemical Vapour Deposition (CVD), based techniques, in common with electroplating discussed before, are the main processes used in the industry to produce metal foams with the lowest relative density (2-5 %) [2, 8]. Fig. 2.3 shows a SEM picture of nickel foam from INCO with 110 PPI [9], the production process at INCO is based on CVD of nickel tetracarbonyl ($\text{Ni}(\text{CO})_4$) onto an open-cell polyurethane substrate [10].

The open structure obtained with this process permits them to be used as a heat exchanger medium, however as was explained in Section 2.1, these foams also have hollow struts [8], and the low quantity of metal reduces the amount of heat that can be extracted compared to using a solid structure. The main use of the metal foams obtained under this process is as a battery electrodes, especially for Nickel-Metal Hydride (NiMH) batteries, and potential uses include as an electrocatalyst in molten carbonate fuel cells [8].

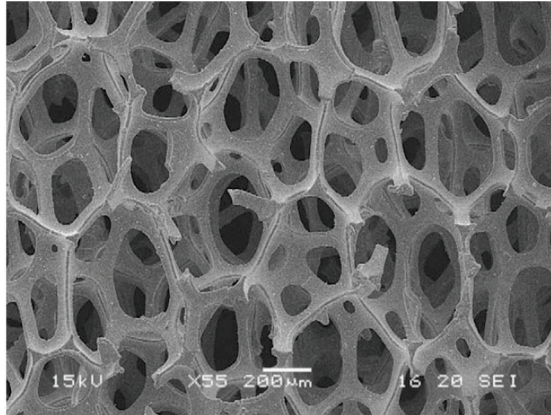


Figure 2.3: Scanning Electron Microscope image of a nickel foam structure obtained by the CVD onto a template process [9].

2.3 Foams from solid-state metal

This method produces metallic foams with macro or microporosity from metal, usually in powdered form; the powder remains in the solid state during the entire process and requires a sintering step before the final metallic foam is obtained. Another way to obtain an open structure by the solid state method is to join particles that contain pore spaces. These hollow spherical particles could be obtained in several ways: either by coating polymer spheres (e.g. Styrofoam), or fertilizer (carbamide in a spherical shape [11]) which acts as a lost core [12], or by combined chemical and electrical deposition of metal onto polymer spheres which are removed in a subsequent step [3].

Another variation of this is coating the polymer spheres by a binder/metal powder suspension (to make a green sphere). After coating, the sphere is heated to produce a cohesive metal shell around the outside, and remove the polymer. The spheres produced by this method range from 0.5 to 10 mm diameter [3, 13, 14]. To manufacture a metallic structure with these hollow spheres, they can be joined by brazing or diffusion bonding [13], thermoplastic polymer/adhesive is also used, for example when spheres of porous aluminium obtained by the Advanced Pore Morphology process (APM) are joined [15]. fully closed cellular structures can be obtained when the interstices between the spheres

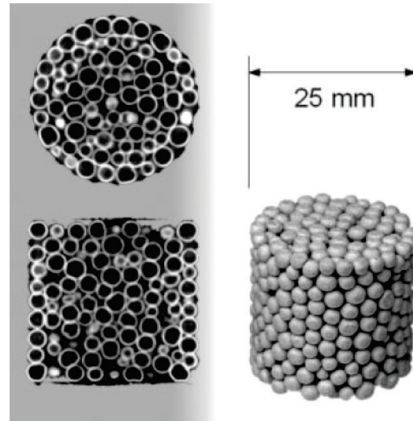


Figure 2.4: Stainless steel sample obtained from hollow-spheres. The left hand side shows X-ray computer tomography images of the cross section [13].

are filled with metallic powder, followed by heat treatment [16]. With the objective to improve the mechanical properties of the cellular structure, large contact areas between the spheres are needed, to achieve this, slight pressure is applied to the green spheres. Fig. 2.4 shows the typical structure obtained.

Another method to obtain hollow spheres consists of gas atomisation of powders; some of the particles produced will have gas trapped inside the liquid droplets. These can be separated from the solid ones, that are also produced when the gas is atomized. The following step in the process is to consolidate the material, done by; sintering, transient liquid phase sintering with the help of a powder additive, or Hot Isostatic Pressing (HIP) [3, 13]. The last of these gives the best consolidation and hence the best results for specific stiffness [13]. Metal foams with cell sizes between 500 and 1000 μm and relative densities of 3 - 12 % have been fabricated [3, 13]. Figs. 2.5(a) and 2.5(b) show the hollow sphere structure obtained from 625 alloy (Nickel-Chromium).

Hollow spheres can also be formed from slurry made up of a decomposable precursor, together with organic binder and solvents. This slurry is sprayed through the outer orifice of a coaxial nozzle [17], and single bubbles are formed by hydrodynamic interaction with the gas passing through the inner orifice. During flight in a tall drop tower, the spheres are hardened by heating to drive off the solvents and volatilize the binder.

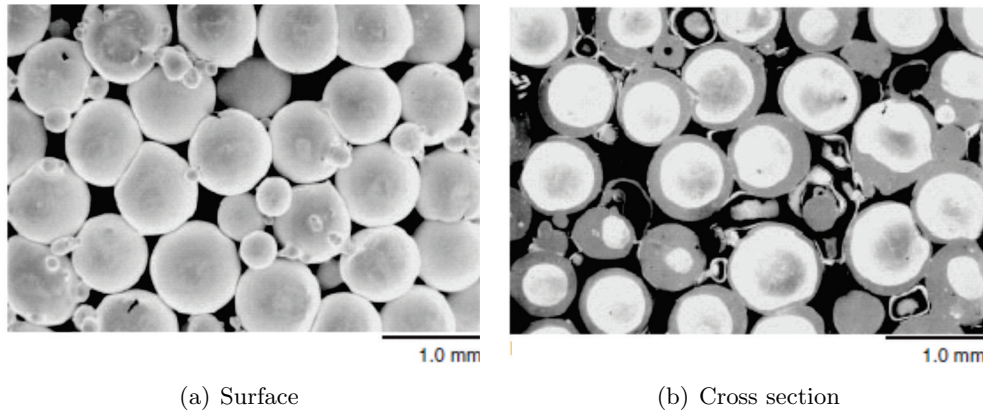


Figure 2.5: Hollow-sphere structure made from Gas Atomized Hollow Powders (a) structure surface (b) structure cross section [13].

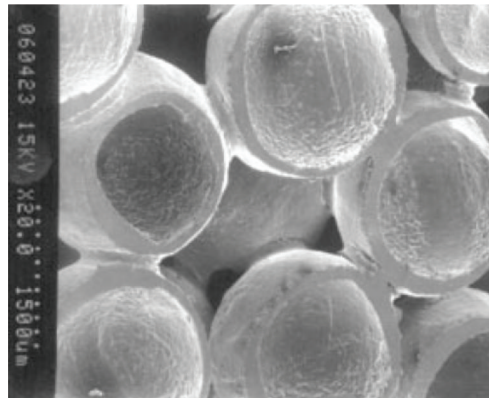


Figure 2.6: Hollow spheres of FeCr bonded together to form a porous material [13].

The process was developed by Georgia Tech producing hollow spheres with diameters in the range of 1 to 6 mm, with wall thickness typically around 100 μm . To obtain a cellular structure the spheres obtained are placed in a mould and are bonded with the help of metal powder slurry [3, 13]. Fig. 2.6 shows the cellular structure obtained.

In solid-state metal process, space holders can be used that do not rely on hollow particles to control the amount and size of porosity. These space holders can be ceramic particles, salts, hollow polymer spheres or certain metals. They are mixed with the metal powder and can be removed at a later stage to leave behind open pores. This process has many similarities with the casting-based methods discussed later, but in this case the empty space is filled with a solid metal (in the form of metal powder)

instead of molten metal. The metal powder is blended with the space-holder material and compacted (this step of the process could be at room or elevated temperature if the space-holder is heat resistant). After compaction and possible sintering step for further consolidation metal foam with interconnected pores results when the space holder is removed; this could be done by, heat treatment or using an aqueous solvent depending on the space holder, obtaining in the metal foam a replica of the shape and size of the space holder [3, 13, 18–22].

Hollow sphere metal foams possess low (or even no) interconnected porosity, and therefore high flow resistance is expected, and it would not be recommended to use them as a heat exchangers. When the spheres are bonded with adhesive (as in [15]), these metal foams would show very low thermal conductivities, due to the affect of the adhesive matrix between the metallic shells of the spheres, and therefore could be used as a thermal insulator [23].

2.4 Foams from liquid metal

There is a great flexibility in foams made from liquid metals, and so this review will concentrate on this type of processing. It is possible to obtain cellular structures from the liquid metal by either direct or indirect methods. The direct method consists of creating gas bubbles in the liquid and the indirect method of casting a melting metal over a solid leachable space holder that is removed after the metal is cooled down and solidified, leaving the pore spaces.

2.4.1 DIRECT FOAMING OF LIQUID METAL

In practice, direct foaming of liquid metals is a family of processes that includes either injecting gas into the liquid metal from an external source or causing gas formation in-situ in the liquid by adding and mixing gas-releasing blowing agents in the metal to be foamed.

In either route bubbles are therefore present in the molten metal. Due to the gas bubbles tendency to "escape" (reaching the molten metal surface quickly) because of the high buoyancy forces in the high-density liquid, the addition of an agent that increases the viscosity of the molten metal is employed. This viscosity-increasing agent is frequently a fine ceramic powder (such as SiC) or alloying elements (such as Ca) that react to form stabilising solid particles in the molten metal [3, 24].

The Melt Gas Injection (MGI) method developed simultaneously by Alcan and Norsk Hydro [25] in the late 1990s, is a continuous gas injection method where the starting material, a metal composite, is molten in conventional foundry equipment. This metal composite consists of an aluminium alloy, such as the casting alloy AlSi10Mg (A359), with reinforcing particles, (actually to increase melt viscosity) frequently SiC or Al₂O₃, with volume fraction ranges from 10 % to 20 %. Some suggestions have been made to optimize the process [26], identifying 16 % of SiC as the optimal amount.

The composite is transferred to a vessel where the gas (air, argon, nitrogen) is injected into it using specially designed rotating impellers or vibrating nozzles. The objective of the impeller is to create fine bubbles in the molten metal and distribute them uniformly; the size of the bubbles can be controlled by adjusting the gas flow rate, the propeller design and its speed of revolution. The function of the reinforcing particles is to retain the gas bubbles in the liquid, retarding their coalescence and reduce the rising of bubbles by increasing the viscosity of the melt [27–29]. Fig. 2.7 shows a sketch of the process. The foam obtained is pulled off the liquid surface by means of a conveyor belt and it is allowed to cool down until it solidifies. Foams made in this process present gradients in density and pore elongation as a consequence of the gravitationally-induced drainage and the shearing forces of the conveyor belt, having as a result diagonally distorted cells in the final foam [3, 25]. The aluminium foams produced by MGI have a porosity in the range from 0.8 to 0.9 corresponding to densities between 0.069 and 0.54 g/cm³ and with a pore size from 25 to 3 mm or less [2, 3, 13]. This process technology also allows the casting of nonrectangular, 2D profiles as well as 3D shapes [3, 13, 25].

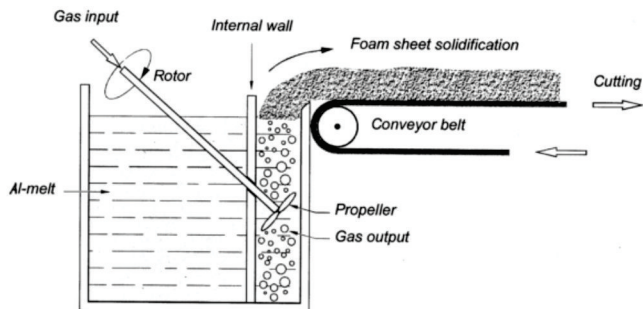


Figure 2.7: The Melt Gas Injection (MGI) process to produce closed cell aluminium foams [3].

Despite being low cost and relatively easy to produce, these foams are too closed to be a useful heat exchanger and the irregular pores mean that properties can be unpredictable.

2.4.2 IN-SITU GAS GENERATION

In this process the foaming gas results from the thermal decomposition of solid components. One version was patented by the Shinko Wire Company Ltd [30], Japan and produces a foam sold as Alporas. This starts by adding Ca or Mg to an aluminium melt at 680°C to stabilize the bubbles as a thickening agent. After this addition, the melt is stirred for 6 minutes, during which the viscosity increases continuously because of the generation of oxides (e.g. CaO , MgO , Al_2O_3 , CaAl_2O_3) owing to the oxygen affinity of these elements [30, 31]. After the melt has reached the viscosity desired, titanium hydride (TiH_2) is added, which serves as a blowing agent by releasing hydrogen gas in the hot viscous liquid as it is unstable at these temperatures. The quantity of gas generated by the decomposition of TiH_2 depends on the temperature, the higher the temperature, the more and faster the gaseous hydrogen is released [32]. The process is shown schematically in Fig. 2.8.

The foam obtained by the Alporas process is a foam with closed-cell pores. The density of the product is in the range of 0.18 to 0.24 g/cm^3 with a mean cell size of 4.5 mm

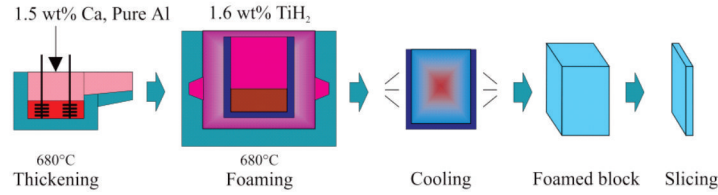


Figure 2.8: Manufacturing process of *Alporas* aluminium foam by in-situ gas generation [30].

[33]. Figures 2.9(a) and 2.9(b) show typical cell structures of two different cell sizes; the foam shown in Fig. 2.9(b), is a grade of *Alporas* optimised for sound absorbency.

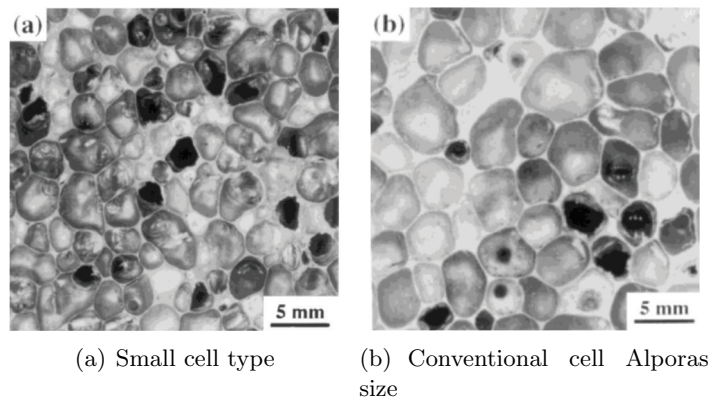


Figure 2.9: Typical *Alporas* cell structure (a) small cell structure and (b) conventional cell structure for sound absorbency [34].

The FORMGRIP (Foaming of Reinforced Metals by Gas Release in Precursors) process combines some of the advantages of the Direct Foaming of Liquid Metal and In-situ Gas Generation processes into one processing technique [1, 13]. The foaming agent (TiH_2) undergoes a pre-treatment that consists of a two-step thermal oxidation sequence (24h at 400°C + 1h at 500°C) to build up a titanium dioxide diffusion barrier layer at the powder surface to reduce the kinetics of gas evolution. In this pre-treatment the titanium hydride is mixed with AL12Si powder in a weight ratio 1:4. This metal powder helps the foaming agent to disperse in the liquid metal. The powder mixture is mixed with a molten composite of Al-9Si/SiC using conventional mechanical stirring at 1200 rpm for approximately one minute. Then, the mixed melt is cast in a graphite mould

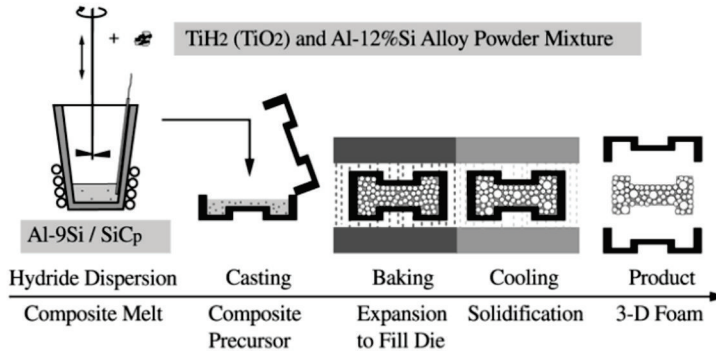


Figure 2.10: Diagram of the FORMGRIP process for the production of nearly net-shape metallic foam components [1].

(30 mm \times 30 mm \times 45 mm blocks were used in laboratory trials). These precursor blocks are almost fully dense, and can be stored if required. When needed, they are cut to size and placed in another mould, which is heated above the solidus temperature of the metal, and the temperature required to cause hydrogen evolution. Finally a cellular structure is obtained with the progressive evolution of hydrogen. Fig. 2.10 shows the FORMGRIP process schematically.

The metal foam obtained by the FORMGRIP process has closed pores; the porosity level and cell size are controlled by three main factors: a) the amount and kinetics of hydrogen evolution, b) composite melt viscosity, and c) critical cell wall thickness for rupture [1]. The porosity level presented in this process is from 0.6 to 0.9 and the cell size range is from 1 to 2.5 mm [1].

A similar method has been developed by the same researchers. The FOAMCARP process uses an alternative foaming agent (CaCO_3) that is easier and cheaper to handle [35, 36]. In this process calcium carbonate (CaCO_3) is added the same metal matrix composite (as for FORMGRIP) when it is molten. The addition is done when the metal melt is in the range 635 to 645 $^\circ\text{C}$. The foaming agent is introduced in to the melt with Al-12Si powder in a ratio 1:2 (foaming agent/ Al-12Si powder) and the melt is stirred for 40-90 s at approximately 1200 rpm. This process also produces a low porosity precursor block [35], with the amount of incorporated carbonate ~ 3.5 wt.%

of the composite mass.

Foam baking may then be carried out in a stainless steel mould, placed in a conventional air furnace with a temperature of 650 °C to 750 °C held at this temperature for 15 min. This lead to the thermal decomposition of the foaming agent and the evolution of gas (CO₂) in the melt [35]. Foams with finer cells (< 1 mm diameter) can be obtained where the baking temperature and calcium carbonate powder size determine size, structure and porosity level [35].

Metal foams obtained through *in-situ gas generation* methods in general, could be applied as a thermal insulation and sound absorbers, due to their closed cells, and therefore this type of metal foam is not suitable for use as heat exchanger because it is impossible for a fluid to flow through it to cause the heat extraction. The cell morphology obtained is almost impermeable to fluid, and for this reason this metal foam is preferred for use as a sound absorber.

2.4.3 POWDER-COMPACT FOAMING TECHNIQUE

The first step to produce metal foams by means of this technique is mixing particles of a foaming agent (such as TiH₂, as used in other processes) with metal powders, alloy powders or metal powder blends. Recently Sn powders have also been added [37] to reduce the foaming temperature. The correct selection of particle size, size distribution and purity is vital for the final properties and characteristics of the metal foam produced. Special care is required in getting a good mixture, because the distribution of alloying elements and the foaming agent must be uniform to ensure uniform pore-size distribution and the high quality of the fabricated foam. The blend is then compacted to ensure the blowing agent is embedded in the metal matrix without any notable residual open porosity which could permit gas escape [2, 13]. The combination of cold isostatic pressing (CIP) and ram extrusion has given good results and a precursor material with nearly 100 % theoretical density. The advantage in using CIPing is

to prevent the contamination of powder and powder de-mixing [13]. Special care has to be taken when the precursor is compacted; as shown by Kennedy [38], appreciable expansion only occurs for precursors with densities greater than 94 %. The precursor material (the compacted mixture) is chopped into billets suitable size.

Alternatively, the mixture can be extruded without prior consolidation, by being placed inside aluminium cartridges (in the case of aluminium or aluminium alloy foaming), before extrusion. The billets are preheated and extruded as rods or any profile. The extruded material then is chopped into small pieces and placed inside a sealed mould, which is heated above the solidus temperature of the metal powder. At this temperature gas evolves from the decomposition of the foaming agent and the compacted material (precursor material) is expanded, producing foam which may be allowed to expand until it fills the mould [2, 3, 13, 39]. When the precursor is placed inside a mould, the final foam obtained has the form of the mould, Fig. 2.11 shows a schematic diagram of the powder-compact foaming process [2]. Sandwich panels can be obtained, when sheets of aluminium or steel are rolled with a foamable precursor material, as after the heat treatment only the foamable precursor will expand. Studies have found the parameters required to obtain the optimum quality of foaming precursor through such as rolling-bonding process when Al-Si alloy powder is used as the main constituent of the precursor [40].

The morphology and expansion of the foam depends on the temperature of foaming and the size of the precursor, and is a function of the heat treatment time. It has been found that the magnitude of expansion, rates of foaming and collapse are closely related to the level oxide content in the aluminium powder [41]. The foam presents a uniform morphology before the point of maximum expansion; after this point, the foam collapses [13]. The above behaviour can be observed in Fig. 2.12, which shows the expansion behaviour of aluminium/TiH₂ when it is foamed at 750 °C.

Picture A in Fig. 2.12, shows the macrograph of the precursor before the heat treatment (at time zero), with 9 mm height and 32 mm diameter. Macrograph B shows

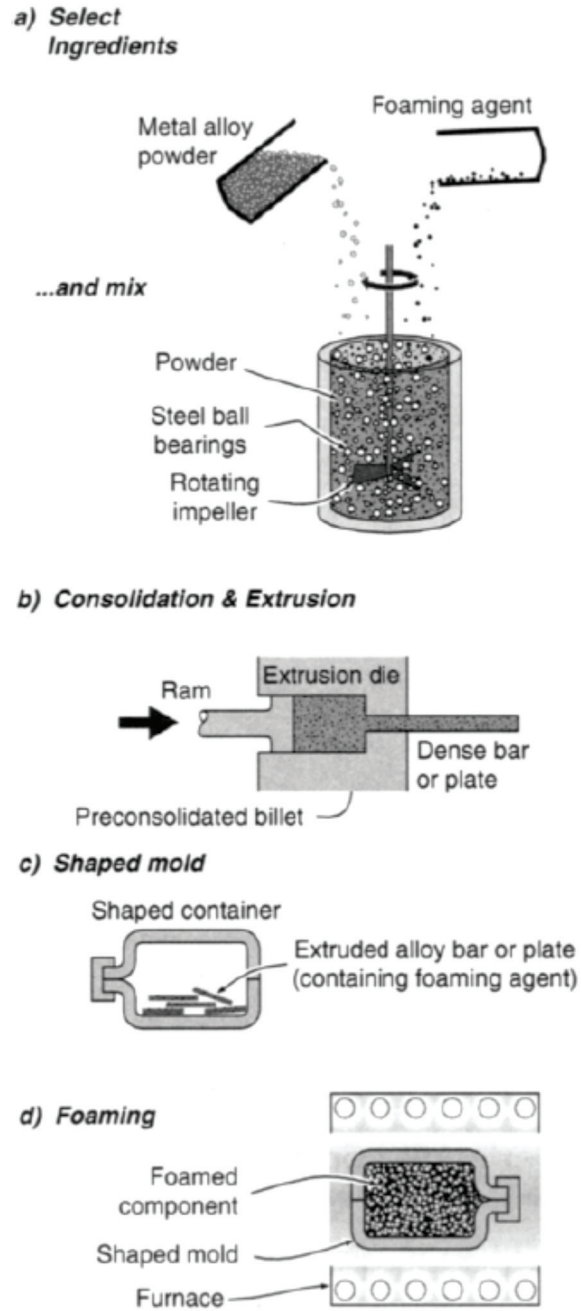


Figure 2.11: Schematic diagram of the powder-compact foaming process (the Fraunhofer and the Alulight process)[2].

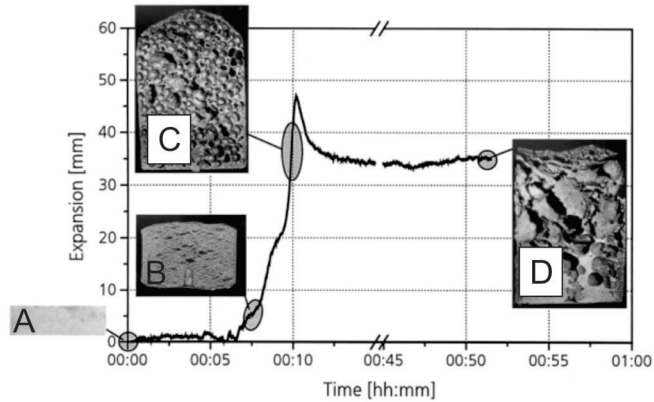


Figure 2.12: Expansion behaviour of aluminium/ TiH_2 at 750°C when a foam is produced by the powder-compact foaming technique [3].

the porosity developed after about 7 minutes of heat treatment and that the sample expansion starts to take place. Micrograph C shows the structure at 10 minutes of heat treatment, the maximum expansion of the sample with the internal porosity remains closed. Micrograph D shows the sample after 60 minutes of heat treatment, where the sample has collapsed. In this process it has been calculated that only 25% of the released hydrogen is effective in forming gas-filled pores [42], therefore efforts have been made to understand and retard the gas released by TiH_2 before the melting point of pure aluminium [43], for example heat treating TiH_2 powder of diameter $33\ \mu\text{m}$ for 15 minutes at temperatures between 400°C to 550°C . The best result obtained was at 500°C where the gas evolution was delayed until after the eutectic melting point in Al-Si alloy powder, and benefits in improving expansion were obtained.

Foams obtained using this process have closed pores and therefore have good properties for thermal isolation, mechanical and acoustic damping, due to the lack of connection of the pores [2, 13]. As with other foams of similar closed cell structure, they are however not suitable for heat transfer.

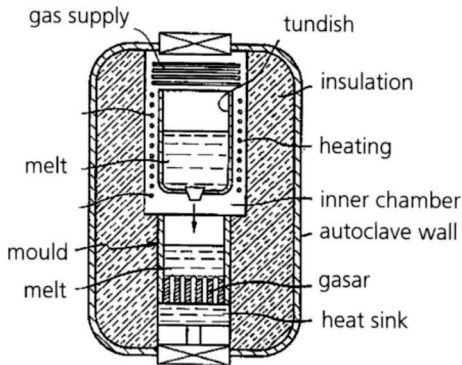


Figure 2.13: Hermetic chamber for gasar syntheses [3].

2.4.4 GAS-METAL EUTECTIC SOLIDIFICATION ("GASARS")

The eutectic system presented by some liquid metals with hydrogen gas can be taken advantage of to produce metal foams. For this to happen, a system where the liquid metal breaks down to a solid and a gas phase is required. The apparatus used to fabricate metal foam by such a method has the capacity to melt the metal in a crucible and solidify it in a casting mould under controllable gas pressure [2, 3, 44]. The bottom of the mould has a water-cooled copper chill and the walls of the mould are isolated and refractory; these characteristics mean that the heat is transferred predominantly axially via the bottom, allowing control of solidification speed of the eutectic growth. Depending on the heat removal direction, radial or uniaxial pore orientations can be created. Fig. 2.13 presents a sketch of the apparatus used to produce "gasars" or "Lotus type" pore structure [39].

The characteristic of this process is the simultaneous formation of gas-bubbles and metal crystals from the liquid. The size and nature of the gas-eutectic structure obtained is largely determined by the gas pressure; solidification velocity and pouring temperature have less of an effect on the metal foams produced under this process. The pressure is the most important technological parameter and it allows different kinds of structure to be obtained. Fig. 2.14 shows a magnesium gasar obtained sectioned normal to the direction of the pores [44].

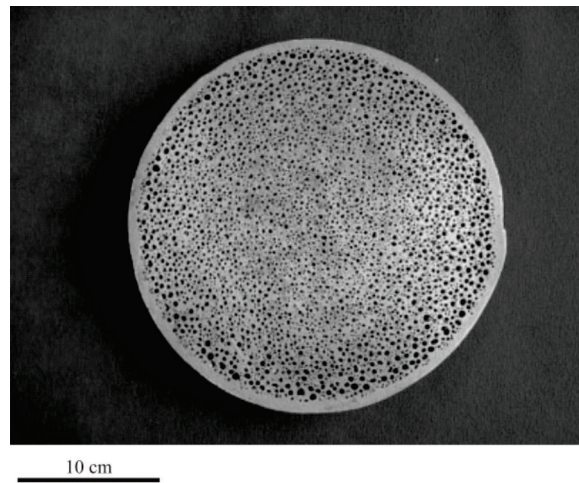


Figure 2.14: Magnesium gasar obtained sectioned normal to the solidification direction [44].

The metal foams obtained by the gasar process can have 0.10 to 0.65 porosity. The pores are elongated having always similar orientation with cylindrical, spherical or ellipsoidal shape. The heat sink condition determines the pore orientation, and the pore diameter is in the range from 10 to 1000 μm , and the length from 100 to 300 μm [3, 44].

Gasar metal foams have been tested as solid-liquid heat exchangers [44], however the pores obtained are highly orientated and the generation of turbulent flow (which causes mixing in the liquid) could thus be lower than in open cell metal foams with random pores. It is known that turbulent fluid flow is preferred to facilitate heat extraction from a solid surface by a fluid [2].

2.4.5 CASTING METHODS

Unlike the previous methods, which produce pores that are mostly closed, (and therefore will be poor for applications where fluids need to pass through the foam), more open structures can be produced by casting techniques.

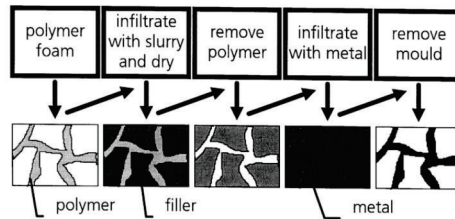


Figure 2.15: Schematic diagram of investment casting metal foam production [3].

Investment casting with polymer foams.

Just as for deposited methods, some techniques use a polymer foam template. The investment casting process starts with the selection of the cell size and density of the open-cell polymer foam. This is then coated with a slurry with high heat resistance; this material must have higher melting point than the metal or metal alloy that will be poured into it to fabricate the foam (it is therefore usually a ceramic powder). The composite (ceramic and polymer) is placed under heat treatment such that the polymer is decomposed or evaporated and the ceramic is hardened (250 to 300 °C). Into this "negative image" of the foam the metal or alloy is poured, then allowed to cool down until solidification takes place. The application of moderate pressure is necessary during the melt infiltration to ensure the complete filling of the mould. After the metal is solidified, the mould is removed by mechanical procedures; as an example water is sprayed to remove the plaster from the composite, leaving the metal equivalent of the open-cell polymer foam selected at the beginning of the process Fig. 2.15 [2, 3, 45].

Foams made by a process of this type are marketed commercially as Duocel foams by the ERG Materials and Aerospace Corporation. They are low density with large open cells and are therefore highly permeable. They are generally potentially suitable as heat exchangers, and have been experimentally investigated for a number of situations [46–51]. The results of these investigations are discussed in more detail in a later section.

Non-uniform pore structures are naturally found in nature e.g. bones and wood, being

more efficient than dense structures in some applications. For example a sandwich beam with a porous core having spatially-varying relative densities has been shown to lead to mass efficiency in load-bearing components [52]. Aluminium open-pore foams with controlled, continuous density gradient have been created using the investment casting method similar to the Duocel process. Brothers et al [53], obtained a cellular structure with a controlled different density in the same sample when the precursor was elastically compressed into the final specimen dimension (e.g. a uniform cylinder if the precursor has the shape of a wedge or pyramid). The samples obtained were analyzed and longitudinal and radial density profiles were obtained showing relative density variations from 2 to 5 % where the precursor was deformed preferentially during reshaping.

Casting around space holder materials.

Metal foams with porosities normally lower than 0.8 and with open cellular structures are obtained by this method, which consists of pouring a molten metal around removable particles or hollow spheres. In the case when hollow spheres are used as space holder, they are not always removable; for example, steel spheres have been used with aluminium to obtain metal foams with closed pores (aluminium-steel composite material) [54, 55]. The more common version uses material in a granular form as a space holder, which are commonly removed during the processing. These granules should be heat-resistant, are in some cases soluble (or removable in other ways) and must be stable when they are in contact with the molten metal; one example of this type is sodium chloride which is commonly used to produce aluminium foams under this method [56, 57]. It is water soluble, its melting point is higher than aluminium (NaCl melting point 801 °C, aluminium melting point 660 °C) and it does not have any interaction when in intimate contact with liquid aluminium [58].

To obtain a complete filling of the interstices, preheating the granules or the metal spheres, and the application of slight external pressure or vacuum in the mould where

the granules are placed is often recommended. This counteracts the surface tension of most metals and increases its flow into the space holder particles [3, 24].

After the metallic melt is infiltrated, the space holder can be easily removed due to the interconnected cellular structure formed. The space holder can be dissolved either by thermal pyrolysis, using an acid or plain water (which is used depends on the space holder used in the production of the metallic foam).

Monolithic NaCl (salt table) has been used as a space holder to fabricate open-pore aluminium foams [59]. Mortensen et al [60], concluded that varying the external pressure when NaCl particles are being infiltrated by molten aluminium the relative density of the foam could be varied between 15 % and 25 %. Goodall et al [61] fabricated the NaCl preform using either sintering or cold isostatic pressing (CIP) and showed that the relative density of the foam could be different depending which process was used to fabricate the preform and that foams obtained with sintered preforms present lower mechanical properties compared with those preforms obtained with CIP for the same relative density.

Ni-Ti based shape-memory alloy open-pore foams have been obtained in a very similar process using SrF_2 salt preform as a space holder; a potential use of this alloy in porous form is in biomedical implants with complex shapes. The NiTi-based molten alloy (melted under high vacuum) is infiltrated into the SrF_2 preform using Ar gas, the final composite obtained is then treated in an ultrasonic bath in a solution of 20 pct HNC_3 in distilled water for 2 hours to remove the SrF_2 salt. After the salt was dissolved a open foam with 0.60 porosity was obtained [62]. Although successful with a range of metals, there is a limitation with the use of single granules of material as a space holder. Above a certain size granules may be difficult to obtain in the correct shape and may not be easy to process into a preform. To overcome this, some workers have developed more advanced ways of creating a preform.

Space holders fabricated with the mixture of NaCl, flour and water (being NaCl the

major component) have been developed to fabricate aluminium foams through the same basic processes as the replication technique, for example Goodall et al [58] fabricated samples using 99.98 % Al and Al-12 Si with 5 mm pore size. Jinnapat et al [21] developed a process to obtain salt beds with a diameter between 1.4 to 2.0 mm by mixing the elements mentioned. In this case an Al-1 wt.% Mg-0.5wt.% Si-0.2 wt.% Cu alloy powder was poured on the top of the salt bed and vibrated until it had completely percolated into the gaps between the salt particles. Then the aluminium powder and the salt spheres were processed according with the process presented in Section 2.3 and samples with a relative density of 21 % were obtained.

In both works the dissolution of the space holder was done with plain water (In the case of Jinnapat et al [21] the water temperature was held at a constant 60 °C). The dissolution of these salt spheres or beads obtained through these processes was faster than for monolithic salt as in both cases they were permeable to the fluid, leading to a combination of dissolution and particle break up, and despite the extra additions to produce the preforms they did not have any noticeable interaction with the molten aluminium.

The material obtained when the space holder is dissolved (or removed by other means) is a metal foam with solid struts (unlike when metal is deposited on a template) that can have different geometries, triangular or circular depending on the density and production process. These profiles could enhance the turbulence when a fluid (gas or liquid) is flowing through it, with the potential to increase the heat transfer. The wide range of structures, includes variations in density, permeability, specific area, etc., of the final metal foam obtained under this process makes it potentially the best method to produce a foam well adapted for the use as a heat exchanger. In this investigation foams produced by investment casting and by casting around a space holder will be examined as these are the methods that have been found to produce foams with the greatest potential for heat exchange. To understand why this is, and to explore the capabilities or metal foams further, application areas (with a particular focus on thermal

behaviour) will now be examined.

Chapter 3

Applications of Metal Foams

The combination of physical and mechanical properties presented by metal foams have led to the suggested use of these materials and in recent years in industrial sectors including: aeronautics, electronics, automotive and construction, and in biological areas, at least on a research level [2, 3, 63]. The way that metal foams will act to show an advantage depends on the morphology, metallurgy, processing and economic aspects [3]. This section of the review concentrates on applications that have been commercialised or where proof of concept studies have been reported. The metal foam morphology is the most important parameter to be considered in selecting for a particular use; for example, the degree of openness of the metal foam pores is an important characteristic that will determine the suitability of the metal foam for some applications, heat transfer included. Fig. 3.1 presents the types of porosity versus some of the various application fields suggested for foams [3]. Table 3.1 reports suggested application areas for different production methods, and references for the use of metal foams (principally those made of aluminium).

In this review we will first consider applications of closed cell foams, and progress to more open forms.

New uses and applications of metal foams are continually being proposed, even though

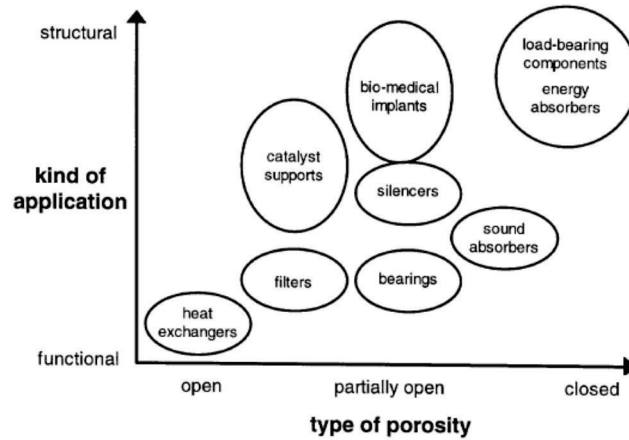


Figure 3.1: Applications of cellular metals grouped according to the degree of "openness" needed, and whether the application is more functional or structural [3].

some foams have high prices and the variation of the size and morphology of the pores in the foam are not controlled systematically in most of the fabrication processes [2, 3].

The automotive, military, railway and aerospace industries are probably the principal markets where these materials have been exploited the most to date, or have greatest potential for the future. The attractive lightweight, capacity to absorb and transfer energy and the higher mechanical resistance compared to ceramic and polymer foams, made them attractive to use [64–66]. Metal foam can be produced with open or closed pores and with several sizes and densities of pores. The choice of the best foam for a particular application depends principally on these characteristics.

3.1 Structural applications

The properties displayed by metal foams such as low density and high energy absorption, make them attractive in lightweight construction and these characteristics are relevant for the transport industry (automotive, aerospace and railway), where the low weight and the potential of high energy-absorption is significant.

There are many areas in a car body structure where metal foams can be used in a



Figure 3.2: Prototypes of crash absorbers based on extruded aluminium hollow sections filled with Cymat aluminium foam [74].

structural role, particularly areas where multifunctional applications can be exploited, like car frame parts or the boundaries of the floor of the passenger compartment [13, 67]. Currently, relatively high performance cars such as the Ferrari Modena Spider F430 and F360, are manufactured with foam parts, which improve the stiffness of the profiles without increasing the car weight significantly; these metal foam parts are produced by Alulight International [68].

These impact resistance aspects of these applications are based on the capacity of the metal foam to absorb large quantity of mechanical energy by plastic collapse when deformed. Thin-walled tubes may be filled with aluminium foam by press-fitting (e.g. the square tube in Fig. 3.2), or by placing a solid precursor into the cavity to be filled and then re-heating to cause the precursor to expand (powder-compact foaming technique), e. g. the circular tube in Fig. 3.2. Higher energy absorption than the sum of the energy absorptions of the cylindrical tube alone and foam alone is obtained when the sample is tested is under uniaxial compression [69, 70]; the same behaviour is found when square tubes are tested [71]. In work performed by Hall et al [72], it was found that the advantage persists in the transversal direction. This property is very attractive as a passive safety system in vehicles, and reductions in fatalities and injuries could be achieved as a result of the implementation of tubes filled by aluminium foams instead of aluminium or steel tubes with thin walls [73].

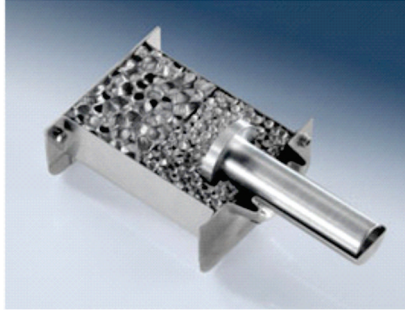


Figure 3.3: Metal foam fitted crashbox manufactured by Metcomb [75].

Using a foam filled crashbox can reduce the repair cost when it is placed between the impact beam and the front rail of the car, because it can reduce or absorb the energy of collision and then simply be replaced. This crashbox absorbs more energy than a empty section of similar mass, due to the collapse capacity of the metal foam when it is under uniaxial compression [70, 74]. Fig. 3.3 shows crashbox manufactured by Metcomb Nanostructures [75], the same concept is used when the metal foam is placed inside the bumper.

Subframes, control arms, cross-members etc. are some examples of highly loaded structural components where cast metal foam is expected to be applied as a solution to problems associated with mechanical vibrations and/or as a passive safety system [76–78]. A composite part was produced by Leitlmeier et al as a prototype of a BMW engine mounting bracket [78], where a *METCOMB* foam was embedded in dense metal by low pressure die casting of aluminium around it. The foam section of the part did not present perceptible infiltration during the casting. Fig. 3.4(a) shows the process to embed *METCOMB* foam and Fig. 3.4(b) the final BMW component produced.

Aluminium foam sandwich (AFS) Fig. 3.5 is a sandwich structure with two thin outer layers of a dense, stiff material separated by a central core of foamed metal [79] which can be used to replace conventional stamped steel parts in a car having a significant weight reduction, these sandwich foams developed by Fraunhofer-IFAM in Bremen and Karmann GmbH, a German car builder, are very stiff at a relatively low weight and are competitive with technologies such as waffle structures or honeycombs, due to it being

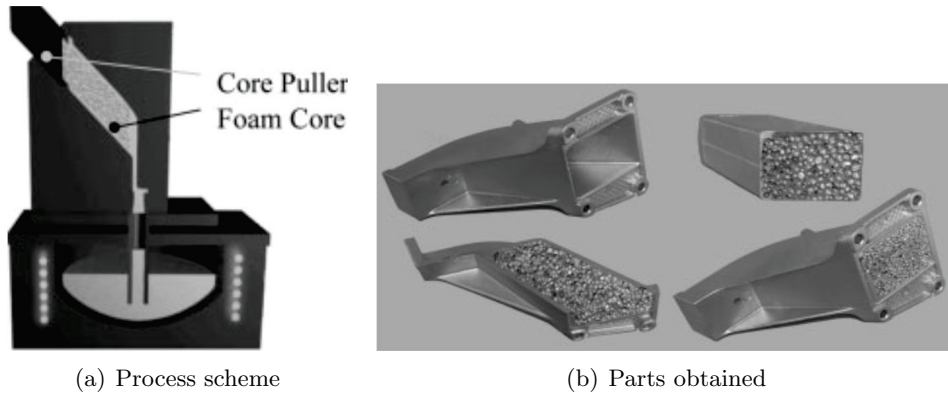


Figure 3.4: Aluminium foam as a core for casting. (a) Schematic diagram of the method of embedding foam cores by low pressure die casting. (b) Prototype of a BMW engine mounting bracket [78]



Figure 3.5: Aluminium foam sandwich (AFS) produced by Karman, Osnabruck (Germany) [80].

possible to manufacture complex shapes by deforming the foamable precursor prior to foaming, something that cannot be done with the competing technology [67].

In order to comply with European legislation, AFS was used to reduce the weight of a small lorry to less than 3.5 tonnes. The application of AFS was in the working platform where the telescopic arm support, Fig. 3.6, had to be increased from 20 to 25 m length, while maintaining the weight of the vehicle below 3.5 tonnes. This could be realized using AFS, because using only aluminium sections would not be able to support the weight of the platform [67, 80]. The implementation of this new material was not



Figure 3.6: Base of a lifting arm for a truck made from AFS sandwich panels. [67].

straightforward, due to the need to redesign the complete construction of the platform [80], but it allowed the lifting height of the system to be increased, while keeping the weight below the required level. This demonstrates the way that metal foams can be used to achieve some design goals within legislative requirements. Architectural panels and solar thermal energy (supporting the reflecting foils) are other actual applications of AFS where the high stiffness-to-weight ratio is exploited [81].

3.2 Sound absorbers

By acting as a barrier to air movements, and by diverting and absorbing the energy from these movements, metal foams can act as sound absorbers.

Using metal foams as sound absorbers has evident advantages over other candidate materials such as glass wool and polymer foams, due to their strength and rigidity, low moisture absorption and fire resistance. The sound absorption coefficient, a , is the ratio of the unreflected sound intensity at the surface to the incident sound intensity; this coefficient is the ability of the material to absorb sound and to be an effective sound absorber, the coefficient must exceed 0.9; this means that 90% of the sound energy is absorbed in the material. Data reported by Lu et al suggest a sound absorption coefficient between 80% and 95% could be achieved in selected frequency ranges in se-

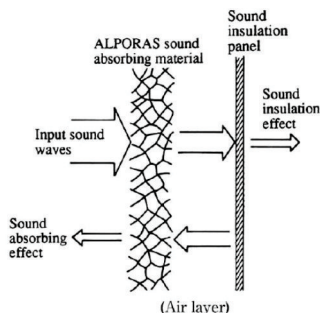


Figure 3.7: Schematic diagram showing how Alporas metal foam could be used as a sound absorbing material [83].

lected aluminium alloy foams [82]. This property makes them attractive candidates for a wide-range of applications in noise and vibration control of automobiles, machinery, aircraft and buildings, particularly where a high temperature environment is present or where the mechanical property advantage can be used.

The manufacture of Alporas metal foams by the Shinko Wire Co., Ltd. has led the development of sound absorbing material with the objective to be installed along the side of a road or highway to reduce the traffic noise [2]. The following advantages have been suggested by the producers; resistance to temperatures as high as the melting point of the aluminium (660°C), no toxic gas emission, no need for the use of supporting elements like glass wool due to it being a rigid material, easy to install, does not absorb moisture and is easy to clean. Fig. 3.7 shows a sketch of the Alporas metal foam functioning as a sound absorbing material; this system comprises the foam, an air layer that reduces the sound pressure behind the barrier and increases the effectiveness of the soundproofing material and the sound insulation panel (which could be an iron plate or other high density material) [34, 83].

3.3 Vibration suppression

As well as absorbing sound in the air, metal foams can act to dissipate and damp vibrations. Structures of ships, aircraft, automobiles and mass transit bodies may

produce excessive vibration because they are subject to a wide range of dynamic loads. As well as affecting comfort, this can lead to damage of the structure. To avoid this, a high damping capacity, expressed by the damping ratio (ξ) is desired (damping ratio can be described in terms of loss factor (η), which is equivalent to twice the critical damping ratio [84]). Metal foams present higher loss factors (η) and damping ratio compared to solid structures fabricated with the same amount of the same material. It has been observed that the damping ratio is highest in foams with lowest densities [85, 86]. Aluminium Foam Sandwich (AFS) panels are being increasingly used in a number of applications to reduce vibrations that can damage the integrity of the structure, such as in turbine shrouds, fan blades, energy absorbers for blast shock waves and cylinders for jet engine intakes, among others [84, 87].

3.4 Filters

Metal foams with good corrosion resistance are being considered for use as filters to trap soot particles in passenger car exhaustment produced by diesel engines. The EURO IV regulations have imposed strict particulate emission limitations for passenger cars in Europe [88]. To reach these objectives is necessary to have a cellular material with good corrosion resistance at temperatures up to 600 to 800 °C with good permeability to not affect the engine performance, as the efficiency of the engine is highly affected by the pressure drop in the exhaust [88]. In practice, this means that foams must have a very open structure. A process to manufacture high temperature resistant Fe-Ni-Cr-Al foams has been presented by Walter et al [89], where a powder metallurgical process allows a nickel foam to be converted into an alloy foam with high temperature corrosion resistance. The filters are produced by coiling the foam strip [89], and these are used to extract solid particles dispersed in the gas.



Figure 3.8: Heat exchanger in the lens of a Scanning Electron Microscope [91]. No scale is provided in this reference, however if the pore size is around 5 mm (typical for this foam type), then the part would be roughly 15 cm diameter.

3.5 Heat Exchangers

With the need to cool systems such as power electronics, and the desire to recapture waste energy, heat exchangers are increasingly important in engineering. The use of metal foams as a heat exchangers offers potential reduction in cost and weight, good fluid mixing due to turbulent flow caused by the random foam structure and potentially an increase in performance owing to the elimination of thermal interfaces between the source of heat dissipation and the heat sink if the foam can be integrated with the component. Normally the need is to cool down the device, or in some cases maintain its temperature in a narrow range, to have optimal conditions for performance, e.g. electro-optic systems where global or local thermal displacements may give rise to alignment-related optic losses [90]. The ERG Materials and Aerospace Corporation produces an aluminium foam (Duocel, believed to be produced by the investment casting process) that is incorporated to the lens of a Scanning Electron Microscope to stabilize its temperature, Fig. 3.8 [91]. More generally, cooling is required; any system integrated with high performance power devices into the megawatt level of power, or those where critical components have to be kept cool would be a suitable application of metal foam as heat exchangers.

In the aircraft industry, gas turbine engines are demanding more cooling capacity from the engine system than the conventional delivery system can offer [92]. Experiments

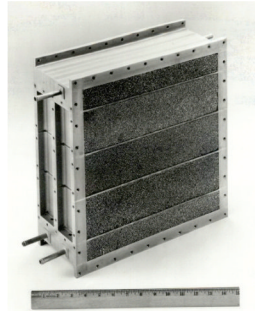


Figure 3.9: Heat exchanger in the CO₂ scrubber used in the Space Shuttle [91].

at laboratory scale and in a full-scale test rig have found that the heat transfer is increased by a factor of two with tubular open cell stainless steel foams when they are compared with a plain bank of staggered tubes. However this increment in the heat transfer is almost neutralized by the increment of the pressure drop in the actual system. This highlights an important issue with heat exchange in that good thermal performance is required but this must be coupled with a low cost in energy to maintain the cooling fluid flow through the heat exchanger. Foams have not been implemented in the above application, but the author of this study, Sabatino et al, suggest that changing the configuration of the turbine fuel tubes to cross-flow instead of counter-flow could reduce the number of tubes by 40 % and this combined with the use of metal foams as a heat exchanger, means the engine could be cooled with more efficiency and the weight and volume of the actual heat exchanger could be reduced considerably [92].

The Space Shuttle and the International Space Station use an aluminium open cell metal foam as a heat exchanger in the CO₂ scrubber, where it also acts as a chemical support matrix, Fig. 3.9. The efficiency and the response rate of the system is increased by the high thermal conductivity presented by the aluminium foam. The whole system occupies less than 0.32 m³ on board the Orbiter and weighs less than 150 kg. The contribution to the weight made by the foam is negligible, but its efficiency helps to save weight elsewhere in the system [93].

These examples for metal foam applications as heat exchangers are quite specific, mostly

for low volume (albeit high value) products. An area where metal foams could be used in much larger amounts would be the cooling of power electronics.

The flexibility presented by metal foams in terms of compatibility with the encapsulation materials of various semiconductor devices, such as ceramic, metallic or composite materials, as well as the capacity to be tailored (i.e. controllable pore size, density, properties being affected by processing and post treatments like annealing or compression), has made them one of the most viable options to dissipate the heat generated by current and future semiconductors and electronic devices [94, 95]. When a metal foam (20 PPI aluminium foam) was attached to a power module it was found to be able to dissipate the energy generated at more than twice the rated power of a state-of-the-art heatsink [95]. As a result, this research suggests that the use of metal foams as heatsinks in military and commercial power modules may offer significant advantages with respect to cost versus performance, volume and weight.

Most thermal applications are for open cell foams, closed metal foams can be used as heat insulating materials, owing to their temperature and fire resistance and as they do not generate harmful gases in the presence of flames [2, 96].

The testing of metal foams for applications involving heat transfer is relatively infrequent. However there are a number of indications, coming from studies of the fundamental heat transfer processes, that this may be one of the applications where metal foams offer the greatest promise. To see why this is we will now look at these investigations in more detail.

Table 3.1: Production methods, physical characteristics and applications of some types of metal foams.

State	Method/ Submethod	Reference	Pore size range/ PPI	Density range (%)	Cells	Application	Reference
Liquid state processes	Gas injection ^{DF}	[2, 3, 13, 24]	3-25 mm	3 - 10	closed	Acoustical, fire resistance, lightweight structure, vibration control, core structure, impact absorbers	[2, 3, 13, 24, 25, 77]
	Blowing agent/gas releasing particles ^{DF}	[1-3, 13, 24]	2-10 mm	7 - 20	closed	Acoustical, fire resistance, lightweight structure, Vibration control, impact absorbers	[2, 3, 13, 24, 30, 35]
	Solid-gas eutectic solidification Gasar	[2, 3, 13, 44]	10 μ m -10 mm	5 - 25	closed	Liquid heat extraction, core structure	[2, 3, 13]
	Powder compact melting technique	[2, 3, 13, 39]	1-5 mm	> 8	closed	Core structure, lightweight structure, medical application	[2, 3, 13, 39]
	Investment casting with polymer foam ^{CM}	[2, 3, 13, 24, 35]	1-5 mm (5-40 PPI)	3 - 20	open	Heat exchangers, lightweight structure, filter, core structure	[2, 3, 13, 24]
	Lattice block materials ^{CM}	[3, 97]	Lattice spacing between 6.5 to 25 mm		open	Lightweight structure	[3]
	Around space holder materials ^{CM}	[2, 3, 13, 24, 58, 59]	1-5 mm	> 20	open	Heat exchangers, lightweight structure, filter, core structure, acoustical	[2, 3, 13, 24]

DF Direct Foaming

CM Casting Method

State	Method / Submethod	Reference	Pore size range / PPI	Density range (%)	Cells	Application	Reference
Solid state processing	Sintering of metals powders and fibers	[2, 3, 98]	200-500 μ m	50 - 80	open	Gas and fluid filtration, flow control	[2, 3]
	Gas entrapment technique	[2, 3]	10- 100 μ m	> 50	closed	Lightweight structure	[2, 3]
	Foaming slurries	[3, 24]			closed and open	Filter, battery electrodes	[3]
	Cellular metals based on space holding fillers	[2, 3, 20, 21, 99, 100]	0.4-2.5 mm	20 - 40	closed and open	Filter, lightweight structure	[2, 3, 99]
Electro-deposition	Metallic hollow sphere structures	[2, 3, 13]	100 μ m - 8 mm	> 20	closed and open	Fire resistance, lightweight structure	[2, 3, 13]
	Metal powder/binder method	[3]	< 1 mm	< 50	closed	Acoustical, vibration	[3]
		[2, 3, 101]	6-70 PPI (4-0.3 mm)	2 - 7	open	Heat exchanger, filters, battery electrode	[2, 3]
Vapour deposition		[2, 3]	6-70 PPI (4-0.3 mm)	2 - 30	open	Heat exchanger, filters, battery electrode	[2, 3]

DF Direct Foaming
 CM Casting Method

Chapter 4

Thermal and Fluid Flow Properties

The permeability to fluid of an open cell foam, coupled with the high conductivity of a metal immediately suggests applications in heat exchange. According to Ashby et al [2] if we compare metal foams with their non-metallic counterparts we will have at least an order of magnitude of thermal conductivity greater, due to the inherently high thermal conductivity of metal. Further to this, the capacity of metal foams to withstand high gas pressure, irradiation and extreme temperatures have aroused a great interest in the study of how heat transfer takes place in these materials for applications in extreme environments.

The heat transfer capabilities of a metal foam is determined by both the metal or alloy from which it is made, and the structural characteristics (in other words the size of the pores in the metal foam, their amount and distribution) of the foam. The effect of these characteristics is important in understanding the complex interplay between service conditions, pore architecture/pore size, thermal conduction, convective heat flow and fluid permeation characteristics [102].

Metal foams have a wide range of potential applications, as detailed in Chapter 3. Of

these, in recent years interest in these materials has increased in particular in applications as heat exchangers, due to the capacity to exchange heat between a fluid and the open cell foam, and hence between a fluid and a solid the foam is in contact with.

Electronic system applications are one of the most challenging areas in heat transfer science. One example is the need to continually increase thermal dissipation, as consequence of the continuing demand of high speed and miniaturization of electronic components [103]. Air cooling, sometimes using dense metal fins to increase surface area, is one of the current technological solutions for cooling in these applications, giving a heat transfer of about $4.2W/cm^2$, while in the near future the power dissipation required in those systems is expected to be around $30W/cm^2$ [65]. The characterization of fluid flow and heat transfer behaviour of metal foams is required so they can be used in these applications [2, 65, 104, 105].

To achieve the requirements of heat dissipation, the metal foam has to be immersed within a flowing fluid (gas or liquid). Air-cooling is still preferred for simplicity (it does not have to be a closed loop system) and because this cooling system does not risk damage from a leak, which would be a problem if the cooling was a liquid. Forced convection in porous media have been studied in the last 60 years, but only during the last 20 it has been studied in metal foams [104].

4.1 Foam conductivity

The thermal conductivity of a cellular material is depends on the conduction through the solid phase, conduction through the gas phase, convection of the gas and radiation. Like any composite of two distinct phases, the conductivity of a porous material will depend on the bulk properties of the two phases involved, and the structure they form. The quantity " k " represents either the electrical or thermal conductivity tensor, which are mathematically equivalent properties and can be estimated in a similar way to other properties, such as effective dielectric constant, effective elastic modulus, etc. Upper

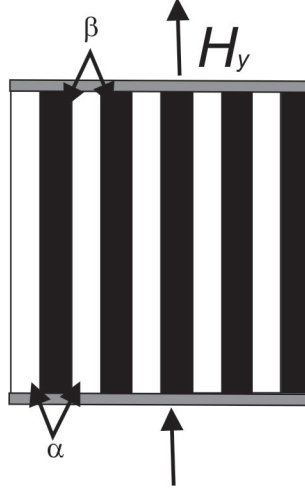


Figure 4.1: Diagram of the structure for the rule of mixtures estimate of thermal conductivity (upper bound).

and lower bounds are established by the rule of mixtures, which gives expressions to describe the maximum and minimum limits of the conductivity of a composite with two phases and are expressed as follows:

Considering a material with two distinct phases, stacked as is shown in Fig. 4.1 (heat flow in Y direction, H_y); since the phases are in parallel, heat flows along each in function of their volume fraction and the thermal conductivity is given by the upper bound of the rule of mixtures as follows:

$$k_u = \Delta_\alpha k_\alpha + \Delta_\beta k_\beta \quad (4.1)$$

where k_u is thermal conductivity (upper bound) of α and β phases, Δ_α is the volume fraction of the α phase layer and Δ_β is the total volume of β ($\Delta_\beta = 1 - \Delta_\alpha$).

For the X direction (heat flow in X direction, H_x , Fig. 4.2), the phases are perpendicular to the direction of the heat flow, and heat must pass through both layers in series. Here the thermal conductivity is given by the following equation:

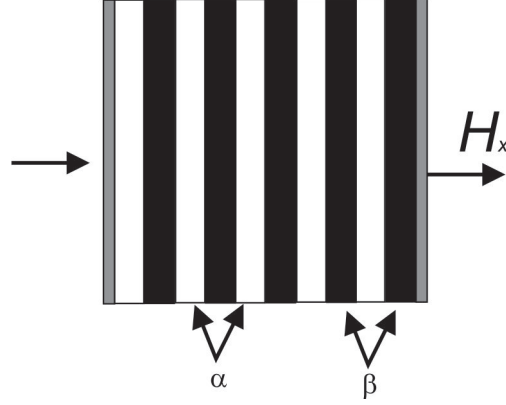


Figure 4.2: Diagram of the structure for the rule of mixtures estimate of thermal conductivity (lower bound).

$$\frac{1}{k_l} = \frac{\Delta_\alpha}{k_\alpha} + \frac{\Delta_\beta}{k_\beta} \quad (4.2)$$

where σ_l is the thermal conductivity (lower bound).

This is a very approximate measure for a physically unlikely structure. When the material is considered as periodically distributed inclusions of material 1 in a continuous matrix of material 2, and it is assumed that material 1 occupies a volume fraction of Δ_β and has a thermal conductivity of k_β and that material 2 has a thermal conductivity of k_α , where $k_\alpha > k_\beta$, the relative thermal conductivity of this material can be bounded using the Hashin-Shtrickman lower k_l and upper bounds k_u for thermal conductivity for a two phase composite as follows [106, 107]:

$$k_l = k_\beta + \frac{\Delta_\alpha}{\frac{1}{k_\alpha - k_\beta} + \frac{\Delta_\beta}{3k_\beta}} \quad (4.3)$$

$$k_u = k_\alpha + \frac{\Delta_\beta}{\frac{1}{k_\beta - k_\alpha} + \frac{\Delta_\alpha}{3k_\alpha}} \quad (4.4)$$

The bounds take into consideration only the volume fractions of the different constituents ($\Delta_\alpha, \Delta_\beta$). This ratio is the key macroscopic parameter that determines the

electrical/thermal characteristics of a heterogeneous material.

Using more detailed equations that capture more of the complex behaviour in these materials, the ratio of thermal and electrical conductivity has been calculated by some authors as the governing equations for electrical and thermal conduction in the material in the porous structure. Goodall et al [108], reports the equations produced by several models that are based on different structural concepts, and which have had applicability to multiple sets of experimental results (Table 4.1).

Table 4.1: Equations specified by various models for relative conductivity of foams as a function of the volume fraction porosity Δ . The parameter k refers to the thermal conductivity, with the subscript f for the foam and 0 for the solid, nonporous metal. Parameter Δ_f is the volume fraction solid phase of the foam [108].

Model	Equation	Equation No.
Hashin-Strinkman upper bound	$\frac{k_f}{k_0} = \frac{2(1-\Delta)}{3-(1-\Delta)}$	(4.5)
Lemlich	$\frac{k_f}{k_0} = \frac{(1-\Delta)}{3}$	(4.6)
Ashby et al	$\frac{k_f}{k_0} = \frac{1}{3} [(1 - \Delta_f) + 2(1 - \Delta_f)^{1.5}]$	(4.7)
Ashby structure	$(1 - \Delta_f) = 3 \left(\frac{k_f}{k_0} \right) - 2 \left(\frac{k_f}{k_0} \right)^{1.5}$	(4.8)
DEM (sphere)	$\frac{k_f}{k_0} = (1 - \Delta)^{1.5}$	(4.9)
DEM (ellipsoids)	$\frac{k_f}{k_0} = (1 - \Delta)^n, n > 1.5$	(4.10)

The application of the models as was mentioned, depends on the structure; for example, the model of Lemlich is applicable in open cell foams with low relative density, such as Duocel samples, in this model the material in the nodes is not taken into consideration. The Ashby et al model takes into account the effect of the material in the node of the structure for open foams with low relative density, however, for cellular structures with high relative density, over 47 %, the conductivity that is predicted exceeds the upper bound specified by the Hashin-Shtrikman model. For foams with high relative

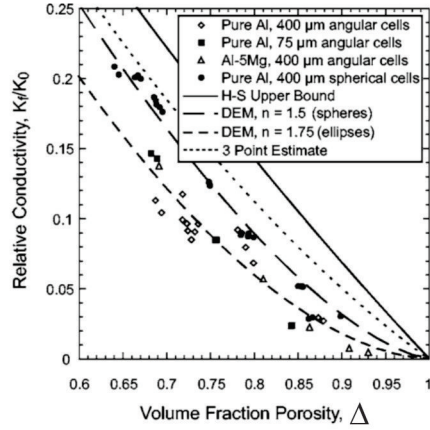


Figure 4.3: Comparison between the models of Table 4.1 and measurements developed by Goodall et al [108].

density, Ashby proposed the "cubic unit cell" that is reported in Table 4.1 as the Ashby structure [108].

The differential effective medium (DEM) scheme proposed two models, one for a non-conducting spherical phase (exponent $n = 1.5$) and one for nonequiaxed nonconducting phase (exponent $n > 1.5$). According to Goodall et al [108], these two models have provided good agreement with data for the conductivity in two-phase materials combining a nonconducting discrete inclusion phase embedded in a conductive matrix (a broad definition that includes metal foams).

Goodall et al [108] fabricated aluminium foams by replication technique with angular and spherical shape using as a preform NaCl particles that were isostatically pressed or sintered. The foams were fabricated with pure Al and Al-5Mg alloy, and with cell sizes of either 75 or 400 μm . Electrical conductivity was measured at ambient temperature in the samples fabricated using the four point technique. The results obtained were compared with the models reported in Table 4.1 and are shown in Fig. 4.3 where it is possible to observe that samples with angular and spherical pores obtained by the author have a good agreement with DEM for spherical and ellipsoidal pores.

In this thesis the Lemlich model was used in Chapter 10 to calculate the effective ther-

mal conductivity (k_{eff}) of Duocel foams and DEM model (for spheres) for the foams fabricated by replication technique, following the correlations found in this previous work.

Dharmasena et al [109], develop an analysis to characterize the electrical conductivity in Duocel aluminium foams with range of relative densities from 4 % to 12 % using the four-probe method to measure the resistivity of the foam and were compared with a model developed. In the method used for the author an inline four-point probe is placed on the surface of a thick sample Fig. 4.4. A direct current is passed through the specimen between the outer probes (P1 and P4), and the resulting potential difference is measured between the inner probes (P2 and P3). This is used to calculate the electrical conductivity σ (units, $\Omega^{-1} \cdot m^{-1}$), which is the reciprocal of the measured resistivity. The experimental measures were compared with a model developed based on tetrakaidecahedral unit-cell representation of the foam structured. The comparison showed that the electrical conductivity increases linearly with relative density in experimental and model results, and those values obtained with the model overestimate the electrical conductivity. With the objective to have a closer agreement with experimental and model results, the author modified the model; i.e. varied the effect of the cross section and reduced of quantity of active ligaments, obtaining a better fit with the experimental results. Despite adjustments the model shows a good representation to obtain the electrical conductivity of the metal foam.

Solorzano et al [110] used the transient Plane Source Technique (TPS) method to measure experimentally the thermal conductivity of metal foam samples of ALSi7 foams with porosities between 0.5 and 0.8 produced by the power metallurgy process. The TPS sensors used in this method consist of a sensor element in the shape of a double spiral. This TPS sensor acts both as a heat source for increasing the temperature of the sample and a resistance thermometer for recording the time dependence of the temperature increase. In the most of the cases the sensor element is made of nickel, which is encapsulated and is placed between two samples of similar characteristics.

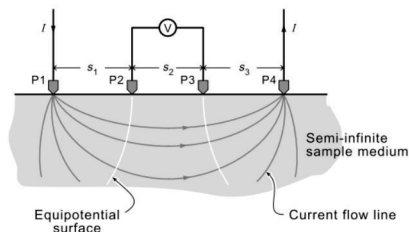


Figure 4.4: Four-point probe method for measuring the electrical conductivity of metal foams [109].

During a pre-set time, 200 resistance measurements are taken and from these the relation between temperature and time is established. As this is a contact method, special care has to be taken to minimize thermal contact resistance between the sensor and the samples that will be measured. Good contact between sample and measurement sensors is required in many thermal property tests, due to the large thermal resistances that can be introduced by even a slightly sub-optimal contact.

Measurements were carried out in the three cardinal directions of the sample (X , Y and Z), where the sensor was in direct contact with the outer skin of the foam (identified in this study as $-Y$, $+Y$, $-Z$ and $+Z$ directions) and where the outer skin was not present (faces $-X$ and $+X$). The internal structure and density of the samples were obtained using a helical medical scanner. The results obtained show that there is an influence on the thermal conductivity when measurements are made on faces with outer skin, having higher values of thermal conductivity than when the measure was done on faces without it (for instance, measure developed in sample identified with number 7 presents 36.5 W/mK thermal conductivity in face with outer skin, and 33.9 W/mK in one face without outer skin). The results obtained as well that the thermal conductivity increase when the porosity decreases.

Analytical and experimental studies have been carried out to understand the difference in the heat transfer mechanisms (convection, radiation and conduction) between cellular polymers and metal using analytical models and experimental data to predict the conductivity of these two cellular materials under diverse structural parameters

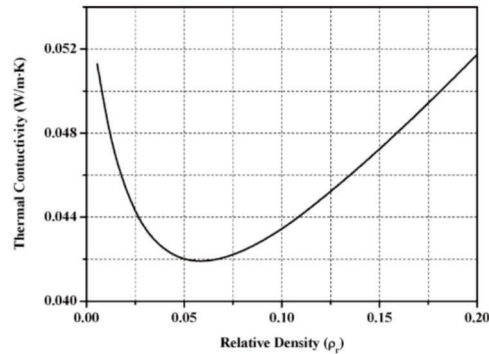


Figure 4.5: Theoretical thermal conductivity as a function of the relative density for low density and cell size $880 \mu m$ [111].

(relative density, cell size and cell geometry) [111].

Closed cell materials based on insulating solids such as polymers, theoretically present a dependence of the conductivity on the amount of material present; however, for densities below 5 % the conductivity was found to increase with further reductions in density. This behaviour was unexpected for the authors of Ref [111] Fig. 4.5, who explain this behaviour due to the strong influence of radiation at very low densities, where the lower amount of solid material means that cell walls are thinner and are therefore more permeable to thermal radiation. This effect is possible in polymeric foams, but would not occur in a metal.

For cellular materials with high thermal conductivity of the base metal the effect of density is dominant. However, the tortuosity of the structure also has a high influence in the conductivity of the porous material, this is shown in the work presented in Fig. 4.6. Several different structures were analysed; idealised hexagonal and, real structures with different density (the parameter d in Fig. 4.6, is the thickness of the cell wall in the metal foam), the results were obtained by simulation for Voroni tessellations (Voroni tessellations is the partitioning of a plane with n points into convex polygons such that each polygon contains exactly one generating point and every point in a given polygon is closer to its generating point than to any other) and real structures. Fig. 4.6 shows that the real structure gives rise to a lower thermal conductivity and this is

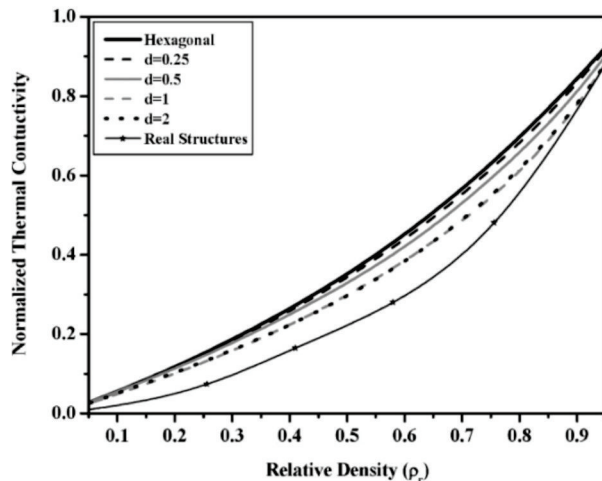


Figure 4.6: Results obtained by simulation for varonoi tessellations and real structures [111].

explained in terms of the tortuous shapes that pores present in the real material.

This aspect of foam behaviour was examined further by Conquard et al [112] develop an analytical model based on finite element methods to estimate the influence of each of the geometrical parameters characterizing the porous structure of the foam (such as solid fraction, shape of the cells, strut cross section and size of the cross section along the length of the strut), on the magnitude of the conductive heat transfer in metallic/ceramic open-cell foams. The agreement of the model was checked with the results from the literature. The numerical study showed that the morphology of the strut forming the open cellular structure is the structural parameter with the greatest effect on the effective conductivity. The magnitude of the conductivity is affected also by the distribution of the solid along the strut length and the concentration of solid matter at the intersection of the struts, which reduces the heat conduction through the foam (which is understandable, as metal at the node does not transport heat through the structure). Conquard et al found that the cell diameter and cell shape do not have any influence in the effective conductivity. In case of the cross sectional shape of the strut, the influence on the effective conductivity is slight and is negligible other than for very low solid fractions and no influence of cell diameter in the effective conductivity

was found.

The above was also found in the work of Bhattacharya et al [113] where analytical and experimental characterization of more than 20 aluminium samples with different densities and pore sizes were developed to determine the effective thermal conductivity k_e (among other thermophysical properties) of foams over a wide range of structures. The experiments were performed with air and water as fluid media and shown that as would be expected the effective thermal conductivity strongly depends on the porosity [113]. As both of these studies used low density foams it is reasonable that conduction along struts dominates, and cell size / shape has a small effect. It has also been shown by Goodall et al [108], that although foams of different structures follow different models, none requires a term for the cell size.

4.2 Foam permeability

In order to produce the best material for a heat exchanger, the aim must be to maximise the heat transfer coefficient (see later) and minimise the pressure drop for fluid flow through the structure. It is therefore critical to have an understanding of the permeability (K) of metal foams. Darcy was the first to perform recorded experiments of flow thorough a porous medium; he discovered that the area-average fluid velocity (u) through a column of porous material is proportional to the pressure gradient and inversely proportional to the viscosity (μ) of the fluid seeping through the porous material and may be represented as follows:

$$u = \frac{K}{\mu} \left(-\frac{dP}{dx} \right) \quad (4.11)$$

where dP is the difference of pressure and dx the length of the column of porous materials.

Since then experimental measurements have been performed on several occasions for

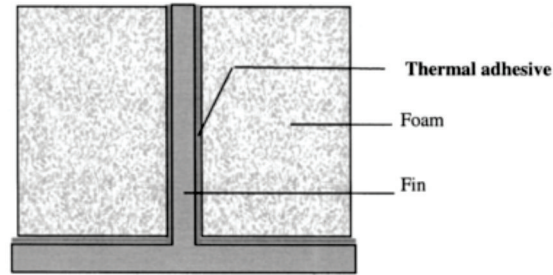


Figure 4.7: Schematic of the 1-finned metal foam heat sink tested, along with other numbers of fins, by Bhattachayra et al in forced convection heat transfer experiments [65].

metal foams. These materials have been studied due to either the higher mechanical resistance than a similar polymer foam or because of their potential engineering applications as mentioned in Chapter 3. The pressure drop across the heat exchanger is an important issue when metal foams are used as heat exchangers under forced convection in many practical applications; therefore it is important that it is characterized. Bhattacharya et al [65], used an experimental set up shown schematically in, Fig. 4.17 to characterize the behaviour of aluminium foams with 20 and 5 PPI incorporated in longitudinal or pin shaped fins having a porosity of 0.9 with a different number of fins used for each sample Fig. 4.7. Bhattacharya et al found, for their finned samples, that the pressure drop increases when the pore size decreases. Fig. 4.8 shows the differences of pressure across samples of 20 and 5 PPI with four fins as a function of flow velocity. It is possible to observe that the pressure drop increases when the pore size is reduced. However, for a given pressure drop a higher heat transfer coefficient can be obtained with 5 PPI than 20 PPI, meaning there is still a potential benefit to use this smaller pore size.

Using water as coolant to determine the hydraulic behaviour of Duocel aluminium foams, in data calculated on a Darcian flow velocity basis, Boomsma and Poulikakos [47] found that in foams that were increased in density, starting with 0.95 and 0.92 porosity, the density affected the permeability. This was achieved by compressing the sample, i.e. as Duocel is available in a limited range of (low) densities Boomsma

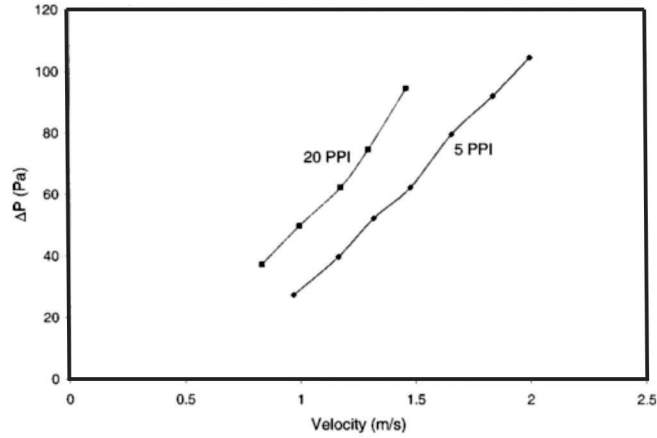


Figure 4.8: Pressure drop characteristics for the samples with four fins [65].

and Poulikakos crushed the foams to increase density before testing, both densities presents the same sensitivity in permeability with the compression, when the aluminium sample is compressed the permeability was reduced. The effect of compression to higher densities (to a highest density of 92 %) was similar for both samples tested.

Peak et al [114], constructed a experimental rig to measure the permeability to air flow of aluminium foams with $90 \times 190 \times 9.1$ mm in width, length and thickness, 0.89 to 0.96 porosities and 0.65 to 2.50 mm cell sizes, is shown in Fig. 4.9. The flow air was supplied by a compressor and regulated by using a rotameter. Before the air entered the test section a flow straightener was used to obtain a well-controlled and calm uniform stream. The pressure drop was monitored by using a micromanometer and an inclined manometer was used as a backup device.

The measurements of pressure drop for three different cell sizes ($d = 0.65$ -2.50 mm) in the x - direction (left to right in Fig. 4.9), are displayed in Fig. 4.10. Peak et al interpreted these results by noting that as the cell size d of a metal foam decreases, the surface-area-to-volume ratio increases and this means additional flow resistance. An empirical quadratic curve fit to the data of Fig. 4.10 allow the permeability (K) of these samples to be found and led to the conclusion that the permeability increases as the cell size d increases for a fixed porosity, and when the porosity increases it results

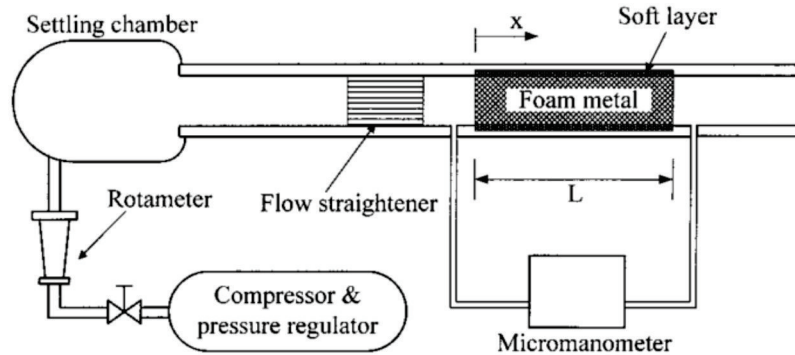


Figure 4.9: Experimental apparatus for the measurement of permeability of aluminium foams [114].

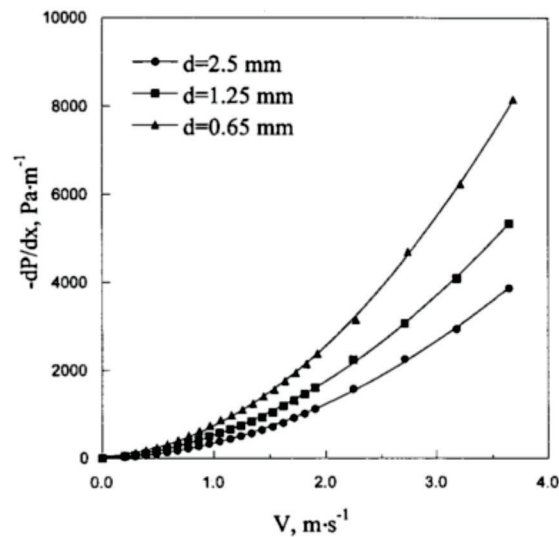


Figure 4.10: Cell size on pressure drop at different air velocities for samples with 0.92 porosity [114].

in a higher value of K in samples with a fixed pore size.

Mancin et al [115] constructed an open circuit apparatus to measure both the heat transfer coefficient and the pressure drop of aluminium open cell foams of the Duocel type with 5, 10, 20 and 40 PPI and different densities at different air flow velocities. The results obtained were compared with data obtained from a proposed model developed from the open literature. The experimental pressure drop values obtained with a pressure transducer placed in the test section are presented in Fig. 4.11. The foam with

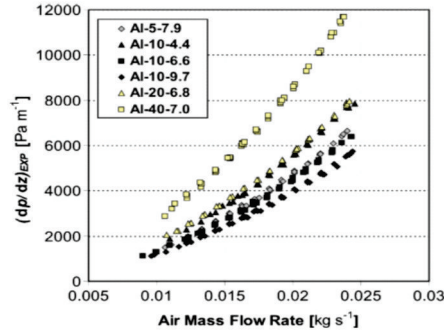


Figure 4.11: Experimental pressure gradient plotted against air mass flow rate for the different foams tested in ref. [115].

the smallest pore size, 40 PPI, and 7.0 % density presents the highest pressure drop among the samples tested. From this experimental data, was found to decrease cell diameter the permeability decreases. The experimental pressure data were compared against different models that were select by the author from the open literature where models proposed by Bhattacharya et al [113] and Du Plessis et al [116] presented the best estimation of the pressure gradients. With the objective to obtain a better agreement between experimental and analytical data a new simple model was developed by the author. The model obtained predicts the experimental data with a 3.5 % standard deviation. The values of permeability K , inertia coefficient f and form coefficient C used to validate the model suggested by the author, were obtained from the database from several independent research groups. The comparison between the experimental data (experimental data from the open literature) and the calculated by the new model proposed has a acceptable agreement with a 18.6 % standard deviation.

As well as simple forced convection, where the fluid is passed through the heat exchanger in one direction, some workers have considered the use of oscillating flow, where the fluid velocity is varied, often sinusoidally. This may enhance heat transfer, and be a more appropriate solution for certain heat exchange situations. Leong et al. [94], studied the effect of oscillating flow over Duocel-type aluminium foam heat sinks with 10, 20 and 40 PPI pore size and 0.9 porosity. Experimental apparatus was constructed in which air was used as the working fluid, and the oscillating flow was provided by

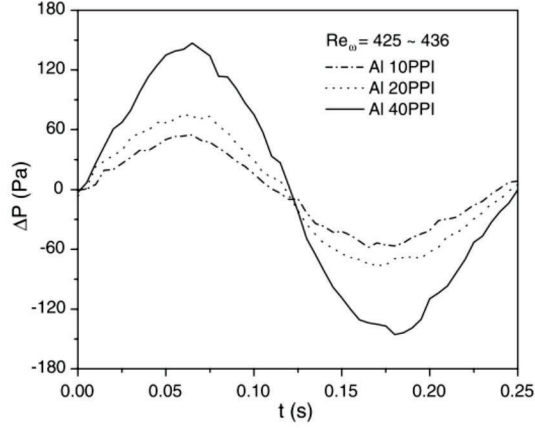


Figure 4.12: Variation of the difference of pressure of oscillating flow in aluminium foam with 10, 20 and 40 PPI pore size at $Re_\omega = 425-436$, where Re_ω is kinetic Reynolds number defined in Eq. 4.12 [94].

reciprocating piston in a cylinder, which was driven by an electrical motor through a crankshaft. The sample was 50 mm by 50 mm by 10 mm and a pressure transducer was placed in the test section to measure the pressure drop across the samples and understand their fluid flow behaviour.

Samples with similar porosity (0.9- 0.91), were tested under the same parameters. Fig. 4.12 shows the sinusoidal profile presented by the pressure drop, due to the reciprocating motion of the driving piston under a kinetic Reynolds number; $Re_\omega = 425 \sim 436$. This was obtained through the following equation:

$$Re_\omega = \frac{2\pi f D_e^2}{v_f} \quad (4.12)$$

where $D_e = 5H/3$ is the hydraulic diameter of channel, v_f is the kinematic viscosity of the fluid and H is the height of the channel. It can be seen in Fig. 4.12 that once again the pressure drop in general increases when the pore size decreases in the aluminium foam.

Despois et al [117], constructed an apparatus to develop a fluid permeability tests to aluminium open foams produced using the replication technique using water and

glycerine as a fluid and developed an analytical model to predict the fluid flow behaviour of this porous system. The aluminium foams characterized had an average cell size of 15 and 400 μm , and a relative density from 12% to 32%. The model developed by Despois et al is a simple equation to obtain the Darcian permeability (K), as a function of foam density and pore diameter based on the assumption that the "bottlenecks" formed where cells interconnect are the dominant source of resistance to flow in a porous medium. Taking into account that many cellular materials that contain nearly spherical pores connected with one another through more or less circular windows, each delineated by solid struts that narrow to a thin edge along the perimeter of the window allow Eq. 4.13. Metal or ceramic foams produced by casting into a mold shaped by using polymeric foams as a removal pattern are represented well under this description.

$$K = \frac{\Delta r^2}{\pi} \left[\frac{\Delta - \Delta_0}{3(1 - \Delta_0)} \right]^{3/2} \quad (4.13)$$

where Δ_0 is the initial packing density of the spherical particles and for a random dense packing of monosized spheres having a value equal to 0.64, r is the radius of the sphere and Δ is the pore volume fraction in a foam. The results obtained experimentally agree well with Equation 4.13 and show that K decreases rapidly when Δ approaches values near to 0.64 meaning that the "bottlenecks" are almost closed. The predictions of the model developed by Despois were found to be satisfactory when is compared with data published in the literature (See Fig. 4.13), and has good agreement with the Du Plessis's model [117] for foam densities lower than 0.2 (i.e. 20 % of relative density).

It can be noted that virtually all of the experimental studies of the fluid flow behaviour of foams have been carried out on Duocel-type investment cast material. This is partly because these foams are commercially available, and partly because researchers suspect they may offer a viable solution as heat exchangers. However, they are not perfect for study of the behaviour of foams in general; as noted above, in some work the foams have had to be crushed to access an interesting density range. There is therefore value

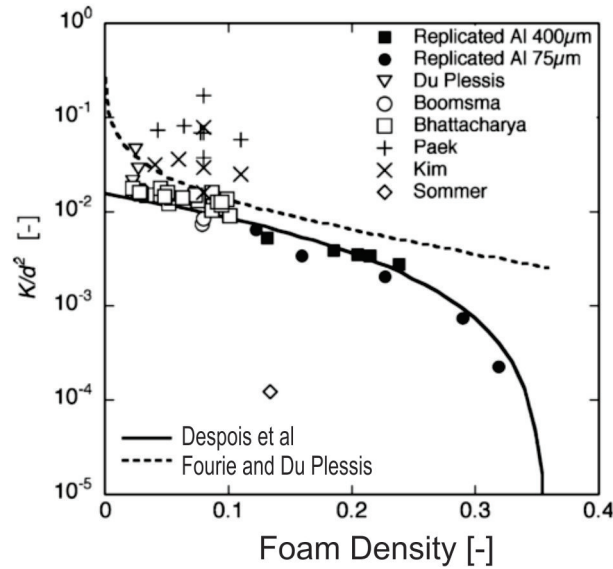


Figure 4.13: Evolution of the permeability K normalized by the pore size squared d^2 as a function of the foam density [117].

in exploring the behaviour of foams made by other routes.

Fourie et al [118] develop a theoretical model which enhance the previous modelling procedure of Du Plessis et al [116]. The analytical model was developed as a function of two measurable geometrical parameters (cell size and porosity) and introduces a characteristic dimension referred to as the representative hydraulic diameter which accounts for the hydrodynamic effects of the triangular cross-sectional shape of on individual strand in the metallic foam (it can be noted that characteristic lengths and distances occur frequently in mathematical treatments of heat and mass transport) comparison of the pressure difference predicted using the equations obtained was made with previous experimental results for aluminium foams with 10, 20 and 30 PPI and porosities from 0.91 to 0.93. The agreement obtained for each of the three metallic foams was within 5 %.

An analysis to estimate the fluid flow properties of metal foams with two models (called the '*fat*' and '*slim*' models) was established by Ahmed et al [119]. The difference between the '*slim*' and '*fat*' models was the volume of matter accumulated at the

strut connection (the nodes). The results obtained with these two models have better agreement with the literature with low air flow rates and when the foam porosity is high, as the strut-based model of foam is a better at low densities.

In non-metallic foams, numerical models have been used to investigate the permeability where the results obtained can be applied to metal foams. Xu et al [120] use a three-dimensional model to predict the permeability of a SiC foams produced by the replication process by representing the foam by a periodically repeats cell with the form of a tetrakaidecahedron. The pore size was from 1 to 3 mm diameter. The results obtained show that the permeability is strongly affected by the porosity and the pore diameter and that the permeability increases quickly with the cell size at a constant porosity and that the permeability is more affected by lower porosities at a fixed pore size. The model was compared with experimental results with good agreement, principally at lower flow rates.

4.3 Key elements of heat transfer

Before examining thermal transport in metal foams some aspects of general heat transfer will be introduced. Whenever there exists a temperature difference in a medium or between media, heat transport will occur. When this involves the passage of heat from one object or phase to another, it is termed heat transfer. This transition of thermal energy (heat) always occurs from the hotter object to the cooler to eventually reach thermal equilibrium and is therefore also dependant on the transport of heat within the object. Heat transport can occur by one of three mechanisms, depending on the medium it has to travel through: conduction, convection and radiation.

Conduction.

Thermal energy is transported by conduction when the energy transfers from a high temperature region to a low temperature region, when they are in direct contact with

each other. In this situation the flux of heat is proportional to the temperature gradients between them as follow

$$\frac{q}{A} \sim \frac{\partial T}{\partial x} \quad (4.14)$$

When the proportionality constant is inserted, this becomes

$$q = -kA \frac{\partial T}{\partial x} \quad (4.15)$$

where q is the heat transfer rate (kJ per unit time), $\partial T/\partial x$ is the temperature gradient in the direction of the heat flow (K/m), A is the surface area (m^2) and k is the thermal conductivity defining the material's ability to conduct heat (W/mK), the minus sign is inserted so that the second principle of thermodynamics is satisfied.

Convection.

The process of heat transport across the boundary between a solid and a fluid is usually a combination of conduction and a process called convection. The convection process is a heat transfer process that involves the movement of a fluid transporting heat and may be 'free convection' or 'forced convection'. Free convection is when hot body is exposed to a cooler environment without any external source of fluid motion. Fluid motion is nevertheless and is entirely generated as a result of density gradients which in turn results from the temperature gradients in the fluid. In forced convection fluid motion is induced externally, often by a pump, fan, or compressor. It would normally be expected that heat transfer is higher under forced convection, as the fluid normally moves more rapidly and so transports heat at a higher rate, but an external power source is required.

The rate of heat transfer from the heated body can be calculated from

$$\dot{q} = -k_l \left(\frac{dT}{dx} \right)_w \quad (4.16)$$

where k_l is the thermal conductivity of the fluid, $(dT/dx)_w$ is the temperature gradient in the wall and $\dot{q}=q/A$ (the heat flux). As the temperature in the boundary layer by the wall is not easily evaluated, the heat transfer rate is commonly written as

$$\dot{q} = h_c(T_w - T_L) \quad (4.17)$$

where T_w is the wall temperature, T_L is the temperature of the fluid a large distance from the wall and h_c is the heat transfer coefficient. This last parameter, the heat transfer coefficient h_c , is effectively a measure of how well thermal energy is transferred from the solid to the fluid.

Radiation.

Thermal radiation or electromagnetic radiation is generated by the thermal motion of charged particles in matter and leads to the transport of heat in the presence of a temperature difference. An ideal thermal radiator will emit energy at a rate proportional to the fourth power of the absolute temperature of the body, and directly proportional to its surface area, and is defined as follows,

$$q_{emitted} = \sigma AT^4 \quad (4.18)$$

where σ is the proportionality constant called the Stefan-Boltzman constant. Other types of bodies, such as polished metal plates, do not radiate as much energy as the blackbody (the ideal thermal radiator); the total radiation emitted ($q_{emitted}$) by these bodies still follows the T_1^4 proportionality. To take account of the "gray" nature of such surface the emissivity factor (ϵ) is introduced in Equation 4.18, which relates the

radiation from the "gray" surface to that of an ideal black surface. When considering the net transport of heat between two bodies at different temperatures, emissivity and the fact that some electromagnetic radiation will be lost to the surroundings as light only travels in straight lines, two new factors are introduced in Equation 4.18

$$q = F_\epsilon F_G \sigma A (T_1^4 - T_2^4) \quad (4.19)$$

where F_ϵ is an emissivity function, and F_G is a geometric "view factor" function.

Nusselt number.

The Nusselt number is a dimensionless number used where the heat transfer coefficient has been obtained experimentally. It gives the ratio of convective and conductive contributions to heat transfer; the larger the number, the more effective the contribution of convection to heat transfer. For a constant heat flux the local Nusselt number is given by

$$Nu = \frac{h_c L}{k_{eff}} \quad (4.20)$$

where L is a linear dimension (m) and k_{eff} is the effective thermal conductivity (W/mK).

Prandtl number.

The Prandtl number (Pr) is the ratio of the kinematic viscosity to the thermal diffusivity, measuring the relative efficiency of a fluid for the transport of momentum (high viscosity / low diffusivity) and energy (low viscosity / high diffusivity), and is expressed as follows

$$Pr = \frac{v}{\alpha} = \frac{c_p \mu}{k} \quad (4.21)$$

where v is the momentum diffusivity (m^2/s), α is the thermal diffusivity (m^2/s), c_p is the specific heat capacity (J/kgK) and μ the absolute or dynamic viscosity (m^2/s). The Prandtl number depends on fluid properties and is a number that relates to the fluid being used in a heat exchanger, and not the heat exchanger itself. Nevertheless, knowledge of this number allows conversion between the expected behaviour with one fluid and another (e.g. air to water).

Reynolds number.

The Reynolds number (Re) measures the ratio of internal forces to viscous forces in the flow and is represented as follow

$$Re = \frac{uL}{\mu} \quad (4.22)$$

where u is the mean velocity of a solid object (which could be the wall of a pipe) relative to the fluid (m/s). Considering the fluid in a tube with a diameter d in (m), when the flow is smooth and the viscous forces are dominant the flow is considered to be laminar. This occurs when the Reynolds number is below a certain value:

$$Re_d < 2300 \quad (4.23)$$

turbulent fluid occurs when the fluid is dominated by inertial forces that produce an unstable and chaotic fluid profile. Depending on the pipe roughness and smoothness of the flow the range accepted for transition from laminar to turbulent flow is $2000 < Re_d < 4000$.

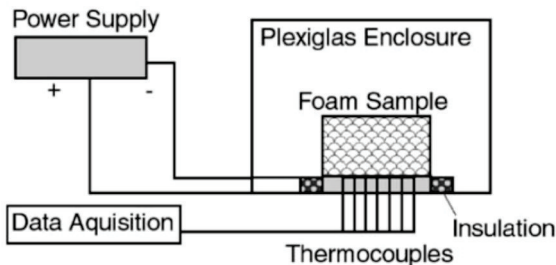


Figure 4.14: Experimental set up constructed by Phanikumar to characterize the buoyancy-induced fluid flow in highly porous aluminium foams [121].

4.4 Heat transfer in foams

4.4.1 BUOYANCY-INDUCED FLOW CONDITIONS

Numerical and experimental methods have been deployed to characterize the heat transfer in a porous metal under buoyancy-induced flow. Phanikumar et al [121] used an analytical and experimental approach to characterize the buoyancy-induced flows in metal foams heated from below at a maximum temperature of $75^{\circ}C$. The aluminium foam analysed were samples with pore sizes from 5 to 40 PPI and porosities from 0.89 to 0.97. The test were developed on natural convection conditions with the sample in a horizontal configuration. The sample was placed in a large plexiglas housing of 0.45 m in height and width and 0.30 m deep. Fig. 4.14.

The experimental results obtained show that for a given Rayleigh number the heat transfer rate decreases as the pore density increases from 5 to 20 PPI. The Rayleigh number is a dimensionless parameter that is a measure of the instability of a layer of fluid due to differences of temperature and density between the top and bottom. Phanikumar et al concluded that this behaviour is due to the resistance to the flow decreasing with an increment in pore size resulting in enhanced mixing and heat transfer and for a pore density the heat transfer increase when the porosity decrease Fig. 4.15. The Local Thermal Equilibrium model (LTE) developed by the workers was in reasonable agreement with the experimental data obtained, having a maximum difference

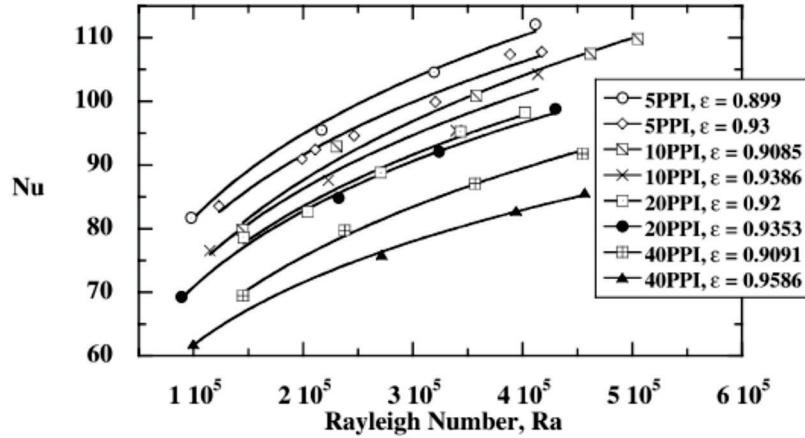


Figure 4.15: Experimental results obtained with aluminium foams [121].

between them of less than 15 %. Phanikumar et al suggested that the enhancements in heat transfer result from the use of metal foams are up to a factor of 4 when air is used as a fluid and 16 when water is used. In either case, this would be a desirable increase in the performance of a heat exchanger using these materials, and is particularly impressive considering the narrow range of foam densities examined; the probability that the optimum foam structure has been found is low.

Samples of a highly temperature-resistant alloy steel (FeCrAlY) with 5 and 10 % relative density and pore size of 30, 60 and 90 PPI were examined to see the heat transfer behaviour under natural convection, the measures were carried out under vacuum and ambient conditions by Zhao et al [122, 123]. The differences between effective thermal conductivity obtained from the temperature measurements in ambient pressure and in vacuum conditions show that the effect of natural convection (which is of course removed under vacuum) on heat transfer is very significant, contributing about 50 % of the overall thermal conductivity measured at atmospheric pressure. For example a sample with 60 PPI and 10 % relative density, presents a thermal conductivity around 0.2 W/ m K under vacuum conditions, while in ambient pressure presents 0.6 W/m K. The results were obtained for a fixed Rayleigh number ($Ra = 48,000$), indicating that for a natural convection under ambient pressure in these foams there is no significant

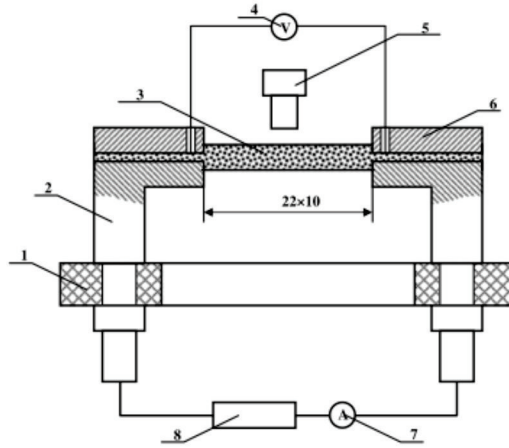


Figure 4.16: Experimental apparatus developed by Hetsroni et al. (1) housing, (2) aluminium contacts, (3) metal foam specimen, (4) voltmeter, (5) IR camera, (6) holder, (7) amperemeter, and (8) power supply [124].

value of Darcy number. This implies that there is no fluid motion and that the heat is transferred by pure conduction, at least the sample for which this was obtained (with a 60 PPI and 10 % relative density sample). The numerical predictions of this behaviour agree generally well with a maximum deviation of 28 % is reported by the author [123].

Hetsroni et al [124] performed the characterization of natural convection in a metal foam strip with internal heat generation using aluminium foam samples with 20 and 40 PPI and with 0.90 and 0.85 of porosity respectively. The samples were tested in an apparatus shown in Fig. 4.16. The internal heat generation was simulated by supplying DC current up to 50 A to the foam sample. The thermal field of the outer side of the porous strip was measured by an IR camera.

The results showed that the metal pore structure with 20 PPI enhanced the heat transfer, compared with the ones obtained for the sample with 40 PPI. Hetsroni et al suggested that it is not only the specific surface area that determines the effective heat transfer but that due to the higher permeability of the foam with large pores, there is a higher flow of the air through the porous medium, in response to the convective forces acting on the air, and that this also contributes to the higher heat transfer. From the

thermal maps obtained through the IR camera, Hetsroni reports that the solid skeleton and the air are not in thermal equilibrium, having a maximum difference between their temperatures of up to 18 %.

4.4.2 FORCED CONVECTION

As was seen in Hetsroni et al's work on natural convection in foams, the rate of fluid flow is very important to the heat transfer obtained. The faster the fluid flows the more energy it will take away and the larger the heat transfer coefficient will be. Therefore, forced convection (where an external source powers the fluid flow) is often used in heat exchange. Calmidi et al. [104] used the experimental set up shown in Fig. 4.17 to characterize aluminium (alloy T-6201, processed by the investment casting method) foams with porosities from 0.89 to 0.97 (see Table 4.2 for more details) under forced convection. The samples were heated by patch heaters, the power input was set between 15-35 W. The cooling air was obtained by connecting the plexiglass tube (where the sample is placed) to a fan/motor assembly downstream of the test sample, the speed of the motor was adjusted to the desired flow velocity which was measured by the pressure drop across an orifice plate. The direction of the air was from left to right in the diagram, and the test took from 5 to 10 min depending on the flow velocity. The heat transfer coefficient was obtained using equation 4.17 and the Nusselt number with equation 4.20.

Table 4.2: Characteristics of metal foam samples used by Calmidi et al [104].

No.	Porosity (fraction)	Pore Size (PPI)
1	0.97	5
2	0.91	5
3	0.94	10
4	0.95	20
5	0.90	20
6	0.92	40
7	0.91	40

The data collected in this study were compared with results obtained from simulations

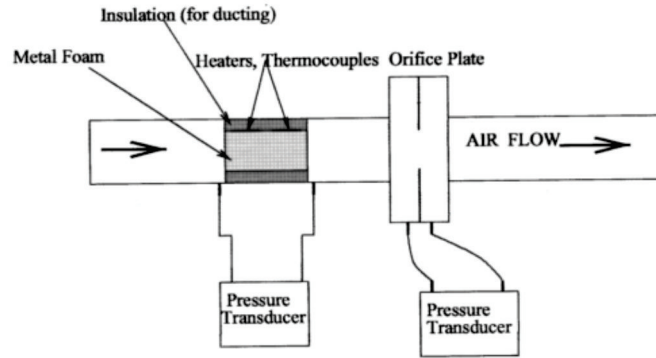


Figure 4.17: Experimental set up used by Calmidi et al. [104], for forced convection heat transfer experiments.

using a numerical code where the experimental conditions were reproduced and the results matched in a reasonable manner. Figures 4.18(a) and 4.18(b) show the very good fit obtained by the authors when these simulations are plotted as a function of the Reynolds number, based on the permeability (Re_K).

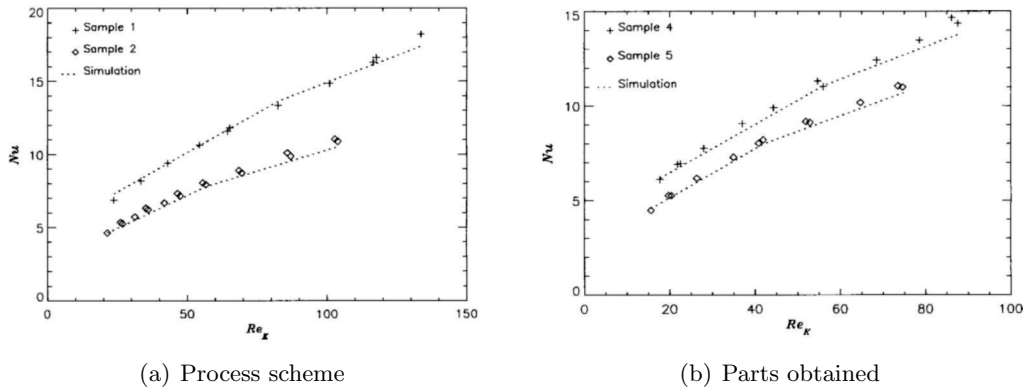


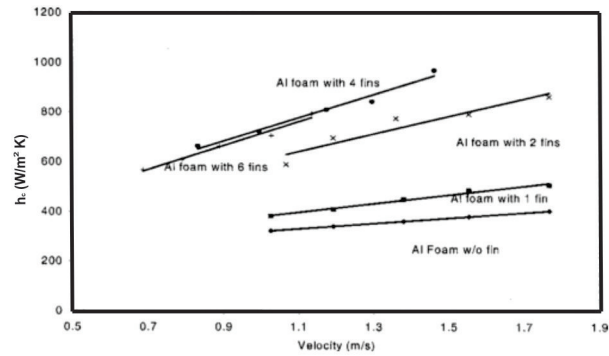
Figure 4.18: Nusselt number as a function of Re_K for (a) 5 PPI and (b) 20 PPI samples (Table 4.2) [104].

Aluminium foams were incorporated into existing heat sink designs to characterize the behaviour when they are under forced convection. Bhattachayra et al. [65] used aluminium foams with a porosity of 0.9 and pore size of 20 PPI and 5 PPI incorporated in normal longitudinal or pin-shaped fins, with a different number of fins used in each case, in order to investigate the heat transfer of metal foam with finned metal in the

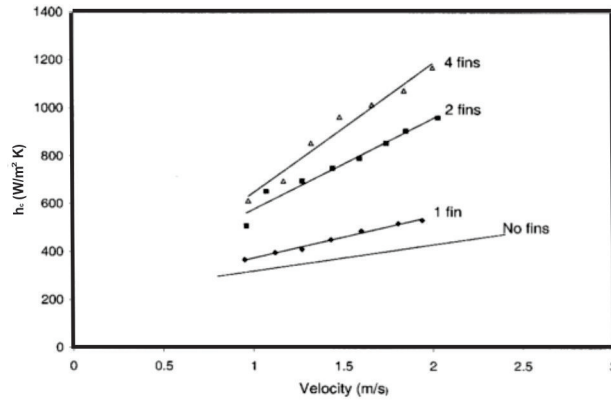
system developed by Calmidi et al. [104]. Fig. 4.7 shows schematically a finned metal plate between two blocks of metal foam. The fin, the foam and the thermal adhesive applied in order to reduce the contact resistance between the metal foam and fins can all be seen. The temperature of the air before and after the metal foam was measured, as well as the temperature in the metal foam and the flow rate.

The results obtained in metal foams with 20 PPI in this experiment show that the heat transfer coefficient increases at a given flow rate when dense metal fins are incorporated in the metal foams. Bhattacharya et al explain this enhancement in the heat transfer with reference of the fact that replacing a strip of metal foam with solid aluminium results in a increment of heat transfer by conduction (about 32 times higher thermal conductivity of the solid aluminium with respect to metal foam) and that a large surface area of heated metal (both foam and fins) is in direct contact with the foam. However, this increment is not linear as would be expected if the effect was simply replacing a less efficient foam with more efficient dense metal. In the last case when the metal foams have 6 fins, the heat transfer coefficient decreases; this is shown in Fig. 4.19(a). The author attributed this behaviour to the interaction of the thermal boundary layers (non-free flowing fluid) formed on the adjacent finned surfaces. The heat transfer coefficients obtained in metal foams with 5 PPI, Fig. 4.19(b) are similar to those obtained from 20 PPI; i.e. the heat transfer increases when fins are incorporated to the aluminium foam. For a particular air velocity the heat transfer coefficient is higher in 20 PPI than 5 PPI samples with the same number of fins due to the higher surface area available for heat transfer. An alternative way of picturing this would be to say that there is the presence of larger number of fibers (i.e. the struts).

Hsieh et al [103] constructed experimental apparatus to characterise the effects of the air velocity, porosity (ε) and pore size on the heat transfer of aluminium foams, Fig. 4.20. As in the experimental apparatus constructed by Calmidi et al [104], the sample is cooled by air at different velocities and the sample is heated on the lower side through resistance heating controlled by a power supply. The sizes of the samples tested was 60



(a) 20 PPI



(b) 5 PPI

Figure 4.19: Heat transfer coefficient as a function of air velocity for (a) 20 PPI and (b) 5 PPI metal foams with finned heat sinks [65].

mm diameter and 65 mm height, and the inlet air velocity was measured by a hot-wire anemometer. The author measured the temperatures of the solid and gas phase to understand the phenomenon of thermal equilibrium between these two phases. Some of the properties of the aluminium foam used in this study are presented in Table 4.3.

The results obtained show that the Nusselt number (Nu) is influenced by the Reynolds number (Re_{Dp} , based on the spherical diameter of the pores), as well as the porosity (ε). If the Reynolds number and the pore density increase (maintaining the same pore size), the Nusselt number increases. This can be observed in Fig. 4.21(a) where aluminium samples with 20 PPI and different densities are compared. Fig. 4.21(b) shows the influence of the pore size on the Nusselt number.

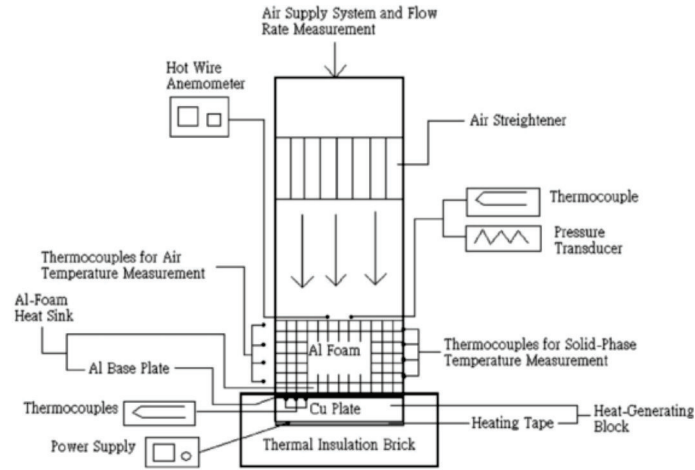


Figure 4.20: Experimental apparatus developed by Hsieh et al for the measurement of heat transfer [103].

Table 4.3: Characteristics of metal foam samples used by Hsieh et al [103].

No.	Pore Size (PPI)	Porosity (fraction)
1	10	0.92
2	20	0.87
3	20	0.91
4	20	0.94
5	20	0.96
6	40	0.94

As was mentioned earlier, the author instrumented the apparatus to be able to measure the temperature of the solid phase and the gas phase, finding that the differences in temperature between these two phases decrease with increases in porosity. Fig. 4.22 shows how the thermal equilibrium is influenced by the Reynolds number (Re_{Dp}), and for the distance away from the heat source. The distance away from the heat source is represented as the dimensionless number z/H , where z is the total height for the sample and H is the height at which the temperature is evaluated.

Mancin et al also constructed experimental apparatus to characterize the heat transfer and the permeability of aluminium [115, 125] and copper foams [126]. The test rig was an open circuit tunnel with rectangular cross section in which the metal foam samples (the majority 100 mm long, 100 mm wide and 40 mm high), were tested to understand

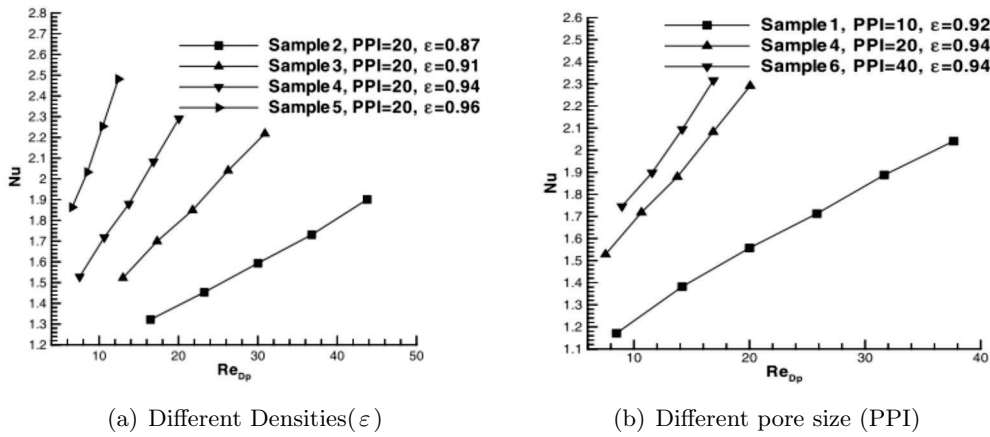


Figure 4.21: Effect of the Reynolds number on Nu for metal foams with (a) different pore densities and (b) different pore size [103].

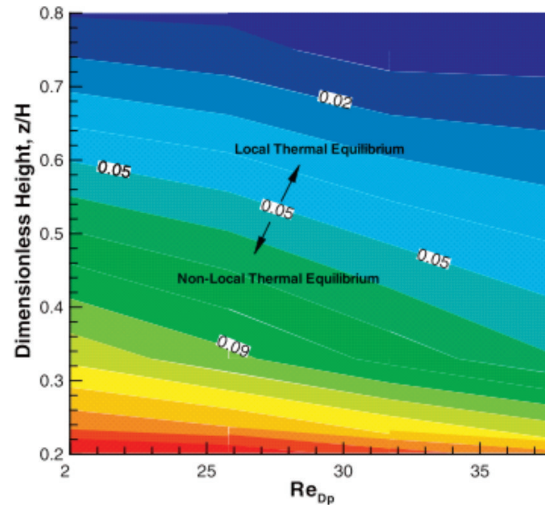
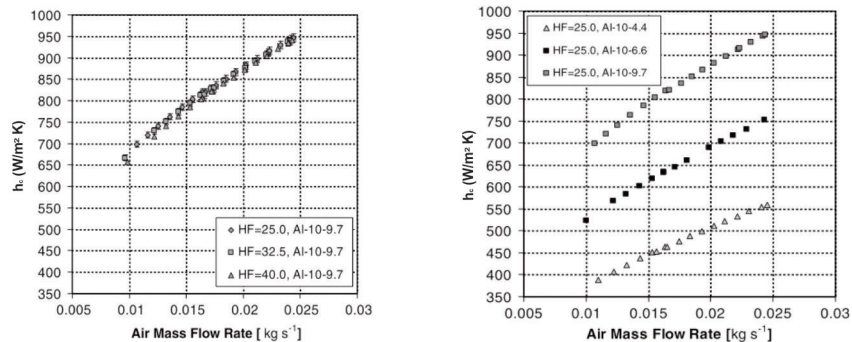


Figure 4.22: The contour of dimensionless temperature difference of 10 PPI and 0.92 porosity sample, plotted in Reynolds Number-dimensionless height coordinates [103].

the behaviour of the sample. The device was heated from the lower face, and was instrumented with 12 thermocouples, of which 6 were installed in the top plate and 6 in the bottom of the test section.

Where aluminium foams were tested, these were again foams produced by the investment casting method and had pore size of 5-40 PPI and porosity that varied between 0.89 and 0.97. The experimental results were compared with a model developed from

the literature. Mancin et al found that the heat transfer coefficient (h_c) obtained through equations 4.16 and 4.17 does not depend on the heat flux imposed (HF), and that it increases with increasing air mass flow rate, Fig. 4.23(a). In tests with the same heat flux imposed, they found that, for a constant pore size, an increase in the global heat flux is obtained when the porosity is decreased, Fig. 4.23(b). The foam with highest heat transfer coefficient found in this work among the samples tested was the foam with 10 PPI of pore size and density of 9.7 %. This sample presents higher global heat transfer than foams with higher heat transfer area per unit volume, such as samples with 40 PPI and 7.0 density, and 20 PPI with 6.8 density. When samples with 10 PPI pore size were compared, the author reports that the sample with 9.7 % presents the thickest fibers. The above and the apparent highest surface area efficiency can explain why 10 PPI sample with 9.7 % density presents highest heat transfer among the samples. The comparison of the experimental heat transfer coefficient with that calculated, made by Mancin et al was deemed satisfactory as it presents a 8.0% standard deviation.



(a) Different heat flux imposed (HF) (b) 10 PPI samples with different densities where HF : heat flux imposed.

Figure 4.23: Global heat transfer coefficient (h_c) against air mass flow rate in samples with 10 PPI when (a) the heat flux imposed is varied and (b) with same heat flux but with different densities [125].

The tests discussed above have all been performed on straight channels. The effect of channels that are not straight on the heat transfer and pressure drop has been investigated principally to understand the behaviour in pin-fin arrays (pin-fin array

consist of a base and an array of embedded pins with the length, thickness, density and materials that can be customized to fit the required application) used to cool systems [127, 128]. Sheng et al [129] studied the heat transfer and pressure drop in porous channels with 90° turned flow (see Fig. 4.24) using aluminium foams with porosity of 0.93, the results were compared with those from straight porous channels. The dimensions of the aluminium foam samples were fixed; the pore size, Reynolds number of the flow and the ratio of the entry width to the porous sink height were the variable parameters. The results obtained show that the friction factor (the friction factor, frequently symbolized as f , is a dimensionless factor that depends primarily on the velocity, density and viscosity of the fluid, and pipe diameter. It is also a function of: size shape and spacing of the wall roughness) of the straight channel was generally lower than the channel in which the flow turned 90° as would be expected, given the change of fluid direction induced. The average Nusselt number when the Reynolds number is lower than 1000 in the configuration in which the flow turned through 90° , slightly exceeded that in the straight flow configuration. This larger Nusselt number could be as a result of the extra turbulence generated when the cooling air flows through the foam in the 90° configuration, although this is not discussed by the author. However, over the range of the Reynolds values examined the average Nusselt number of both configurations of the cooling channel (straight and 90°) was almost the same.

Most of the investigations reported for heat transfer characterization cover experiments in rectangular channels; there are few reports of research investigating heat transfer in circular cross section channels even though such forms are easier to analyse for their rotational symmetry; this could be because the majority of heat exchange applications will require a flat interface configuration. Zhao et al [130, 131] develops an analytical solution for a tube heat exchanger filled with metal foam and compare this with experimental results. Copper and FeCrAlY metal foams are characterized, and have a very good agreement with the analytical model. This predicts that the Nusselt number increases with increasing relative density and with reducing pore size. A double tube

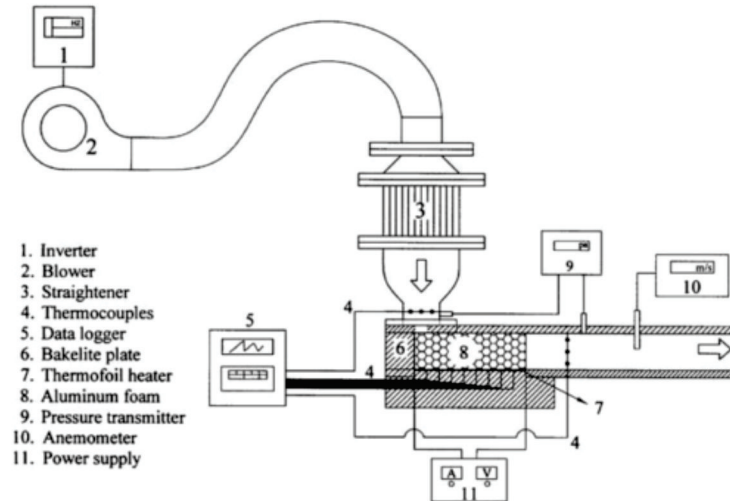
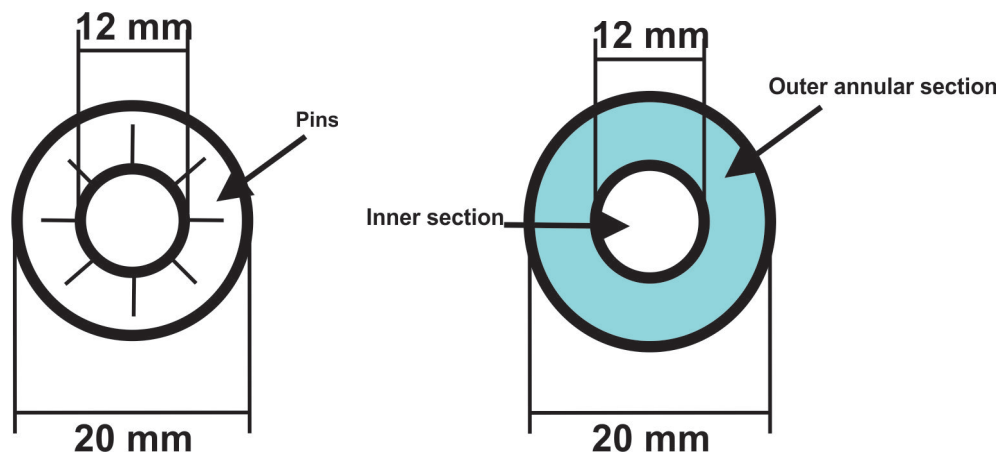


Figure 4.24: Flow channel with 90° turned flow [129].

heat exchanger filled with metal foam was also analysed and was compared with a conventional heat exchanger with an inner grooved tube and fins (figures 4.25(a) and 4.25(b)). The heat transfer performance of the exchanger with the metal foam was found to be superior to the finned tube counterparts, being three times higher than the performance of the longitudinally finned tube and even better than the best non-foam heat exchanger tested, a spiral finned tube [131].



(a) The heat exchanger with inner grooved tube and fins.

(b) Metal-foam filled heat exchanger.

Figure 4.25: Tube heat exchanger diagram (a) with inner grooved tube and fins, and (b) with inner and outer annular section filled with metal foams [131].



Figure 4.26: A helically finned (top) and metal foam covered tube [132].

The good performance of heat exchangers with spiralling fins has been noted and compared to metal foams in other work (both of these will act to increase heat transfer by improving the turbulent mixing within the fluid). Joen et al [132] studied a new design of heat exchanger where the thermal-hydraulic performance of a tube covered with metal foam is compared with a helically finned tube, Fig. 4.26. The work reports that increasing the foam thickness gives an increase the heat transfer coefficient and at the same time an increase in the pressure drop. When the foam height increases the surface area of the foam increases, then the heat extraction is benefited and the permeability of the foam decreases. Brazing the metal foam to the tube enhanced the heat transfer (reducing the thermal resistance between the foam and the tube) while using epoxy glue had devastating effects on the heat transfer performance (with a reduction in heat transfer of about 70 %). Brazing the metal foam to the tube, using higher thickness of the foam and thin struts are found to give benefits at higher air velocities (higher than 4 m/s) compared with the spiral finned tubes; the heat transfer obtained is higher with a lower pressure drop when are compared at the same air velocity.

4.4.3 OSCILLATORY FLOW

In some applications, a simple, unidirectional cooling fluid flow would not be suitable. As noted by Leong et al [133] uni-directional flow through a porous channel gives rela-

tively high temperature differences along the surface that is being cooled. Heat transfer will be higher near where the cooling fluid enters because of the greater temperature difference driving heat transfer. The operating speed of a modern high-speed microprocessor is influenced by the surface temperature of the components (which should be as low as possible) but also by the temperature uniformity; it is therefore important to maintain the uniformity over the surface.

As mentioned in Section 4.2, Leong et al. [94], studied the effect of oscillating flow over aluminium foam heat sink with 10, 20 and 40 PPI pore size and 0.90 porosity. Experimental apparatus was constructed in which air was used as the working fluid, and the oscillating flow was provided by reciprocating piston in a cylinder, which was driven by an electrical motor through a crankshaft. The sample was 50 mm by 50 mm by 10 mm and was attached to a copper plate using thermal grease to reduce the thermal resistance. A constant power heat source was connected to the bottom of the sample through the copper plate. Eight thermocouples were fixed into eight narrow slots in the copper plate to record the temperature in different locations.

In oscillating flow, defining the heat transfer behaviour is more complex than with steady state. Leong et al characterized the heat transfer performance obtained with the samples tested by use of the cycle-average local Nusselt number, which is defined based on the cycle-average surface temperature with the following equation:

$$Nu = \frac{h_x D_e}{k_f} \quad (4.24)$$

with k_f being the thermal conductivity of the fluid, D_e the hydraulic diameter and h_x the local heat transfer coefficient, respectively, where h_x was calculated as follows:

$$h_x = \frac{Q}{A_{heated} (T_w - T_i)} \quad (4.25)$$

where T_w and T_i are the cycle-average local surface and the bulk air inlet, Q and

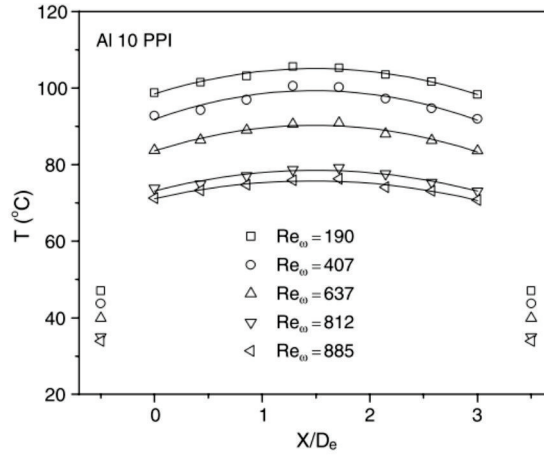


Figure 4.27: Cycle average temperature distribution on the surface test section for a 10 PPI pore size sample [94].

A_{heated} are the power input. Leong et al show that for the same heat input, 20 W, when the Reynolds number increases the temperature distribution decreases for all pore sizes. The largest temperature is found in the centre of the test section, presenting a convex shape when the wall temperatures are plotted against the hydraulic diameter. For all pore sizes (10 , 20 and 40 PPI) Fig. 4.27 shows the temperature distribution on the surface of the test section versus the hydraulic diameter at different kinetic Reynolds numbers for a sample with 10 PPI pore size.

For the Nusselt number calculated from equation 4.24, Fig. 4.28 is obtained where in this case the distribution is concave when the Nusselt number is plotted versus the hydraulic diameter.

4.4.4 THEORETICAL APPROACHES

There are many approaches to modelling and simulating flow through pores structures [113, 119, 120, 134–142]. Among these there are some more accessible analytical approaches to compute the thermal and fluid flow behaviour. One such model was developed by Lu [134] to be used to analyze and guide the design of the optimum foam structure that would maximize heat transfer per unit pumping power in a system. A

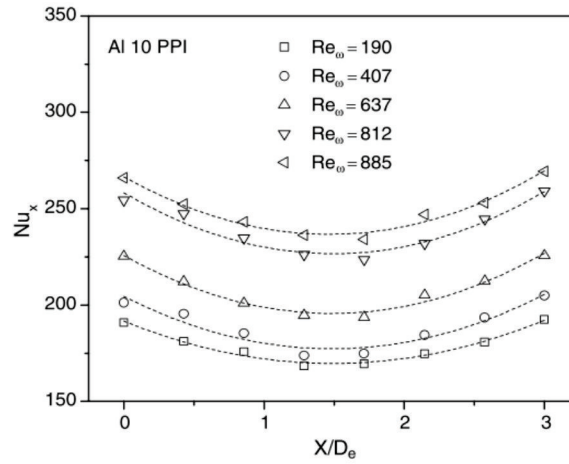


Figure 4.28: Cycle average Nusselt number distribution on the surface test section for a 10 PPI pore size sample [94].

simple cubic geometry of cells sandwiched between two plates was proposed, Fig. 4.29, where it is assumed that $T_1 \geq T_2$, (T_1 temperature of upper plate and T_2 temperature of bottom plate), and where a cooling fluid with temperature T_0 ($< T_2$) and pressure p_o is forced into the foam. Lu [134] chose this geometry for simplicity, but it nevertheless has the capacity to capture the effect of different variables like foam density, cell size and fluid velocity. Such simplifications in foam structure have been successfully employed for other properties, the most well known being the mechanical description of foams derived by Gibson and Ashby.

The model was developed in three steps; the heat transfer from a single cylinder of type denoted Z (oriented parallel to the flow) with length b is explored as these are the only ones that contribute to heat extraction as they are oriented across the temperature gradient. If the cylinder's temperature is higher than T_2 , heat is lost not only by convection to the fluid but also by conduction to the environment, when T_2 is higher than the cylinder temperature the heat is extracted from both the lower plate and the upper plate. Using this approach the Z cylinders are analyzed unconnected to the square array in the (x, y) -plane.

In the experimental part of this study, a high flow velocity was used and the porous

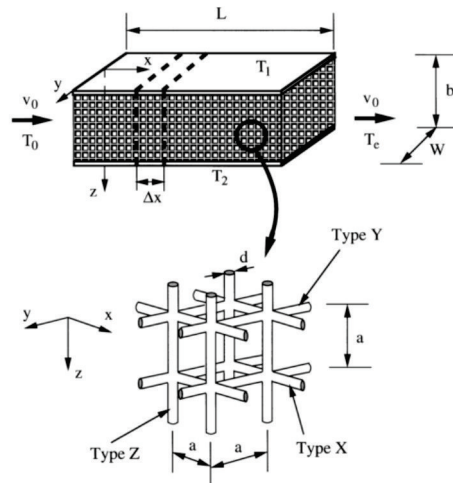


Figure 4.29: Notations and cubic unit cell of an open-cell foam under forced convection [134].

media is restricted, so therefore the assumptions of thermodynamic equilibrium and Darcian flow are invalid. Despite this oversimplification of the geometry and heat transfer overall the prediction of this model shows good agreement with the experiments. The simplicity of the model allows it to be used to give guideline predictions for the heat transfer performance for wide range of open-cell foams.

A model recently proposed by Ghosh [135], is also based on an analytical approach with a simple cubic geometry. This was disintegrated into a group of independent y -direction struts from which the author obtains the governing equation Fig. 4.30. (in the model developed by Lu [134] the foam was modelled as inter-connected cylinders). With this simple model Ghosh [135] developed a deep analysis which takes into account the finned-foam surface area efficiency and the interstitial heat transfer coefficient which gives good agreement with experiments for heat transfer, pore densities, Nusselt number and temperature variations with flow velocity. These experimental data were obtained by Giani [143] with metal foam samples provided by Porvair made of Fecralloy (Fe-10Cr-5Al-2Y) with three different pore sizes 10, 20 and 40 PPI.

As an example of this excellent agreement obtained by Ghosh to the experimental data obtained by Giani [143], Fig. 4.31 shows the heat flux versus the pore size where

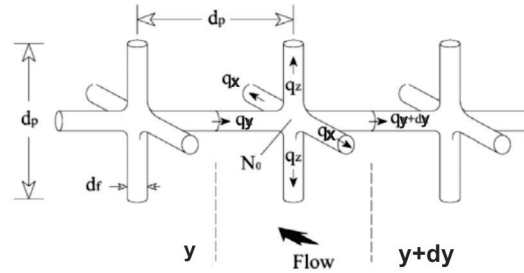


Figure 4.30: Differential element for deriving governing foam equation [135].

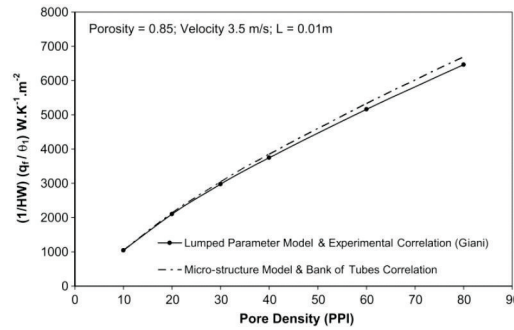


Figure 4.31: Comparison of experimental and predicted variation in heat flux passing through a foam sample with respect to pore size [135].

the data predicted using the Tubes Correlation are in very good agreement with the experimental data.

An analytical model with a more realistic representation of the actual aluminium foam structure was developed by Bai et al [136], based sphere-centered open-cell tetrakaidecahedron, and compared with experimental data from test of flow behaviour using air as the coolant gas. The model also gives a good agreement with the data from Leong et al. [94].

4.5 Summary of trends in heat transfer and permeability

For a better understanding of the trends in heat transfer and permeability a summary of the general effect of common variables (pore size, density, porosity, Nusselt and Reynolds number) is shown in Fig. 4.32, where it is possible to observe how the heat

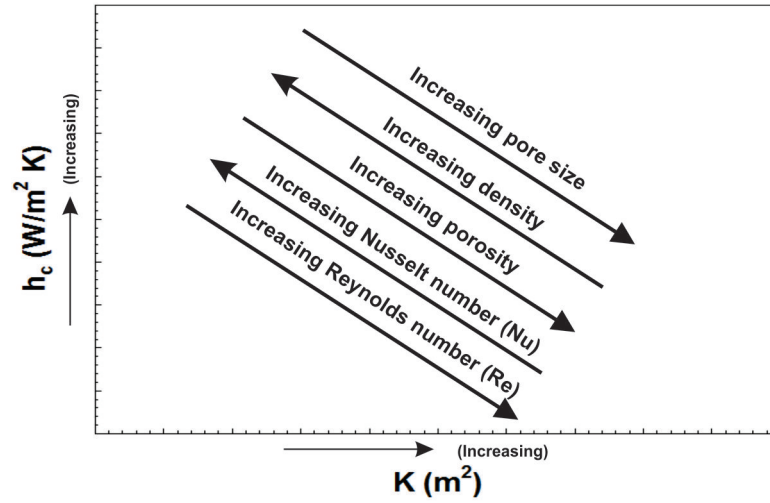


Figure 4.32: Schematic diagrams of the trends in permeability and the heat transfer in metal foam with common variables.

transfer and permeability increase or decrease depending on the variable evaluated in the metal foam.

Chapter 5

Experimental Procedure

Foam samples in this work were processed following the fabrication process which will be described below. Both the foams processed in-house and aluminium foams commercially available were thermally and physically characterized employing the procedures and techniques that will be described in this chapter.

5.1 Replication technique

For the work presented here, a single foam production method was selected. Because of equipment availability and the versatility of method, the replication technique was chosen. This method involves casting in the liquid state over a removable space-holder phase, in particulate form, and a gas pressure being applied to cause infiltration. The space holder particles are interconnected and therefore the foam obtained is an open pore foam.

The replication technique has three principal steps:

- 1.- Fabrication of the open pore pattern from a space holder material. This is called the preform.
- 2.- Infiltration of the liquid metal into the preform.

3.- Removal of the preform from the solidified metal to produce a metal foam.

5.1.1 FABRICATION OF THE OPEN PORE PATTERN (PREFORM)

The material used for the open pore pattern or preform can be of several different types (examples of which include pure salt (NaCl), alumina, polystyrene, and some resins, such as phenolic resin [2, 3, 58, 144, 145]). To use these materials in the replication technique imposes certain requirements, and this may make it difficult to find the ideal material that could be used in an industrial process. The principal requirements are: to maximise control over the foam topology, increase the ease of dissolution of the preform (which can take a long time, even in some cases days) and avoid reaction with the metal to be infiltrated [3, 58, 59]. One material that has been suggested to allow the preform to achieve this is a mixture of salt, flour and water [2, 58], suitable for use when aluminium is used to produce metal foams. This mixture produces a paste which can be used to make a preform that is easy to manufacture and dissolve [21, 58], and therefore has great potential to be used in industry.

The principal properties required for the material used to produce the preform are: it has to be chemically stable in contact with the molten metal, it has to be easy to remove once the metal is cooled and it should also be easy to handle and inexpensive if possible [59].

Following the method in [58], the materials selected to produce the preform were; commercial salt (table salt or cooking NaCl), plain white flour (domestic grade supplied by Tesco or Morrisons supermarkets) and water (H₂O). These materials were mixed together with salt usually being the major component. Salt can resist processing at temperatures up to around 740 °C (its melting point is 801 °C [146]) and does not have any reaction with the aluminium.

The flexibility presented by the paste obtained by mixing the constituents (NaCl, Flour and water), is an important advantage of this process. The paste can be manipulated to

obtain virtually any form, such as cylinders, cubes, pyramids and spheres around 2 to 10 mm in diameter (the range within which the paste can be shaped and is heat treatable without unwanted expansion) without any problem. The paste can be shaped by hand, or by any usual shaping operations used in the pharmaceutical or food industry, where one particular shape is required.

The preform produced with the desired shape is placed under heat treatment with the objective to eliminate the water and to remove the flour by pyrolyzation, the remaining carbon being removed by reaction with the atmospheric oxygen [58].

5.1.2 INFILTRATION OF THE LIQUID METAL INTO THE PREFORM

After the preform is fabricated with the characteristics required, the preform is ready to be infiltrated. As some metals do not wet the preform material, like aluminium with NaCl, it is necessary to apply pressure (most easily done by using an inert gas in a closed system) to fill the open spaces in the preform. However, this pressure applied should not be too high, or the preform material, which is itself porous, could be penetrated by the molten metal. Before the molten metal is infiltrated it is also recommended to pre-heat the bulk of preform to avoid premature solidification of the melt [2, 3]. Once the molten metal is infiltrated, the composite (metal-preform) is left to cool down until solidification takes place.

5.1.3 REMOVAL OF THE PREFORM

The preform could be leached out from the composite with a suitable solvent or it could be removed by pyrolysis, depending on the nature of the preform material. For example water can be used for leaching when the preform is salt [21, 58] or thermal pyrolysis is applied when polymer spheres are used as space holders [3]. The composite (metal-preform) can be machined before the space holder is removed, this can help to retain the foam shape, especially if the metal used to produce the foam does not present

grater resistance when it is cut.

5.2 Machining (Electro Discharge Machining)

The thermal contact resistance between the metal foam sample and the copper cylinder was one of the principal concerns when the heat transfer characterization was carried out (Subsection 7.1.2), and this can be reduced significantly if the sample has the most accurate dimensions. To be able to obtain this, the aluminium foams were machined using the non-traditional machining process Electro Discharging Machining or EDM.

On this method electrical energy generates an electrical spark and material removal mainly occurs due to thermal energy of this spark. EDM is mainly used when difficult or very precise geometries are required.

The EDM machining process is based on a potential difference applied between the tool and workpiece. Both the work material and the tool must be conductors of electricity. As the dielectric medium, kerosene or de-ionized water is used. Generally the tool is connected to the negative terminal of the generator and the workpiece is connected to positive terminal. A gap is maintained between the tool and the workpiece. The electric field established depends on the gap between the workpiece and the tool. When this gap is reduced the intensity of the electric field in the volume between the tool and the workpiece becomes greater than the strength of the dielectric and it breaks allowing that the movement of electrons and ions can be visually seen as a spark. Thus the electrical energy is dissipated as the thermal energy of the spark. Then this thermal energy (which can raise the local temperature higher than 10000 °C) removes the material from the workpiece by instant vaporization and melting. The small scale of these sparks allows the position of the cut to be determined precisely, and the non-loading nature of the process means that when it is applied to metal foams the structure remains undisturbed.

5.3 Heat transfer measurements

To investigate the heat transfer in metal foam samples an experimental technique is needed which can be applied to such foam samples produced and described later. To do this analysis a device is required to measure fluid flow and temperature changes when the metal foam is cooled by a fluid flowing through it. This device was developed in this work, and the development process is described in Chapter 7. Here a brief account of the final device is given. To monitor the performance of the foam at transferring heat the properties that need to be measured are: the temperature of the foam, the pressure drop across the foam, the flow rate and temperature of fluid before and after flow through the foam. The concept used to characterise the heat transfer and the permeability performance of the aluminium foams is as follows: heating a thick-walled cylinder of copper in which the foam is placed, while cooling the foam by forced convection by flowing a fluid through it. The difference in temperature between the copper block and the incoming air gives the driving temperature difference for the heat to be transferred. How effective the foam is at doing this can be assessed by measuring the temperature difference in the cooling air before and after the specimen. A general view of the experimental apparatus is shown in Figure 5.1. The apparatus consists of two steel chambers, one of which is connected to the cooling fluid (in this case air), between which is the copper cylinder. The steel chambers are the locations where the measurement of air temperature before and after the sample, and the pressure drop are performed.

The copper cylinder has the role of the heat store, supplying thermal energy at a steady rate to the foam and smoothing out variations from the heater. It is one of the most important aspects of this work (as it forms the test section); therefore a range of issues were considered in its the design. The most important are:

- 1.- The thermal isolation of the copper cylinder.
- 2.- Thermal instrumentation.

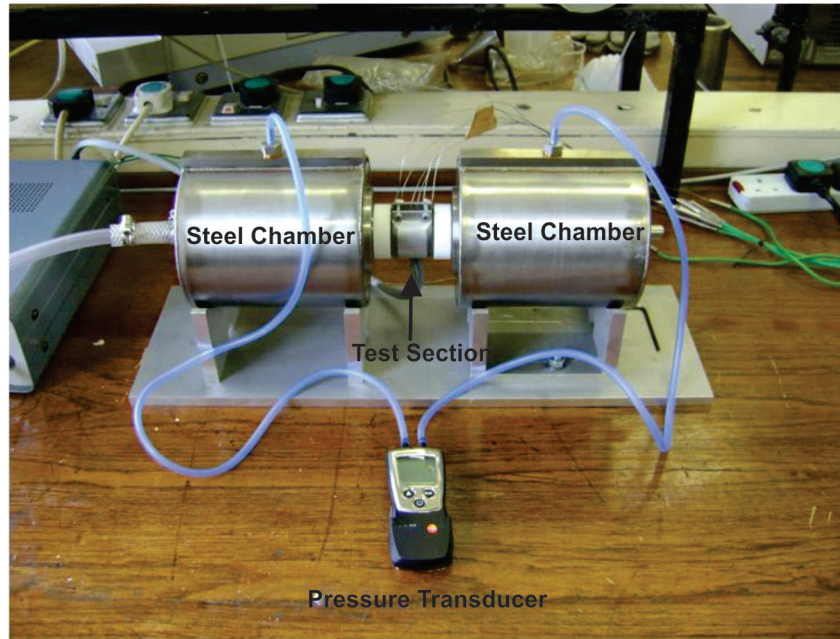


Figure 5.1: General view of the experimental apparatus constructed to characterize the heat transfer behaviour of metal foams.

3.- The thermal resistance between the metal foam and the copper cylinder.

These factors will be discussed in more detail where the rig is described later.

5.3.1 DATA ACQUISITION SYSTEM

To fully characterise the heat transfer of a metal foam sample, in addition to the measurement of the temperature of the copper cylinder, the temperature of the cooling fluid was measured. To do this, a 1 mm diameter thermocouple was inserted inside each of the two steel chambers, before and after the sample, using such a small diameter ensured that the thermocouple had low thermal inertia, and responded rapidly to changes in gas temperature. The steel chamber has 13 cm diameter and 15 cm length, and the thermocouple was inserted to the midpoint of the cylinder. The temperatures from the copper cylinder and the cooling gas were collected by a data acquisition system supplied by National Instruments. The hardware consists of a chassis (model cDAQ-9172 with 8-slot). Four slots of this chassis were used to measure the temperature with 2

modules (model NI-9211). Each module has the capacity to log 4 thermocouples. To store the temperatures from the copper cylinder as well as the two steel cylinders a program was developed using LabView software. This program has the capacity to store readings from each thermocouple at a rate of 1 to 10 Hz and display a graph of temperatures with time. The heating system consisted of a Watlow band heater with 36 mm internal diameter and 28 mm width, attached to a 240 Volts and 250 Watts supply. The band heater is fastened on the copper cylinder by two screws and the temperature is controlled by a Watlow EZ Zone PM PID controller.

To measure the pressure drop of the flow, a hole was made on the opposite side from the thermocouple entry in each of the steel chambers. A pressure transducer was connected to both of these holes to measure the difference of the pressure as a result of the pressure drop when the cooling fluid is flowing through the metal foam. The differences of pressure between 0.01 to 50 mbar a Testo 510 device was used to obtain the measurement and for differences of pressure higher than 50 mbar, a Digitron 2027 was utilized, both devices were supplied by RS Components.

5.4 Test procedure

The steps followed in every test are as follows:

- After application of a thin layer of Electrolube thermal adhesive over the internal cylinder surface of the copper cylinder, Fig. 5.2(a), the sample was mounted, Fig. 5.2(b).
- The copper cylinder with the foam inside was placed on the rig (between the two steel chambers, 5.1).
- Once the copper cylinder was mounted, the thermocouples were inserted into it. The master thermocouple was inserted in the position T3 (Fig. 7.4, centre of the

copper cylinder) in all tests in order to have better control and less fluctuation of the temperature during the test.

- Once all the thermocouples were in position the power to the band heater was turned on, and allowed to reach the temperature desired.
- After a stabilization period, i.e. when the 5 thermocouples inserted in the copper cylinder displayed the same temperature (that was desired for the test) for 5 minutes with a tolerance of $\pm 1^\circ\text{C}$, the injection of the cooling air was started.
- The test continued until the temperature of the thermocouples inserted in the copper cylinder and air after cooling the sample (outlet air temperature) reached a stable point, which was taken to be when the temperature of all thermocouples changed less than 1°C in one minute. The data from the thermocouples were logged by the data acquisition system, Subsection 5.3.1, in real-time.

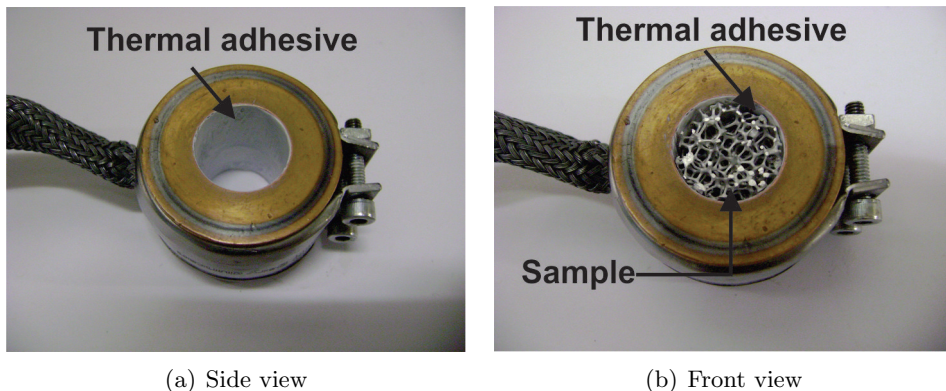


Figure 5.2: Sample mounted in the copper cylinder. (a) Copper cylinder after applied thermal adhesive. (b) Sample of Duocel foam mounted in the copper cylinder.

5.5 Heat transfer coefficient calculation

When the stable point has been reached, the Heat Transfer Coefficient (h_c) can be calculated. To calculate the Heat Transfer Coefficient for the foam samples the key data collected are:

- The gas flow rate v (m^3/s)
- The temperature of the incoming air before passing through the foam, T_{in} ($^{\circ}C$)
- The temperature of the outgoing air after passing through the foam, T_{out} ($^{\circ}C$)
- The mean temperature of the copper cylinder in the last 3 minutes of the test once stabilization has been reached, T_{Cu} ($^{\circ}C$)

First of all the calculation of the air heat flow for each air flow rate has to be done using the following formula:

$$\frac{q}{A_{cyl}} = \dot{q} = \dot{m}C_p(T_{out} - T_{in}) \quad (5.1)$$

where q is the heat flow rate (W), A_{cyl} is the contact area between the sample and the heated cylinder (area of the cylindrical hole in the heated copper block), \dot{q} is the heat flux supplied to air ($J/m^2 s$), \dot{m} is the air mass flow rate (g/s), C_p is the specific heat of the air at constant pressure ($1.005 kJ/kg^{\circ}K$) [147] and the last term is the air difference between outlet and inlet air temperature ($^{\circ}C$).

To find the Heat Transfer Coefficient h_c , for each of the samples tested, Newton's law of cooling was used as follows:

$$h_c = \frac{\dot{q}}{T_{Cu} - T_{in}} \quad (5.2)$$

5.6 Structural characterization

The structural characteristics of the metal foams are very important as they have a strong effect on the properties of the foam, which affects the applications that may be suitable. The most important are arguably the pore size and morphology of the porosity, and these characteristics are measured through its characterization. The determination of the pore size and relative density of the foams was done with the

procedures described below.

5.6.1 DENSITY MEASUREMENT

The foam density for Duocel, Corevo and replication technique samples were calculated by weighing and measuring the sample, then the weight was divided by the calculated weight assuming that the sample was 100 % dense.

Assuming that one sample with 19 mm diameter and 32 mm length is completely solid aluminium, the weight was calculated from the density as follows:

$$\rho = \frac{m}{V} \quad (5.3)$$

where ρ is the sample density (g/cm³), m is the sample mass (g) and V sample volume (m³), the mass obtained assuming that the sample is a solid material is 25.7 g. The mass of each one of the samples was divided by this number, to obtain the relative density of each.

5.6.2 PORE SIZE CHARACTERIZATION

For some samples, a pore size was reported by the manufacturer; in the case of Duocel the pore size is reported in PPI (Pores Per Inch) as follows:

$$PPI = \frac{25.4mm}{NP} \quad (5.4)$$

where NP = Number of pores counted along one inch in the sample. Corevo reported the diameter of a preform sample as pore size, and samples produced in the laboratory by the replication technique, the pore size is the diameter of the preform spheres fabricated. In all the cases, the true pore size could be slightly different, and so this was measured experimentally.

5.7 Scanning Electron Microscopy (SEM/EDS)

Samples produced in-house under the replication technique were fabricated using silica crucibles so it was necessary to examine the chemical composition of the foam to determine if silicon was picked up by the aluminium foam. To determine qualitatively the chemical composition of the metal foam obtained under replication technique, Scanning Electron Microscopy was used.

Scanning Electron Microscope (SEM) uses a focused beam of high energy electrons to generate a variety of signals at the surface of the samples that is been analyzed. The signals generated for these interactions can be detected and then information can be revealed about the sample including external morphology, chemical composition and crystalline orientation and structure of the material of the sample.

5.7.1 ENERGY-DISPERSIVE X-RAY SPECTROSCOPY (EDS)

The interaction of the electron beam with the sample produces a variety of emissions, one of them is the x-Rays. This emission is detected using an energy dispersive (EDS) detector which separates the characteristic x-rays of the different elements into an energy spectrum. Special software is used to analyse the energy spectrum in order to determine the abundance of the specific element.

Chapter 6

Development of Foam

Fabrication Method

Aluminium open-cell foams with single and graded pore sizes were fabricated and their thermal and fluid flow behaviour were characterized. Because of the flexibility of the method, the replication technique was selected for the production of the metal foams fabricated in-house.

6.1 Fabrication of the open pore pattern (preform)

Figure 6.1 shows schematically the method used for the fabrication of the open pore preform.

6.1.1 MIX COMPOSITION

As described in Subsection 5.1.1, the materials selected to produce the preform were; commercial salt (table salt or cooking NaCl), plain white flour (domestic grade supplied by Tesco or Morrisons supermarkets) and water (H_2O). These materials were mixed together, with salt usually being the major component, following the method in [58].

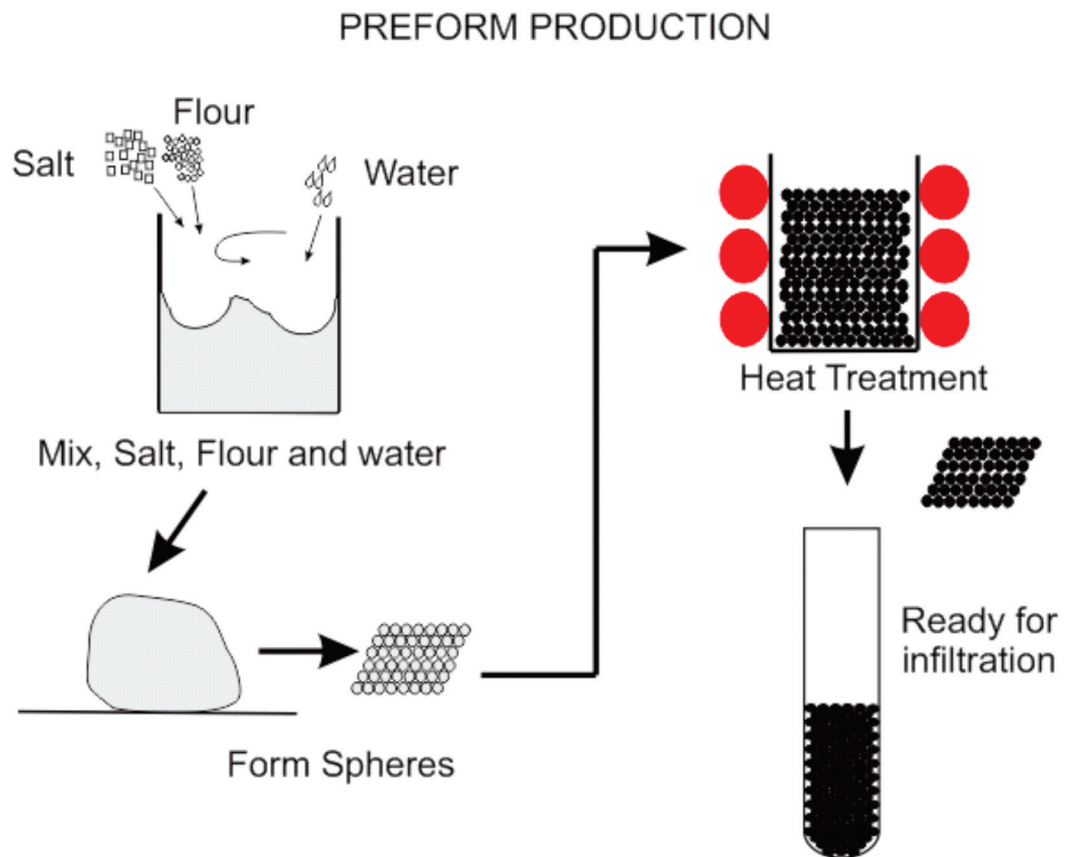


Figure 6.1: Schematic diagram of the first stage of the replication technique as used in this work for the production of preforms, allowing processing of metal foam structures.

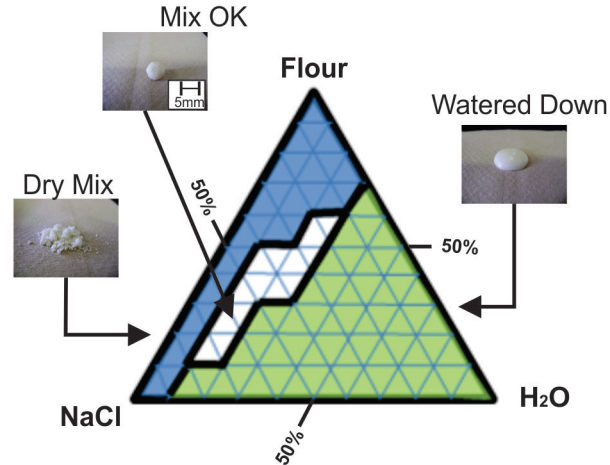


Figure 6.2: Ternary-style diagram obtained during process development of the mixture of NaCl, H₂O and flour. The diagram shows three zones; the green zone where the paste is liquid and the shape required cannot be retained; the blue zone, in which the paste is dry and cannot be shaped, and the white zone; in this area the paste is easily shaped and the shape is consistent and can hold throughout the process. The composition used in this work is indicated.

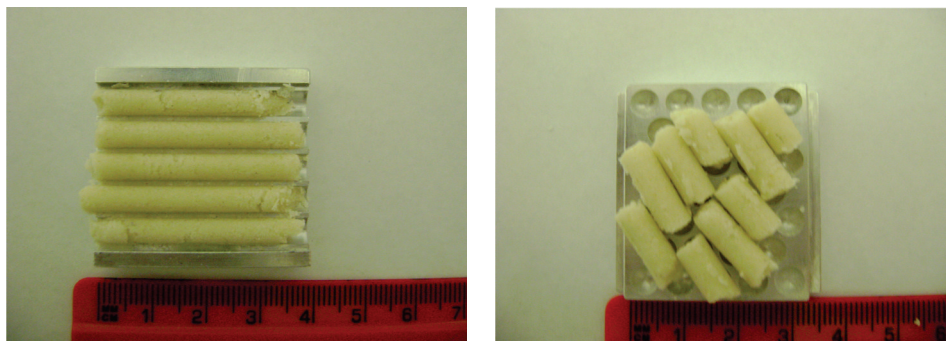
To optimise the paste it was necessary to vary the amount of NaCl, flour and water in different proportions to get the consistency required of the mixture. The required properties for the preform were to have a consistency such that the desired shape could be easily obtained and that this shape could hold throughout the replication process (manufacture, heat treatment to set the preform shape and metal casting) and also easy removal by dissolution in water after cooling and machining the metal foam.

A ternary-style diagram of the mix of these three components was obtained, Figure 6.2, which helps as a guide in the manufacture of the preform. The composition used in this work to produce the preforms used in the manufacture of all the replicated metal foams was: 60 % salt, 25 % flour and 15 % H₂O (with all values given being in wt %).

6.1.2 MANUFACTURE OF THE PREFORM

In this project the initial shape desired for the pores in the foam was a sphere with 5 mm diameter. The initial spheres fabricated were made by hand, but to produce the quantity necessary to fabricate 3 foam samples (atypical number used for repeats, approx. 200 spheres), takes between 2 to 3 hours, and the spheres show large variations in size (found to be ± 2 mm, where the diameter desired was 5 mm). To obtain a higher reproducibility of the size and shape in the smallest fabrication time possible, a process with two different moulding steps was developed.

Once mixed, the paste is put in a first mould, consisting of 2 halves machined from aluminium block. In this step cylinders with a diameter of 5 mm are formed (for an end aim of producing 5 mm diameter spheres). Producing this initial shape facilitates the next step in the production of the spheres by getting close to the desired final shape; yet, unlike spheres, cylinders can be formed from a quantity of paste by manual pressure on the mould. This mould, called mould 1, is shown in Figure 6.3(a). Once the cylinders have been produced with mould 1, they are chopped in small pieces of approximately 1 cm length, then placed between the two halves of mould 2 which has spheres machined in it, this can be observed in Fig. 6.3(b).



(a) Mould 1, paste cylinders

(b) Chopped cylinders over one half of the Mould 2

Figure 6.3: The first stage in the manufacture of the 5mm paste spheres. (a) Mould 1 with the paste in cylindrical form after the first step and (b) Small pieces (1 cm length approximately) of cylinder formed in mould 1 placed over the lower half of mould 2. The scale in both images is in cm.

After squeezing the cylinders by hand with a pressure estimated to be between 31 to 33 kPa in this mould, spheres are ejected. Figure 6.4(a) presents the paste after being squeezed showing the paste in spherical form. After the paste is squeezed to a spherical shape, the remaining paste (the excess paste that remains between the two halves of the mould when the paste is squeezed) between the spheres is removed. The final spheres obtained after the excess has been eliminated are shown the Fig. 6.4(b). Two sphere sizes of 5 and 3 mm were fabricated following the steps described above.

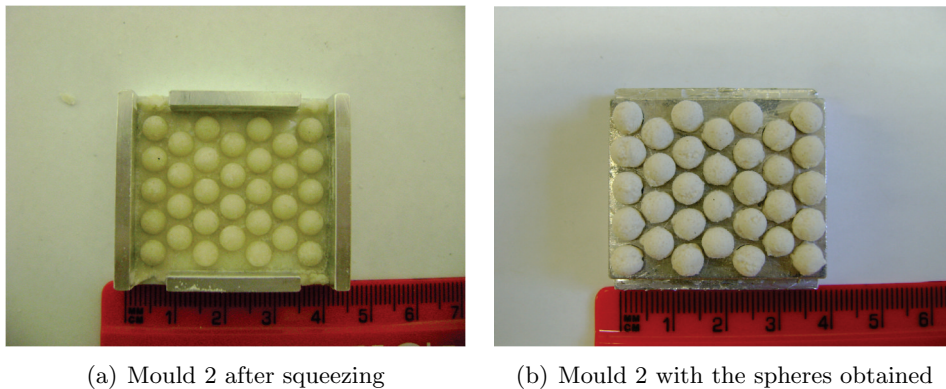
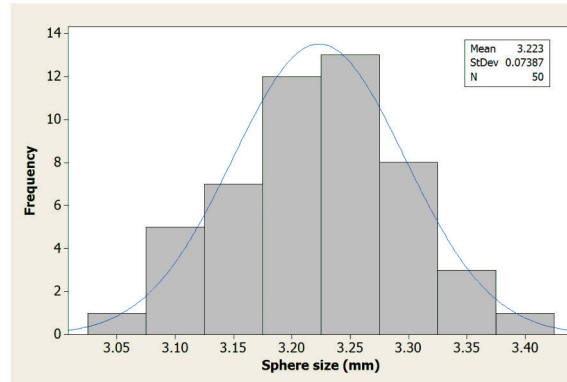


Figure 6.4: Mould 2, the final step to produce spheres for the preform. (a) Paste in sphere after being squeezed and (b) spheres obtained after the excess paste is eliminated. The scale in both images is in cm.

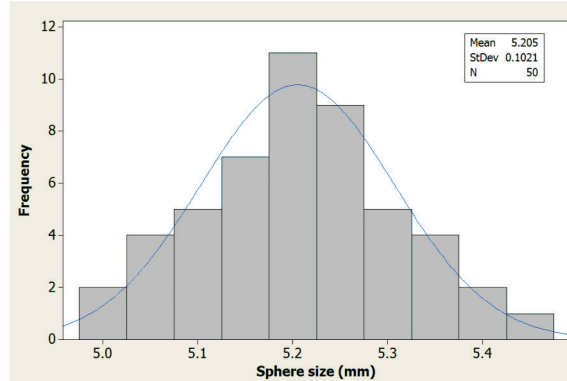
Figures 6.5(a) and 6.5(b) present the sphere size histogram obtained for the spheres fabricated with the process developed. It is possible to observe that the mean size is 3.22 mm for a nominal 3 mm diameter sphere and 5.20 mm for a 5 mm sphere respectively. The third preform used for the fabrication of aluminium foams by the replication technique was 1 mm size; this preform was obtained using dense salt grains sorted for size by sieving normal table salt.

6.1.3 HEAT TREATMENT OF THE PREFORM

The spheres produced using the process explained in the previous section are now ready to be heat treated. The heat treatment has the objective to eliminate the water and to remove the flour by pyrolyzation, the remaining carbon being removing by reaction



(a) Sphere size histogram for 3 mm spheres



(b) Sphere size histogram for 5 mm spheres

Figure 6.5: Sphere size histogram obtained from paste spheres fabricated with the process developed. (a) Histogram obtained for a nominal 3mm and (b) 5mm sphere diameter respectively.

with the atmospheric oxygen [58].

After the heat treatment, a NaCl sphere with fine internal porosity is obtained. As the formulation and precise grade of flour used in this investigation is different to previous work, such as [58], a specific heat treatment was developed. The outcome is in Figure 6.6. The heat treatment starts from room temperature to 80 °C with a 60 minute dwell to promote evaporation of water. The second temperature ramp is up to 100 °C to complete water evaporation. The time the spheres are exposed to this temperature is 60 minutes. These two first ramps in the heat treatment are essential to eliminate water from the open pore pattern. If omitted, conversion of water to steam at higher temperature would break up the spheres; this was observed to take place in

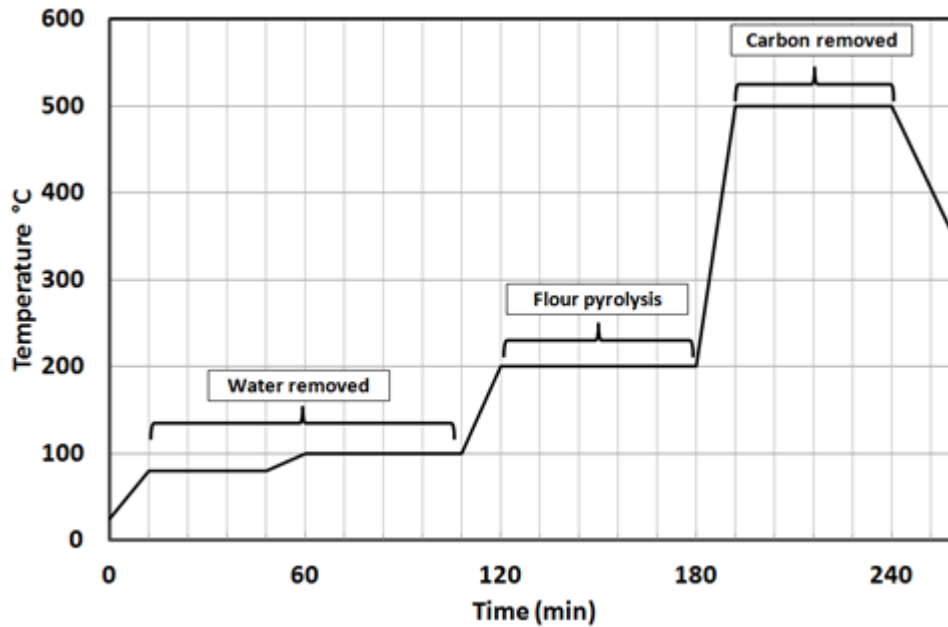


Figure 6.6: Heat treatment for the spheres to eliminate water and flour from the paste.

early experiments. The following two ramps are to eliminate the flour. The third ramp is up to 200 °C and is followed by a dwell of 60 minutes. The objective is to pyrolyze the flour present (i.e. convert it to carbon by decomposing the organic compounds). In the last ramp the temperature is elevated to 500 °C where the dwell is 60 minutes. At this temperature the remaining flour in the preform, principally in the centre of the sphere, is pyrolyzed and the majority of the remaining carbon is oxidized forming CO₂ which is removed. The preform is left inside the furnace to cool from 500 °C to room temperature to be sure no thermal shock is experienced.

It is important to emphasize that the heat ramp rate is the most important parameter that has to be controlled in the first two stages of heat treatment, because if the velocity is greater than 5 °C/min the spheres may explode or expand significantly, due to the rapid evolution of water vapour.

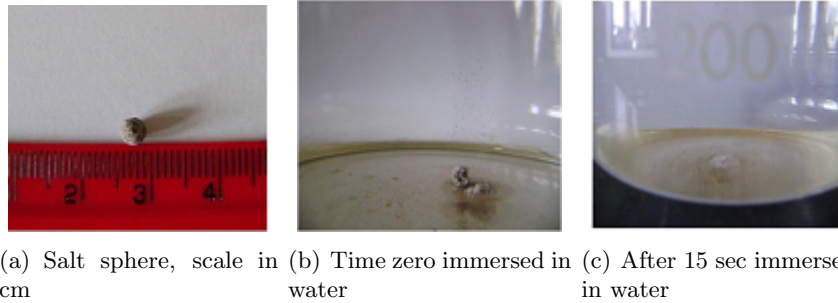
It is further important to emphasise that, in contrast to the earlier work of [58], the paste spheres were not compacted together before heat treatment. Instead the process was performed on individual spheres. This provided a stock of spheres that could be

poured loose into a crucible, as described in Subsection 6.2. This gives greater ease of processing and reproducibility in the spheres themselves, as there is no change to their form from the compaction process. It does however require more careful processing to achieve different densities, as this must be controlled during the infiltration step, rather than by compacting the preform. This is similar to that used on a salt preform processed using flour, in a alternative process [21].

6.1.4 DISSOLUTION IN WATER OF THE PREFORM

The easy dissolution of the preform is the second important characteristic that it is required to have. The dissolution behaviour of the preform was investigated experimentally as, even though dissolution was found to be good in other work that used this type of preform [21, 58] it was important to confirm that the slight changes of composition cause no major change in behaviour. This was done as follows; a sphere obtained after the heat treatment was placed into a beaker filled with tap water. The time was recorded from the moment the sphere was put in the water until the sphere was finally dissolved or had collapsed into small grains.

The results obtained show that the 5 mm diameter NaCl spheres dissolve in less than 15 seconds and in the instant that the sphere was immersed in the water the sphere began to collapse. This process is shown in Figures 6.7(a), 6.7(b) and 6.7(c). These results confirm what was previously found in [58] and indicate that the properties sought for the preform material have been satisfied.



(a) Salt sphere, scale in cm (b) Time zero immersed in water (c) After 15 sec immersed in water

Figure 6.7: Dissolution in water of an NaCl sphere produced in this work. (a) Sphere obtained on the basis of the composition and heat treatment developed, (b) Sphere immersed in water already beginning to collapse at time zero and (c) Sphere totally collapsed in water after 15 sec.

6.2 Infiltration of the preform with aluminium

After the heat treatment the NaCl spheres are placed inside a quartz crucible. The crucible has the following dimensions; 3 cm diameter and 20 cm length and is formed with a rounded base containing a hole of approximately 2 mm diameter. The quantity of preform spheres placed inside the crucible is enough to fill a depth of between 5 and 6 cm. On top of the spheres 35 g of aluminium grade 99.7 % ingot material supplied by William Rowland Ltd. was placed for each casting process. Even though the aluminium needed in the sample is less than 10 g, the excess aluminium used in the fabrication of the aluminium foam assured the full filling of the internal spaces of the preform when the preform is being infiltrated. Once the aluminium is added, the crucible is connected to an argon gas supply by sealing around the top of the crucible, and is positioned inside an induction coil. The aluminium is then melted by electromagnetic induction.

As the preform is NaCl, an ionic solid, it is not wetted by the liquid aluminium [59], and pressure must be applied to the molten metal to cause infiltration. The pressure is applied through an inert gas, in this case argon, used to drive the molten aluminium into the preform. The crucible has a hole made in the base to permit the free flow through of the inert gas and the exit of any gas contained within the preform spaces. Figure

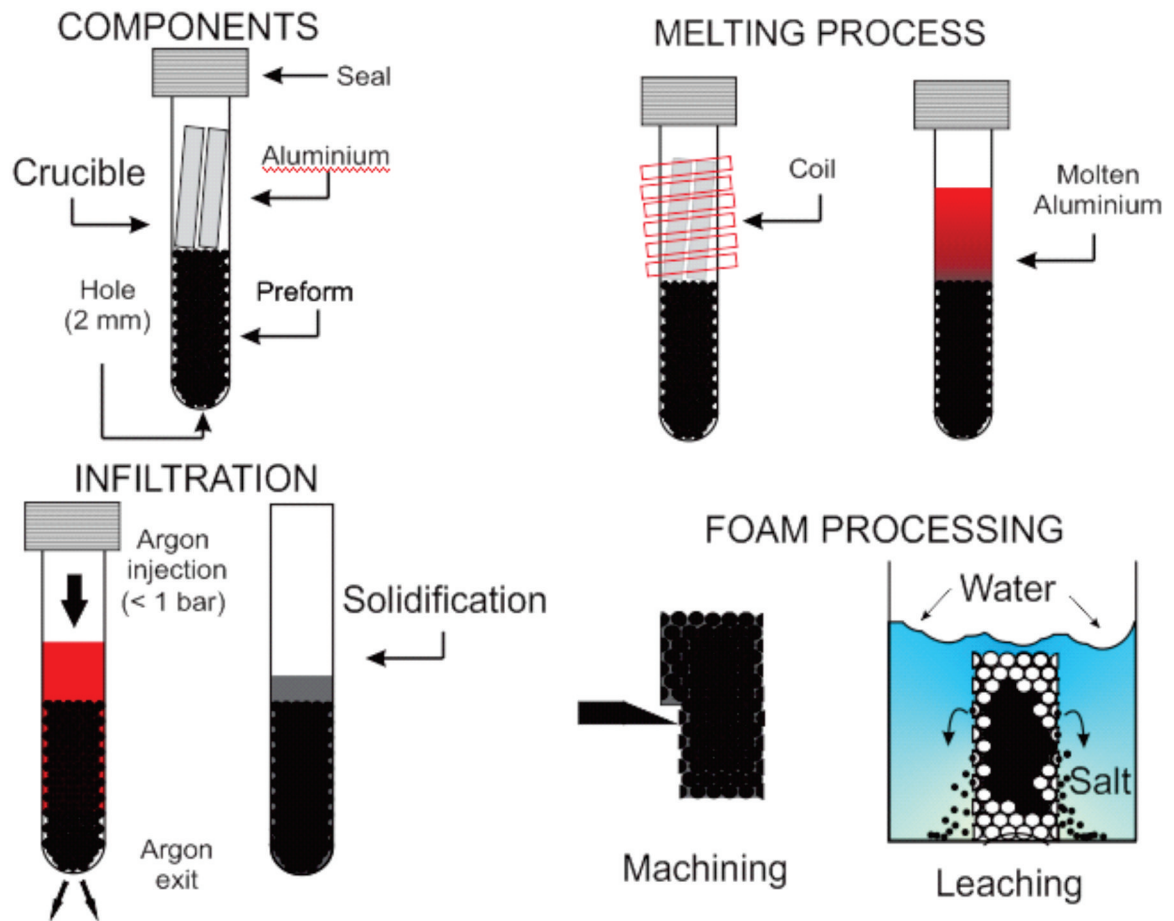


Figure 6.8: Diagram of the infiltration of the preform with aluminium.

6.8 shows a schematic diagram of the crucible, with the inert gas supply connected, positioned inside of the coil.

Once the liquid metal has infiltrated in the preform, the power of the coil is cut and the crucible cools to room temperature, producing a composite of aluminium and salt.

An example of this is shown in Figure 6.9.

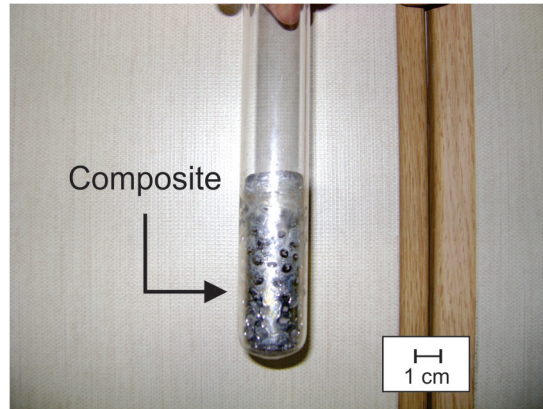


Figure 6.9: NaCl/Al composite obtained after preform has been infiltrated with aluminium.

6.3 Removal of the preform

The composite of NaCl/Al obtained can be machined before the space holder is removed (this helps to retain the foam shape). Cylindrical and cuboid geometries can be machined from it without major difficulty and the tolerances obtained can be very good. The aluminium is easily machined compared with, for example, steel, and the presence of NaCl does not offer significantly greater resistance, although it does mean that machines need to be carefully cleaned after cutting the composite to avoid corrosion.

In this work conventional machining by sawing was used to remove excess aluminium and give a rough shape. Final machining to precisely the required size was performed after leaching the salt using Electro Discharge Machining (EDM).

Once the composite had been roughly machined it was placed under flowing tap water to remove the preform. The removal process takes less than 1 minute and finally the metal foam is obtained. Figures 6.10(a) and 6.10(b) show examples of metal foams with cuboid and cylindrical shapes produced in this work.

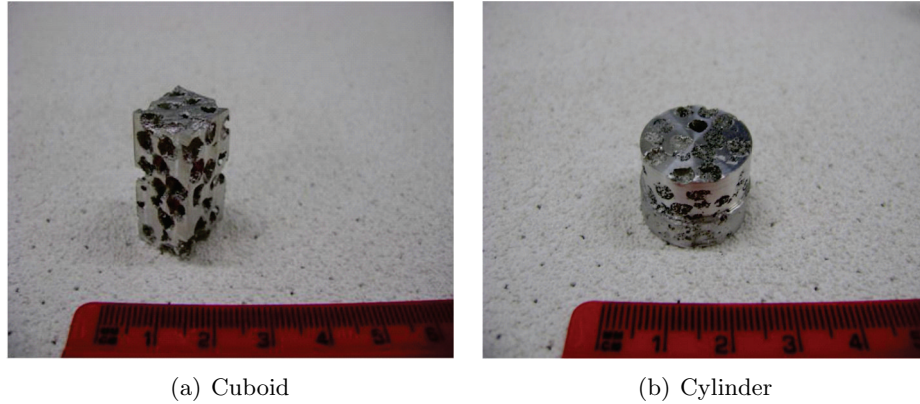


Figure 6.10: Aluminium foams obtained in different shapes after machining, the scale is in cm. (a) Cuboid shape and (b) Cylindrical shape.

6.4 Density measurement

As explained later, as well as the laboratory made samples, commercial foam samples produced by similar (Corevo) and different (Duocel) techniques were obtained for testing. The foam density for Duocel, Corevo and replication technique samples were calculated following the method described in Section 5.6.1. The results obtained for the in-house samples (Replicated) and the commercially available foams (Corevo and Duocel) are reported in Table 6.1.

Table 6.1: Density of Duocel, Corevo and replicated metal foam samples used for thermal and hydraulic experiments.

Sample	Manufacturer	Mass (g)	Nominal Relative Density (%)	Real Relative Density (%)
5 PPI-5.2	Duocel	1.313	5.2	5.09
5 PPI-7.9	Duocel	2.026	7.9	7.85
5 PPI-11.5	Duocel	2.702	11.5	10.48
10 PPI-4.9	Duocel	1.302	4.9	5.05
10 PPI-7.9	Duocel	2.063	7.9	8.00
10 PPI-9.9	Duocel	2.665	9.9	10.33
20 PPI-4.1	Duocel	1.228	4.1	4.70
20 PPI-8	Duocel	2.007	8	7.78
20 PPI-10.5	Duocel	2.546	10.5	9.87
40 PPI-8.6	Duocel	2.067	8.6	8.01
F65	Corevo	4.368	-	16.94
F64	Corevo	6.382	-	24.75
F56	Corevo	7.213	-	27.97
F55	Corevo	4.106	-	15.92
F51	Corevo	6.596	-	25.57
F36	Corevo	11.435	-	44.34
5 mm	Replicated	8.240	-	31.95
3 mm	Replicated	9.576	-	37.13
1 mm	Replicated	9.005	-	34.92
1-3 mm	Replicated	9.485	-	36.78
1-5 mm	Replicated	8.069	-	31.29
3-5 mm	Replicated	8.151	-	31.60
1-3 mm smt	Replicated	8.878	-	34.42
1-5 mm smt	Replicated	8.405	-	32.59
3-5 mm smt	Replicated	8.828	-	34.23

6.5 Chemical analysis of fabricated samples (SEM/EDX)

The aluminium foams processed by the replication technique were fabricated using a silica crucible as described in Subsection 6.2. This could lead to pick up of silicon by the aluminium foam. Silicon in aluminium in significant amounts could decrease its thermal conductivity by 20 to 30% [148] with an obvious affect on the properties measured here. The solid solubility of silicon in aluminium at the eutectic temperature, 577 °C, is 1.65 % wt [148] therefore, Scanning Electron Microscopy (SEM) with Energy-Dispersive X-Ray Spectroscopy (EDS) detector [149], was used to analyze and determine the silicon

content in aluminium foams processed by the replication technique [150]. Using the "spot" mode a sample was analyzed at 1, 6 and 15 μm from the surface that had been in intimate contact with the silicon crucible when samples were fabricated. Figs. 6.11(a) and 6.11(b) for 1 μm , 6.12(a) and 6.12(b) for 6 μm , as well as 6.13(a) and 6.13(b) for 15 μm , show the position in the sample where the analysis was performed and the spectrum obtained for each one of the spots respectively is also shown.

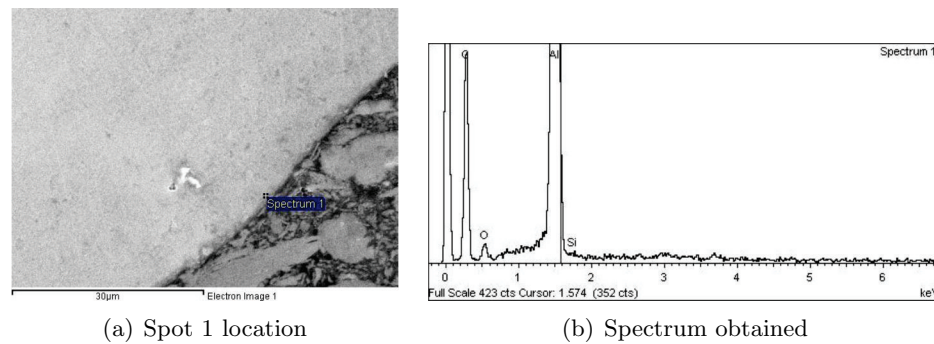


Figure 6.11: EDS Spot 1: (a) position and (b) spectrum obtained at 1 μm .

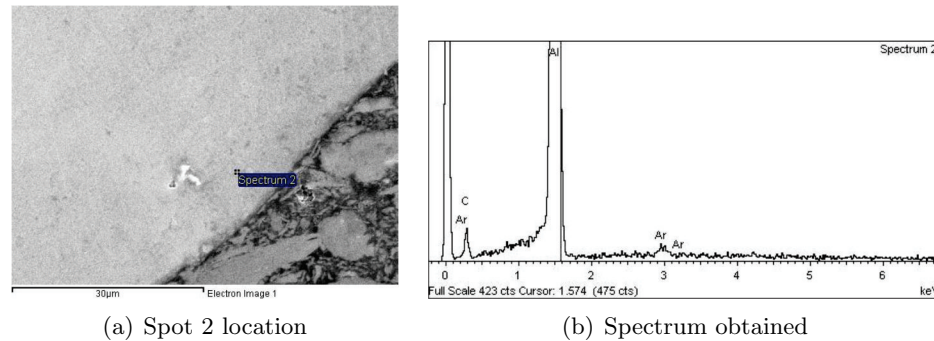


Figure 6.12: EDS Spot 2: (a) position and (b) spectrum obtained at 6 μm .

The analysis shows that there is no detectable presence of silicon in the samples, this can be observed in the EDS spectrum of x-ray counts vs energy (keV) where the presence of aluminium is displayed through the peaks at characteristic energy with no presence of silicon in any of the analysis points. These low levels are likely to result from rapid solidification once the foam is formed, and the short processing time. Considering that the outer surface was in any case removed by machining, the effect of any dissolved silicon on the behaviour measured can be considered negligible.

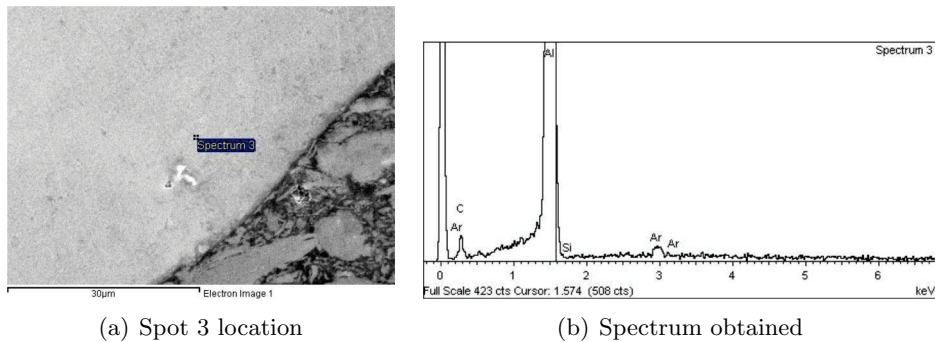


Figure 6.13: EDS Spot 3: (a) position and (b) spectrum obtained at 15 μm .

6.6 Structural characterization

Table 6.6 reports the pore size measured on each of the samples characterized. On each sample, the pore size was measured 10 times in different locations with a digital micrometer (Mitutoyo) taking care to record the largest diameter possible, and the mean value of these measurements is reported.

The true pore size obtained (with the exception of samples 10 PPI-9.9, 20 PPI-4.1 and 40 PPI-8.6) is lower than that reported by the manufacturer. These differences between the pore size reported by the manufacturer and that measured could be due to the experimental difficulty in measuring the pore size directly on the sample; however the differences are less than 0.5 mm for 5 mm pore size, and 0.3 mm for pores smaller than 5 mm. The measured values will be used in the calculation of the thermal and fluid flow properties of the samples.

Table 6.2: Pore size of Duocel, Corevo and laboratory-made aluminium foams, reported by the manufacturer and measured.

Sample	Manufacturer	Nominal Pore Diameter (mm)	Mean pore size measured, (mm)	Difference
5 PPI-5.2	Duocel	5.08 ^a	4.78	0.29
5 PPI-7.9	Duocel	5.08 ^a	4.65	0.42
5 PPI-11.5	Duocel	5.08 ^a	4.71	0.37
10 PPI-4.9	Duocel	2.54 ^a	2.43	0.11
10 PPI-7.9	Duocel	2.54 ^a	2.61	0.04
10 PPI-9.9	Duocel	2.54 ^a	2.49	-0.07
20 PPI-4.1	Duocel	1.27 ^a	1.47	-0.02
20 PPI-8	Duocel	1.27 ^a	1.24	0.22
20 PPI-10.5	Duocel	1.27 ^a	1.46	0.19
40 PPI-8.6	Duocel	0.63 ^a	0.65	-0.04
F65	Corevo	5	4.66	0.33
F64	Corevo	5	4.31	0.68
F56	Corevo	5	4.72	0.27
F55	Corevo	5	4.77	0.22
F51	Corevo	2	1.96	0.03
F36	Corevo	2	1.98	0.01
5 mm	Replicated	5	4.92	0.08
3 mm	Replicated	3	2.87	0.13
1 mm	Replicated	1	0.91	0.09

^a Pore Diameter= 25.4/PPI

Chapter 7

Test Method Development

As yet, no standard equipment exists for the measurement of heat transfer through porous materials. As discussed in the literature review, most research in this area has been carried out using bespoke test rigs. For this reason it was decided to create a test rig specifically for this work that would allow the heat transfer behaviour of the foams produced in-house as well as examples of commercially available aluminium foams to be investigated. As this equipment is new and unique, the design will be discussed in detail, along with the various test and checks that were performed to ensure reliability.

7.1 Final rig design

Before discussing the adaptations, the final design used for the experiments will be deffromscribed. Fig. 7.5 shows the schematic diagram of the experimental apparatus used to measure the temperatures and the differences of pressure in order to characterize the thermal and hydraulic behaviour of the aluminium foams at different flow rates. Key features of the design are: the steel chambers, the copper cylinder (test section), the ceramic discs and the plastic O-rings, they will be explained with detail in the following subsections.

7.1.1 STEEL CHAMBERS

The cooling air after coming out from the gas cylinder first goes into a stainless steel chamber, placed before the copper cylinder. This steel chamber has the function of reducing turbulence and stabilizing the air flow before it cools down the aluminium foam, which is heated in the copper cylinder by the band heater and it also facilitates the measurements of temperature and pressure change. The second steel chamber is placed after the copper cylinder; it receives the air after the aluminium foam has been cooled and once again causes air turbulence to be reduced and the air temperature and pressure to be accurately recorded. A pressure transducer is connected between these two steel chambers to measure the pressure drop across the sample. The volume of each chamber is 1583 cm^3 , which compares to a test volume in the rig of 11 cm^3 , less than 1% of the chamber volume. This large difference in volume guarantees that the air is stabilized before and after the test section (the copper cylinder) for reliable measurement.

7.1.2 COPPER CYLINDER (TEST SECTION)

The copper cylinder is the place where the test actually occurs; here the samples of aluminium foam were placed to be characterized. The copper cylinder has 32 mm length and 40 mm external diameter having a chamfer of two millimetres where an electrical resistance band heater is placed. The copper cylinder has a central cavity of 32 mm length and 19 mm of diameter; this is where aluminium foam samples were placed. Figures 7.1(a) and 7.1(b) show schematic diagrams of the cylinder.

As was mentioned in Section 5.3, the copper cylinder has the role of the heat store, supplying thermal energy at a steady rate to the foam and smoothing out variations from the heater. The following issues were considered in its design:

- 1.- The thermal isolation of the copper cylinder.

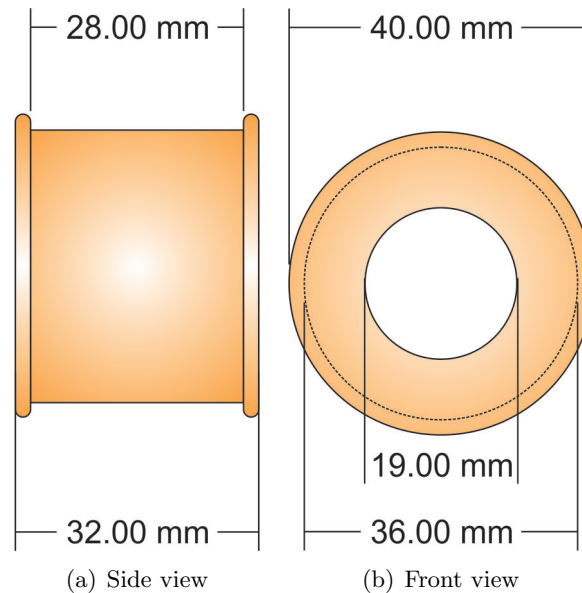


Figure 7.1: Copper cylinder dimensions. (a) Side view and (b) front view of the rig copper cylinder (test area).

2.- Thermal instrumentation.

3.- The thermal resistance between the metal foam and the copper cylinder.

These aspects will now be explained in detail.

The thermal isolation of the copper cylinder.

The copper cylinder was designed to heat the metal foam and conserve the heat energy transferred by a band heater to only pass this heat energy through the metal foam. The band heater is held in place by a chamfer of two millimetres on the cylinder 7.1(b), fastened in place by two screws 7.2. The cylinder ends are embedded in two MACOR discs. This material is a machinable glass ceramic with low thermal conductivity (1.46 W/m °C at 25°C [151]) which is positioned between the cylinder and the two steel chambers 7.3. To prevent any thermal loss through the gap where the band heater is fastened on the copper cylinder, a piece of alumina blanket insulation is put over this section.

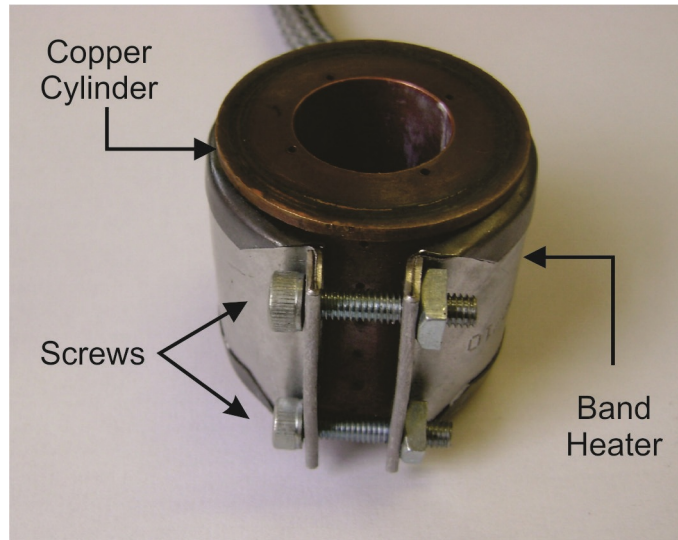


Figure 7.2: Band heater fastened around the copper cylinder, held in place by two screws.

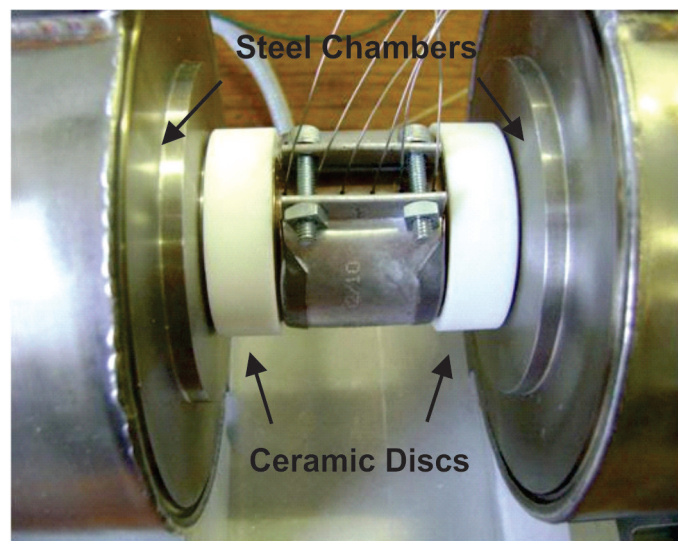


Figure 7.3: MACOR ceramic discs between the copper cylinder and steel chambers.

Thermal instrumentation.

In order to obtain the thermal behaviour of aluminium foam it is necessary to record its temperature. To do this in the copper cylinder five holes were drilled (0.6 mm diameter). Five thermocouples of 0.5 mm diameter were inserted in these holes, four to measure the temperature of the metal foam and one to feed back to the temperature control of the band heater (master thermocouple). The hole depth was 7 mm, this is one millimetre less than the total thickness of the copper cylinder wall. This one millimetre left is between the end of the thermocouple and the interface between the copper and the metal foam (Fig. 7.4), and therefore the thermocouple will gauge the temperature of the interface where the foam is attached, simulating the possible application of a foam being used to cool a hot surface. This method of taking readings allows different samples to be compared more precisely; if the thermocouples were to be placed inside the foam, then it would not be possible to place them in the same locations in different samples and expect to obtain consistent results, as sometimes these locations would coincide with a strut, and sometimes with a pore. This does mean that some accuracy may be sacrificed due to the 1 mm gap between the interface and the measurement point, however, the high thermal conductivity of copper means that any difference should be small, and the consistent use of the same position means that all samples should be comparable.

The thermal resistance between the metal foam and the copper cylinder.

Wherever two materials are placed in contact, there will be a thermal resistance [152]. This arises from imperfect contact between the two surfaces. To have accurate and reproducible tests, the objective is to reduce the thermal resistance between the copper cylinder and the metal foam, and also to ensure that it is always of the same value. There are two main factors to take into account; a) the foam must be cut so that it fits the interior of the copper cylinder precisely and b) the thermal contact between the

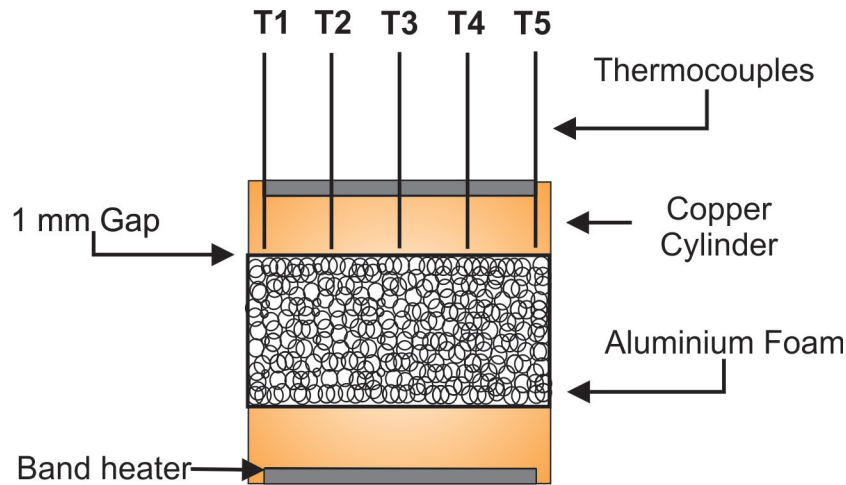


Figure 7.4: Thermocouples inserted into the copper cylinder having 1 mm gap between the metal foam and the thermocouple.

metal foam and the copper cylinder must as good as possible. The metal foam samples were cut into their final shape with 19 mm diameter and 32 mm length. In order to have the most accurate dimensions, the metal foams were cut by a Mitsubishi 110 SA Wire Electrical Discharge Machining (EDM) device using 0.25mm diameter solid brass wire as the electrode material, de-ionized water was used as the dielectric fluid with co-axial flushing. This machine has a stated tolerance of less than 0.01 millimetre [153]. To reduce the contact resistance between the metal foam and the copper cylinder, a thin layer of Electrolube thermal adhesive with 2.9 W/m-K thermal conductivity [154] was applied between the contact surface of the metal foam and the copper cylinder. For each sample, the paste was applied over the entire surface of internal hole through the copper cylinder. The quantity of thermal adhesive applied was kept to 1 g. The quantity of 1 g of thermal adhesive was standardized using a spatula with a mark that limited the quantity of thermal adhesive that was applied in every test. The decision to use thermal adhesive between the copper cylinder and the sample was made based on the discussion in Subsection 7.7.4.

7.1.3 CERAMIC DISCS

As mentioned in Subsection 7.1.2, the thermal isolation of the copper cylinder (the test section), is one of the most important issues addressed in the design of the experimental apparatus, to ensure that the thermal energy transferred by the band heater only passes through the metal foam that is being tested. Therefore, each of the test section ends is embedded inside a ceramic Macor disc (with a thermal conductivity of $1.46 \text{ W/m}^\circ\text{C}$ at 25°C [151]), to minimise the heat conduction (lost thermal energy) between the copper cylinder and the steel chambers. The ceramic disc has external dimensions of 14 mm length and 46 mm diameter. It has two grooves, in the front and back face, where a plastic O-ring is placed to obtain a hermetic contact between it and the copper cylinder and with the steel chamber. The ceramic disc has a chamfer in the front and in the back face to allow the copper cylinder and the front face of the steel chamber to be embedded on it, the geometry and dimensions are shown in Fig. 7.5.

7.1.4 PLASTIC O-RINGS

The experimental apparatus has four peroxide cured O-rings of Ethylene Propylene Diene Monomer (EPDM) to give a hermetic contact between the copper cylinder and the ceramic disc, and the ceramic disc with the steel chamber, preventing losses of gas from the system. The geometry and dimensions are shown in Fig. 7.5.

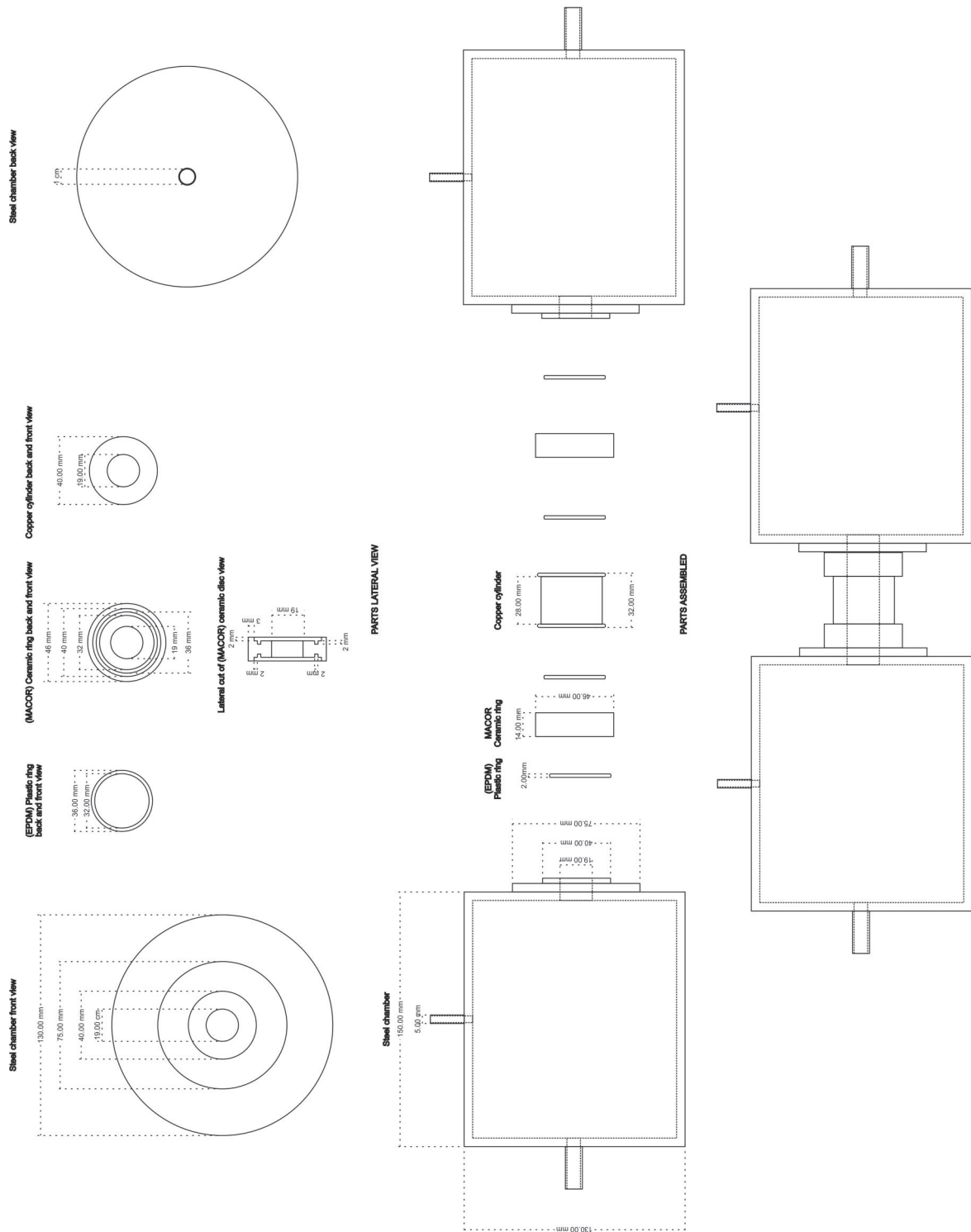


Figure 7-5: Dimensions of the components that constitute the final rig designed to characterize the heat transfer of aluminum foams.

7.2 Verification of the temperature homogeneity

Temperature homogeneity in the copper cylinder is assumed in the analysis, and so must be verified in the experiments. To understand the temperature distribution in the copper cylinder when heat is applied by the band heater, two types of test were performed, one where 4 thermocouples were inserted in the front face of the copper cylinder with two different depths (this was carried out with the objective to know the homogeneity of the temperature around the circumference of the cylinder) and the other where 6 thermocouples were inserted in along the length of the copper cylinder to two different depths (this test was carried out to know the longitudinal homogeneity of the temperature in the copper cylinder).

7.2.1 FRONT FACE RESULTS

Four thermocouples were inserted in the front face of the copper cylinder. 0.6 mm diameter holes were machined in the block and 0.5 mm thermocouples were used. The thermocouple depths were 3 and 15 mm (see figures 7.6(a) and 7.6(b) respectively) from the front face of the copper cylinder, with 90 degrees between them and the hole to inset by 1 mm from the interface with the sample, with the objective to simulate the same separation between sample and the thermocouple in all the tests that will be carried out, Fig 7.6(c). Once inserted, the band heater was turned on and left until the temperature desired was reached; test temperatures were 323, 353, 373, 423, and 473 K. After five minutes of stabilization period at the desired temperature, data acquisition was started and the temperature of all thermocouples was logged. After two minutes of data recording the test finished and the band heater was turned off.

The results obtained at 3 mm depth show that for test temperatures below 373 K the average difference between the thermocouple readings is less than 0.56 K, which represents 0.15% error (the greatest difference was presented by thermocouple No. 4). For higher temperatures the difference is larger, but the percentage error is still low

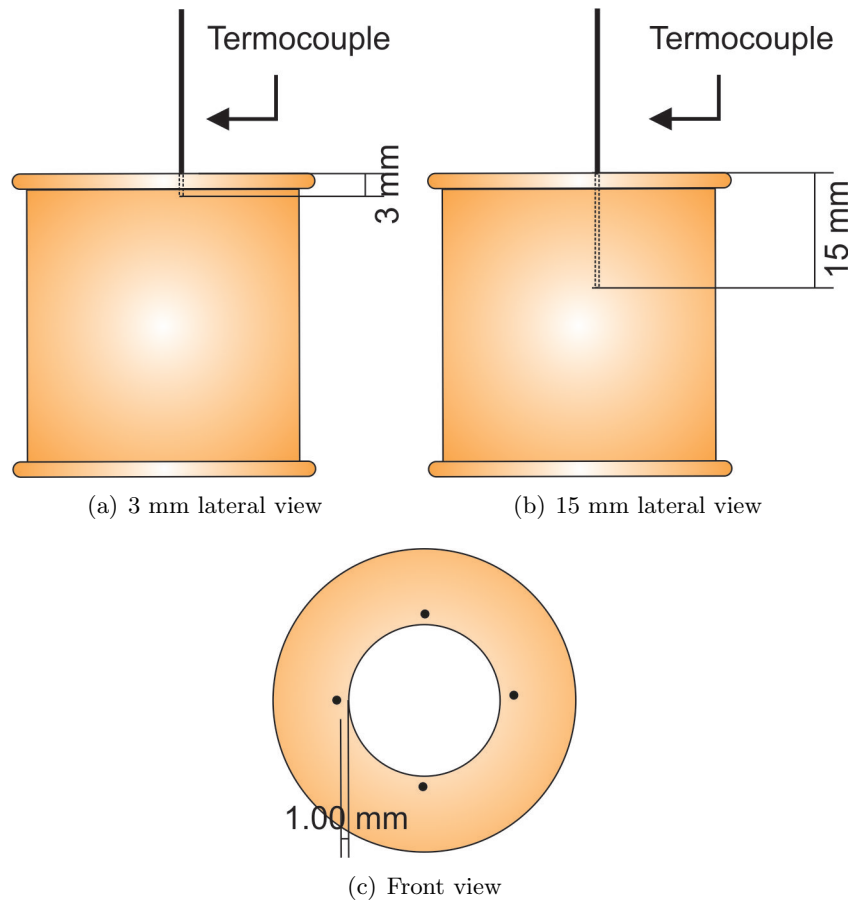


Figure 7.6: Thermocouple position to measure temperature homogeneity around the circumference of the copper cylinder. (a) Lateral view, 3 mm thermocouple depth position, (b) 15 mm thermocouple depth position and (c) Front view distribution (90°).

enough to not significantly affect the results (at 373 K thermocouple No. 4 shows a difference of 0.83 K, representing 0.22 % error). The results are shown in Fig. 7.7 where T1 is Thermocouple 1, T2 is Thermocouple 2, and so on. As would be expected, the results for thermocouples placed deeper in the copper block (15 mm, Fig 7.8) show better homogeneity, with the maximum temperature difference for any test temperature being 0.47 K, which represents 0.12 % error in the test at 373 K. This difference is within the expected accuracy of the thermocouples and indicates that the temperature distribution around the cylinder is uniform. Near the edge, where there may be more thermal losses, the variation increases with higher temperature but still remains within a ± 1 K bound.

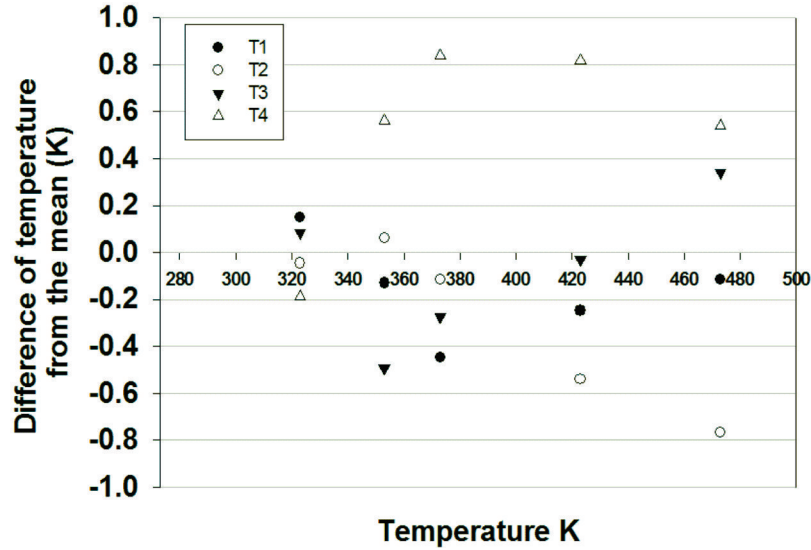


Figure 7.7: Circumferential temperature homogeneity test result. The difference of each thermocouple measurement from the mean of all thermocouples, for readings taken 3 mm from the edge of the copper block. At this depth the differences in temperature tend to increase when the temperature increases.

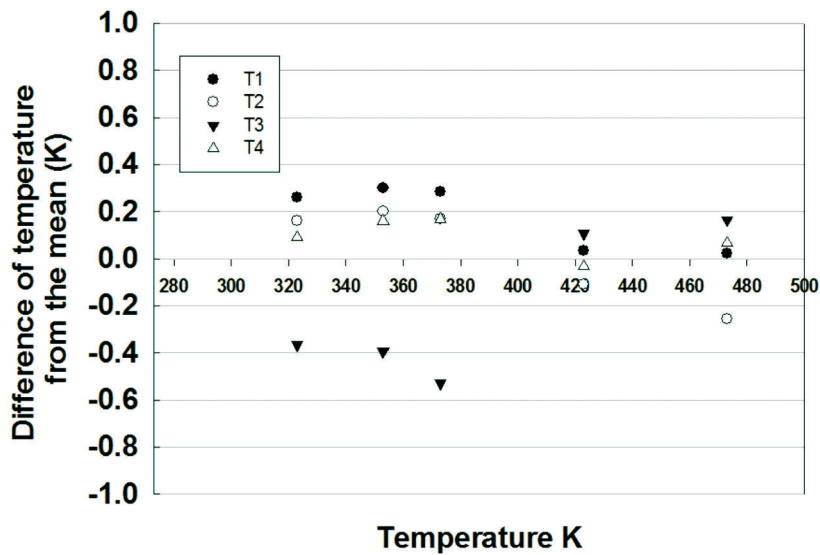


Figure 7.8: Circumferential temperature homogeneity test results. The difference of each thermocouple measurement from the mean of all thermocouples, for readings taken 15 mm from the edge of the copper block. At this depth the differences in temperature remain roughly constant with temperature increase.

7.2.2 LATERAL RESULTS

The tests were performed at 3 mm from the surface of the cylinder, to determine if close to the surface the temperature has the same behaviour as near the position of the metal foam (in the actual test, measurements were carried out at a depth of 7 mm), Fig. 7.4. The tests were performed at the same temperatures using an identical procedure to the test discussed above around the circumference of the copper cylinder. For these tests 6 thermocouples with 0.5 mm diameter were inserted into machined holes with a diameter of 0.6 mm, with a gap of 5.6 mm between them. This separation was selected to space the thermocouples evenly along the length of the cylinder, Fig. 7.4 (where T1 is thermocouple No 1, T2 is thermocouple 2, and so on). The results obtained at 3 mm depth show excellent temperature homogeneity along the length with the largest temperature differences being only 0.46 K (representing only 0.09 % error at 473 K), for thermocouple No 1 (nearest the edge), Fig. 7.9. As expected, the temperature homogeneity is even better than this already good level at 7 mm depth, where the greatest temperature difference was 0.19 K at 473 K representing only 0.04 % error (this highest difference of temperature was presented for thermocouple No. 6, also at the edge) Fig. 7.10. As these variations are all well within the thermocouple accuracy, this demonstrates that there are no significant variations along the axis of the cylinder.

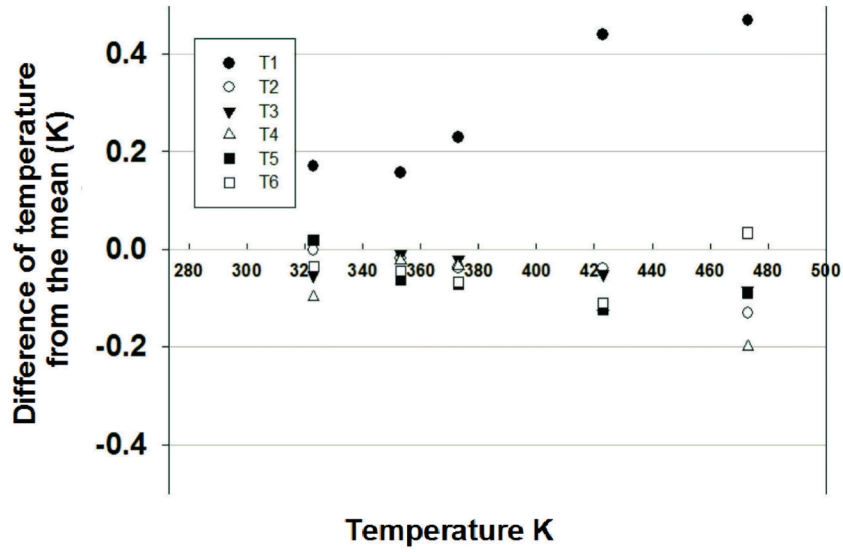


Figure 7.9: Longitudinal temperature homogeneity test results. The difference from the mean of the temperatures presented by the 6 thermocouples at 3 mm depth.

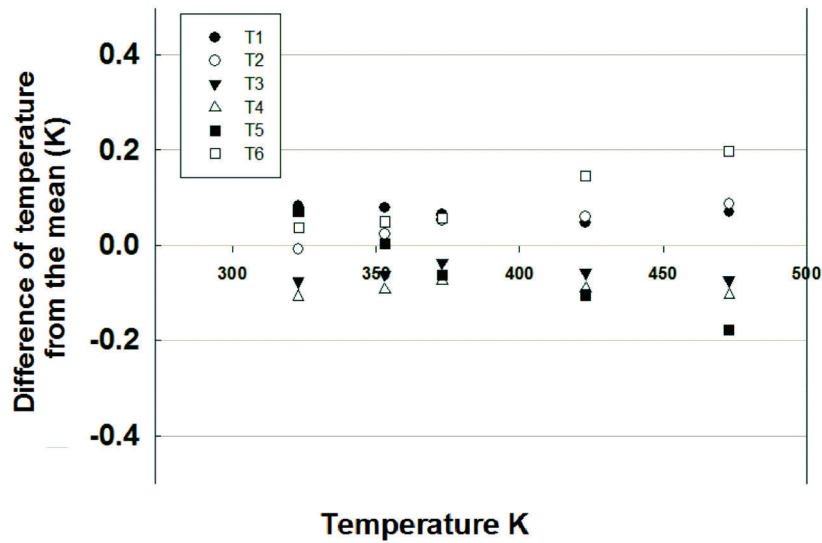


Figure 7.10: Longitudinal temperature homogeneity test results. The difference from the mean of the temperatures presented by the 6 thermocouples at 7 mm depth.

7.3 Blank test

The copper cylinder with no sample inside was mounted in the rig between the two steel chambers (Fig. 5.1), and the thermocouples were inserted. The power to the band heater was turned on, and after 5 minutes of stabilization period at 150 °C, the flow of compressed air at 25 l/min (0.5 g/s) was started. The power of the band heater was left on and after 15 minutes of test the power was turned off. Fig. 7.11 shows the thermal history of the gas passing through the copper cylinder without a sample. The graph plots three lines; the first of these, identified as T_{Cu} , starting at 150 °C, represents the temperature of the copper cylinder during the test. This temperature is almost constant with time, with only small fluctuations seen (which are likely to be due to the band heater being switched on and off to maintain a constant block temperature). The other two lines are T_{out} , the outlet air temperature (dotted line) and T_{in} , the inlet temperature of the cooling air, (dashed line). A slight increment of, on average, 1.2 °C is seen between the air at the inlet and the outlet, and taking the measurements a heat transfer coefficient of 2.74 W/m²K can be calculated. This value obtained is considered insignificant because it represents less than 3.33%, compared with the heat transfer coefficient obtained for a particular foam, a Duocel aluminium foam with 5 PPI and 0.94 of porosity (ε), which was the lowest heat transfer obtained in this research work indicating that to this level of accuracy the zero reading of the equipment is correct.

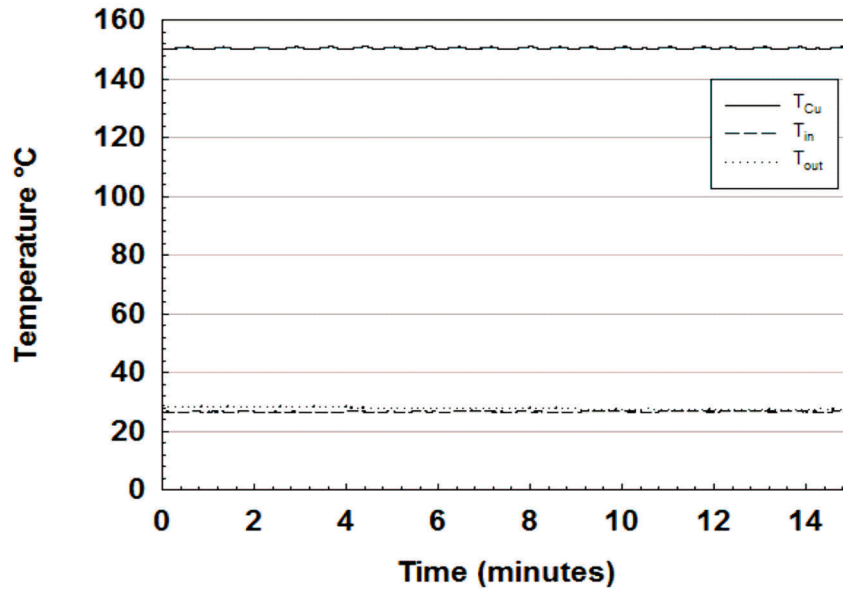


Figure 7.11: Temperature behaviour of the cooling air and copper cylinder when the rig is tested without a sample.

7.4 Dummy sample tests

The results obtained in section 7.3, show that the energy transfer from the copper cylinder to the air is low in the absence of a sample placed in it. Therefore, tests were performed with different samples that might show an effect. The first material tested was AISI 430 stainless steel wire, (this material is frequently used to fabricate wire kitchen cleaners). The wire has a relatively low thermal conductivity of 26.1 W/m K and was wrapped to have a pore density of 0.96. This material with relatively low thermal conductivity and low density demonstrates the sensitivity of the rig to record low values of heat extraction. Following the steps described in section 5.4, the material was tested in the rig with the same parameters that were used in the blank test (start temperature of 150 °C and an air flow of 25 l/min, (0.5 g/s)).

Fig. 7.12 shows three lines displaying the thermal behaviour of the cooling air before and after cooling the sample and the copper cylinder as was shown in Fig. 7.11. In this test T_{Cu} starts at 150 °C, at the time that the cooling air is injected (time

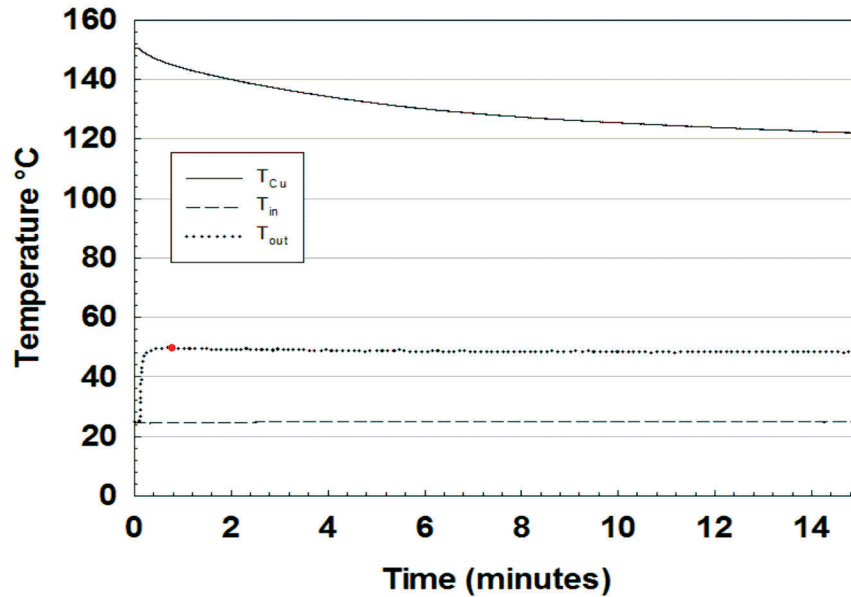


Figure 7.12: Temperature behaviour of the cooling air and copper cylinder when a bundle of AISI 430 steel wire is tested in the rig.

zero), immediately the temperature begins to fall until the stable point is reached; this was determined as being when the temperature of the copper cylinder (T_{Cu}) and the temperature of the outlet air, T_{out} , change less than 1°C in one minute. This stable point was reached when the copper cylinder was cooled down to 121.9°C and the outlet air temperature, T_{out} , increased to 48.2°C . Once the stable point was reached the test was stopped; in this test this happened after 15 minutes of the test.

Fig. 7.12 also shows the behaviour of the temperature of the outlet air, T_{out} . It is possible to observe, opposite to the behaviour of the copper cylinder temperature, the temperature of the outlet air starts to increase at the time that the cooling air is injected, reaching a maximum temperature of 49.83°C at 40 seconds after test initiation (red dot in Fig. 7.12). After reaching this maximum temperature, it begins to decrease until the stable point explained above is reached. The inlet air temperature, T_{in} , does not present any change during the test. As explained in Section 5.5, this temperature is used for the calculation of the coefficient of heat transfer. Using the formulas from Section 5.5 we obtain a heat transfer coefficient of $h_c = 105 \text{ W/m}^2\text{K}$ for this first

material tested in the rig. This is significantly higher than the blank test indicating that the rig is sensitive to the effect of this sample. It would be anticipated that the aluminium foams to be examined will have a larger effect than this steel wire.

7.5 Testing Aluminium Foam

This section presents the characteristic thermal behaviour of a foam, showing the example of a Duocel aluminium metal foam with 10 PPI and 4.9 % density, identified as 10 PPI-4.9. Fig. 7.13 shows the characteristic performance when a metal foam is tested in the rig. The line identified as T_{Cu} , temperature of the copper cylinder, starts at 150 °C and begins to fall at the moment that the cooling air is applied; however, in this test it is possible to observe that the temperature is reduced faster than with the steel wire.

The stable point reached for the temperature of the copper cylinder, T_{Cu} , after 15 minutes of testing was 103 °C. The temperature increment of the cooling air outlet, T_{out} , at 31 seconds of testing reaches its highest temperature at 67.37 °C, then starts to fall until the stable point at 54.9 °C is reached at around 15 minutes of testing. The inlet cooling air temperature, T_{in} , does not change during the test, maintaining its value between 25 – 26 °C.

With the values of T_{Cu} , T_{out} and T_{in} obtained and using equations 5.1 and 5.2 from Section 5.5 we obtain a heat transfer coefficient of $h_c = 456 \text{ W/m}^2\text{K}$ for this aluminium foam sample.

The heat transfer coefficient obtained from the aluminium foam tested in this first attempt was 4.3 times higher than that obtained with the steel wire (105 W/m²K) under the same test parameters. This higher h_c from the aluminium foam was expected due to the increased thermal conductivity of the aluminium over the 430 AISI stainless steel (aluminium thermal conductivity; 237 W/mK and for the 430 AISI stainless steel; 26.1 W/ mK). Also the density and the pore size of the foam sample are slightly

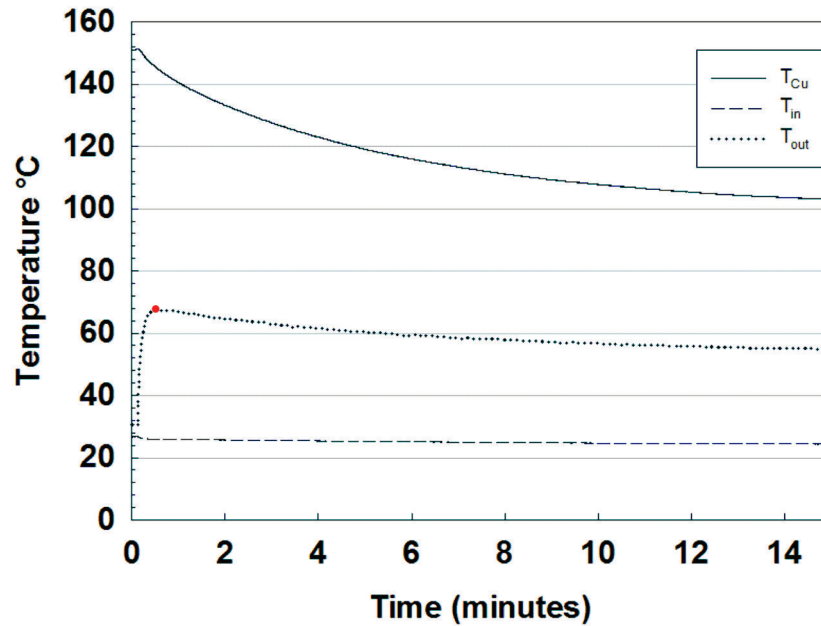


Figure 7.13: Temperature behaviour of the cooling air and copper cylinder when 10 PPI-4.9 Duocel aluminium foam is tested on the rig. The red dot identifies the highest temperature reached by T_{out} .

larger. The above results shows that the rig is able to characterize and distinguish the heat transfer coefficient of several materials and confirms that physical and thermal properties will be reflected in the heat transfer coefficient obtained.

7.6 Long Duration test on Aluminium Foam

As described in Section 7.5, the test is stopped when the temperature of the thermocouple inserted in the copper cylinder and the air after cooling the sample T_{out} reaches a stable point, which is taken to be when the temperature of thermocouples changes less than 1°C in one minute. This stable point was reached after 15 minutes of testing, however an extended test was performed with the objective to know if the thermal behaviour of the sample changes significantly over longer test times. Fig. 7.14 shows the thermal behaviour of the sample when the cooling air is injected for 120 minutes.

Fig. 7.14 shows T_{Cu} , T_{in} and T_{out} , (the temperature of the cooper cylinder, inlet and

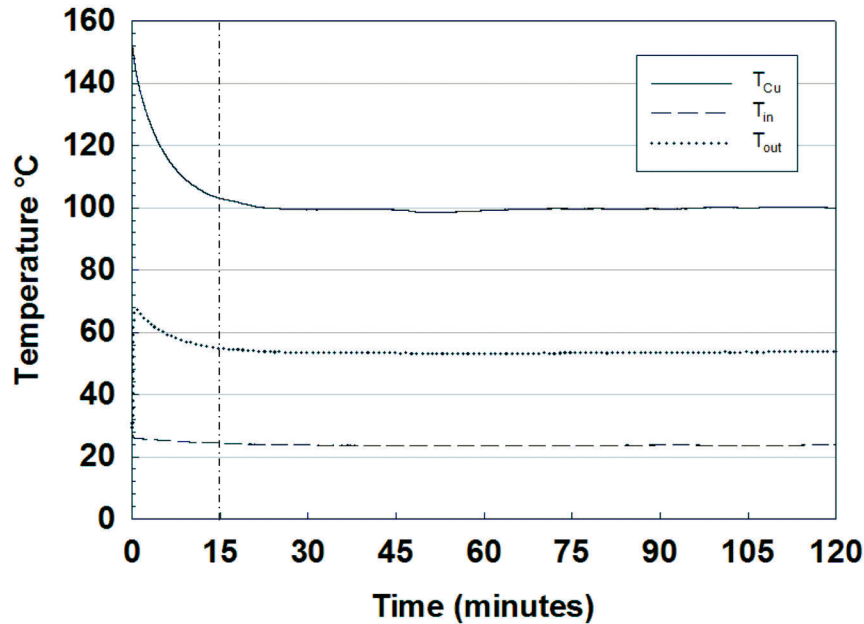


Figure 7.14: Temperature behaviour of the cooling air and copper cylinder when 10 PPI-4.9 Duocel aluminium foam is tested for 120 minutes.

outlet cooling air respectively) and also shows a dotted line at 15 minutes test. This line shows where the stable point was reached following the criterion introduced previously. However the temperature of the copper cylinder, inlet and outlet cooling air continue decreasing. To examine the effect of these differences on the heat transfer coefficient, it was calculated at 15 and 120 minutes.

The heat transfer coefficient obtained at 15 minutes was $178 \text{ W/m}^2\text{K}$ and at 120 minutes the value was calculated as $181 \text{ W/m}^2\text{K}$, showing a difference between them of only 1.7%. One important issue that has to be taken in to account is that this sample 10 PPI-4.9 has low density and with these characteristics the heat extraction is slower than if it is compared with samples with higher densities so other samples would be expected to have lower densities. With the objective to test all the samples under the same parameters and to have test of a reasonable duration, the test time established based on this behaviour was 15 minutes.

7.7 Contact between foam and copper cylinder

To achieve reliable results, it is important that the thermal contact between the heated cylinder and the foam sample is good and reproducible. As is described in the Subsection 7.1.2, there are two factors to take into account to reduce the thermal resistance between the aluminium foam and the copper cylinder. They are; a) the foam must be cut so that it fits the interior of the copper cylinder precisely and b) the thermal contact at the interface between the metal foam and the copper cylinder must be as good as possible. To evaluate the last mentioned point and obtain the best and most reproducible contact possible between the copper cylinder and the metal foam (and therefore get the best accuracy in the test) a series of experiments were performed. Tests were done using Duocel aluminium foam with 50 PPI, 7.1 % nominal density (6.8% real density). Table 7.1 reports the parameters and the three different ways of contact of the aluminium foam and the copper cylinder evaluated. Details of the three different tests are described in 7.7.1, 7.7.2 and 7.7.3.

Table 7.1: Test parameters used to evaluate the contact between the copper cylinder and the aluminium foam.

Test	Flow rate g/s	Temperature °C
Clamped Sample	0.3	150
	0.4	150
	0.5	150
	0.6	150
	0.7	150
	0.8	150
Brazed Sample	0.3	150
	0.4	150
	0.5	150
	0.6	150
	0.7	150
	0.8	150
Thermal Paste	0.3	150
	0.4	150
	0.5	150
	0.6	150
	0.7	150
	0.8	150

7.7.1 CLAMPED SAMPLE

A copper cylinder with the dimensions described in Figs. 7.1(a) and 7.1(b) was cut longitudinally as shown in Fig. 7.15(a). Then the sample was inserted in the copper cylinder, ensuring that both sides of the interface were clean. Next by placing the band heater around the cylinder the sample was clamped, Fig. 7.15(b). This "clamp" was made when the gap in the copper cylinder was closed by tightening the band heater until intimate contact between the two surfaces of the cut was obtained. Then the sample was tested and the heat transfer coefficients, h_c , at each flow rate were obtained following the equations of section 5.5.

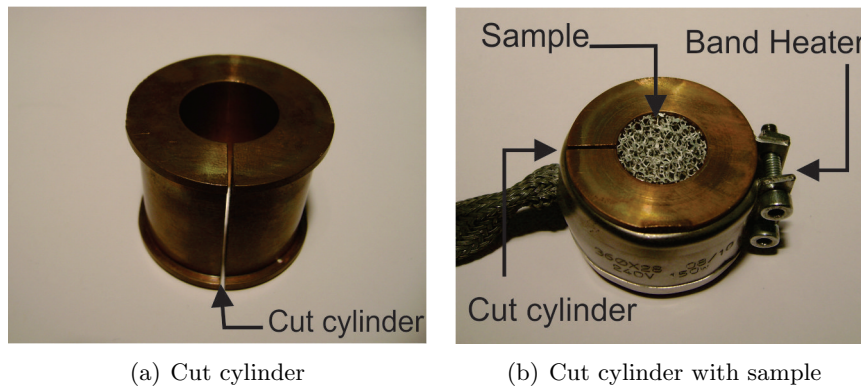


Figure 7.15: Copper cylinder used to clamp the sample. (a) Copper cylinder cut longitudinally (b) cut copper cylinder with the sample and the band heater in position.

7.7.2 BRAZED SAMPLE

A mix of 70% aluminium powder (-325 mesh, 99.5%) and 30% copper (-325 mesh, 10% max +325 mesh, 99%) provided by *Alfa Aesar*, with a suspension of 40% PMMA (Poly Methyl Methacrylate) and 60 % water (H_2O) was made to form a braze joint between the metal foam and the copper cylinder. The aluminium and copper would form a eutectic and act as a brazing alloy while the PMMA acts as a carrier and gets removed by thermal decomposition during the heat treatment. Once the paste was prepared, it was evenly applied over the surface of the internal hole in the copper cylinder, then the

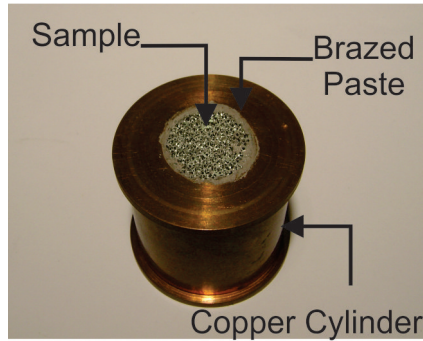


Figure 7.16: Copper cylinder with brazing paste and the sample in position before heat treatment.

aluminium foam was mounted, Fig. 7.16. The copper cylinder was placed under heat treatment in a *Centrum Furnace* with the conditions described in Table 7.2. Once the aluminium foam was brazed to the copper cylinder, it was mounted in the rig with the band heater and the test was carried out.

Table 7.2: Heat treatment parameters.

Parameter	Quantity	Units
Temperature	530	°C
Atmosphere	300	torr
Time	120	min
Heating rate	10	°C/min

7.7.3 THERMAL PASTE SAMPLE

A thermal paste test sample was prepared following the same standard procedure as described in 5.4.

7.7.4 TEST COMPARISON

Experimental heat transfer coefficients obtained from the different contact tests with varying air mass flow rate are plotted in Fig. 7.17. The *clamped sample* presents the lowest heat transfer coefficients, meaning that clamping the sample with the copper cylinder presents the highest thermal resistance among the tests developed. This indi-

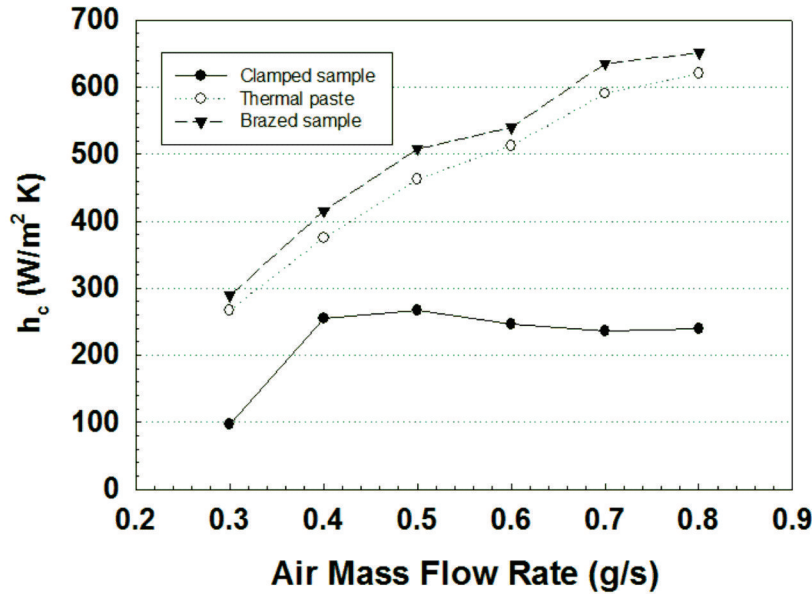


Figure 7.17: Heat transfer coefficients obtained to evaluate the contact between the 50 PPI with 7.1 % density Duocel aluminium foam and the copper cylinder.

cates that the mechanical contact achieved is not very good. This could be because the surface conformity between the foam and the cylinder is not good, or because clamping in this way does not compress the interface evenly. The highest heat transfer coefficients were obtained with the *brazed sample*, and results from the lowest thermal resistance between the sample and the copper cylinder obtained with the metallurgical contact between the foam and cylinder.

The *thermal paste sample* presented on average heat transfer coefficients 7% lower than those obtained by the *brazed sample*. This is understandable as, even though both methods give a similar physical contact, the braze material is metal, and has a higher thermal conductivity than the paste. Even though the lowest thermal resistance was presented by *the brazed sample*, *the thermal paste* method was used in the test carried out in this work, due to the quicker nature of the test, and the advantage of being able to test samples in a single copper cylinder (as the brazed samples cannot be easily removed after testing). It must be remembered that the results are likely to be lower (by around 7 %) than for the brazed joint. As all the samples are tested in the

same manner, then the comparison between them should be valid.

7.8 Error analysis

Table 7.3 reports uncertainties of the different devices as well as the thermal resistance introduced by the thermal paste used between the metal foam and the copper cylinder. Based on superposition of errors, equation 7.1 the total error in the measurement of the heat transfer can be calculated [155]:

$$\frac{\Delta h_c}{h_c} = \sqrt{\left(\frac{\Delta x}{x}\right)^2 + \left(\frac{\Delta y}{y}\right)^2 + \dots + \left(\frac{\Delta z}{z}\right)^2} \quad (7.1)$$

where x, y, \dots, z are the chain errors in the rig. The total error calculated was found to be 9.1% when the differences of pressure measurements are done with *Testo* transducer and 8.6% when *Digitron* device is used.

Table 7.3: Uncertainties in the rig.

Device	Uncertainty
Flow meter	± 5.0 %
Thermocouple	± 0.05 %
Thermal resistance Cu and Metal foam	7.0 %
Pressure transducer Digitron	± 0.15 %
Pressure transducer Testo	± 0.03 mbar

The measured uncertainties were plotted only when the comparison of the heat transfer coefficient obtained between the different metal foams analyzed on the rig was very close, in order to conclude if the difference presented was for the characteristics in the sample or by the uncertainty on the rig. For pressure drop the uncertainty was plotted only in Duocel foams due to in Corevo and Replicated samples the size of the symbol in the graph always was bigger than the error bar.

Chapter 8

Heat Transfer of Single Pore Size Foams

The experimental results obtained are presented as heat transfer (h_c) and pressure drop coefficient (ΔP) for different pore sizes and porosities (ε) for Duocel samples (supplied by The ERG Aerospace Corporation, Oakland, CA), samples of replication processed Corevo foam provided by Constellium, and for aluminium foams produced in the laboratory by the version of the replication process developed in this work. The shape and dimensions of all samples tested were the same: cylinders with 19 mm diameter and 32 mm length. The samples were tested following the steps described in Section 5.4 with 15 minutes of compressed air injection (cooling flow) at different flow rates. As described in Section 7.6, the 15 minutes of testing are enough to obtain the thermal behaviour of the samples at steady state. The heat transfer coefficients were calculated using the parameters and equations of Section 5.5.

Air-cooling is still the preferred option to dissipate the thermal energy generated for electronic devices [65]. An optimal heat exchanger is a material with the highest heat transfer coefficient and the lowest pressure drop possible [2]. The general testing methodology is to explore the heat transfer coefficient at a range of gas speeds for

the variables under test. This is done as flow rate is one of the most likely variables for real heat exchangers. Flow rate is defined by the air mass flow rate (g/s). The typical test range is 0.3 g/s to 0.8 g/s, which, at the pressure used equates to 15 to 45 litres/ minute. As well as the heat transfer coefficient, the pressure drop across the sample is important. When a fluid (gas or liquid) passes through a pipe with a rigid structure which contains interconnected channels it suffers a restriction. This restriction (a resistance to flow) reduces the initial flow pressure. This difference between the initial pressure (the original pressure of the flow) and the final pressure (the pressure of the flow after it has passed through the rigid structure) is known as the pressure drop (ΔP). The characterization of fluid flow was obtained when the samples were tested for their thermal behaviour, via the pressure transducer connected between the two steel chambers (Section 5.3). The results obtained for pressure drop are presented as ΔP (mbar) versus air mass flow rate (g/s).

8.1 Heat transfer coefficient of Duocel foams

The Duocel aluminium foams tested were believed to be produced using the *Investment casting method (Duocel process)* [2, 3, 13]. Aluminium foams with 0.5 to 5 mm pore size and volume fraction metal as low as 5 % can be obtained through this process [2, 3, 13]. Duocel samples reported in Table 8.1 were characterised and tested to obtain their thermal and fluid flow behaviour. As an initial test, a Duocel sample with 10 PPI and 9.9 vol % solid (as described in Table 8.1) was tested at 100, 150 and 200 °C with the conditions given in Table 8.2, to investigate the effect of the initial temperature and flow rate. The heat transfer coefficients for the different temperatures and flow rates were obtained using Equation 5.2.

Fig. 8.1 plots the error bars graph of heat transfer coefficient calculated for different temperatures and flow rates and shows no evidence that the heat transfer coefficient does not depend on the initial temperature of the heated block (in agreement with

Table 8.1: Characteristics of Duocel metal foam samples used for thermal and hydraulic experiments.

Sample	Pore size (mm)	Nominal Density (%)	Measured Density (%)	Porosity (ε)
5 PPI-5.2	5	5.2	5.09	0.94
5 PPI-7.9	5	7.9	7.85	0.95
5 PPI-11.5	5	11.5	10.48	0.89
10 PPI-4.9	2.5	4.9	5.05	0.94
10 PPI-7.9	2.5	7.9	8.00	0.92
10 PPI-9.9	2.5	9.9	10.33	0.89
20 PPI-4.1	1.2	4.1	4.70	0.95
20 PPI-8	1.2	8	7.78	0.92
20 PPI-10.5	1.2	10.5	9.87	0.90
40 PPI-8.6	0.6	8.6	8.01	0.91
50 PPI-8	0.5	8	7.65	0.92

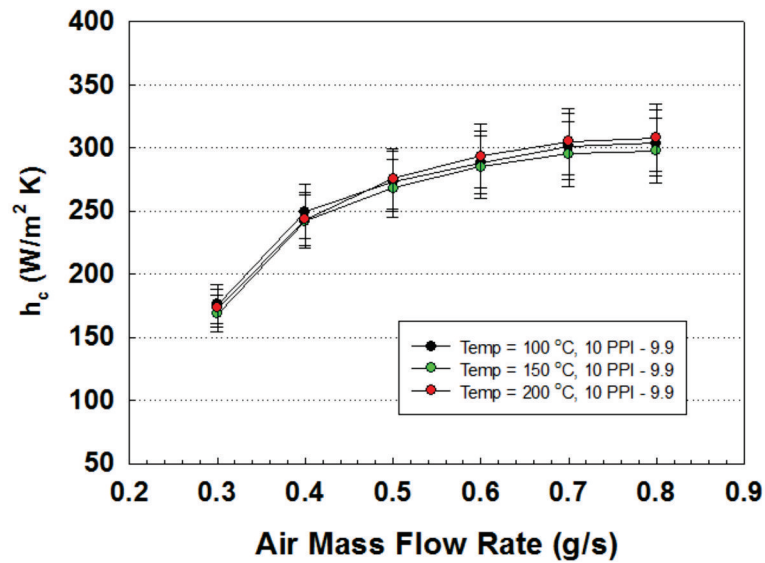


Figure 8.1: Heat transfer coefficient obtained at 100, 150 and 200 °C in the 10 PPI-9.9 Duocel sample.

other studies [65, 125]), and that it increases when the flow rate increases. The lowest air mass flow rate, 0.2 g/s, presented the lowest heat transfer coefficient for the three different temperatures tested. The largest heat transfer coefficient at this flow rate was 176 W/m²K obtained at 200 °C and the lowest 168 W/m²K obtained at 150 °C, having as a result a difference between them of only 4.2 %. This difference is within

Table 8.2: Test parameters applied to 10 PPI-9.9 Duocel sample.

Sample	Flow rate g/s	Temperature °C
10 PPI- 9.9	0.3	100
	0.4	100
	0.5	100
	0.6	100
	0.7	100
	0.8	100
	0.3	150
	0.4	150
	0.5	150
	0.6	150
	0.7	150
	0.8	150
	0.3	200
	0.4	200
	0.5	200
	0.6	200
	0.7	200
	0.8	200

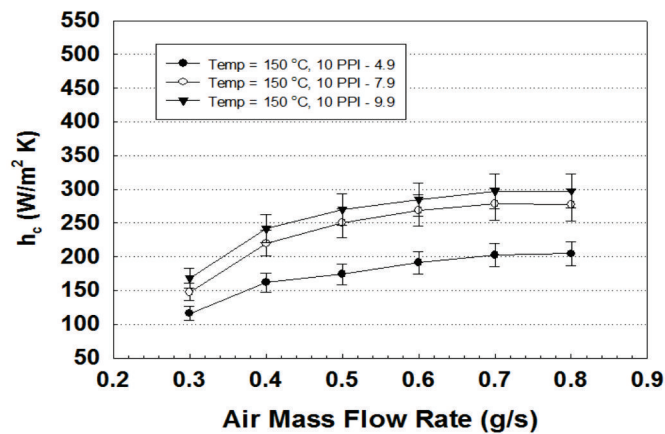
the measurement uncertainties of the rig, discussed in Section 7.8, and therefore is not considered significant. The highest heat transfer coefficient was obtained at 0.8 g/s air mass flow rate, the highest air mass flow rate used in the test for all temperatures tested. At this rate, the largest heat transfer coefficient obtained was 307 W/m²K at 200 °C while the smallest was 297 W/m²K at 150 °C, representing a 3.3 % change.

The same behaviour was presented by the sample with 5 PPI pore size and 7.9 vol % solid, and the sample with 20 PPI pore size and 8 vol % solid. As the behaviour was found to be quite insensitive to the temperature, an intermediate value of 150 °C was used to compare the different samples examined in this work.

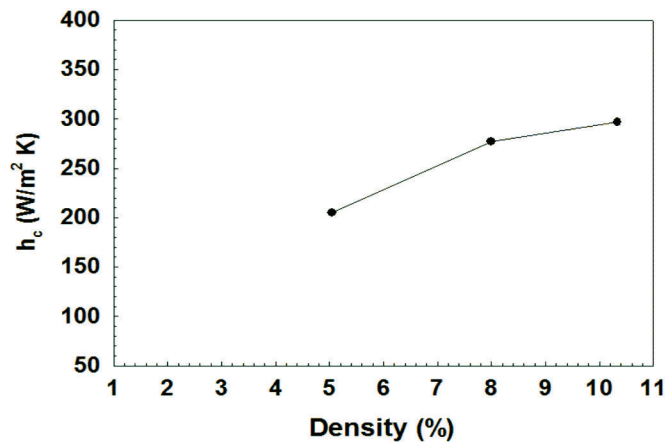
8.1.1 INFLUENCE OF DENSITY ON THE HEAT TRANSFER IN DUOCEL FOAMS

Samples identified as 10 PPI-4.9, 10 PPI-7.9 and 10 PPI 9.9 were used to characterize the influence of density on the heat transfer in Duocel foams. Tests were performed at 150 °C with 0.2, 0.3, 0.4, 0.5, 0.6, 0.7 and 0.8 g/s air mass flow rate (flow rates are reported in Table 8.2). Fig. 8.2(a) shows that the sample with highest density (the lowest porosity) presents the highest heat transfer for these three samples. Sample 10

PPI-9.9 presented, for all the flow rates tested, the highest heat transfer coefficient, while sample 10 PPI-4.7 presented the lowest heat transfer coefficient in the six flow rates tested. Sample 10 PPI-9.9 shows 1.3 and 1.08 times the heat transfer coefficient of 10 PPI-7.9 and 10 PPI-4.7 respectively. Fig 8.2(b) shows how the heat transfer coefficient increases when the density increases at 0.8 (g/s) air mass flow rate; over this range the increase is roughly linear, and the highest heat transfer coefficient was obtained by the sample with the highest density. In all of these figures the density used is that measured in the work, rather than the nominal value provided by the supplier.



(a) Heat transfer and flow rate



(b) The variation in heat transfer with density at 0.8 g/s

Figure 8.2: Heat transfer coefficient obtained at 150 °C in Duocel samples. (a) Heat transfer coefficient obtained at 150 °C for 10 PPI-4.9, 10 PPI-7.9 and 10 PPI-9.9 Duocel samples, and (b) heat transfer coefficient at 0.8 g/s with respect of the density.

Figs. 8.3(a) shows the heat transfer coefficient obtained in 5 PPI-5.2, 5 PPI-7.9 and 5 PPI-11.5 samples, and 8.3(b) shows the heat transfer coefficient obtained in 20 PPI-4.1, 20 PPI-8 and 20 PPI-10.5 samples. These samples present similar behaviour in the variation in the heat transfer coefficient with flow rate and density as 10 PPI samples; the heat transfer coefficient increases when the air mass flow rate increases and the density increases. Fig. 8.3(a) shows that the influence of the volume fraction solid at 5 PPI pore size is similar to 10 PPI; as the density is increased the heat transfer increases.

The highest heat transfer coefficient presented by the three pore sizes tested (5, 10 and 20 PPI) was given by samples with 20 PPI (the smallest pore size) for all air mass flow rates. Samples with 20 PPI show that the heat transfer coefficient increases 30 % between 20 PPI-4.1 to 20 PPI-8 samples and from 20 PPI-8 to 20 PPI-10.5 sample increase about 16 %, i.e. the increase of heat transfer coefficient is roughly linear with density increase, with the increment in heat transfer coefficient per vol % solid being about 7 W/m²K in these samples. 20 PPI samples have notable behaviour for the first two air mass flow rates used in the test, compared with 10 PPI and 5 PPI samples. Fig. 8.3(b) shows that the initial slopes of the line describing the heat transfer behaviour of all three 20 PPI metal foams tested is steeper than those shown by the samples with 5 and 10 PPI. Once higher flow rates are achieved, the slope is less, closer to that seen in other pore size foams. This could be due to the more complex flow paths in small pore size material, which means that when the flow rates are low the air is not caused to flow through the foam as effectively as at higher flow rates, thus reducing the heat transfer coefficient at these low speeds.

The influence of the density on the thermal behaviour of a porous material can be explained with k_{eff} , the effective thermal conductivity of a fluid filled porous media, which depends on the porosity of the solid ε and the conductivities of the solid and the fluid phases λ_s and λ_f [156] a simple rule of mixtures approach gives:

$$k_{eff} = \varepsilon\lambda_f + (1 - \varepsilon)\lambda_s \quad (8.1)$$

On this basis, it is easy to observe that the effective thermal conductivity is increased if the porosity is decreased. Shih et al [51, 103] report that the pore density affects the cooling performance of aluminium foams in the way predicted. Bhattacharya et al [113] analysed aluminium foams and showed a strong dependence of the effective thermal conductivity on the density and Zhao et al [122] came to the same conclusion with steel foams.

If the foam density is increased, we therefore expected the conduction to go up. This will mean that thermal energy is distributed through the foam faster, and the local heat transfer is thereby increased.

8.1.2 INFLUENCE OF PORE SIZE ON HEAT TRANSFER IN DUOCEL FOAMS

Duocel samples with different pore sizes but similar densities were tested under the same range of flow rates. Fig. 8.4 shows the heat transfer coefficient against the air mass flow rate for the following Duocel samples: 5 PPI-7.9, 10 PPI-7.9, 20 PPI-8, 40 PPI-8.6 and 50 PPI -8, the characteristics of these samples are reported in Table 8.1. The heat transfer is found to be influenced by the pore size; when the pore size decreases, the heat transfer increases. This can be observed in Fig. 8.4, where the heat transfer coefficients obtained for different samples with similar densities but different pore sizes are shown. This shows that the 50 PPI-8 sample with the smallest pore size, 0.5 mm diameter, presents the highest heat transfer coefficient over all the flow rates among the five samples in the trial, while 5 PPI-7.9 sample with the biggest pore size, 5 mm diameter, presented the smallest heat transfer coefficient of those tested.

For example, the 50 PPI-8 sample presents 3.4 times the heat transfer of the 5 PPI-7.9 sample, at a flow rate of 0.3 g/s (this sample had h_c 123 W/m²K while the 50 PPI-8 sample gave 427 W/m²K). Moreover, the heat transfer at the smallest flow rate

presented by the 50 PPI-8 sample is larger than the heat transfer presented by the 5 PPI-7.9 at even the highest air mass flow rate. However it should be noted that this higher heat transfer behaviour is reached with a high difference of pressure as shown in Fig. 8.8 in Section 8.2.2.

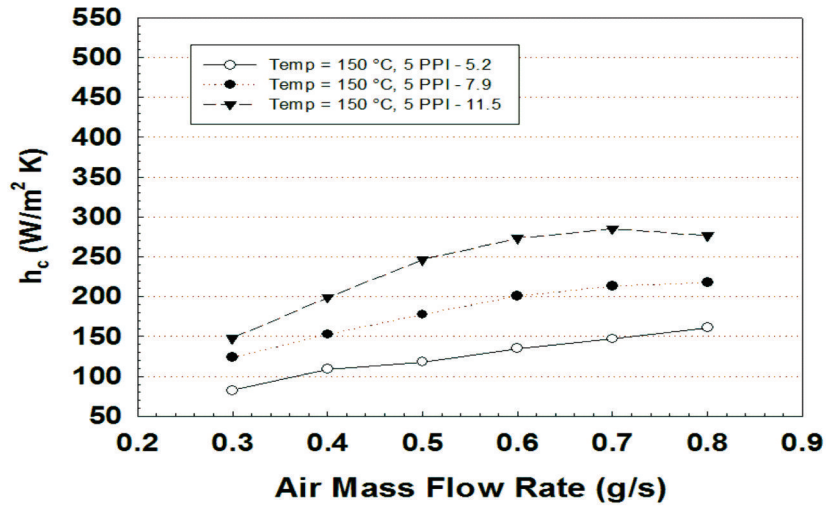
The heat transfer is influenced by the pore size through its relationship to the ligament thickness, the ligament thickness being related to the heat transfer [157]. The specific surface area of a foam increases when the pore size decreases at a constant density, and this enhances the surface area available for heat transfer, and therefore increases the coefficient [50, 105]. At a constant density, when the pore size in a metal foam is decreased the thickness of the ligaments (the struts in foams of this type) will increase, as observed by Hutter et al [157]. The ligament diameter affects two heat transfer mechanisms. Firstly, the heat conduction through the foam is reduced with thin struts, and secondly, thicker ligaments induce more turbulent fluid flow, having as a result an increase in the heat transfer [122, 158]. Bhattacharya et al [105] characterized the heat transfer in aluminium foams with different pore sizes but with similar density and also found that at lower pore sizes the heat transfer increased and that corresponded to thicker ligaments.

Duocel foams are commercially available, and have been used for investigation of heat transfer by other workers. Heat transfer coefficients obtained here for 5 PPI, 10 PPI and 20 PPI samples were compared with data from the literature. The 10 PPI samples were compared with Mancin et al [125]; Fig. 8.5 shows the heat transfer coefficients from that study and here against air mass flow rate.

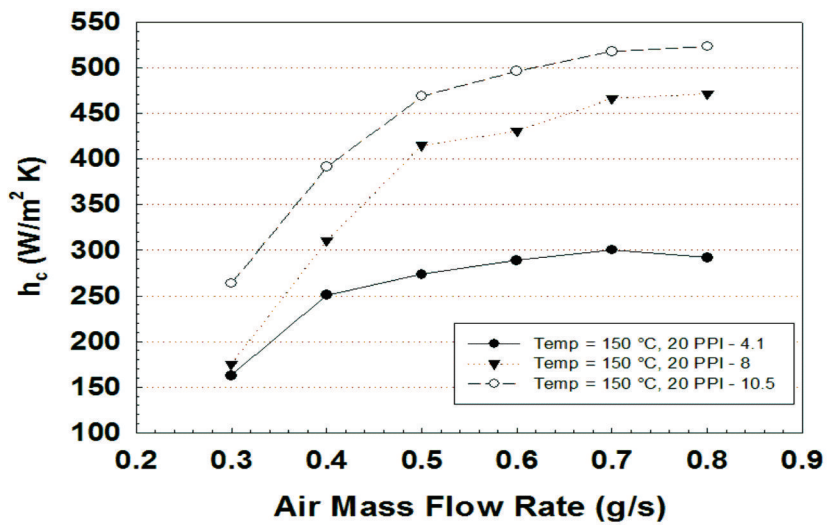
Metal foam heat transfer characterization work by Mancin et al was performed at higher air mass flow rates than those used in this work, and there is also a slight difference in the densities, due to processing variations. However, the results obtained here show a clear tendency to follow Mancin's results. It must also be remembered that there could be a transition in behaviour between the two flow rates, perhaps explaining the slightly different shape of the trends produced.

Samples with 5 and 20 PPI were compared with results obtained by Bhattacharya et al [65]. Fig. 8.6(a) shows the comparison with 20 PPI and 8.6(b) 5 PPI samples. 20 PPI samples show good agreement among the results; the trend is similar and the values are only slightly different. However for 5 PPI the difference between the two sets is around 30%, these heat transfer coefficients obtained being the highest in all the air mass flow rates. This could be due to the difference in density between the literature data and samples tested here. On the other hand, there is a similar density difference with the 20 PPI samples, where agreement is better. This could therefore be an indication of the pore size/sample size effect. In a 5 PPI sample, there will be an average of only 3.8 cells across the diameter, which may be too few. In a mechanical test, 6 to 7 pores are recommended [159, 160].

The results obtained with Duocel samples show generally good agreement with similar characteristics to samples reported in the literature, and therefore there is confidence in using the method to examine heat transfer coefficients in Corevo and laboratory made metal foams, both fabricated by versions of the replication technique.



(a) 5 PPI samples



(b) 20 PPI samples

Figure 8.3: Heat transfer coefficient obtained at 150 °C in Duocel samples. (a) 5 PPI-5.2, 5 PPI-7.9 and 5 PPI-11.5 samples, and (b) 20 PPI-4.1, 20 PPI-8 and 20 PPI-10.5 samples.

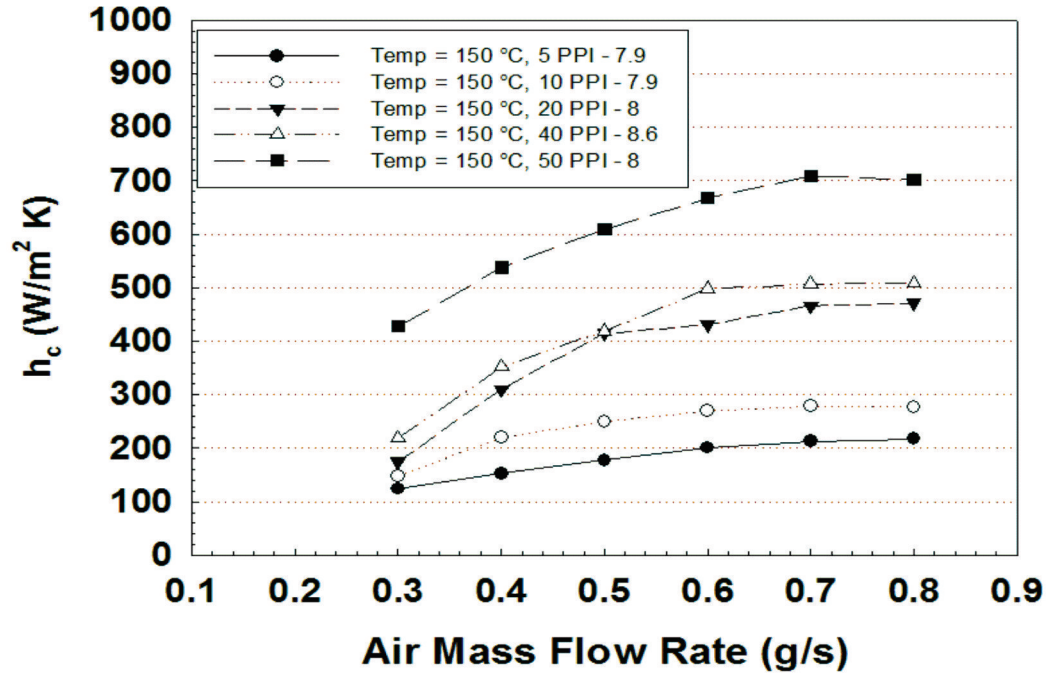


Figure 8.4: Heat transfer coefficient obtained at 150 °C in samples with 5, 10, 20, 40 and 50 PPI with similar density (between 7.9 - 8.6).

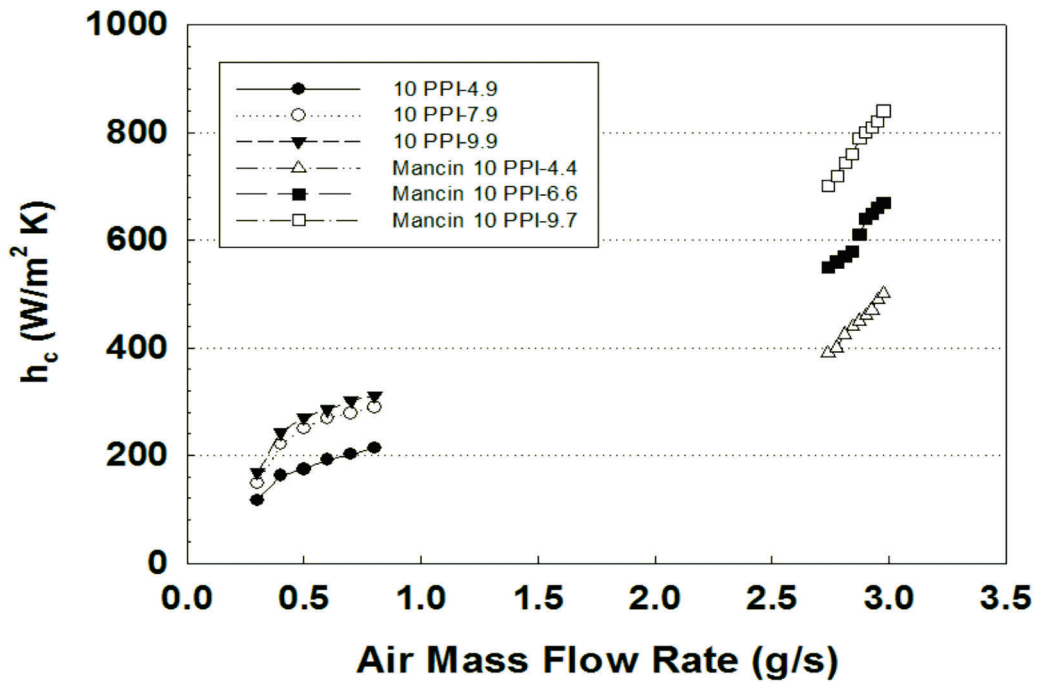
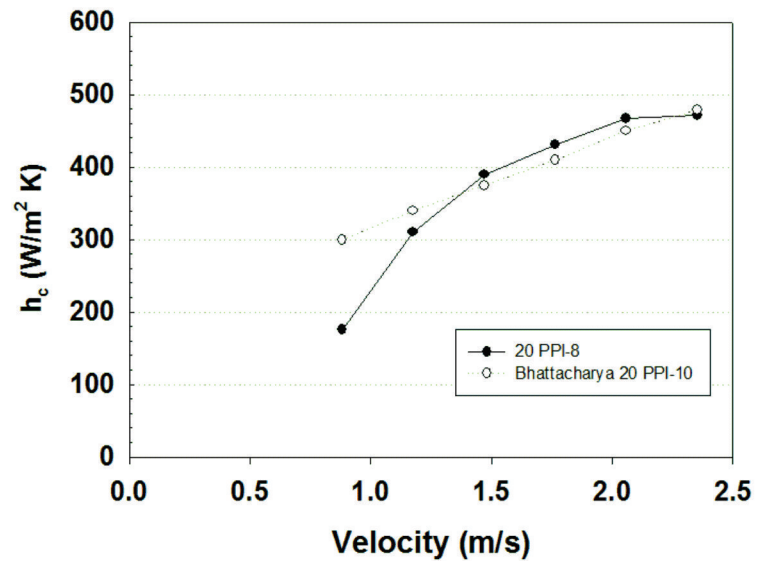
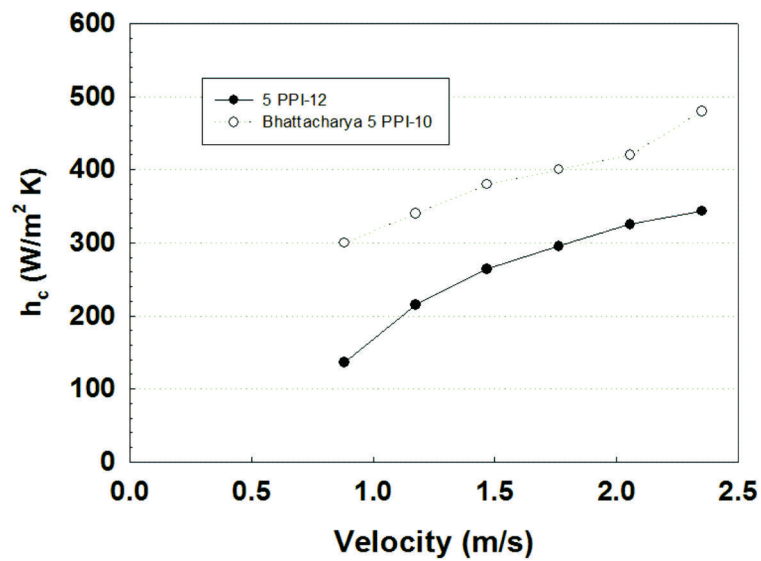


Figure 8.5: Comparison of heat transfer coefficients obtained in 10 PPI samples with data from Mancin et al [125].



(a) 20 PPI samples



(b) 5 PPI samples

Figure 8.6: Comparison of heat transfer coefficients obtained in (a) 20 PPI- 8 and (b) 5 PPI-12 Duocel samples with data from Bhattacharya et al [65].

8.2 Duocel foams pressure drop

The fluid flow characterization of Duocel samples was obtained when they were tested for their thermal behaviour, via the pressure transducer connected between the two steel chambers, Section 5.3. The results obtained are presented as $\Delta P(mbar)$ versus air mass flow rate (g/s). Characteristics of the foams are reported in Table 8.1, and test parameters (temperature and air mass flow rate) are the same used to characterise the heat transfer behaviour.

8.2.1 INFLUENCE OF DENSITY ON PRESSURE DROP IN DUOCEL SAMPLES

Fig. 8.7(a) plots the experimental pressure gradients obtained for 5 PPI-5.2, 5 PPI-7.9 and 5 PPI-11.5 samples. Pressure drop (ΔP) increases with air mass flow rate and when the density of the sample increases. At the lowest two rates the pressure gradients are only slightly different among the three samples. When the air mass flow rate increases the differences of pressure diverge. They are similar for samples 5 PPI-11.5 and 5 PPI-7.9, the difference between them being 10 % with 5 PPI-11.5 having the highest pressure gradient. 5 PPI-5.2 sample presents the lowest pressure gradient in all the air mass flow rates tested and when it is compared with the sample with the highest density (the 5 PPI-11.5 sample), the differences of pressure drop are found to be 30 % lower than those presented by the 5 PPI-11.5 sample.

Results for samples 10 PPI-4.9, 10 PPI-7.9 and 10 PPI-10.5 are plotted in Fig. 8.7(b). The pressure differences among the samples at low air mass flow rates are again similar. The pressure gradient increases when the air mass flow rate increases, the sample with highest density, 10 PPI-10.5, presents the highest differences of pressure about 17 % higher than 5 PPI-4.9 sample and 8 % higher than 10 PPI-7.9 sample.

Similar behaviour was once again presented by 20 PPI-4.1, 20 PPI-8 and 20 PPI-10.5 samples and can be observed in Fig. 8.7(c). 20 PPI samples show the same influence

with respect the air mass flow rate, i.e.; the pressure difference increases when the air mass flow rate increases. 20 PPI-10.5 and 20 PPI-8 samples have practically the same behaviour, while if the 20 PPI-10.5 sample is compared with the 20 PPI-4.9 sample, the pressure gradient is 20 % higher for the sample with the highest density.

The increase in the pressure drop in samples with the same pore size but with different densities can be explained by the additional drag forces which are more evident when the air mass flow rate increases. This could be caused by changes to the strut shapes (e.g. triangular to circular) or the increase in the cross sectional area of the strut with density [113, 115, 118]. The general effect of structure on fluid flow is discussed later.

8.2.2 INFLUENCE OF THE PORE SIZE ON THE PRESSURE DROP IN DUOCEL FOAMS

To understand the influence of pore size on the pressure gradient, 5 PPI-7.9, 10 PPI-7.9, 20 PPI-8, 40 PPI-8.6 and 50 PPI-8 samples were tested, the characteristics of these samples are reported in Table 8.1. As far as possible with foams of this type, they are selected to have the same density. Fig. 8.8 shows the influence of the pore size in the fluid flow behaviour when samples with similar densities but different pore sizes are tested under the same conditions.

The pressure differences increase when the air mass flow rate increases and when the pore size decreases. The highest pressure drop was presented by the 50 PPI- 8 sample; the sample with the smallest pore size (about 0.5 mm diameter). This sample shows more than 50 % higher pressure gradient compared to all the other samples, for instance, if it is compared with the sample with the largest pore size, 5 PPI-7.9 sample, it has an 85 % larger pressure difference across it.

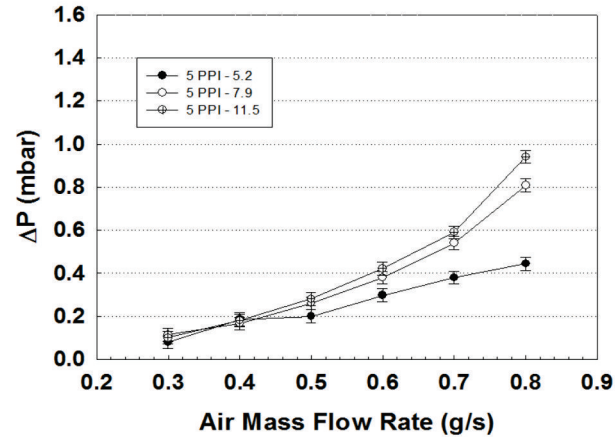
The pressure gradients presented by 5 PPI-7.9 and 10 PPI-7.9 samples were below 0.9 mbar with less than 10 % difference between them. 40 PPI-8.6 and 20 PPI-8 samples present pressure differences in the range between 0.188 to 1.6 mbars. These samples (20 and 40 PPI) showed a greater effect on the pressure differences if they are compared

with the 5 PPI-7.9 sample. The pressure gradient presented by these samples is 65 % higher than the pressure drop presented by 5 PPI-7.9.

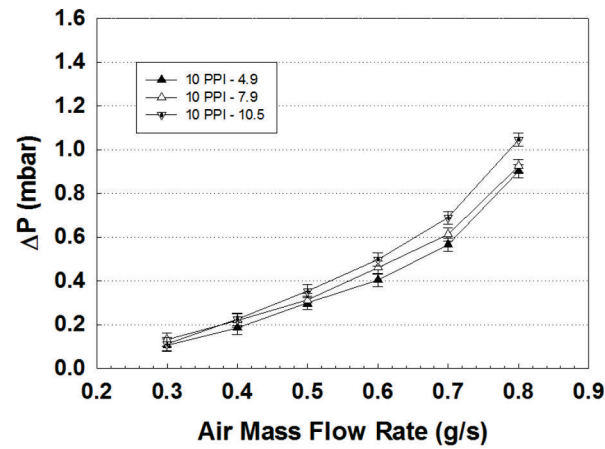
According to Hutter et al [157], the pore size defines the size of the smallest open channels in the porous media, and holding the density constant and decreasing the pore size results in a higher pressure drop. This is also explained as the reduction of the pore size increases the specific surface area and therefore the permeability is reduced through wall friction effects [47, 161]. Some authors, such as Xu et al [120], report a strong dependence of the permeability on pore size at a constant density, and found that the variation in the permeability is almost linear with respect to the pore size.

The pressure drop for samples with 5 and 20 PPI was compared with results obtained by Bhattacharya et al [65], as was done with the heat transfer coefficient (h_c) results. The results obtained show reasonable agreement with the two samples compared with Bhattacharya et al [65]. The 20 PPI sample (Fig. 8.9(a)) shows a similar trend however for some flow rates, a lower pressure drop is presented by the sample tested here (by about 20 % where the difference is largest). This difference in pressure drop is similar to the difference in density between the two samples, with the 20 PPI sample tested here having a lower density, which is likely to explain the difference. The 5 PPI samples (Fig. 8.9(b)), show a similar trend, and have better agreement with the data of [65]. In the case of 5 PPI samples, the sample characterized here has 20 % higher density with respect to the sample in the work of Bhattacharya et al.

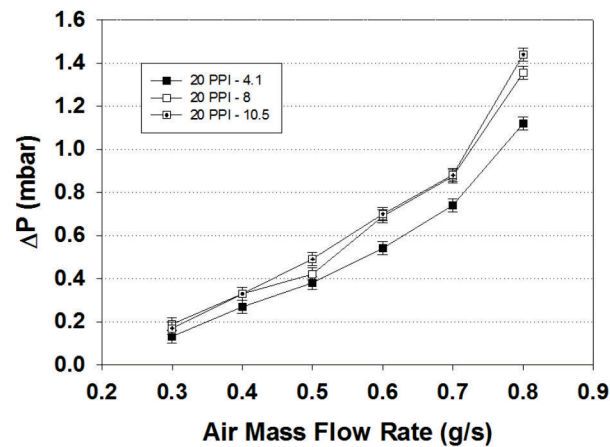
As concluded in the section examining heat transfer characterization, the results obtained for pressure drop with Duocel samples show good agreement with those from the literature and gives confidence that the method can be used to examine the pressure drop in Corevo samples and samples fabricated by the replication technique in the laboratory.



(a) 5 PPI



(b) 10 PPI



(c) 20 PPI

Figure 8.7: Difference of pressure against air mass flow rate for Duocel samples. (a) 5 PPI samples with 11.5, 7.9 and 5.2, (b) 10 PPI samples with 10.5, 7.9 and 4.9, and (c) 20 PPI samples with 10.5, 8 and 4.1 density respectively.

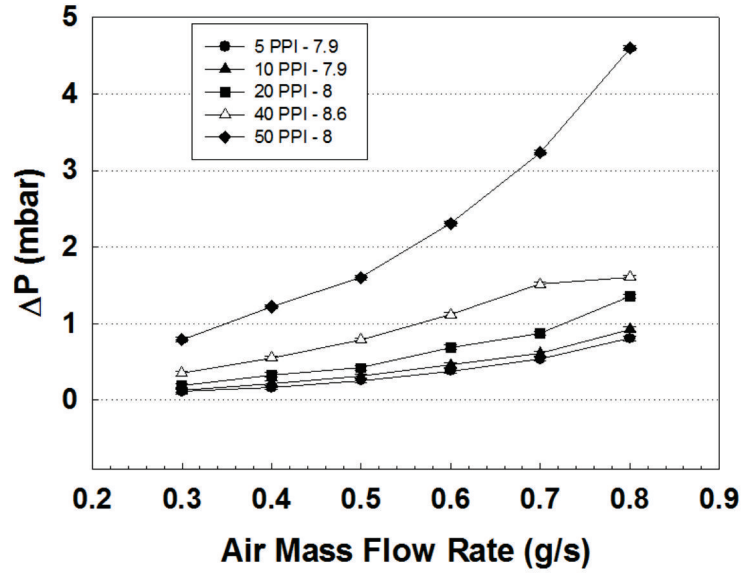


Figure 8.8: Pressure drop in 50 PPI-8, 40 PPI-8.6, 20 PPI-8, 10 PPI-7.9 and 5 PPI-7.9 Duocel samples.

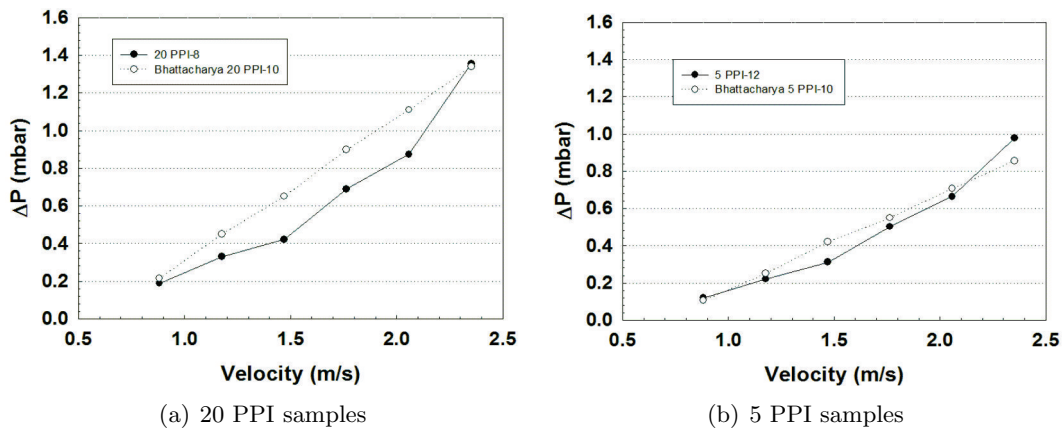


Figure 8.9: Comparison of pressure drop obtained in (a) 20 PPI- 8 and (b) 5 PPI-12 Duocel samples with data from Bhattacharya et al [65].

8.3 Corevo foams heat transfer coefficient

Samples produced by Constellium (commercially named Corevo foams) with the characteristics reported in Table 8.3 were tested under the parameters and procedure established in section 8.1. Constellium produces metal foams using the replication technique, with approximately cylindrical pores between 2 and 5 mm in diameter and height (height is always the same as the diameter within experimental error) and with different densities. The open pore pattern was fabricated through a similar process to the method developed in this work which was described in Subsection 6.1.2.

Table 8.3: Characteristics of Corevo metal foam samples used for thermal and fluid flow experiments.

Sample	Nominal pore size (mm)	Measured pore size (mm)	Nominal (%)	Porosity (ε)
F55	5	4.77	15.9	0.84
F65	5	4.66	16.9	0.83
F64	5	4.31	24.7	0.75
F56	5	4.72	27.9	0.72
F51	2	1.96	25.5	0.74
F36	2	1.98	44.3	0.55

8.3.1 INFLUENCE OF DENSITY ON THE HEAT TRANSFER IN COREVO FOAMS

Samples with 5 mm and 2 mm pore size were tested to understand the influence of the densities in samples with a porosity lower than 0.85. As reported in Table 8.3, the density of the samples is not lower than 15 vol % solid, so as explained earlier, an increase in both the heat transfer coefficient and the pressure drop over those measured for Duocel foams is expected. Fig. 8.10 shows the heat transfer coefficient obtained when Corevo samples of 5 mm with a range of densities were tested under the same test parameters.

As in Duocel foams, samples present an increase in the heat transfer coefficient when the air mass flow rate and the density increase. Sample F56 with 27.97 % density

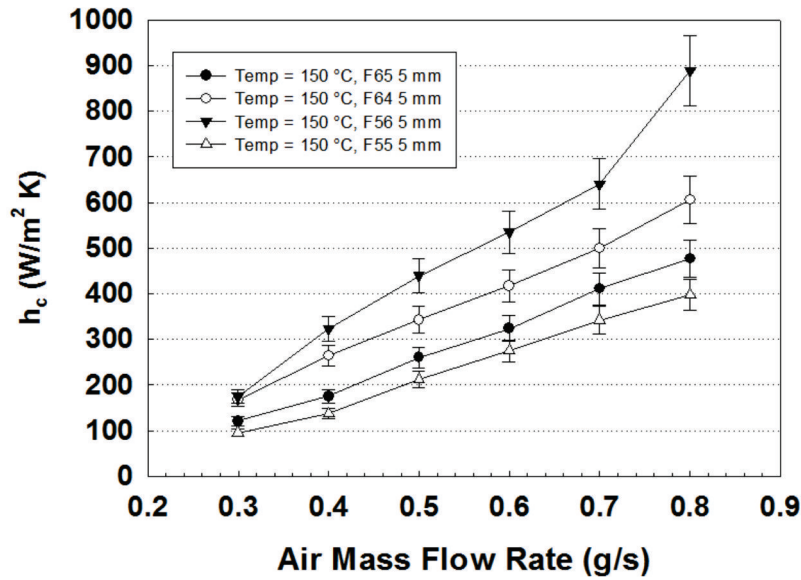


Figure 8.10: Heat transfer coefficient obtained at 150 °C in samples with 5 mm pore size and different densities.

(the highest density of Corevo samples with 5 mm) presents the highest heat transfer coefficient in all the air mass flow rates of the test. At 0.3 g/s flow rate the F56 sample presents a heat transfer coefficient of 174 W/m² K which is 7 W/m² K (or 4 %) higher than the F64 sample with 24.75 % density (the second highest density). The differences increase at higher flow rates. At a flow rate of 0.8 g/s, sample F56 presents a heat transfer coefficient of 888 W/m² K which is 30% higher than that shown by the F64 sample. The F55 sample with 15.92 % density presents the lowest heat transfer coefficient in all the tests; this sample, which also has the lowest density among the Corevo samples tested, has a heat transfer coefficient about 50 % than that of F56. The lower heat transfer coefficient obtained with samples with higher porosity is due to the reduction in solid material, in this case aluminium, which has a higher thermal conductivity than the fluid and transports heat into the air. This general conclusion has been reached by several different investigations [51, 103, 113, 157].

The F51 and F36 samples with 2 mm pore sizes and different densities were tested and the results obtained are presented in Fig. 8.11. F51, the sample with the lowest density among these two samples, presents a slightly higher heat transfer coefficient at the first

three air mass flow rates of the test. At 0.3 g/s the difference between them is 30%, this difference reduces with higher air mass flow rates and at 0.6 g/s and above, the F36 sample presents a higher heat transfer coefficient.

There is a substantial difference between samples F36 and F51, which rises to around 30 % at the highest flow rates tested. These test results were repeated and found to be reliable. It can be seen that the relation between h_c and air mass flow rate is not linear in sample F51, and at 0.6 g/s, and beyond there seems to be a lower dependence of the heat transfer coefficient on the air mass flow rate. If we compare the general shape of the line that describes the heat transfer behaviour of the 50 PPI-8 Duocel sample (Fig. 8.4), against the line of F51 (Fig. 8.11) it is possible to observe that the shape of the two lines is similar; both F51 and the Duocel samples show a smaller increase in transfer coefficient at high gas flow rates. Real pore sizes reported in Table 8.3 shows that F51 and F36 samples have almost the same pore size (1.96 and 1.98 mm). This small difference in pore diameter plus more importantly the high difference in density (F51 is almost 50 % lower in density than the F36 sample), could explain why the F51 sample does not have the linear or slightly upward curve behaviour with increasing air mass flow rate observed in all high density samples tested in this work; Corevo, and the replicated, multiple pore size and segmented samples. It is possible that in this particular sample, with the lowest density of the smallest pore size material, the limiting factor in the overall heat transfer process is no longer the transfer from foam to air (which the small pore size will cause the foam to do very well; the specific surface area will increase when the pore size is reduced, and this will result in an increase in heat transfer [157]). If this process is very efficient, at high air flow rates, the limiting stage may become the transport of heat through the foam, which will be made more difficult by the low conductivities of low density foams. Thus when the air flow rate is increased above a certain value the heat transfer can no longer increase as the transport through the foam is unaffected by the air flow.

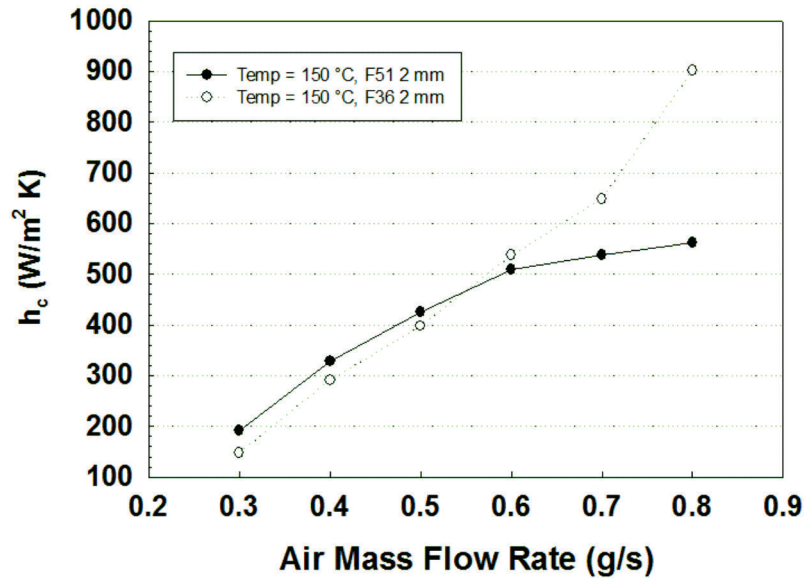


Figure 8.11: Heat transfer coefficient obtained at 150 °C in samples with 2 mm pore size and different densities.

8.4 Corevo foams pressure drop

The fluid flow behaviour was investigated for Corevo samples, showing much larger pressure difference than those presented by Duocel samples (if we compare the 50 PPI-8 Duocel sample with the F56 sample, both of which present the highest pressure difference in the group of samples they represent, we see a difference of 38 times). This is likely to be due to the much higher density of Corevo foams following standard trends observed in foams generally [117].

8.4.1 INFLUENCE OF DENSITY ON THE PRESSURE DROP IN COREVO FOAMS

Corevo samples reported in Table 8.3, were tested to explore the influence of density and flow rate on the pressure drop. Fig. 8.12 shows the experimental pressure gradient obtained for 5 mm pore size samples. The pressure difference is seen to be influenced by the air mass flow rate and the sample density. The pressure gradients across the samples F55 and F65 were slightly different, with sample F56 having a 13 % higher

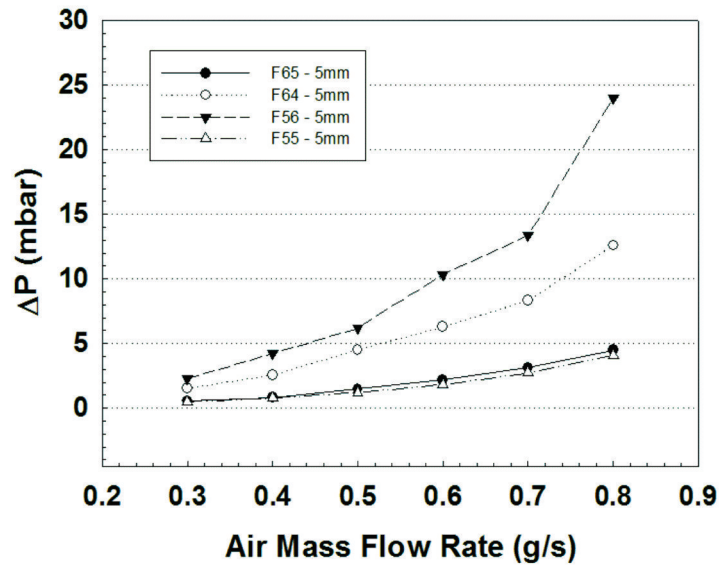


Figure 8.12: Difference of pressure in Corevo samples with 5 mm pore size and different densities.

pressure drop than sample F65. The highest pressure drop in all samples with 5 mm pore size is found in sample F56, which is 80 % higher than the F55 sample. In these higher density foams there is a different picture to describe the structure. Rather than being an array of struts connected at nodes, they can be pictured as individual pores connected by open windows. Corevo sample density reported in Table 8.3 is similar to the material tested in the work of Despois et al [117] having densities over 20 %. These workers identified the interpore windows as the critical features for fluid flow as these get smaller (which happens as density goes up), the passage of fluid is made harder. The permeability exhibits a gradual decrease with density until it approaches 36 %, when the average interpore window shrinks to zero and closes off with a transition to isolated pores in the sample. The results obtained with Corevo samples show the behaviour predicted by Despois, where the sample with the highest density, (sample F57 with 27 % metal) reports the highest pressure drop.

The F51 and F36 samples with 2 mm pore size were tested and the behaviour is plotted in Fig. 8.13. The data were plotted on different Y axes scales due to the large pressure differences presented by sample F36. The F36 sample has 44.3 vol % solid, which is

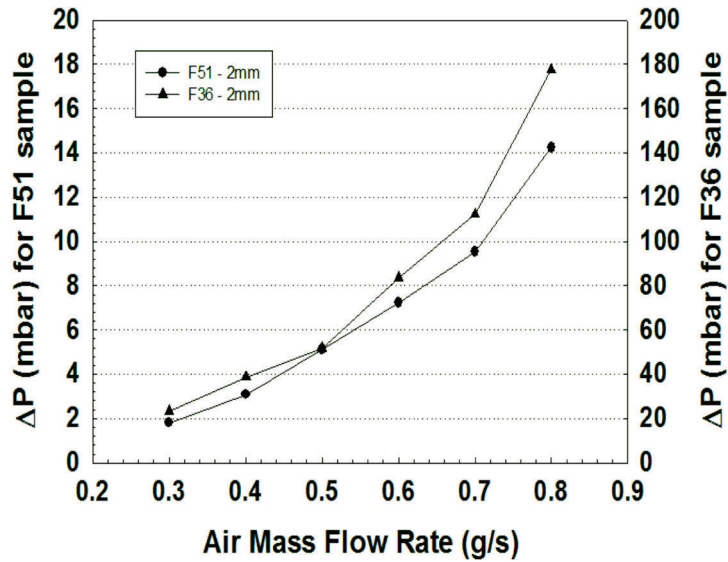


Figure 8.13: Pressure drop obtained in Corevo samples with 2 mm pore sizes and different densities.

almost twice that of F51 (25.5 %) although the pore sizes (reported in Table 8.3) show that both samples, F51 and F36 have the same real pore size. As reported on Table 8.3, F36 sample is over 36 % dense. At this density some pores are likely to be closed, or at least have lower connectivity than the ideal, so that the resistance to air flow through the sample is much higher.

8.5 Heat transfer of laboratory made replicated foams

Samples with single pore size obtained by the version of the replication technique developed were tested to obtain their heat transfer behaviour. Table 8.4 reports the characteristics of these single pore size replicated foams.

Table 8.4: Characteristics of Replicated metal foam samples used for thermal and fluid flow experiments.

Sample	Pore size (mm)	Density (%)	Porosity (ε)
1 mm	1	34.92	0.6507
3 mm	3	37.13	0.6282
5 mm	5	31.95	0.6804

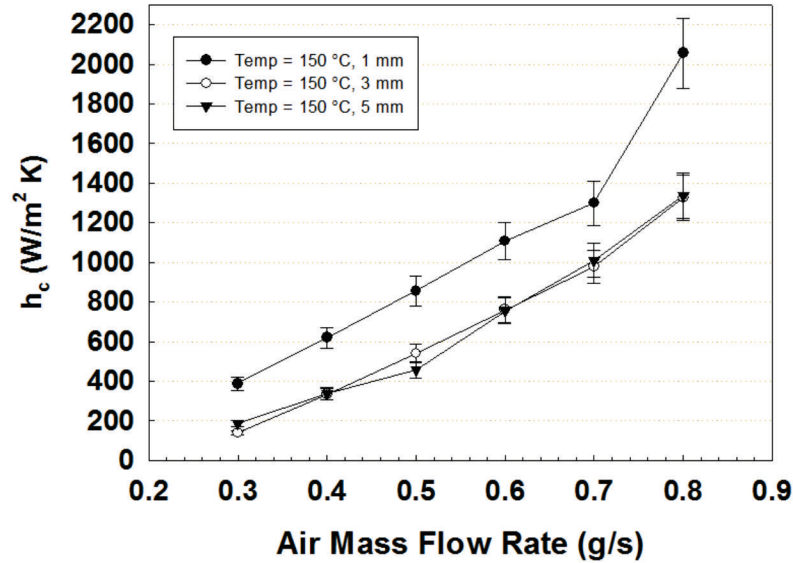


Figure 8.14: Heat transfer coefficient obtained at 150 °C in samples with 1, 3 and 5 mm obtained by the replication technique.

Samples with spherical pore shape of 1, 3 and 5 mm pore diameter obtained by replication technique were tested on the rig. Fig. 8.14, shows the heat transfer coefficients against the different air mass flow rates. The heat transfer coefficient obtained from these samples presented values over 1200 W/m²K, however this high heat transfer coefficient coincides with the high pressure differences shown in Fig. 8.15.

The sample with 1 mm pore size presents the highest heat transfer coefficient in all the air mass flow rates of the trial. Samples with 3 and 5 mm pore sizes show almost the same values of heat transfer coefficient, although it appears that the 5 mm pore samples presents the highest surface area efficiency as it has a lower density than the 3 mm pore sample [125, 157]. The sample with 1 mm pore size has 34.92 % density, which is somewhat lower than the density presented by the 3 mm sample (37.13 %), suggesting that the heat transfer coefficient is governed more by the pore size rather than the density in this type of sample. For the 5 mm pore size sample, the density was 31.95 %; in this case the sample with 1 mm pore size presented higher density and, obviously, lower pore size, characteristics that benefit the heat transfer coefficient but increase the pressure drop [47, 50, 130]. The heat transfer coefficient obtained for 1

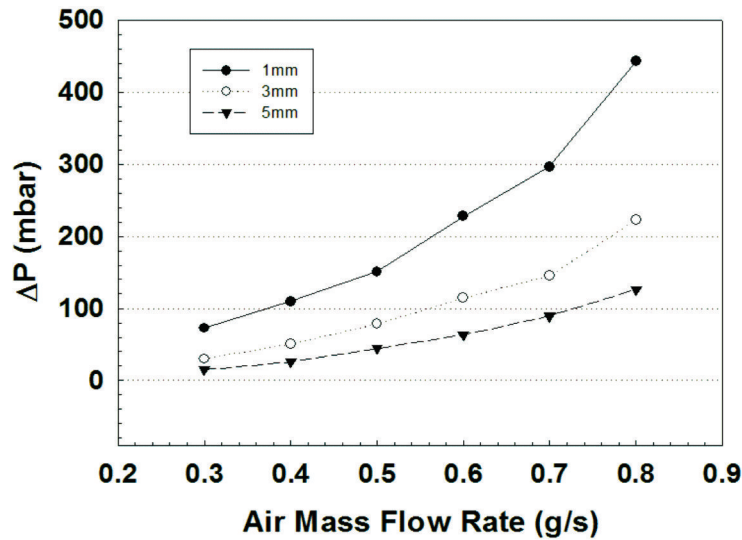


Figure 8.15: Gradient pressure obtained in replication technique samples with 1, 3 and 5 mm pore sizes, densities are reported in Table 8.4.

mm pore size is 38 % higher than that found for samples with 3 and 5 mm pores.

8.6 Pressure drop of laboratory made replicated foams

Replicated samples present a pressure gradient higher than the maximum pressure gradient presented by the Corevo samples. As was reported in Table 8.4, the densities of these samples are higher than 30 %, at these densities, permeability decreases rapidly [117]. Fig. 8.15 plots the differences of pressure obtained in samples made by the replication technique against air mass flow rate.

Pressure gradient increases when the air mass flow rate increases and when the pore size decreases. The sample with 1 mm pore size has, for all the air mass flow rates, the largest pressure drop, even though it does not have the highest density (34.92 %, slightly lower than 37.13 % presented by the 3 mm pore size sample). This means that the metal foams fabricated by the replication technique have high dependence of pressure drop on pore size particularly at small pore size. This behaviour was also found by Xu et al [120] where the permeability decreases faster with pore size at smaller pore size

in numerical simulations over a range of porosity from 1 to 3 mm. The sample with 5 mm pores shows the lowest pressure drop, this sample has the largest pore size and the lowest density among the single pore size replicated samples, and it has a better performance than the 3 mm sample, as it shows similar heat transfer but lower pressure drop in all the air mass flow rates. The sample with 1 mm pore size presents 50 % higher pressure drop than 3 mm pore size and 80 % more than 5 mm pore size sample.

8.7 Heat transfer coefficient as a function of the pore size

So far the results have been presented for each type of foam separately, considering the heat transfer coefficient (h_c), as a function of the air mass flow rate. However, to visualize and understand better the thermal behaviour of the samples with single pore size, the effect of pore size on the heat transfer coefficient (h_c), will be addressed for all of Duocel, Corevo and replicated samples.

8.7.1 DUOCEL SAMPLES

Figs. 8.16(a), Fig. 8.16(b) and Fig. 8.16(c) show the heat transfer with respect the pore size for Duocel samples with 5, 8 and 10 vol % solid respectively at different air mass flow rates. Figures show that the heat transfer coefficient decreases when the pore size increases, and that the influence of the pore size is greatest at low density.

Fig. 8.16(a) shows that the heat transfer coefficient decreases by 28 W/m²K (about 8 %) when the pore size increases from 0.63 to 1.27 mm (from 40 to 20 PPI) at 0.8 g/s. Further increases in pore size lead to a greater reduction in heat transfer coefficient, for example doubling the pore size to 2.54 mm gives around a 30 % decrease. Similar behaviour is observed in the rest of the flow rates.

There is one particular behaviour when the samples with 5 vol % solid were tested

at 0.4 g/s air mass flow rate, where there is an increase of 13% in the heat transfer between the two smallest pore size samples. At this particular air mass flow rate the 1.27 mm pore size (20 PPI) sample has the highest heat transfer properties even though it is not the smallest pore size or the highest density. Mancin et al [125] also found that the sample with the highest heat transfer coefficient was not the sample with the smallest pore size and highest density (the characteristics that improve the heat transfer behaviour). This particular sample (10 PPI and 9.7 density) presented this higher heat transfer coefficient over all the flow rates tested with about 20 % larger heat extraction over 40 PPI and 7.0 % density sample which, due to the pore size and the small difference in density, was expected from the results of Mancin et al to show the highest heat transfer coefficient [125].

Samples with 8 vol % solid present 25 % lower heat transfer in the smallest pore size, versus the largest Fig. 8.16(b). The sample with 2.54 mm pore size (20 PPI) presents approximately a 10 % increase in heat transfer coefficient at this density in all the air mass flow rates tested. Fig. 8.16(c) shows the behaviour when samples with 10 vol % solid are tested, it can be observed that the heat transfer coefficient in all the air mass flow rates decreases by 30 % and 20 % when the pore size goes from 0.63 to 1.27 mm diameter and 1.27 to 2.54 mm diameter respectively. When the pore size increases from 2.54 to 5.08 mm (from 10 to 5 PPI), the decrease in heat transfer is the only 8 %.

The above analysis shows that the heat transfer coefficient is highly dependent on the density, this can be observed if we compare the reduction in the heat transfer coefficient when it is analyzed at the highest air mass flow rate, 0.8 g/s, for the three different densities (5, 8 and 10 vol % solid), see Fig. 8.17. In samples with 5 vol % solid at the highest air mass flow rate, when the pore size increases from 0.63 to 1.27 mm (40 to 20 PPI), the heat transfer coefficient reduces by 8 %. Making the same comparison in samples with 8 and 10 % vol solid, the differences between the heat transfer coefficient with the same change in the pore size at the same air mass flow rate (0.8 g/s), the differences are 27 and 38 %. When the pore size increases at a fixed density, the

8.7. HEAT TRANSFER COEFFICIENT AS A FUNCTION OF THE PORE SIZE¹⁵⁹

specific surface area decreases due to the reduction in number density of the ligament [103, 113, 130], and this will reduce the real area available for heat transfer.

8.7.2 COREVO SAMPLES

Corevo foams analyzed have 5 mm and 2 mm nominal pore size. With the objective to characterize and understand better the thermal and hydraulic fluid flow, the pore size was measured manually and the mean value of 20 measurements is reported in Table 8.3. The values obtained show a difference between the pore sizes in different samples of the same type of less than 1 mm. Fig. 8.18 shows the heat transfer coefficient with respect to pore size at different air mass flow rates.

The Corevo foam samples analysed had 5 mm nominal pore size, with different densities as reported in Table 8.3. The comparison with Corevo foams with 2 mm pore size is not presented as these samples have very different behaviour which is discussed below.

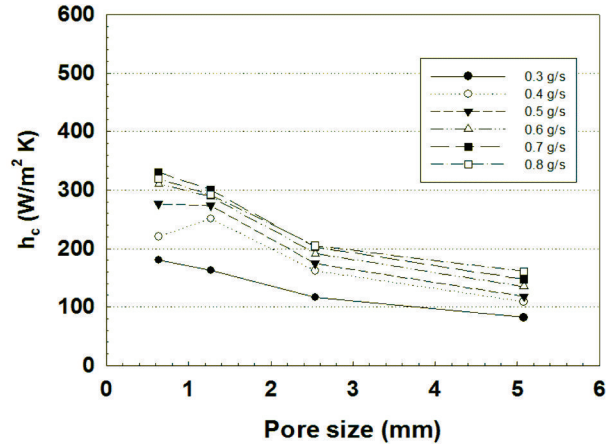
Fig. 8.18 shows that there is a decrease in heat transfer when the pore size increases and the density decreases for the samples with the smallest two pore sizes, behaviour that is in agreement with several prior investigations [50, 105, 122, 157, 158]. However, the sample with 4.72 mm pore size, the second largest pore size, presents the largest heat transfer coefficient, being outside the trend of a general decrease in this parameter with increasing pore size shown by the other samples. This particular sample (F56) has the largest density in the Corevo samples analysed (27.9 vol % solid) and seems to have the highest surface area efficiency (the surface area efficiency is influenced by temperature gradients in the surface being cooled, and is a function of the geometry of the pores, at least in lower density Duocel foams [125, 130]). This sample has about 40 % higher heat transfer coefficient compared with sample F55 with 4.72 mm pore size, (F56 has 4.66 mm pore size and 16.9 vol % solid). When the samples with the two smallest pore sizes are compared, the heat transfer coefficient decreases by 24 % with, as would be expected, the sample with the smallest pore size having the best

performance.

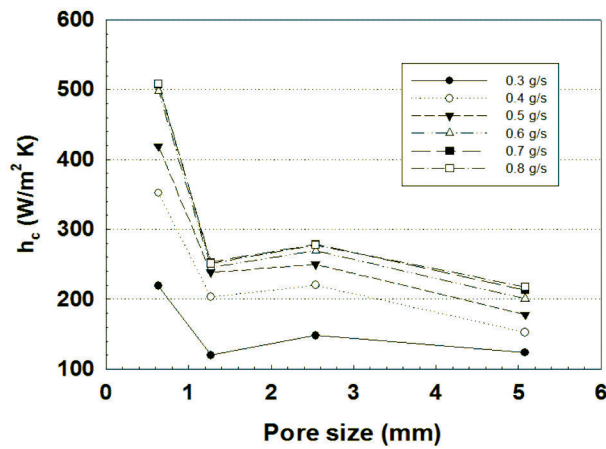
8.7.3 REPLICATED SAMPLES

The analysis performed on Duocel and Corevo samples was done in the samples processed on the laboratory using the replication technique. Fig. 8.19 shows the heat transfer with respect to the pore size at different air mass flow rates of samples with 1, 3 and 5 mm pore sizes and different densities as reported in Table 8.4. The replicated samples present similar behaviour to the Duocel and Corevo samples; i.e. the heat transfer coefficient decreases when the pore size increases. When the pore size increases from 1 mm to 3 mm the heat transfer coefficient decreases by 40 %, and when the pore size increases from 3 to 1 mm, the heat transfer coefficient decreases, for air mass flow rates of 0.5 and 0.6 g/s, by 15 and 0.5 % respectively. For the other air mass flow rates (0.4, 0.7 and 0.8 g/s) the heat transfer coefficient increases less than 4 %. In the case of 0.3 g/s, the heat transfer increases by 25 %.

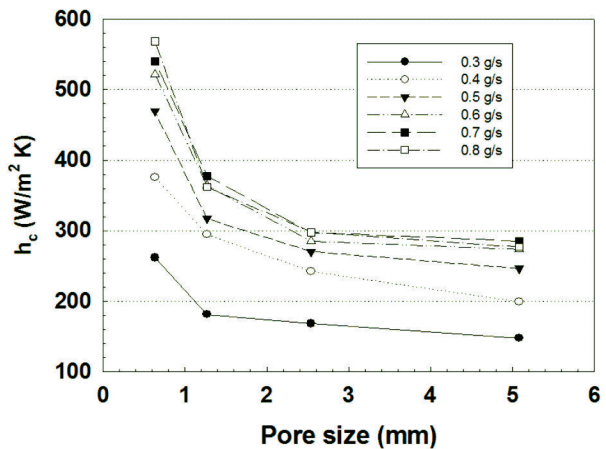
8.7. HEAT TRANSFER COEFFICIENT AS A FUNCTION OF THE PORE SIZE 161



(a) 5 vol % solid



(b) 8 vol % solid



(c) 10 vol % solid

Figure 8.16: The variation in the heat transfer coefficient with the pore size in Duocel samples. (a) 5 vol % solid (b) 8 vol % solid, and (c) 10 vol % solid.

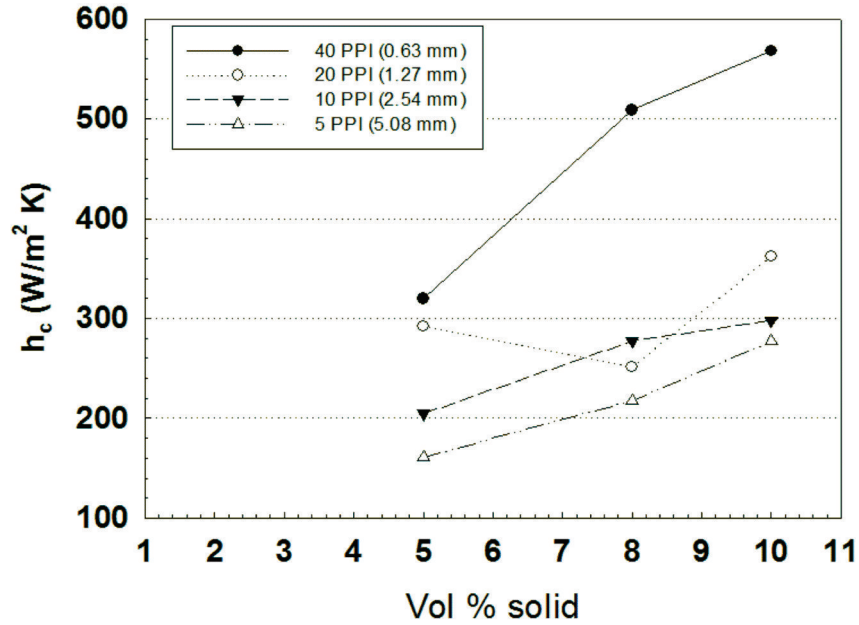


Figure 8.17: The variation in heat transfer coefficient for three different densities in samples with 5, 10, 20 and 40 PPI at 0.8 g/s.

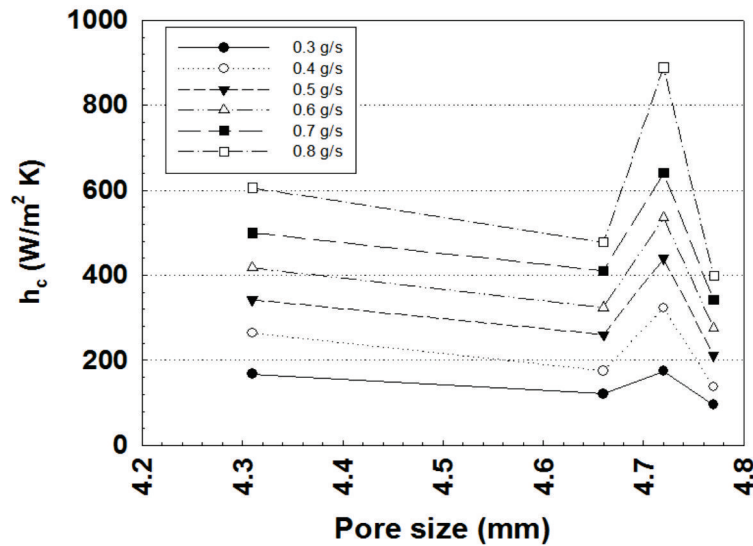


Figure 8.18: The variation in heat transfer coefficient with pore size of Corevo metal foams with nominal 5 mm pore size at different air mass flow rates. As noted in the text the anomalous behaviour of the sample with 4.72 mm pore size is likely to be due to the higher density of this sample.

8.7. HEAT TRANSFER COEFFICIENT AS A FUNCTION OF THE PORE SIZE 163

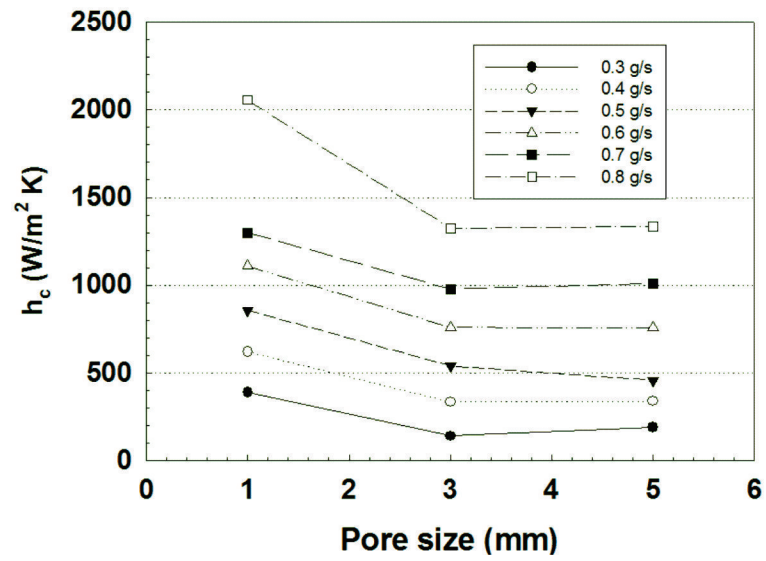


Figure 8.19: Heat transfer coefficient respect to pore size for replicated technique samples with 1, 3 and 5 mm pore size at different air mass flow rates.

8.8 Comparison between single all pore size samples

The heat transfer and pressure drop of Duocel samples with 5, 10, 20 and 40 PPI with 10 vol % solid, Corevo samples with nominal 5 mm pore size and replicated samples with 1, 2 and 5 mm pore size were plotted together. Fig. 8.20 shows the heat transfer with respect to the pore size of the three types of metal foams at 0.8 g/s air mass flow rate. The same relative behaviour was seen at other flow rates and so has not been plotted.

Fig. 8.20 shows that Duocel samples present the lowest heat transfer coefficient, the heat transfer coefficient of the replicated samples being around 7 times higher than Duocel, and also around 2 times higher than Corevo samples, when compared to samples with 5 mm pore size. However, the pressure gradient across replicated samples is around 130 times higher than Duocel and 30 times higher than Corevo samples when the same comparison is made, as can be seen in Fig. 8.21. The large density differences between the samples represent a high difference in heat transfer coefficient and pressure drop in addition to pore size. The increase in the specific surface area and ligament diameter resulting from higher density reduces the permeability [50, 105, 122, 125, 130, 157, 158]. Corevo samples have a higher heat transfer coefficient as described in Subsection 8.7.2. However, this increase in h_c is accompanied by increase in the pressure drop, as shown in Fig. 8.21.

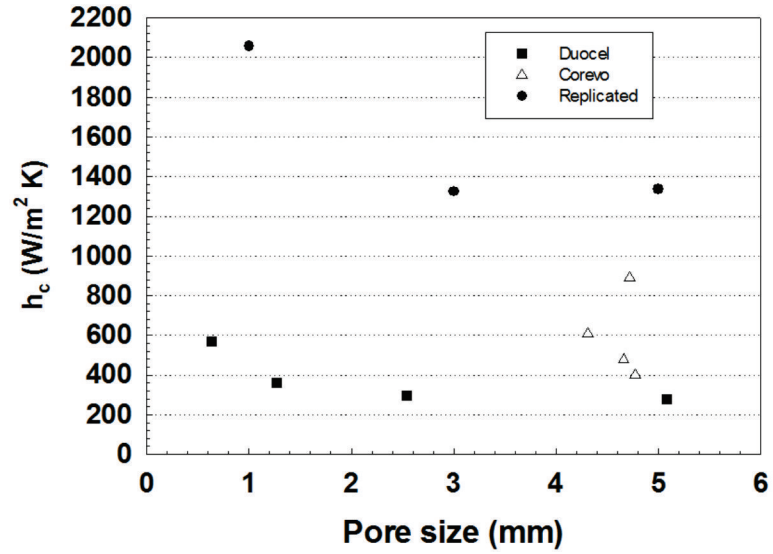


Figure 8.20: Heat transfer coefficient with respect to pore size for Duocel, Corevo and Replicated samples at 0.8 g/s air mass flow rate.

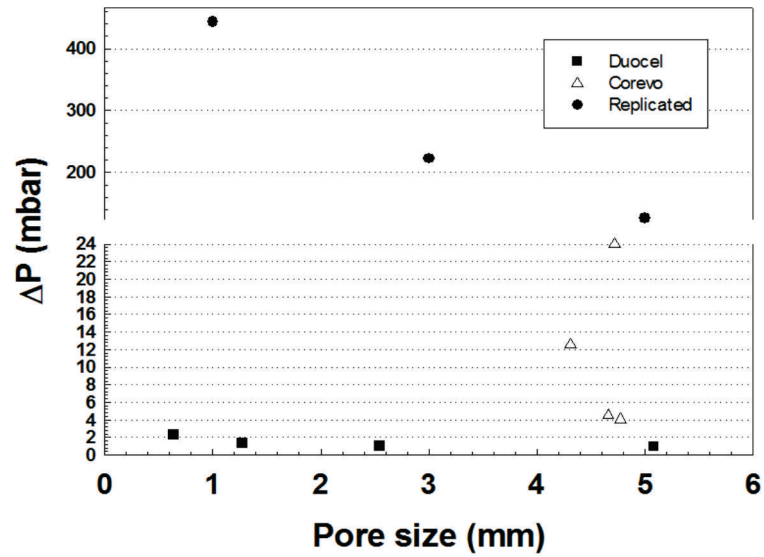


Figure 8.21: Pressure drop obtained in Duocel, Corevo and Replicated samples at 0.8 g/s air mass flow rate. Note that to display all the data on one graph, a split scale has to be used.

Chapter 9

Heat Transfer of Multiple Pore Size Foams

As a variation in pore size and density can have such a large effect on the heat transfer coefficient and pressure drop, it was hypothesised that a sample with variable pore size might be capable of being optimized even further. That is to say that the best structure in the first part of the heat exchanger may not be the same as the best structure towards the end. Multiple pore size samples fabricated by the replication technique were tested to obtain the thermal and fluid flow behaviour. Integrated samples (samples where the preform is controlled to have multiple pore sizes, with different sizes being present in different regions) were processed and have the following characteristics and identification: 1 and 5 mm pore size, identified as 1-5 mm, 1 and 3 mm identified as 1-3 mm, and sample with 3 and 5 mm, identified as 3-5 mm, Fig. 9.1(a) shows a 1-5 mm integrated sample. It should be noted that these samples were not partitioned equally, the smallest pore size in the sample had 10.66 mm length in every sample, i.e. 1-5 mm sample had 10 mm length of 1 mm pore size ($1/3$ of the length of the sample) and 21.32 mm length of 5 mm pore size ($2/3$ of the length sample). This decision was made such that the quantity of small pore size material (which is more challenging to

infiltrate) did not pose processing difficulties.

The manufacture of these foams was done following the procedure described in Section 5.1, where the smallest pore size part of the preform was always placed in the bottom of the crucible, with the largest pore size part of the preform placed on top, and above this the pieces of aluminium to be melted and infiltrated. Therefore, the last part infiltrated with the molten aluminium was always the side where the smallest pore size part of the preform was placed, and it was found to be difficult to obtain more than 15 mm length of fully infiltrated sample. In order to have the same condition in every sample to be characterized, it was decided that the smallest pore size always would have 10.66 mm length (1/3 of the total length sample).

To try and better understand the thermal and fluid flow behaviour found with the integrated samples, the same overall pore structure was created by combining slices obtained from samples fabricated with a single pore sizes i.e.; samples with 1, 3 and 5 mm pore sizes only, with cylindrical shape, originally 19 mm diameter and 32 mm length, which were segmented in 10.66 mm length slices (10.66 mm is 1/3 of the length of the sample). Then samples were made up to have the same overall structure as shown in Fig. 9.1(b). These samples were identified as 1-5 mm smt, 1-3 mm smt and 3-5 mm smt respectively.

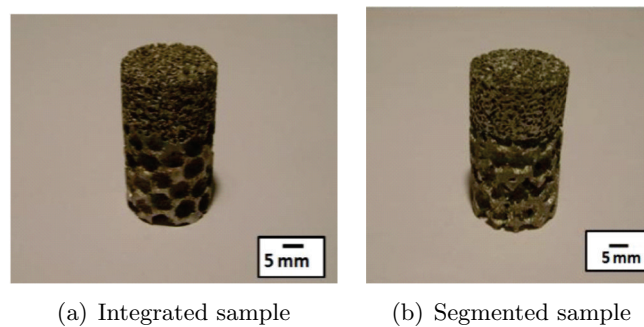


Figure 9.1: Multiple pore size samples processed by the replication technique. (a) Sample with 21.33 mm of the length being 5 mm pore size and 10.66 mm of the length having 1 mm pore size (the total sample length is 32 mm) (b) Sample with the equivalent structure created by stacking slices obtained from samples fabricated with a single pore size.

These multiple pore size samples (integrated and segmented) were tested in two ways; at first the sample was placed with the smallest pore size where the cooling gas enters, then as a second trial the sample was switched so the largest pore size received the cooling gas first. The position of the samples in these two types of trials is described in Sections 9.2 and 9.4 in more detail.

9.1 Fabrication and characterization of integrated samples

Integrated samples were processed by the replication technique. To fabricate these samples, taking the example of the sample with 1 and 5 mm pore sizes, NaCl grains of 1 mm size were obtained by sieving commercial salt (table salt or cooking NaCl). The 1 mm grains obtained were placed in a crucible and over them spheres of 5 mm diameter salt paste, fabricated by the process developed here (described in Subsection 6.1.2) were placed. Then the sample was fabricated following the steps described in Section 6.2 to infiltrate the aluminium. After dissolution of the NaCl the foam obtained was machined by EDM to a cylindrical shape with 19 mm diameter and 32 mm length with the following proportions: 10.66 mm length of the smallest pore size (1/3 of sample total length) and 21.33 mm (2/3 of sample length) of the large pore size material. One example of this type of aluminium foam is shown in Fig. 9.1(a). In samples with 3 mm pore size, the spheres were produced following the same paste-based process used for the 5 mm spheres. Table 9.1 reports the structural characteristics of the integrated and segmented multiple pore size samples.

Table 9.1: Characteristics of Replicated metal foam samples with multiple pore size used for thermal and fluid flow experiments.

Sample	Pore(s) size (s) (mm)	Density (%)	Porosity (ε)	Integrated /Segmented
1-3 mm	(1/3) 1 and (2/3) 3	36.78	0.63	integrated
1-5 mm	(1/3) 1 and (2/3) 5	31.29	0.68	integrated
3-5 mm	(1/3) 3 and (2/3) 5	31.60	0.68	integrated
1-3 mm smt	(1/3) 1 and (2/3) 3	34.42	0.65	segmented
1-5 mm smt	(1/3) 1 and (2/3) 5	32.59	0.67	segmented
3-5 mm smt	(1/3) 3 and (2/3) 5	34.23	0.65	segmented

9.2 Testing integrated samples

To characterize the thermal and hydraulic behaviour of these samples, two tests had to be performed on each; the first trial consisted of putting the smallest pore size on the side where the cooling gas enters the sample, this is shown in Fig. 9.2(a). The identification of the samples in this position is of the form 1-3 mm, 1-5 mm and 3-5 mm signifying the two pore sizes involved. After testing of the full range of air mass flow rates at 150 °C, the sample was inverted for the second trial Fig. 9.2(b). In this case on the largest pores are on the side where the cooling gas enters, and the samples in this position are identified as 3-1 mm, 5-1 mm and 5-3 mm respectively (i.e. the first number represents the pore size that is first receiving the gas).

9.2.1 HEAT TRANSFER COEFFICIENT OF INTEGRATED SAMPLES

Fig. 9.3(a) shows the heat transfer behaviour of the three samples when they are placed with the smallest pore sizes on the side where the cooling gas enters. Heat transfer coefficients obtained for these samples are higher than for Corevo but are lower than the replication technique samples with only one pore size. The 1-5 mm sample presents the lowest heat transfer in all the air mass flow rates, the 1-3 mm sample shows on average the highest heat transfer coefficient among the samples, although at the first two lowest air mass flow rates it has about 10 % lower heat transfer coefficient than the sample

3-5 mm. The behaviour presented by the integrated multiple pore size samples at this position when they are tested in the rig (smallest pore size section first) is similar to samples with single pore size, i.e. samples with smaller pore sizes and higher density present larger heat transfer coefficients and also larger pressure drop values, as is shown in Fig. 9.5(a). This behaviour is in agreement with the literature on foams with single pore sizes [47, 50, 105, 117, 120, 122, 157, 158, 161].

Fig. 9.3(b), shows the thermal behaviour when the samples are placed with the largest pore size on the side where the cooling gas enters. In this position the sample that presents highest heat transfer coefficient was the sample with 1 and 5 mm pores (position 5-1 mm). This sample has about 20 % higher heat transfer coefficient than the sample with 1 and 3 mm pore size, although in the highest air mass flow rate of the trial (0.8 g/s), the difference between them is much narrower, only 4 %. When the sample with 5-1 mm is compared with the sample 5-3 mm in the lowest two flow rates of the trial, 0.3 and 0.4 g/s, the differences in the heat transfer coefficient between them is lower than 10 %. After these two lowest air mass flow rates, the difference in the heat transfer coefficient start to increase gradually, and in the highest air mass flow rate, sample 5-1 mm, displays 20 % higher heat transfer coefficient than the sample with 5-3 mm.

If we compare Figs. 9.3(a) and 9.3(b) is possible to observe that the heat transfer presented by the three samples is larger when they are tested with the largest pore size placed first to receive the cooling gas. For a better comparison, Figs. 9.4(a), 9.4(b) and 9.4(c) display the heat transfer coefficients versus air mass flow rate for each of the samples when they are tested in the two trials; when the small pore size is placed first and when the largest pore size is placed first to receive the cooling gas.

Fig. 9.4(a), shows the heat transfer coefficient obtained with the sample with 1 and 3 mm pore size when it is placed in the two positions. The increase in the heat transfer coefficient presented by the sample when the largest pore size is placed to receive first the cooling air (position 3-1 mm) is 25% higher on average in all the air mass flow rates

of the test. The increase in the heat transfer coefficient was constant at all the air mass flow rates, with exception at 0.7 g/s where the increment was only 6%, this value was not checked (the test was not repeated) so this difference could be a wrong measure.

The sample with 1 and 5 mm pore sizes presented an increase of about 50% in the heat transfer coefficient in all the air mass flow rates; this can be observed in Fig. 9.4(b). The increase was found when the sample was tested with the largest pore size on the side where the cooling air enters (position 5-1 mm), in the same way as the sample with 1 and 3 mm. The sample with 3 and 5 mm pore size also presented an increase in the heat transfer coefficient when placed with the biggest pore size first to receive the cooling gas. The increase in this sample was 30% on average in all the air mass flow rates of the test, Fig. 9.4(c).

To explain this behaviour, the flow of gas through the individual elements of the samples needs to be considered. It is well known that the smaller the pore size of a foam, the lower its permeability will be [47, 117, 120, 157, 161]. This means that a higher pressure drop will be required to flow gas through smaller pore sizes for a given flow rate, see Fig. 9.5(b). This means that the flow rate of the gas in front of any small pore size section may be reduced compared to that in a large pore size foam (i.e. there may be a "bow wave" effect as the gas decelerates). If the small pore size section comes after the large pore size section, the dwell time of the fluid within the large pore size foam is thereby increased over what it would otherwise be, allowing greater exchange of heat to take place.

9.2.2 INTEGRATED SAMPLES PRESSURE DROP

The experimental pressure drop results obtained are presented in the same manner as the thermal behaviour in these type of samples. The fluid flow behaviour is first plotted when the sample is placed with the smallest pore size on the side where the cooling gas enters and then when the sample was inverted, so the largest pore sizes is now the

side that receives first the cooling gas. Figs. 9.5(a) and 9.5(b) show the differences of pressure obtained when the samples are tested in both positions.

Fig. 9.5(a) and 9.5(b) show that in the sample with 1 and 5 mm pore sizes there is a slight increase in the pressure differences when the smallest pore size is placed first. Figs. 9.6(a), 9.6(b) and 9.6(c) shows the pressure drop for each sample when they are tested in both test positions.

The sample with 1 and 5 mm pore sizes presents a pressure drop increase of 18% and the sample with 1 and 3 mm pore size shows an increase of 8% when they are tested with the smallest pore size on the side where the cooling gas enters. The sample with 3 and 5 mm pore size presents practically the same results (within the error in the equipment), with the increase being only 3.5 %. Within the limits of the accuracy of the rig, the asymmetric pressure drop behaviour can only be said to be seen in an integrated sample with a large pore size difference. This behaviour must result from the way the gas is forced to pass from small to large pore sizes as it is not observed in segmented samples (see next section). It is possible that microstructural features act like non-return valves, bending to permit gas flow easily in one direction, but impeding it when the sense of flow is reversed. However, microstructural investigations have failed to find features of this type. What is perhaps more likely is that the entrance of smaller pores into the larger ones can lead to the formation of tapered channels through which the gas must pass. As has been noted in other heat exchanger designs [162], this can lead to asymmetric pressure drop behaviour, with higher resistance when the gas is flowing along a narrowing channel direction.

9.2.3 PRESSURE DROP "BOW WAVE" EFFECT IN INTEGRATED SAMPLES

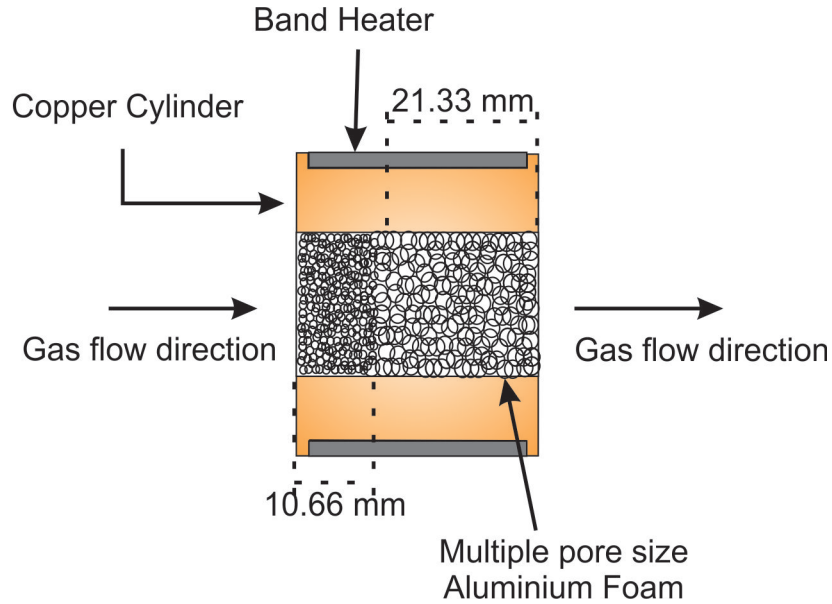
Figure 9.7 shows the integrated foam structure where the small pore meets the larger one. The sample with 5 and 1 mm pore size was sectioned in middle in order to observe the structure when the small pore size meets the larger ones.

When the figure is magnified, it is possible to observe how the small pores (1 mm) meet the larger one (5 mm). This magnified structure is represented in a diagram in Fig. 9.8, where is as well represented the metal foam and the graph showing the pressure drop behaviour when the air enters on the side where the larger pore size is placed.

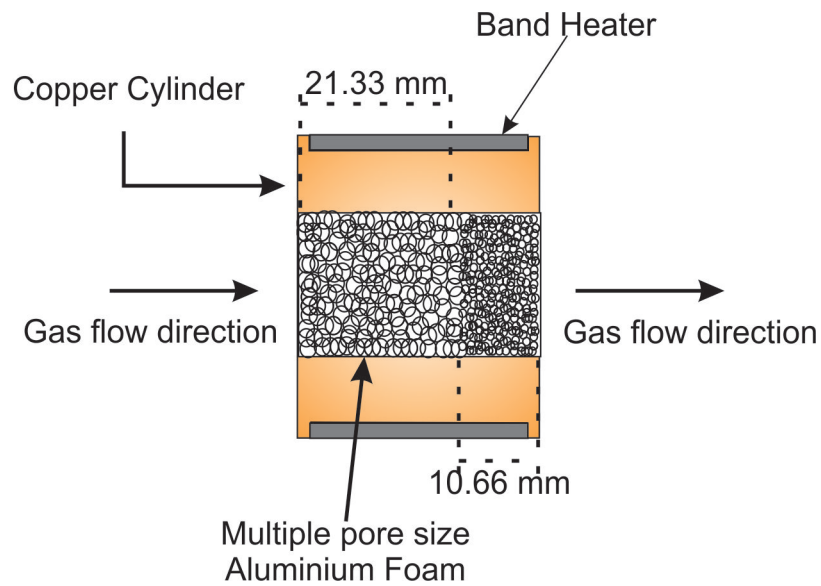
The diagram shows how the fluid behaves when a sample with these characteristics is tested on the rig. What is observed in the diagram and in the picture of the integrated sample is that, when the big pore meets the smaller pore, the increased number of the pore-pore windows increases the surface area in contact with the foam and increases the turbulence, as reported in several works [46, 113, 115, 136, 157, 163], small pore size increase the turbulence and therefore there is a restriction of the fluid to flow through the sample resulting in a larger difference of pressure in this section of the sample (small pore section).

Figure 9.9 shows the bow wave effect when the air enters in the side where smallest pore size is placed. In this case, the flow suffers higher restriction (when it is compared when the larger pore size is placed on the side where the air enters) when the fluid goes through the foam section with the smallest pore size, then when the fluid passes from the smallest to the largest pore size a new restriction takes place, now the area to fluid is reduced having as a result that when the sample is tested in this position the pressure gradient is larger, i. e.;

$$\Delta P_A < \Delta P_B \quad (9.1)$$

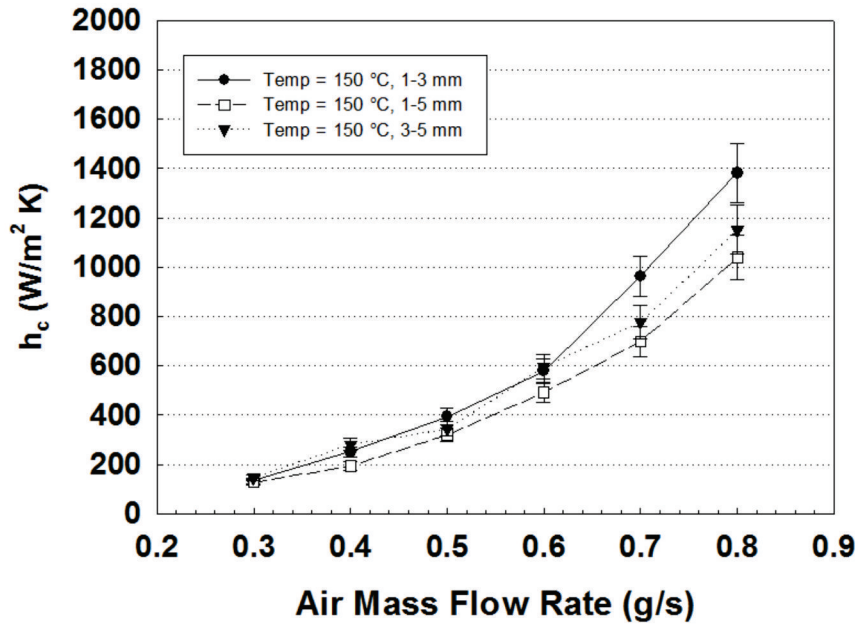


(a) Smallest pore size first.

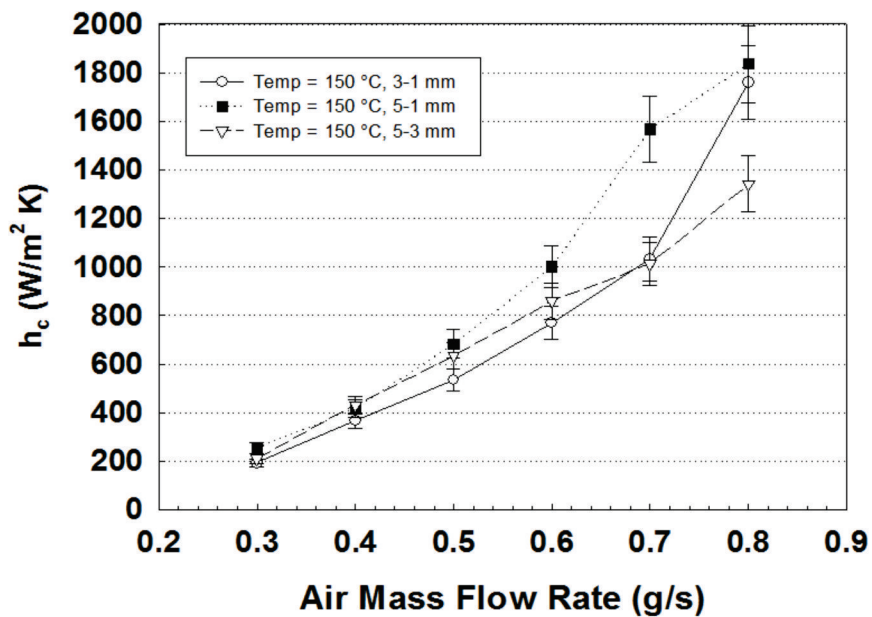


(b) Largest pore size first.

Figure 9.2: Position of the multiple pore size samples in the rig (a) Sample placed with the smallest pore size in the side where the cooling gas enters and (b) sample switched so the largest pore size of the sample is placed where the cooling air enters.

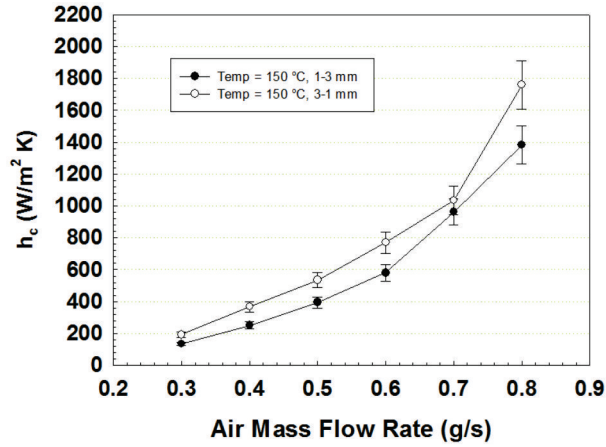


(a) Smallest pore first

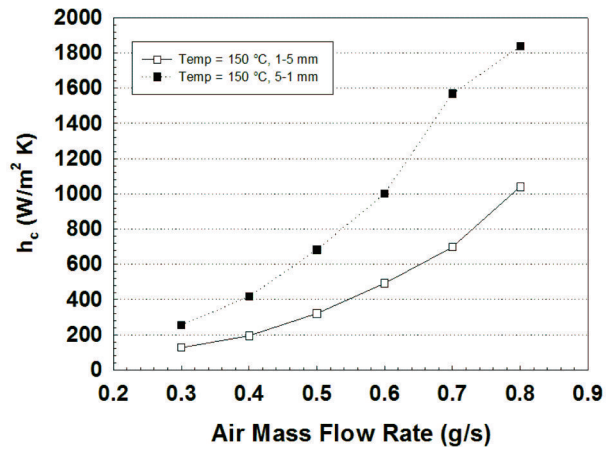


(b) Largest pore first

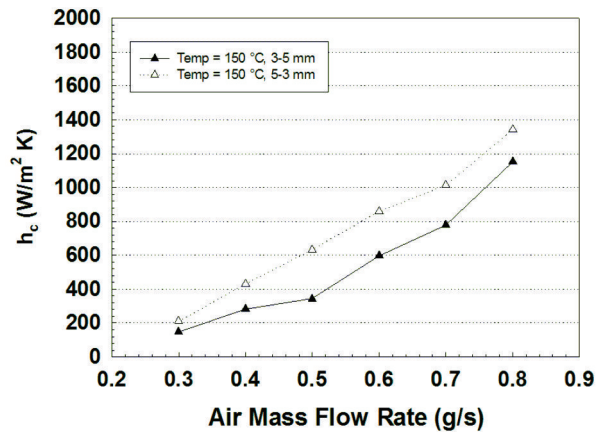
Figure 9.3: Heat transfer coefficient obtained at 150 °C in integrated samples obtained by the replication technique. (a) Heat transfer coefficients obtained for the three samples (1-3, 1-5 and 3-5 mm) when the smallest pore size is placed on the side where the cooling gas enters and (b) when samples are inverted.



(a) Sample with 1 and 3 mm pore size

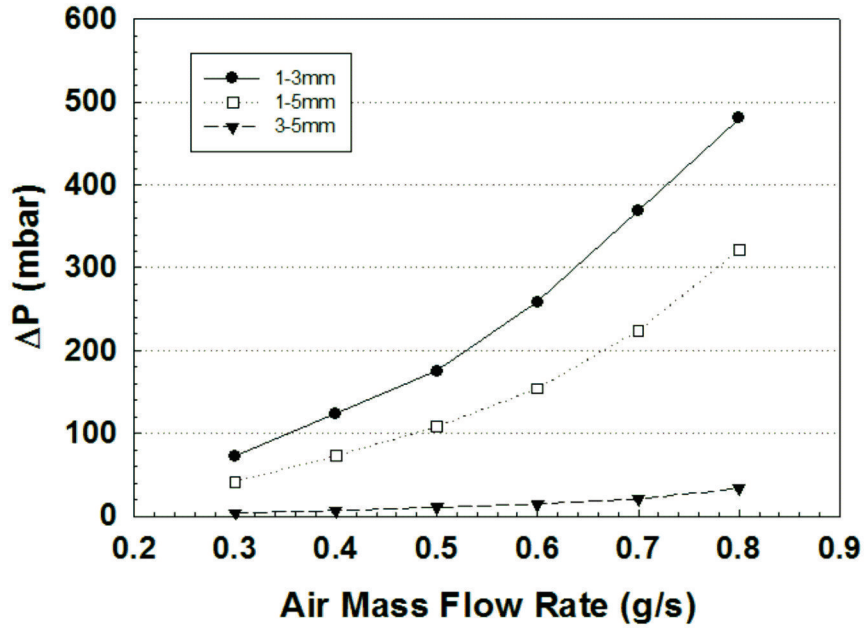


(b) Sample with 1 and 5 mm pore size

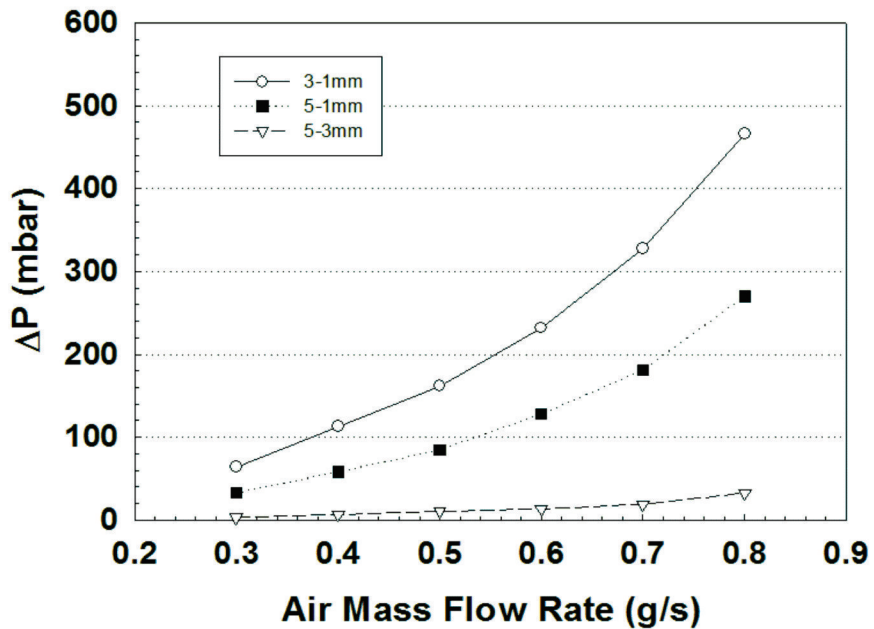


(c) Sample with 3 and 5 mm pore size

Figure 9.4: Heat transfer coefficient obtained by integrated samples with different pore sizes in the same sample when it is tested in the two trial positions. (a) Sample with 1 and 3 mm pore size, (b) 1 and 5 mm pore size, and (c) 3 and 5 mm pore size.

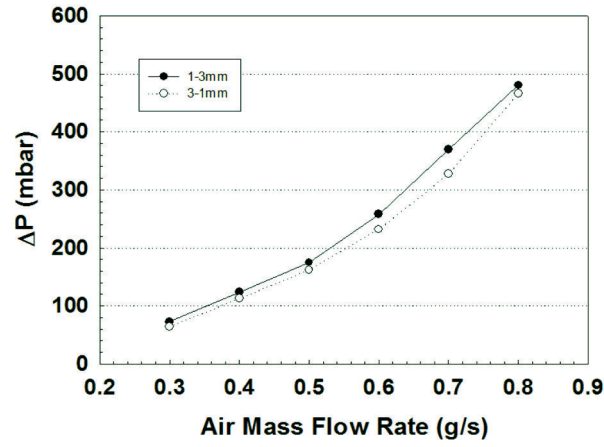


(a) Smallest pore size first

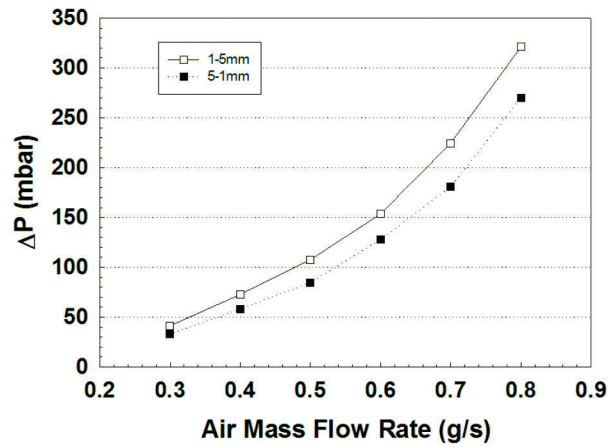


(b) Largest pore sizes first

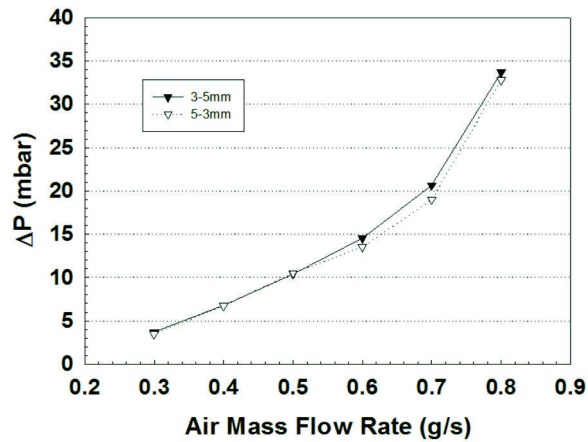
Figure 9.5: Pressure drop obtained in integrated samples with two pore sizes in the same aluminium foam. (a) Samples tested with the smallest pore size on the side where the cooling gas enters and (b) when the sample was inverted.



(a) Sample with 1 and 3 mm pore size



(b) Sample with 1 and 5 mm pore size



(c) Sample with 3 and 5 mm pore size

Figure 9.6: Gradient pressure obtained integrated samples with different pore sizes in the same sample when they are tested in the two trial positions. (a) Sample with 1 and 3 mm pore size, (b) 1 and 5 mm pore size, and (c) 3 and 5 mm pore size.

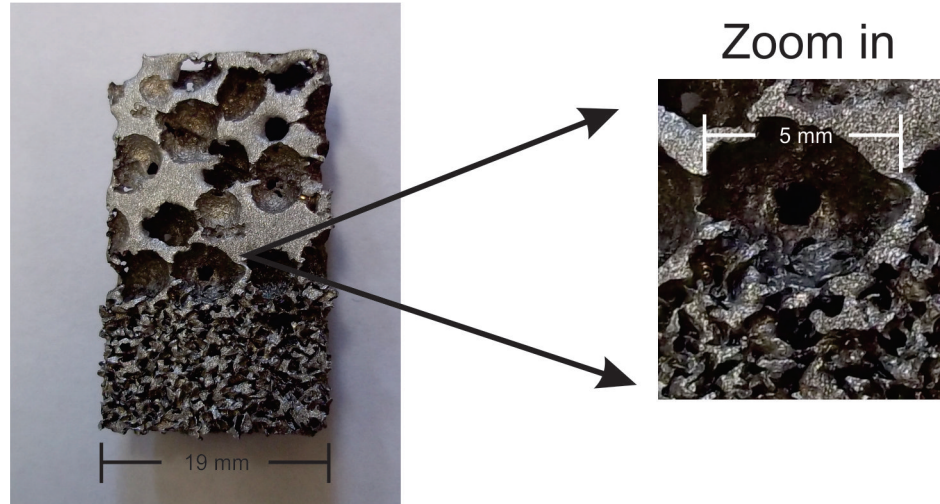


Figure 9.7: Structure obtained in the border when the small pore meets the larger one in an integrated sample.

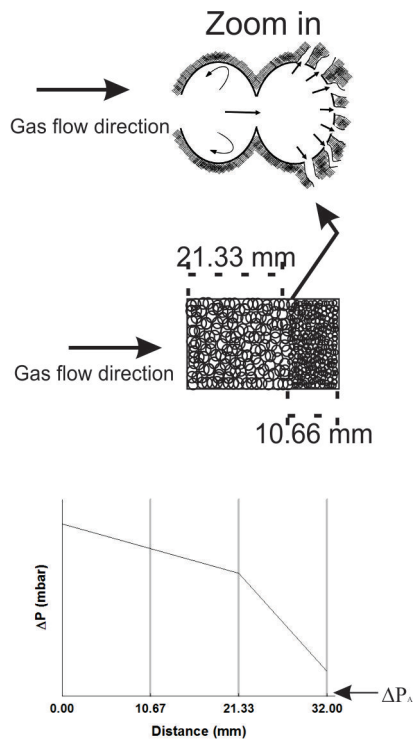


Figure 9.8: Metal foam diagram and graph showing the bow wave effect when a integrated sampled is tested with the largest pore size in the side where the air enters.

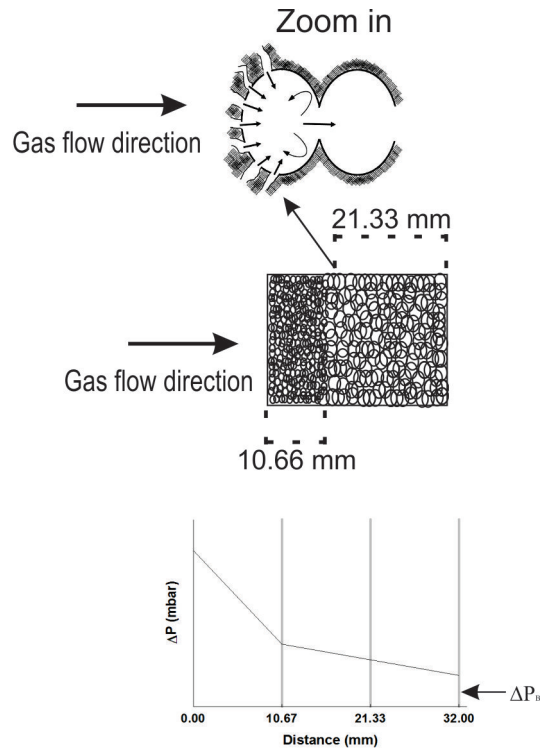


Figure 9.9: Metal foam diagram and graph showing the bow wave effect when a integrated sampled is tested with the smallest pore size in the side where the air enters.

9.3 Fabrication of segmented samples

The behaviour presented by the integrated samples with different pore sizes shows that there is an increased in heat transfer coefficient, and in the case of sample with 5 and 1 mm pore size (sample 1-5 mm) lower pressure drop, when the sample is placed with the largest pore size on the side where the cooling gas enters. To understand better this behaviour the same overall pore structure as in the integrated samples were created by slices obtained from samples fabricated with single pore sizes as follows; samples with 1, 3 and 5 mm pore sizes, with cylindrical shape, 19 mm diameter and 32 mm length, were segmented in 10.66 mm long width slices (10.66 mm is 1/3 of the length sample), so then samples were made up to the same overall structure as shown in Fig. 9.1(b), Table 9.1 reports the characteristics of these samples. These samples were identified as 1-5 mm smt, 1-3 mm smt and 3-5 mm smt respectively. Note that slices were placed together in the rig, without any form of bound or conductive paste being placed between them. It was considered that, as the heat flow would be expected to be lateral only, this would not impact the results.

9.4 Testing segmented samples

The procedure of the trial was kept the same as for the integrated samples; the sample first was placed with the smallest pore size on the side where the cooling air enters, then the test was carried out over the range of air mass flow rates. Then samples were inverted to have the largest pore size within the sample first to receive the cooling gas. Fig. 9.10(a) and 9.10(b) show sketches that describe the position of the sample in the trial.

9.4.1 HEAT TRANSFER COEFFICIENT OF SEGMENTED SAMPLES

Fig. 9.11(a) and 9.11(b) show the heat transfer behaviour of the segmented samples tested under the same parameters as the integral samples. Fig. 9.11(a) shows that the sample which presents the highest heat transfer coefficient is again the sample with 1 and 3 mm pore size. It presents 40 % more heat transfer coefficient when it is compared with the 1-5 mm smt sample, and 42 % when it is compared with the 3-5 mm smt sample. These two samples, 1-5 mm stm and 1-3 mm stm present practically the same behaviour in the trial. The segmented samples tested in this position seem to have the same behaviour as the single pore size samples, where the largest heat transfer coefficient is given by the smallest pore size and largest density, the 1-3 mm smt sample having the largest density and with the smallest pore size combination among the samples. When the 1-3 mm smt sample is compared with 1-5 mm smt, in spite of having almost the same density with a difference of only 5.3 %, the 1-3 mm smt sample presents higher heat transfer coefficient meaning that in segmented samples there is also a big influence of the pore size that constitutes the sample on the heat transfer and pressure drop, see Fig. 9.13(a).

Fig. 9.11(b) shows the thermal behaviour when the samples are switched (largest pore size close to the entrance of the cooling air). Sample 3-1 mm smt presents the highest heat transfer coefficient of the three samples tested. At the lowest two air mass flow rates of the trial (0.3 and 0.4 g/s), its h_c is 12 % higher than sample 5-1 mm smt, and 17 % higher than sample 5-3 mm smt. At 0.5 g/s, the three samples; 3-1 mm smt, 5-1 mm smt and 5-3 mm smt, present almost the same heat transfer coefficient 612, 611, and 633 W/m²K respectively, having differences between them of less than 5 %. In the following flow rates of the trial the increase of the heat transfer coefficient of sample 3-1 mm is an average 15 % in average with respect to samples 5-1 and 3-5 mm smt.

Segmented samples, similar to the integrated samples, present an increase in heat transfer coefficient when they are tested with the largest pore size placed on the side where

the cooling gas enters. Figs. 9.12(a), 9.12(b) and 9.12(c) show the heat transfer coefficient of the samples when they are tested in the second position.

The sample with 1 and 5 mm pore size slices presents the largest improvement in the heat transfer coefficient when it is tested with the largest pore size on the side where the air enters Fig. 9.12(a), this increment is 34 % in average over the whole trial, while the sample with 3 and 5 mm pore size slices presents an increase of 30 % over the whole trial, Fig. 9.12(b). The sample with 1 and 3 mm pore size slices presents almost the same behaviour and it seems that the position in which the sample is tested does not have any influence in the heat transfer coefficient, Fig. 9.12(c).

9.4.2 PRESSURE DROP ACROSS SEGMENTED SAMPLES

The trials were carried out under the same conditions as for the thermal behaviour. Figs. 9.13(a) and 9.13(b) show the experimental pressure drop obtained for the segmented (smt) samples tested with the largest pore size placed on the side where the cooling air enters, and when the position of the sample was switched.

Figs. 9.13(a) and 9.13(b) show that as for other foam samples the pressure gradient increases when the air mass flow rate increases. The 1-3 mm smt sample presents the highest pressure gradient while the lowest is shown by the 3-5 mm smt sample. The gradient pressure of segmented samples does not present a significant change when their position is switched. The difference in pressure drop is 8 % between the 1-5 mm smt sample and the 1-3 smt sample. The 3-5 mm smt sample presents only 5 % difference. This can be observed in Fig. 9.14(a), 9.14(b) and 9.14(c).

1-5 mm smt and 1-3 mm smt samples show a 50 % reduction when their fluid flow behaviour is compared with those obtained for the integrated samples with the same pore sizes. The reduction in pressure drop in the 1-5 mm smt sample is accompanied by a lower heat transfer coefficient however, for the 1-3 mm smt sample the heat transfer coefficient remains similar when the sample is tested the two positions. The behaviour

of the sample 1-3 mm smt shows that the influence of the pore size is stronger than the density, as the 1-3 smt sample has 6.4 % lower density than the integrated sample and even though the segmented sample has lower density, it presents almost the same heat transfer. The sample with 3-5 mm pore size presented an increase of 70 % in pressure drop but the heat transfer decreases by 20 % with respect to the integrated sample. The 3-5 segmented sample has a density 7.6 % higher than integrated sample with the same pore size, again showing that integrated and segmented samples with multiple pore size are affected more strongly by the pore sizes present in pressure drop but not in heat transfer than single pore size.

9.4.3 PRESSURE DROP "BOW WAVE" EFFECT IN SEGMENTED SAMPLES

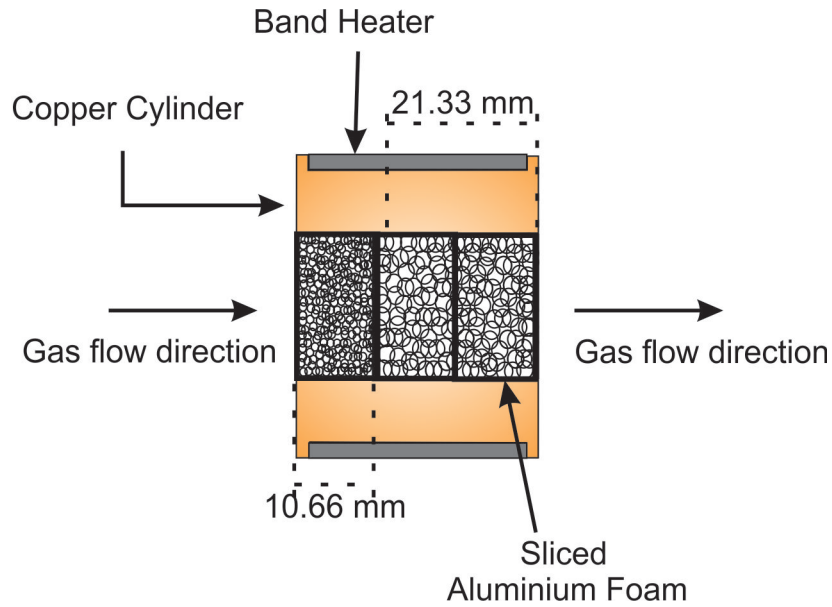
Figure 9.15 shows a segmented sample with 1 and 5 mm pore size. In the figure is possible to observe the structure when the slide with 1 mm pore meets the slide with 5 mm pore size. The magnified figure shows that there is a gap between the two slides and that the structure is different to the structure obtained when it is compared with a integrated sample, i. e. the 5 mm pore now is the window on which the fluid can flow through having more area to flow and therefore less restriction and lower pressure drop if it is compared with the integrated one.

Fig. 9.16 shows the diagram of the sample and the magnified view, as well as the representation of the pressure drop of the fluid when it is flowing through the sample when the biggest pore size is placed on the side where the air enters. It can be observed in the magnified diagram that the air flows through the pores and gap as well so therefore, the restriction to flow is lower than on integrated samples. The diagram shows that the pore now is the window to fluid so the area to fluid is bigger than in a integrated sample because in this case this window is around 5 mm while on integrated sample is around 2 mm.

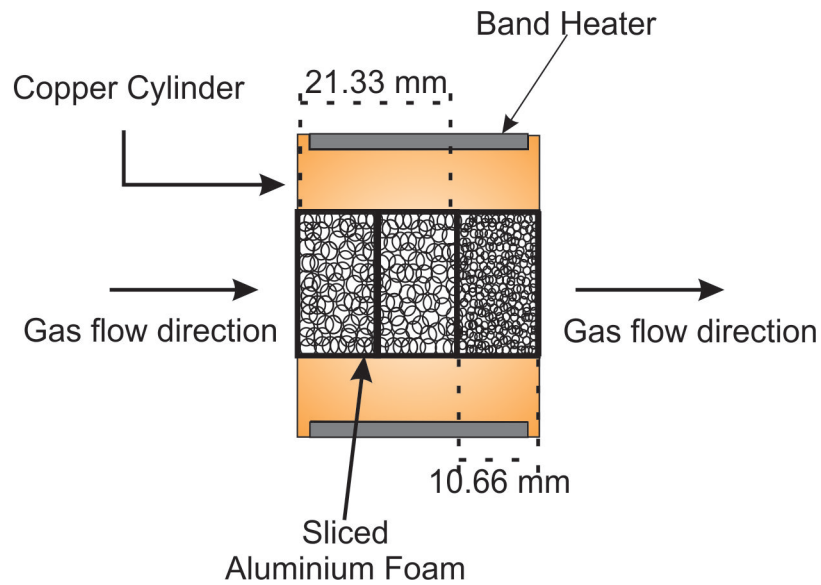
Figure 9.17 shows sample and zoom in diagram structure as well as the representation

of the pressure drop when the fluid is flowing through a segmented sample that is placed with the smaller pore size where the air enters. In this sample the restriction to fluid starts when the fluid goes through the small pore section and when the fluid leaves this section and goes to the section with the bigger pore size, there is no restriction in the border where the small and bigger pore size meets due to the big window to fluid and also for the gap between the slides. This can be observed in Fig. 9.17, therefore the pressure gradient are similar when the segmented samples is tested in the two positions, i. e.;

$$\Delta P_A \approx \Delta P_B \quad (9.2)$$

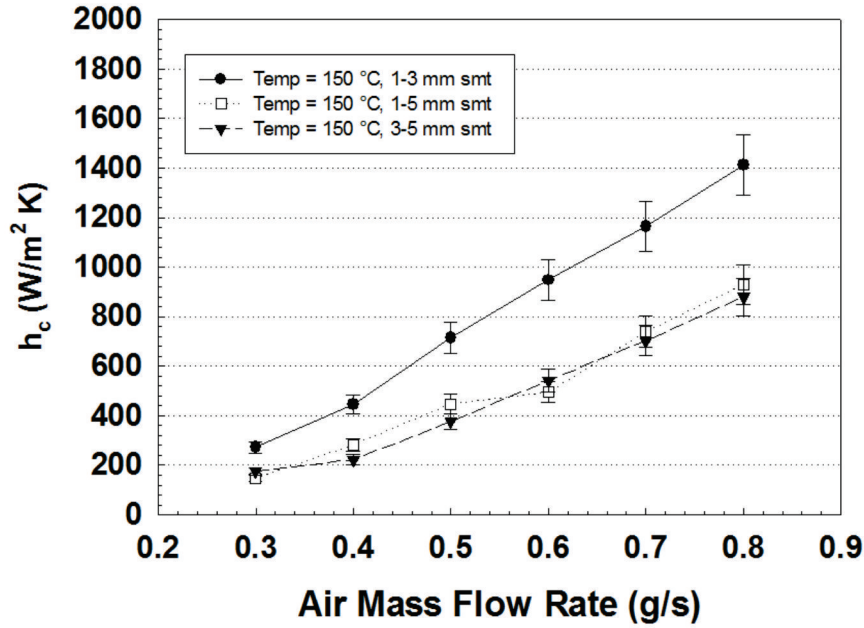


(a) Smallest pore size first.

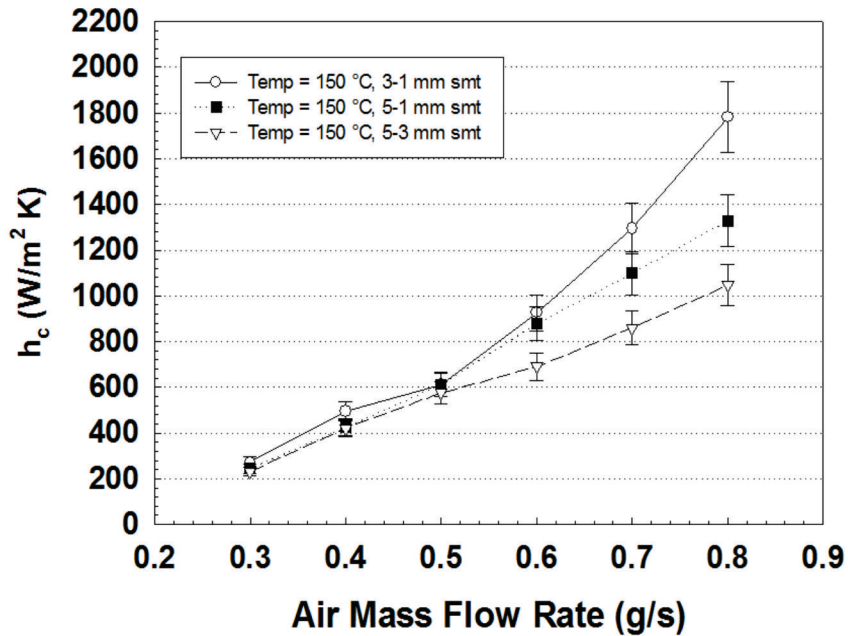


(b) Largest pore size first.

Figure 9.10: Position of the multiple pore size samples in the rig (a) Sliced sample placed with the smallest pore size in the side where the cooling gas enters and (b) sliced sample inverted so the largest pore size of the sample is placed where the cooling air enters.

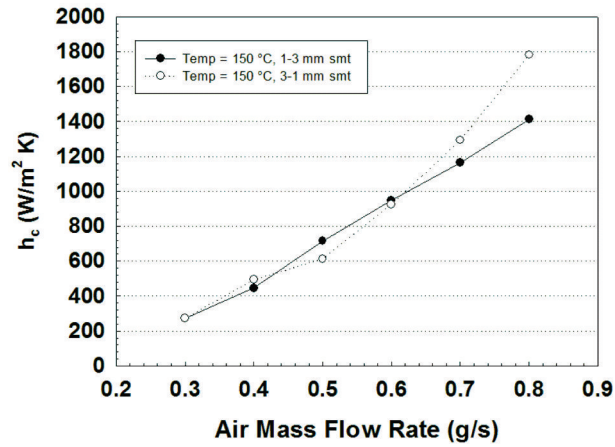


(a) Smallest pore first

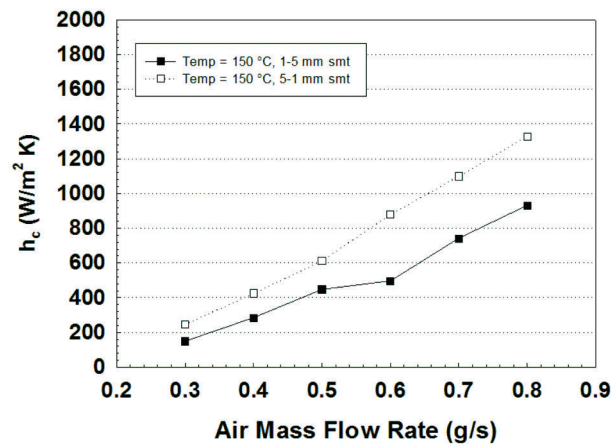


(b) Largest pore first

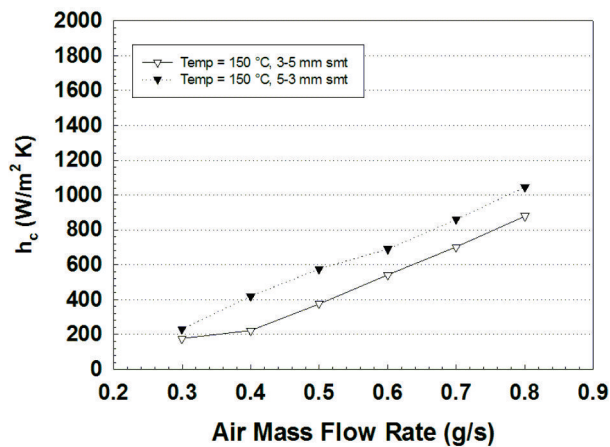
Figure 9.11: Heat transfer coefficient obtained at 150 °C with samples that were made up with slices to obtain the same overall structure as the integrated samples. (a) segmented samples placed in position where the smallest pore size was the first to receive the cooling gas and (b) samples switched so the largest pore is the first to receive the cooling gas.



(a) Sample with 1 and 3 mm pore size slices

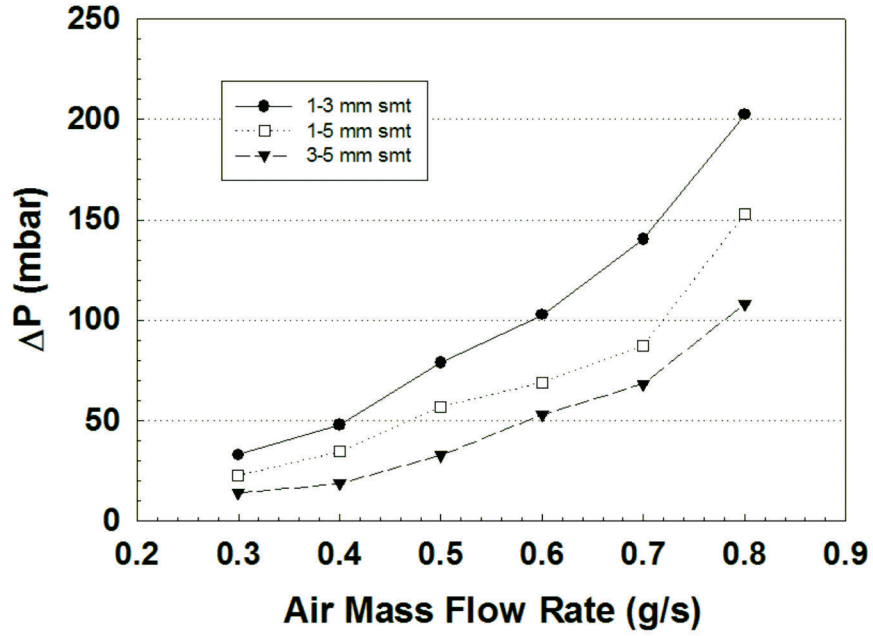


(b) Sample with 1 and 5 mm pore size slices

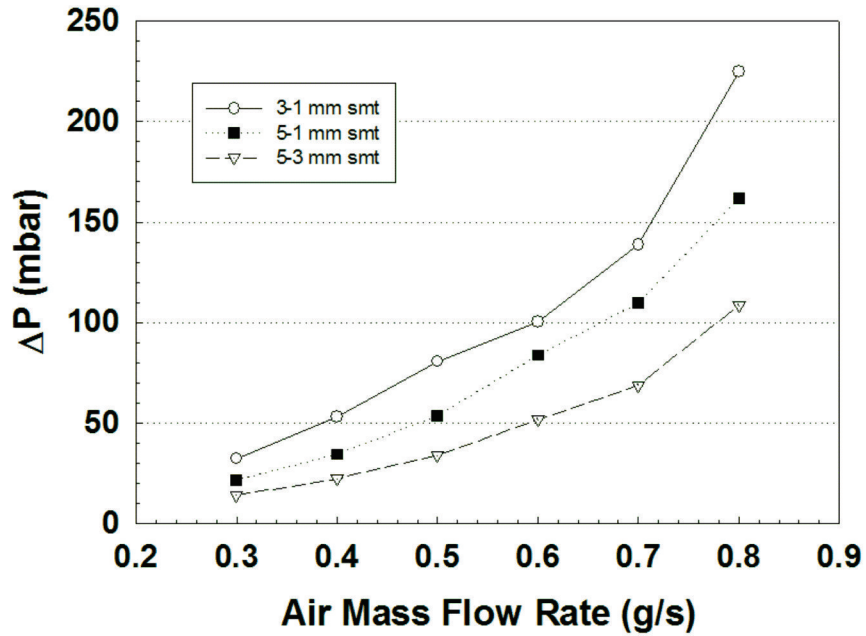


(c) Sample with 3 and 5 mm pore size slices

Figure 9.12: Heat transfer coefficient obtained at 150 °C with samples that were made up with slices to obtain the same overall structure as the integrated samples. (a) Sample with 1 and 3 mm pore size slices, (b) 1 and 5 mm pore size slices and (c) 3 and 5 mm pore size slices.

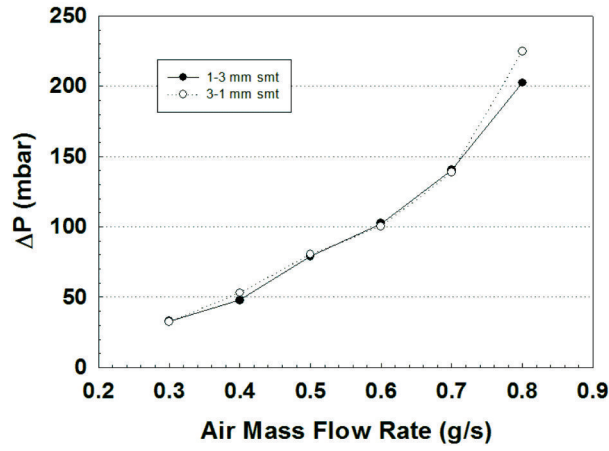


(a) Smallest pore size first

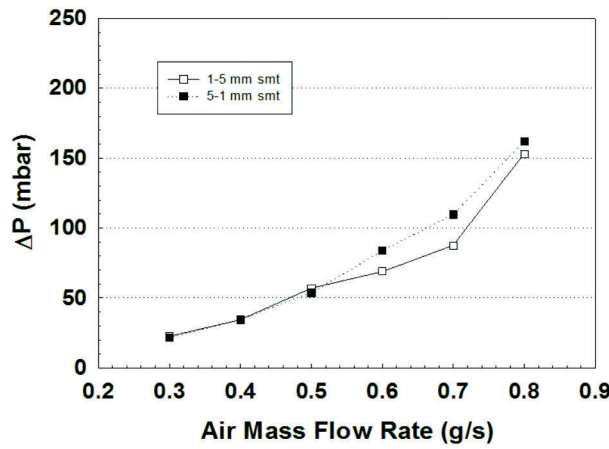


(b) Largest pore size first

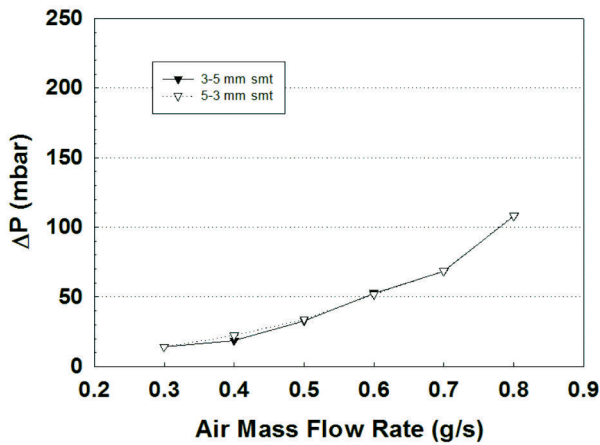
Figure 9.13: Pressure drop obtained with samples that were made up with slices to obtain the same overall structure as the integrated samples. (a) Segmented samples placed with the smallest pore size on the side where the cooling gas enters and (b) when the samples are inverted.



(a) Sample with 1 and 3 pore size slices



(b) Sample with 1 and 5 pore size slices



(c) Sample with 3 and 5 pore size slices

Figure 9.14: Pressure drop obtained by samples that were made up with slices to obtain the same overall structure as the integrated samples. (a) Sample with 1-5, (b) sample with 1-3 and (c) sample with 3-5 mm pore size.

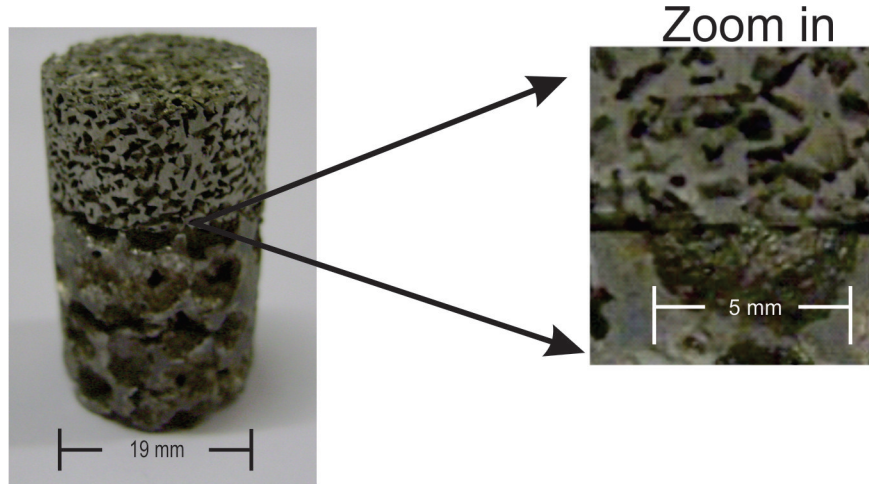


Figure 9.15: Structure obtained in the border when the small pore meets the larger one in a segmented sample.

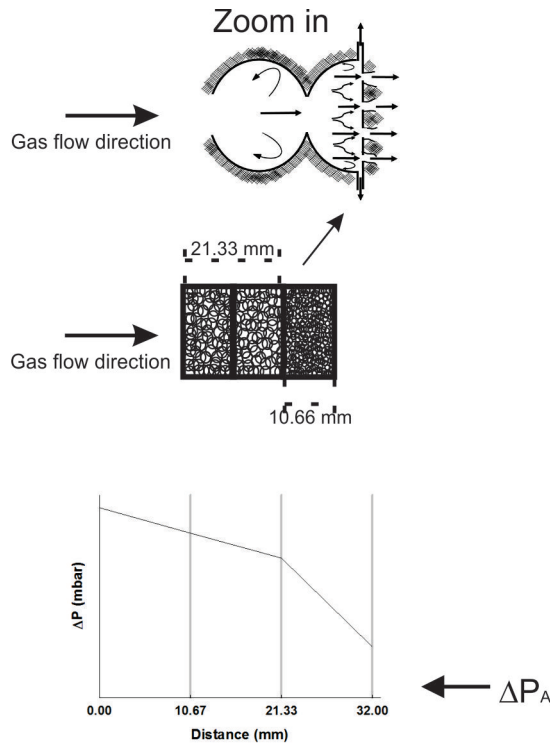


Figure 9.16: Metal foam diagram and graph showing the bow wave effect when a segmented sample is tested with the largest pore size in the side where the air enters.

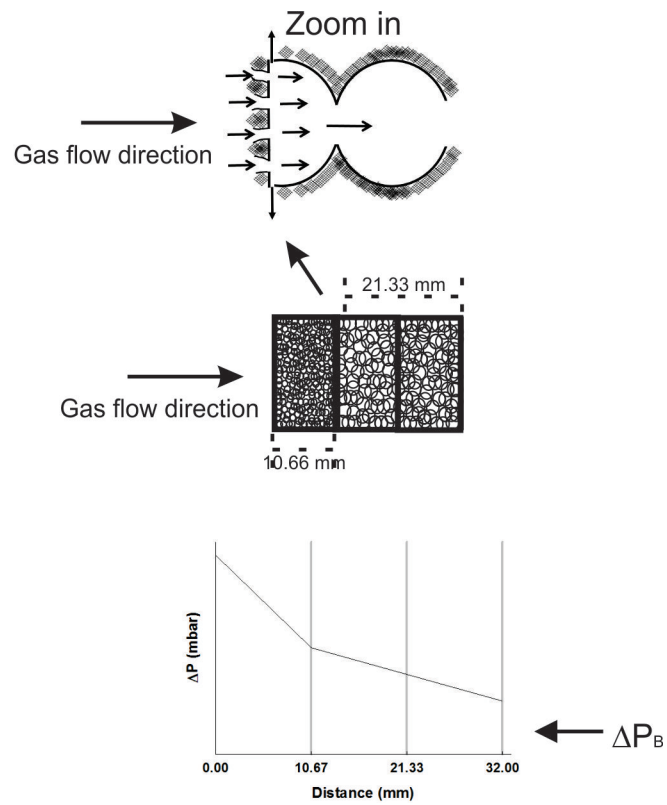


Figure 9.17: Metal foam diagram and graph showing the bow wave effect when a segmented sample is tested with the smallest pore size in the side where the air enters.

Chapter 10

Heat Exchangers Analysis and Comparisons

10.1 Nusselt number

To compare the rates of heat transfer by conduction and convection in the metal foam samples the Nusselt number was calculated and plotted as a function of the Reynolds number. The Nusselt number (Nu), Eq. 4.20, is defined by the ratio of the heat transfer coefficient (h_c) and the conductive heat transfer coefficient (between the fluid and solid) and was calculated from experimental data where the effective thermal conductivity, k_{eff} , was obtained using equations found to be effective for the relative conductivity (electrical in the previous study, but this should apply equally well to thermal properties) of the foam as a function of the pore volume fraction (Δ). The equation 4.6 specified by the *Lemlich model* is known to give a good fit for Duocel samples [108], therefore:

$$k_{eff} = k_{Al} \frac{(1 - \Delta)}{3} + k_{air} \Delta \quad (10.1)$$

where $k_{Al} = k_0$ from equation 4.6 and is the thermal conductivity of aluminium (237 W/mK), and k_{air} thermal conductivity of the air (0.0262 W/mK). For replicated samples (Corevo and in-house fabricated) equation 4.9 for spheres has the better fit [108] so, the effective thermal conductivity for these samples is obtained as follows:

$$k_{eff} = k_{Al}(1 - \Delta)^{1.5} + k_{air}\Delta \quad (10.2)$$

Nusselt number was plotted as a function of the Reynolds number and it (Reynolds number) was calculated according to Equation 4.22 as a function of the permeability as follows

$$Re = \frac{\rho\sqrt{K}}{\mu}v_f \quad (10.3)$$

where ρ is the air density at the mean temperature ($kg \cdot m^{-3}$), μ is the air dynamic viscosity ($kg \cdot m^{-1}s^{-1}$), v_f is the frontal velocity (ms^{-1}) and K is the permeability in (m^2) which is estimated using the method of Despois et al [117] with the following equation for samples with a pore volume fraction (Δ) larger than 0.64:

$$K = \frac{\Delta r^2}{\pi} \left[\frac{\Delta - \Delta_0}{3(1 - \Delta_0)} \right]^{3/2} \quad (10.4)$$

where Δ_0 is the initial packing density of the spherical particles ($\Delta_0 = 0.64$) and r is the average pore radius in the foam. For samples with a pore volume fraction lower than 0.64 the permeability was obtained with the following equation at low fluid velocities:

$$v_f = -\frac{K}{\mu} \frac{dP}{dx} \quad (10.5)$$

where dP is the difference of pressure ($mbar$) and dx is the sample length (0.032m).

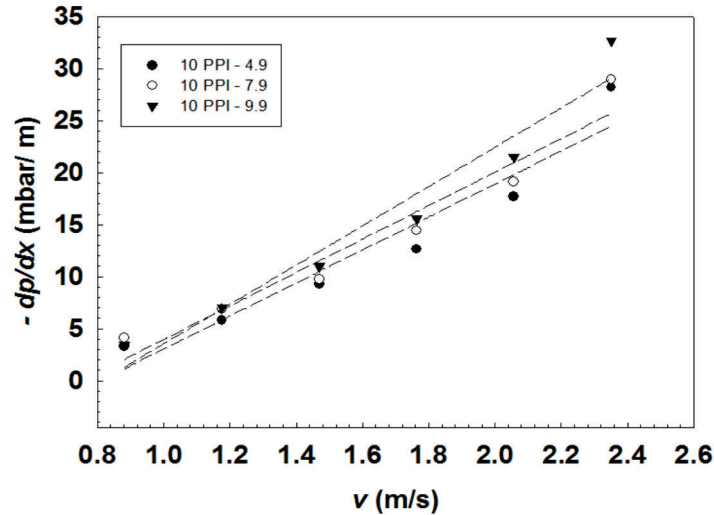


Figure 10.1: Pressure gradient ($-dp/dx$), measured on foams of 10 PPI with different densities as a function of the fluid velocity.

A plot of the measured flow rate versus pressure drop in 10 PPI samples with different densities is shown in Fig. 10.1. This plot is linear, showing that flow is indeed in the regime of validity of Darcy's law (flow entirely governed by viscous friction within the fluid [117]).

Figure 10.2 shows the Nusselt number as a function of the Reynolds number for Duocel samples with similar pore density but with different pore size. It can be seen that the Nusselt number increases as the Reynolds number increases and the pore size is decreased, meaning that the heat transfer in samples with lower pore size and high flow rate is governed by convection (interpreted as being the mixing of the fluid caused by the foam) rather than conduction. This shows that the foams are most effective when pore size is small and density is high, as found in earlier sections. Samples with the largest pore size show the highest Reynolds numbers and give lower restriction of the cooling air flow, resulting in lower heat extraction.

The Nusselt number for Duocel samples with 10 PPI pore size and different densities were evaluated. Fig 10.3 shows that the Nusselt number increases when the porosity increases. Values of Nusselt number presented by Duocel samples are over one, meaning

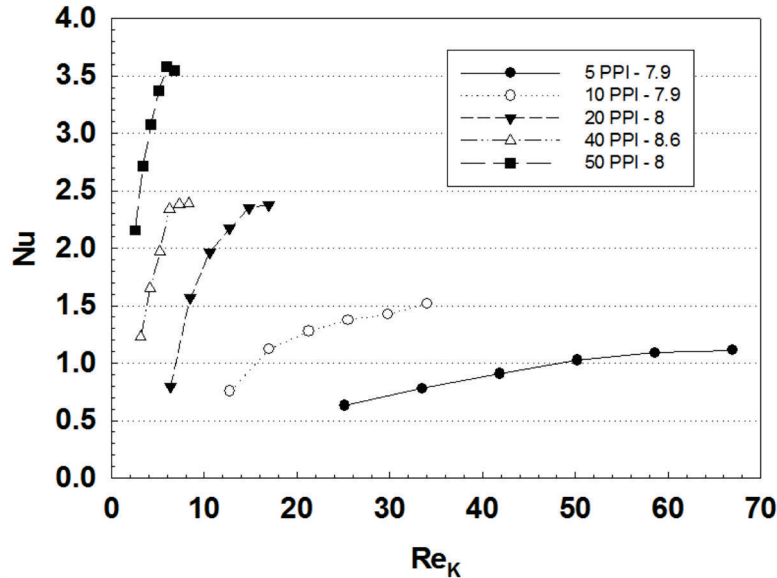


Figure 10.2: Nusselt number as a function of Reynolds number in Duocel samples with different pore size and similar density.

that under flow conditions characterised by these Reynolds numbers the heat transfer is predominantly by convection. Aluminium foam samples with 10, 20 and 40 PPI with different densities were evaluated by Hsieh et al [103], and the Nusselt number as a function of the Reynolds number shows similar behaviour as found with Duocel samples in this work.

Nusselt number as a function of Reynolds number for 5 mm pore size Corevo samples with different relative densities, shows that the Nusselt number increases when the Reynolds number and the density increase, Fig. 10.4. The Nusselt number obtained is however less than one, meaning that less fluid motion and mixing is taking place and the heat transfer is principally by conduction at the Reynolds numbers evaluated in this work. This is likely to be due to the higher density of these foams; the pore interconnections are fewer and smaller than Duocel, and this will limit mixing. The larger amount of metal will also promote the transport of heat into the liquid through foam conduction.

It was observed that Corevo samples with the highest pore density presented higher

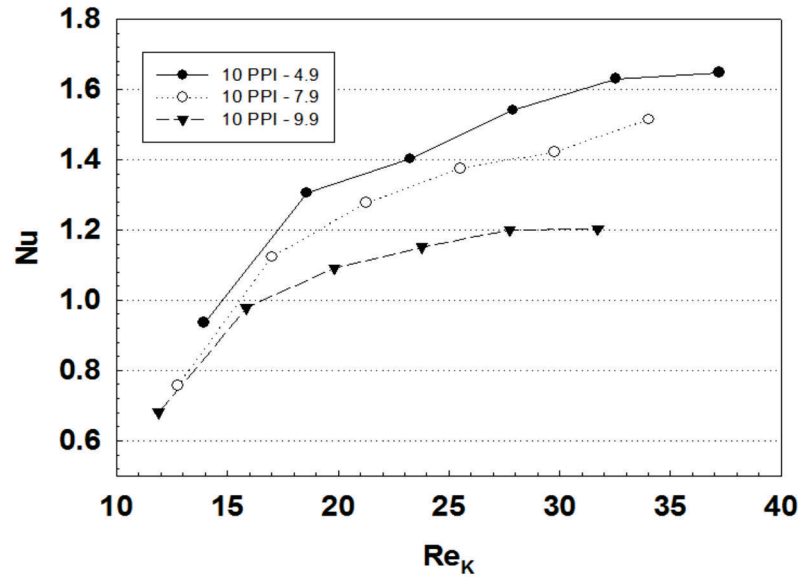


Figure 10.3: Nusselt number as a function of Reynolds number in Duocel samples with different density and 5 PPI pore size.

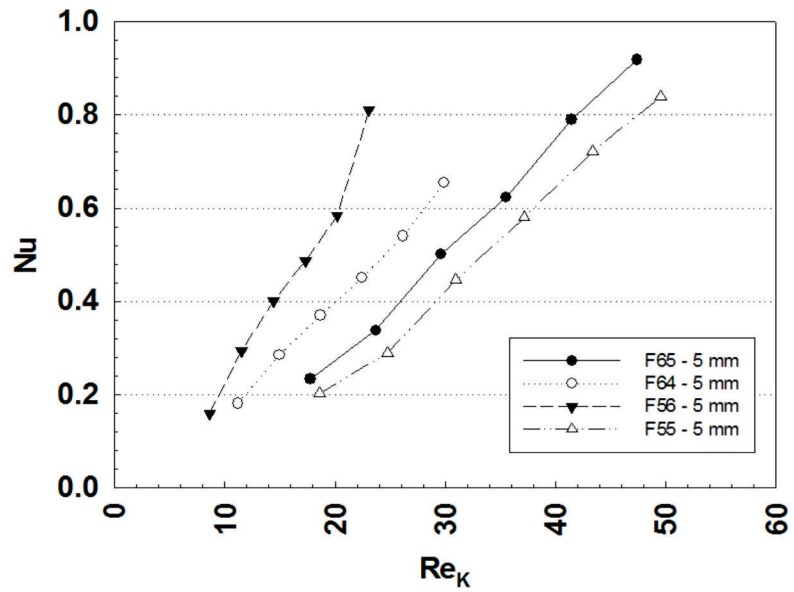


Figure 10.4: Nusselt number as a function of Reynolds number in Corevo samples with different density and 10 mm pore size.

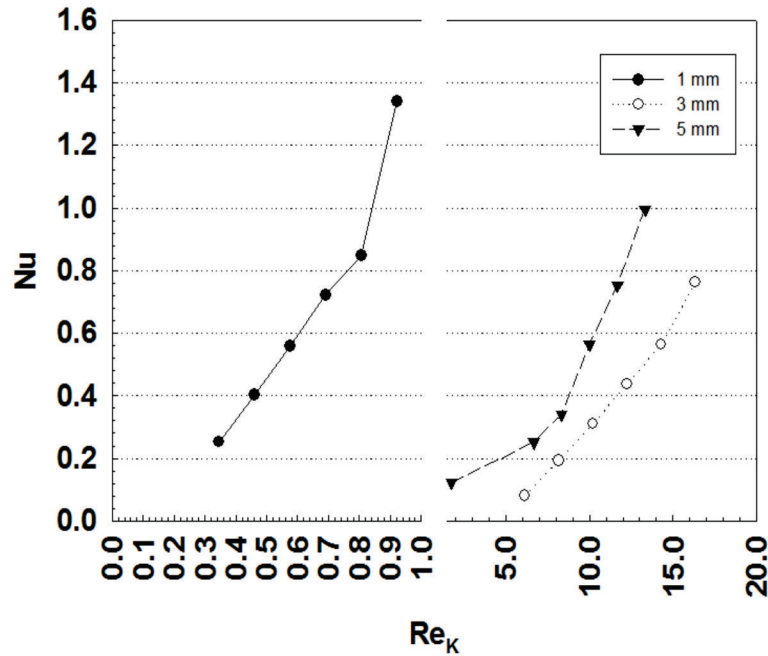


Figure 10.5: Nusselt number as a function of Reynolds number in in one pore size replicated samples.

Reynolds numbers that those with the highest relative density. F55 sample has the highest pore density and presents the largest measured pore size (see Table 8.3), therefore the permeability is higher. The above could explain this sample having the highest Reynolds number compared to other Corevo samples, however sample F65 presents smaller pore size than F56, which should increase the Reynolds number of this sample; it is possible that features within the foam structure are responsible for this difference.

Figure 10.5 shows the Nusselt number obtained with the experimental data for in-house fabricated replicated samples with a single pore size. The Nusselt number increases when the pore size decreases, the 5 mm pore size sample presents the largest porosity among the replicated samples (see Table 8.4) however, the highest Nusselt number was found for the 1 mm pore size sample, meaning that the Nusselt number is more influenced by the pore size than the relative density. Samples with 3 and 5 mm pore size showed a heat transfer governed by conduction while the sample with 1 mm pore size has behaviour dominated by convection under the Reynolds numbers evaluated.

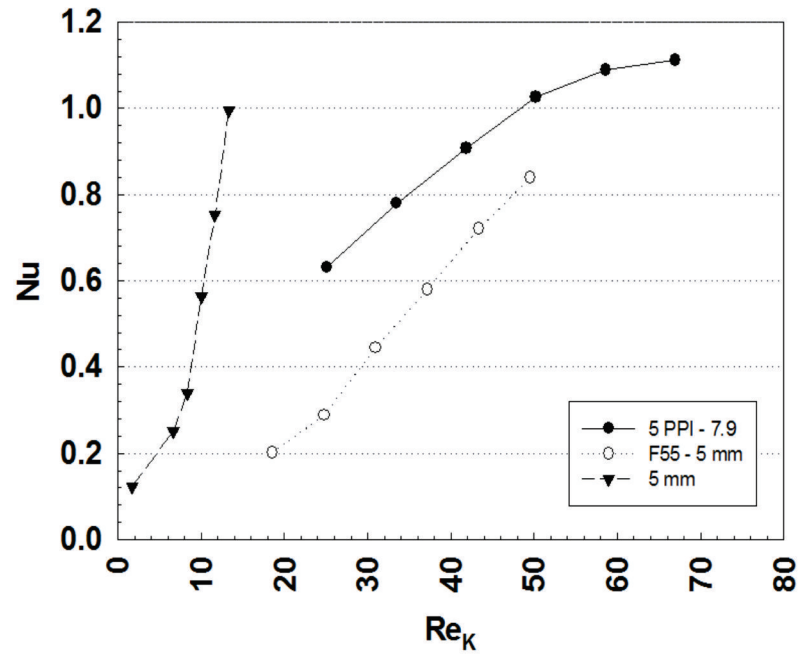


Figure 10.6: Nusselt number comparison as a function of Reynolds number between Duocel, Corevo and replicated samples with 5 mm pore size.

5 PPI - 7.9 Duocel ($\varepsilon = 0.92$), F55 - 5 mm Corevo ($\varepsilon = 0.84$) and replicated samples with 5 mm pore size ($\varepsilon = 0.68$) were compared in Fig. 10.6. The F55 Corevo sample was selected because presents the highest porosity of this sample type and is closest to the Duocel type of foams to aid comparison. The lowest permeability was presented by the replicated sample (represented by the lowest Reynolds number seen among these three samples) as would be expected given the much lower porosity; it appears that this structure does not allow free flow of the air and this reduces the heat extraction.

The Corevo sample presents higher permeability compared to the replicated sample, but nevertheless the heat transfer is still governed by conduction. The Duocel sample presents the highest permeability of all the samples and the heat transfer for the last three Reynolds numbers is dominated by convection. The pore size and the relative density presented by the Duocel sample seems to be favourable for convective heat transfer to allow the flow of the cooling air and permitting the mixing of air promoting heat transfer.

10.2 Comparison of experimental data with modelling

The heat transfer coefficients obtained (h_c) from the experimental data were compared against values obtained through the model developed by Mancin et al [125]. This Model is based in an analytical model suggested by Ghosh [135]. Using Microsoft Excel, equations suggested by Mancin et al [125] were calculated using experimental data for the porosity (ε), relative density, mean pore diameter, the fiber thickness and the area per unit volume. The model used (equations and nomenclature) to calculate the heat transfer coefficient is displayed in the Appendix.

The fiber thickness was calculated following part of the procedure suggested by Richardson et al [164] as follows; a picture of each of the samples was taken and then magnified by a factor of 10. The fiber thickness (taken as being the strut thickness) was measured in the image using a micrometer (Mitutoyo) and 35 measurements were performed on each of the samples then, the mean value of the 35 measurements of each sample was calculated. The fiber thickness values are reported in Table 10.1.

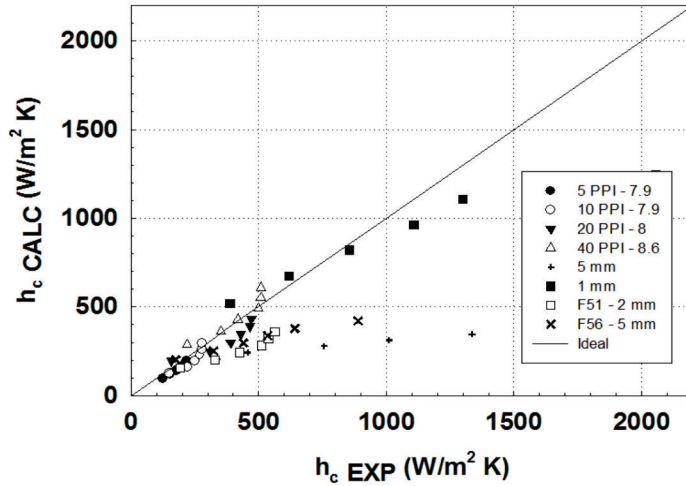
Table 10.1: Geometrical properties of samples compared with Mancin [125] model.

Sample	Fiber thickness (mm)	Area per unit volume (m^2/m^3)
5 PPI- 7.9	0.58	314
10 PPI- 7.9	0.57	748
20 PPI- 8	0.44	1220
40 PPI- 8.6	0.40	1811
F55	0.71	745
F65	0.83	737
F64	1.03	666
F56	0.91	639
F51	0.52	657
F36	0.66	488
1 mm (Replicated)	0.83	2883
3 mm (Replicated)	0.92	977
5 mm (Replicated)	1.94	603

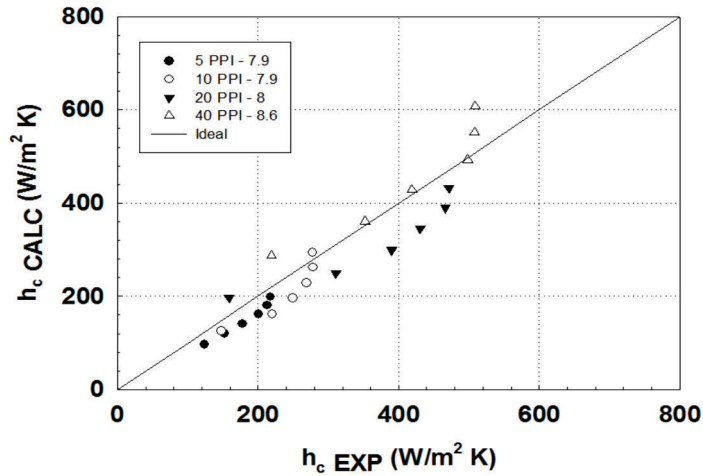
For Duocel samples the area per unit volume was obtained from data available on the

ERG Duocel webpage [91]. For Corevo and laboratory made replicated samples the area per unit volume was calculated using the relative density and the pore size of the samples assuming the pores were perfect spheres and neglecting interpore windows. The values are reported in Table 10.1.

The heat transfer coefficient was estimated using this model for Duocel, Corevo and replicated single pore size samples. Fig 10.7(a), shows the comparison between the calculated and experimental values obtained for Duocel samples with different pore size but similar densities, 1 and 5 mm replicated samples; and F51 - 2 mm and F56 - 5 mm Corevo samples. In the figure it is possible to observe that the heat transfer coefficient values calculated with the model are generally underestimated. The values obtained for Corevo and replicated samples were more than 35 % lower than the experimental results, with the exception of the 1 mm pore size replicated sample whose values had a good agreement, less than 20 % difference between the calculated and experimental heat transfer coefficient. The fact that better agreement is found with smaller pore sizes for the replicated samples may reflect the fact that in this materials the pores have the angular shape of salt grains, whereas for larger pore sizes and for Corevo foams the pore shape is spherical and cylindrical respectively, this will affect the calculation of the area per unit volume (m^2/m^3). With Duocel samples, the comparison of the majority of the data is satisfactory having a good fit between both values; the maximum error was presented by the 20 PPI - 8 sample where the experimental data differs by about 20 % from the prediction, the Fig. 10.7(b) shows only Duocel samples with a maximum scale of $800 W/m^2K$ for a better appreciation of the agreement between the calculated and experimental values.



(a) Duocel, Corevo and replicated samples



(b) Duocel samples

Figure 10.7: Comparison between experimental and calculated heat transfer coefficient (h_c). (a) Duocel, Corevo and replication technique samples, and (b) Duocel samples only.

10.3 Performance comparison and suggestions

Thermal and fluid flow behaviour for the Duocel, Corevo, replicated (both single pore size and graded) samples have been reported in detail in chapters 8 and 9. Figures 10.8(a) and 10.8(b) show the heat transfer coefficient and pressure drop for Duocel, Corevo and replicated with both single and graded pore-size samples. Even though in figures 10.8(a) and 10.8(b) samples with different pore size and density are plotted, it is possible to observe that Duocel presents the lowest heat transfer coefficients and the multiple pore size replicated samples the highest. This large difference between the heat transfer coefficient obtained among the samples cannot be attributed solely to the different thermal conductivity of the alloy from which the sample are made; replicated foams made in-house were fabricated with pure aluminium grade 99.7 % Al (~ 237 W/mK). Duocel samples are made with 6160 alloy (218 W/mK) and Corevo samples were fabricated with AS7G06 alloy (160 W/mK). The difference between the base metal thermal conductivity is about 9 % between Duocel and replicated, and 30 % between replicated and Corevo; while the difference in the heat transfer obtained with the replicated and Duocel samples is over 70% if a comparison between 5 PPI-7.9 Duocel, F55 - 5 mm Corevo and 5 mm replicated is made.

However, the pressure drop obtained with replicated samples (in both the cases of single and multiple pore sizes) are over 300 times larger than those presented by Duocel, meaning that the better performance between the foam samples evaluated is presented by Duocel, which has a better heat transfer-pressure drop ratio, i.e. in the 40 PPI - 8.6 Duocel sample (the sample which presents the largest pressure drop among Duocel samples) the ratio is 333 W/m² K mbar, while in the 3 mm pore size replicated sample which has the lowest pressure drop of its type is only 6.25 W/ m² K mbar.

A grid heat exchanger was also evaluated in the rig. This material was an aluminium alloy heat exchanger with a dimension of 1.2 cm width, 2.5 cm length and 0.025 cm thickness for each grill, Fig. 10.9(a). As seen in the Figure, each grill had a series

of cuts, with the metal deformed to make slots. The test was performed with 7 grills having density of 5.3 %, and a different copper cylinder was used with a hole of the same geometry as the heat exchanger, Fig. 10.9(b). The results obtained are shown in Figs 10.8(a) and 10.8(b) and show a heat transfer-pressure drop ratio of 400 W/m² mbar, having the best performance among the materials evaluated in this work at least for when maximum heat transfer for a minimum pressure drop is required. In the same figures, 10.8(a) and 10.8(b), the data obtained from the blank test is presented and shows that there is neither a measurable and significant pressure drop nor heat extraction so clearly the metal foams do have some benefit. The fact that the heat transfer coefficients are higher in these materials (albeit with higher pressure drop) means that there are some applications where they may be able to be used effectively.

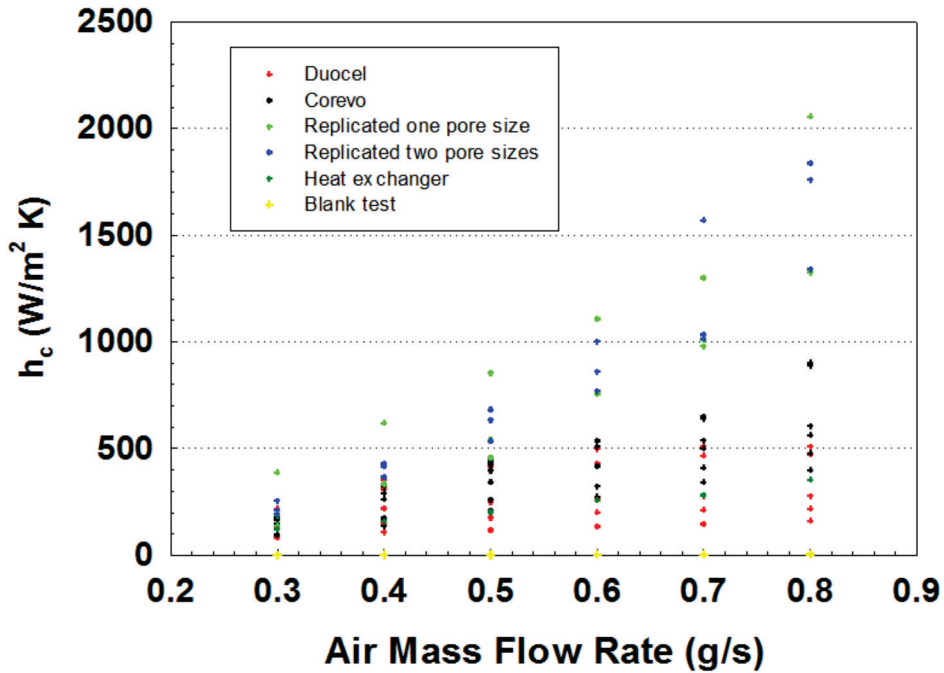
Chapters 8 and 9 show that there is an increment of the heat transfer and pressure drop when the foam density increases and pore size decreases in all the samples evaluated. When the relative density increases (with a constant pore size), the pore density decreases and therefore, there is more metal contained within the foam increasing the effective thermal conductivity (k_{eff}). The results obtained in Section 10.1 show that when the density increases the Nusselt number is near or lower than 1 meaning that the heat extraction occurs principally by conduction (Fig.10.3). At the same time the permeability decreases due to the thickness of the strut increasing and the size of the windows between the pores is reduced, generating bottlenecks where the resistance of the fluid to flow is encountered.

When the porosity increases with a constant relative density, the thickness of the struts decreases and according to Bhattacharya et al [113] the cross section of the struts changes from circular to triangular. This new triangular shape and the thickness induce more turbulent flow and also increase the surface area per unit volume, thereby increasing the heat transfer by convection in the aluminium foam. When the pore size decreases while the relative density is fixed, the fluid flow is more restricted when it is flowing through the metal foam and the permeability decreases [115]. Table 10.2

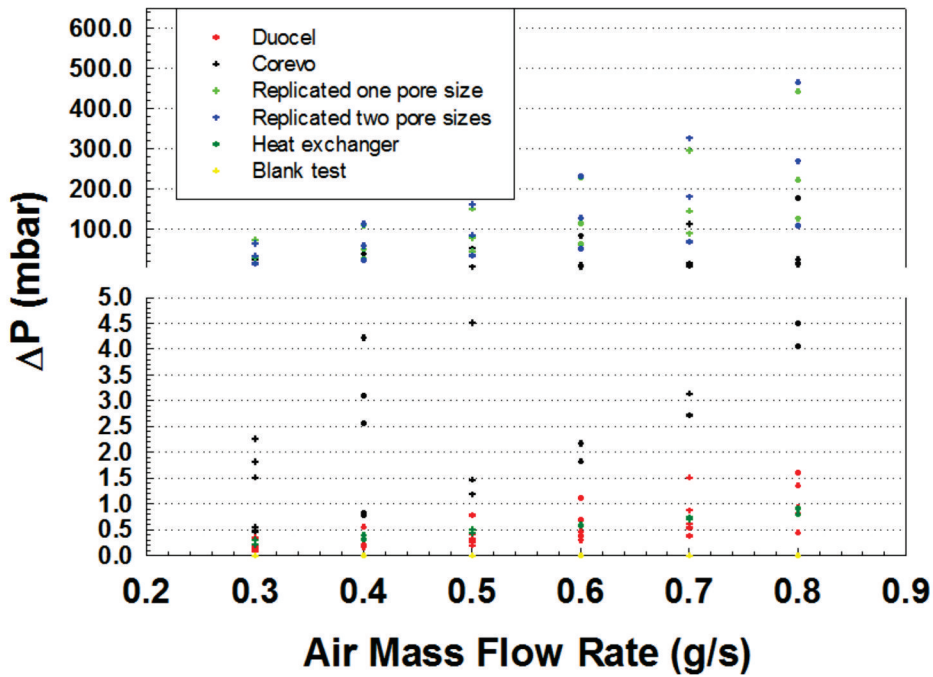
reports the pictures and diagrams of the strut geometry presented in the metal foams characterized in this work, as well as the effect on the heat transfer.

The range of fluid velocities encountered in real applications varies depending on the type of heat exchanger. For example, flow rates in electronic circuit board applications are typically from 0 to 2.5 m/s, air cooled condensers from 3 to 15 m/s, airborne from 4 to 60 m/s and air cooled heat exchangers from 0.18 to 4.5 m/s, among others [2, 13, 165–167]. Table 10.3 reports the applications and parameters when a metal foam is used as a heat exchanger. The evaluation of the metal foams in this work was carried out in the range from 0.88 to 2.35 m/s which is on the range of electronic circuit boards, where the use of cooling devices is recommended due to the large amounts of heat generated. From the results shown here, it can be stated that if the electronic device has a restriction on the pressure drop on the basis of the noise that is generated, as would be the case in personal computers, then the best option would be to use Duocel metal foams.

In electronic devices where such a restriction does not apply, for example in industrial environments or large scale computing servers the replicated and Corevo types of foam would be recommended. For graded replicated samples positioned such that the largest pore size is first to receive the cooling air, the results show that the metal foam has higher heat extraction with lower difference of pressure, suggesting that this behaviour could be fruitfully explored in the future heat exchanger design.



(a) Heat transfer coefficient



(b) Pressure drop

Figure 10.8: Comparison between Duocel (5 PPI- 7.9, 10 PPI - 7.9, 20 PPI - 8, 20 PPI - 8.6 and 40 PPI - 8.6), Corevo (F65 - 5 mm, F64 - 5 mm, F56 - 5 mm, F55 5 mm, F51 2 mm and F36 - 2mm), replicated single pore size (1, 3, and 5 mm) and replicated multiple pore sizes (3-1 mm, 5-1 mm and 5-3 mm) samples at different flow rates for (a) heat transfer coefficient (h_c) and (b) pressure drop (ΔP).

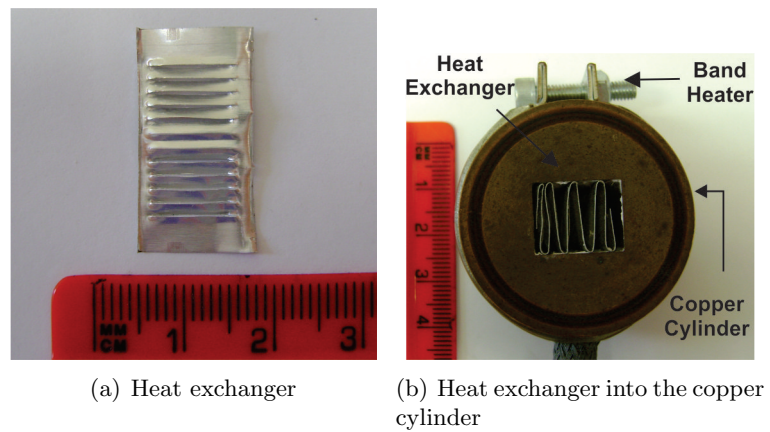


Figure 10.9: Heat exchanger tested on the rig, the scale is in cm. (a) One grid heat exchanger and (b) 7 grills of the heat exchanger into the copper cylinder (test section).

Table 10.2: Characteristics and strut shape effects in heat transfer of Duocel, Corevo and Replicated samples.

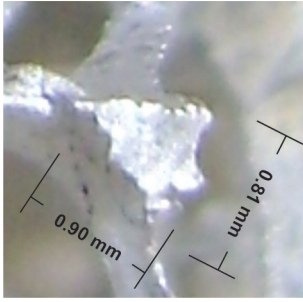
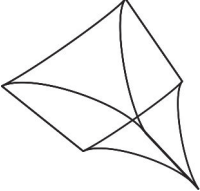
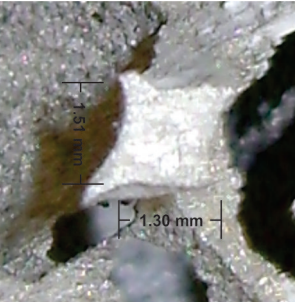
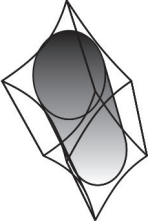
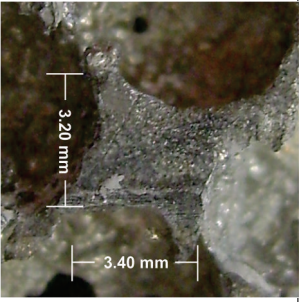
Sample	Image	Diagram of idealized structure	Shape effects
Duocel			<p>Triangular shape and thin thickness introduce more turbulent flow and also increase the surface area per unit volume, this geometry increases the heat transfer by convection in the aluminium foam. However the heat transfer depends on the solid structure, this triangular structure depends on density (low density) and production process (frequently investment casting), therefore the heat transfer coefficient is restricted by the solid in the strut [113, 118].</p>
Corevo			<p>Circular shape depends on the density and production process as triangular shape does, in this case the structure is obtained with large density and when it is fabricated by replicated technique. Circular geometry enhance the turbulence when the fluid is flowing through it and increase the heat transfer however, due to the high density in this kind of foams, the heat transfer is governed by conduction [113, 118].</p>
Replicated			

Table 10.3: Characteristics and strut shape effects in heat transfer of Duocel, Corevo and Replicated samples.

Flow Velocity (m/s)	Application	Typical h_c Wm^2K^{-1}	h_c	Typical ($mbar$)	ΔP	References
0 to 2.5	Electronic circuit	50-200		0.2-0.8		[2, 13, 65, 168]
3 to 15	Air cooled condensers	700-1000		3 - 12		[2, 13, 115, 166]
0.18 to 4.5	Air cooled heat exchanger	200-500		0.15-1.2		[2, 13, 167, 169]

Chapter 11

Conclusions and Further Work

11.1 Conclusions

In this work the replication process with paste was further developed and a bespoke test rig was designed, constructed and evaluated for the purpose of measuring the thermal and fluid flow behaviour of different aluminium foams. From the results obtained some conclusions can be drawn.

11.1.1 REPLICATION TECHNIQUE FOR FOAM MANUFACTURE

- Aluminium foams can be produced by the replication process with a preform fabricated with a mix of salt (NaCl), water (H₂O) and flour, with salt being the major component.
- A ternary diagram was produced as a guide in the manufacture of the preform.
- The composition with the best performance used in the manufacture of the preform of all samples made in this work was: 60 % salt, 25 % flour and 15 % H₂O by weight.
- To eliminate the water and flour from the preform a heat treatment is needed where the water is vaporized at 100 °C during 60 minutes and the flour is removed by pyrolyzation

at 500 °C during 60 minutes. The dissolution in water of the salt sphere obtained after the heat treatment took less than 15 sec.

- Pressure must be applied with an inert gas to the molten aluminium to infiltrate it into the preform. This pressure should not be higher than 2 bar to avoid infiltration of the aluminium into the preform.
- According with the results obtained from the Energy Dispersive X-Ray Spectroscopy from the Scanning Electron Microscope there is no presence of silicon in the aluminium of the foams that were fabricated by the replication technique and therefore no pick up from the quartz crucible in the method used.

11.1.2 TEST METHOD DEVELOPMENT

- A test rig was designed consisting of a copper test section in which the sample was placed, with steel chambers placed before and after. This test rig was assessed for homogeneity and to confirm reliability of the measurements.
- Measurements on the lateral and front faces at different depths on the copper cylinder show differences in all cases lower than 1 K, representing an error lower than 0.5 %.
- A trial with a dummy sample with low thermal conductivity (26.1 W/m K) shows that the rig has a high sensitivity even for low performing samples.
- The thermal resistance between the metal foam and the copper cylinder is strongly dominated by the join material used between them. A brazed joint is the best performing however, thermal paste is almost as effective and this was used due to the quicker nature of the test and the advantage to be able to test samples in a single copper cylinder.

11.1.3 HEAT TRANSFER AND PRESSURE DROP

- The test on 10 PPI - 9.9 Duocel sample at three different initial temperatures shows that the heat transfer coefficient does not depend on the initial heat temperature and that it increases when the air mass flow rate increases.
- The heat transfer coefficient calculated in Duocel samples with fixed pore size and different relative density shows that the heat transfer increases when the porosity decreases.
- Duocel samples with similar porosity show an increase in the heat transfer coefficient when the pore size decreases. Among Duocel samples tested, the sample with 50 PPI presents the largest heat transfer coefficient in all air flow rates.
- In Duocel samples with the same pore size but different relative density the pressure drop (ΔP) increases when the pore density and the flow rate increase.
- The 50 PPI - 8 sample has the highest heat transfer coefficient and pressure drop among Duocel samples being an example of the trade off seen between these two properties.
- 5 and 2 mm pore size Corevo samples show that the heat transfer and the pressure drop increase when the relative density increases at a fixed pore size. F56 - 5 mm and F36 - 2 mm samples with the largest relative density showed the highest heat transfer and pressure drop between samples with the same pore size.
- F56 - 5 mm sample presented the largest pressure drop and heat transfer coefficient among Corevo samples. If a comparison is made between this sample and the Duocel sample 50 PPI - 8, then the Corevo sample showed 1.2 times larger heat transfer coefficient but with 4.5 times larger pressure drop.
- Replicated samples made in the laboratory showed the same behaviour as Duocel and Corevo samples, the heat transfer and pressure drop increase when the density increases and the pore size decreases.

- Heat transfer coefficient and pressure drop depend strongly on the pore size and relative density suggesting that mixing of the air is found when the pore size decrease and the porosity decrease. This best air mix also generates a flow resistance when the air is flowing through the aluminium foam.
- The largest flow resistance (larger pressure drop) is obtained when the pore size is reduced and the relative density is increased.
- Nusselt number calculation shows that the heat transfer in Duocel samples is governed by convection while in Corevo and laboratory made replicated samples with a single pore size is principally by conduction, and that the Nusselt number increases when the flow rate increase.
- Integrated graded samples show asymmetric thermal and fluid flow behaviour, presenting larger heat transfer coefficient and slightly lower pressure drop when the largest pore size is placed on the side where the cooling air enters.
- Segmented samples show asymmetric thermal behaviour, however the pressure drop does not change.
- Duocel experimental and calculated heat transfer coefficient have good agreement. However, Corevo and replicated samples did not show this good fit, suggesting that the model has to be modified to obtain a better fit in the heat transfer coefficient with metal foams obtained by replication technique (of which both Corevo and the in-house made foams are examples).
- The asymmetric behaviour is attributed to the increased resistance to fluid flow of the smaller pore size foam, slowing the fluid and allowing greater heat exchange to take place in the large pore size.
- Differences in the pressure drop between integrated and segmented samples are possibly due to asymmetry in flow through the structures formed in integrated samples.
- Duocel samples presented the best heat transfer - pressure drop ratio being a suitable

choice for electronic devices with noise restriction. Where there is not this limitation, Corevo and Replicated material can be used.

11.2 Further work

Improvements in the preform manufacturing process could be investigated in order to reduce the time required to obtain the final preform of pyrolised salt only. this would be an important development for industrial processing. Larger containers and molds or manufacturing using food machines could be used to produce a larger quantity of dough and give the desired shape in an easier way, and also allow production of larger samples which could be cast in larger rig. The time for the heat treatment could be reduced particularly in the final step, at 500 °C, when the greatest thickness of the preform is less than 5 mm. This could reduce the time and increase the preform resistance.

The flexibility presented by the paste obtained by mixing the constituents (NaCl, flour and water) is an important advantage in the manufacture of the preform which can be therefore used to fabricate any shape desired for example: squares, triangles, cylinders etc. with sizes lower than 10 mm and higher than 2 mm. Once the preform with the size and shape desired is obtained, aluminium foam can be fabricated with different pore sizes and shapes in a single sample to further characterize its thermal and fluid flow behaviour as well as other properties of interest, such as mechanical properties.

The results obtained in graded and segmented samples suggest that this behaviour can be used to improve the performance in heat exchangers, trying to obtain higher heat transfer coefficients with minimal pressure drop. Integrated samples with the lowest pore size being the largest proportion in the samples are to be for further investigations. If this was to be done segmented samples should also be fabricated to compare the thermal and fluid flow characteristics with integrated ones.

Tube heat exchangers could be fabricated by the replication technique using the type of preform studied in this work and casting the molten aluminium directly into and

around outside, producing the foam and tube in an integrated form in a single operation. These components could then be characterized for the thermal, mechanical and fluid flow properties to be compared with the ones obtained with tube heat exchangers that have been fabricated by inserting an aluminium foam core in the centre of a tube. It would be that the lower thermal resistance in an integrated sample would give better properties.

Bibliography

- [1] V. Gergely and B. Clyne. The FORMGRIP Process : Foaming of Reinforced Metals by Gas Release in Precursors. *Advanced Engineering Materials*, pages 175–178, 2000.
- [2] M.F. Ashby, A.G. Evans, N.A. Fleck, L.J. Gibson, J.W. Hutchinson and H.N.G. Wadley. *Metal Foams: A Design Guide*. Elsevier, 2000.
- [3] J. Banhart. Manufacture, characterisation and application of cellular metals and metal foams. *Progress in Materials Science*, 46(6):559–632, January 2001.
- [4] H.N.G. Wadley. Cellular Metals Manufacturing. *Advanced Engineering Materials*, 4(10):726–733, October 2002.
- [5] Q. Tian and X. Guo. Electroless copper plating on microcellular polyurethane foam. *Transactions of Nonferrous Metals Society of China*, 20:283–287, May 2010.
- [6] O Olurin. Strength and ductility of as-plated and sintered CVD nickel foams. *Composites Science and Technology*, 63(16):2317–2329, December 2003.
- [7] D. Queheillalt, D. Hass, D. Sypeck, and H. Wadley. Synthesis of open-cell metal foams by templated directed vapor deposition. *Materials Research*, 16(4):1028–1036, 2001.
- [8] V. Paserin, S. Marcuson, J. Shu, and D. Wilkinson. The chemical vapor deposition technique for Inco nickel foam production manufacturing benefits and potential

- applications. Technical report, Inco Technical Services Limited and McMaster University, Ontario, Canada, 2003.
- [9] F. Bidault, D.J.L. Brett, P.H. Middleton, N. Abson, and N.P. Brandon. A new application for nickel foam in alkaline fuel cells. *International Journal of Hydrogen Energy*, 34(16):6799–6808, August 2009.
- [10] V.A. Ettl, J. Babjak and V. Paserin. No 4957543, 1990.
- [11] B. Jiang, N.Q. Zhao, C.S. Shi, X.W. Du, J.J Li, and H.C Man. A novel method for making open cell aluminum foams by powder sintering process. *Materials Letters*, 59(26):3333–3336, November 2005.
- [12] M. Jackel, German Patent 3 210 770, 1982.
- [13] D. Hans-Peter and B. Kriszt. *Handbook of Cellular Metals: Production, Processing, Applications*. Wiley-VCH Verlag GmbH & Co. KGaA, 2002.
- [14] A. Evans, J. Hutchinson, and M. Ashby. Cellular metals. *Solid state and Materials Science*, (3):288 – 303, 1998.
- [15] K. Stöbener and G. Rausch. Aluminium foampolymer composites: processing and characteristics. *Journal of Materials Science*, 44(6):1506–1511, August 2008.
- [16] SmarslyW, Track W. German Patent 3 902 032, 1990.
- [17] L. B. Torobin, US Patent 4 671 909, 1987.
- [18] Y Y Zhao and D X Sun. A novel sintering-dissolution process for manufacturing Al foams. *Scripta Materialia*, 44(1):105–110, 2001.
- [19] Y.Y. Zhao, T. Fung, L.P. Zhang, and F.L. Zhang. Lost carbonate sintering process for manufacturing metal foams. *Scripta Materialia*, 52(4):295–298, February 2005.

- [20] A. Mansourighasri, N. Muhamad, and A.B. Sulong. Processing titanium foams using tapioca starch as a space holder. *Journal of Materials Processing Technology*, 212(1):83–89, January 2012.
- [21] A. Jinnapat and A.R. Kennedy. The manufacture of spherical salt beads and their use as dissolvable templates for the production of cellular solids via a powder metallurgy route. *Journal of Alloys and Compounds*, 499(1):43–47, June 2010.
- [22] A. Bansiddhi and D C Dunand. Shape-memory NiTi foams produced by replication of NaCl space-holders. *Acta biomaterialia*, 4(6):1996–2007, November 2008.
- [23] T. Fiedler, A. Öchsner, I. V. Belova, and G. E. Murch. Recent Advances in the Prediction of the Thermal Properties of Syntactic Metallic Hollow Sphere Structures. *Advanced Engineering Materials*, 10(4):361–365, April 2008.
- [24] G. J. Davies and S. Zhen. Metallic foams: their production, properties and applications. *Journal of Materials Science*, 18(7):1899–1911, July 1983.
- [25] R. Surace, L. A. C. De Filippis, E. Niini, A. D. Ludovico, and J. Orkas. Morphological Investigation of Foamed Aluminum Parts Produced by Melt Gas Injection. *Research Letters in Materials Science*, 2009:1–9, 2009.
- [26] De Filippis, R. Surace, S. Bruno, and A. D. Ludovico. Multi-Objective optimization of aluminium foam manufacturing parameters. *International Journal of Simulation Modelling*, 8:81–89, 2009.
- [27] S. W. IP, Y. Wang, and J.M. Toguri. Aluminum foam stabilization by solid particles. *Canadian Metallurgical Quarterly*, 38:70–81, 1999.
- [28] W. Deqing and S. Ziyuan. Effect of ceramic particles on cell size and wall thickness of aluminum foam. *Materials Science and Engineering*, 361(1-2):45–49, November 2003.
- [29] D Leitlmeier, H P Degischer, and N Babcsa. Foamability of Particle Reinforced Aluminum Melt. *Materials Science and Engineering Technology*, 29:22–29, 2003.

- [30] T. Miyoshi, M. Itoh, and S. Akiyama. ALPORAS Aluminum Foam : Production Process , Properties , and Applications. *Advanced Engineering Materials*, 0071(4):179–183, 2000.
- [31] N. Babcsán and J. Banhart. Metal foams towards high-temperature colloid chemistry. Technical report, Technical University Berlin, Institute of Materials Science and Technology, Berlin, 2006.
- [32] B. Matijasevic-Lux, J. Banhart, S. Fiechter, O. Görke, and N. Wanderka. Modification of titanium hydride for improved aluminium foam manufacture. *Acta Materialia*, 54(7):1887–1900, April 2006.
- [33] J. Banhart. Manufacturing Routes for Metallic Foams. *Journal of the Minerals, Metals and Materials Society*, pages 22–27, 2000.
- [34] Patent No. 1566284, ALPORAS, 1987, Sound absorbing materials, Shinko Wire Co., Ltd., 2 July of 2009.
- [35] V Gergely, D C Curran, and T W Clyne. The FOAMCARP process : foaming of aluminium MMCs by the chalk-aluminium reaction in precursors. *Composites Science and Technology*, 63:2301–2310, 2003.
- [36] V. Gergely, D. C. Curran, and T. W. Clyne. Advances in the melt route production of close cell aluminium foams using gas-generating agents. In *TMS annual meeting*, number February, 2002.
- [37] L. Aguirre-Perales, I. Jung, and R. Drew. Foaming behavior of powder metallurgical AlSn foams. *Acta Materialia*, 60(2):759–769, January 2012.
- [38] A R Kennedy. Effect of compaction density on foamability of Al TiH₂ powder compacts. *Powder Metallurgy*, 45:75–79, 2002.
- [39] B.H. Smith, S. Szyniszewski, J.F. Hajjar, B.W. Schafer, and S.R. Arwade. Steel foam for structures: A review of applications, manufacturing and material properties. *Journal of Constructional Steel Research*, December 2011.

- [40] G. Zu, B. Song, Z. Guan, L. Wang, and G. Yao. Preparation of aluminum foam sandwich by rolling-bonding/powder metallurgy foaming technology. *Journal of Wuhan University of Technology-Mater. Sci. Ed.*, 26(4):671–674, July 2011.
- [41] S. Asavavisithchai and A.R. Kennedy. The effect of oxides in various aluminium powders on foamability. *Procedia Engineering*, 32:714–721, January 2012.
- [42] F. Baumgärtner, I. Duarte, and J. Banhart. Industrialization of Powder Compact Foaming Process. *Advanced Engineering Materials*, (03):168–174, 2000.
- [43] A.R. Kennedy and S. Asavavisithchai. Effect of Ceramic Particle Additions on Foam Expansion and Stability in Compacted Al-TiH₂ Powder Precursors. *Advanced Engineering Materials*, 6(6):400–402, June 2004.
- [44] V. Shapovalov and L. Boyko. GasarA new Class of Porous Materials. *Advanced Engineering Materials*, 6(6):407–410, June 2004.
- [45] L. Wang, H. Li, F. Wang, and J. Ren. Preparation of open-cell metal foams by investment cast. *China Academic Journal Electronic Publishing House*, 2(1):56–59, 2005.
- [46] K Boomsma. Metal foams as compact high performance heat exchangers. *Mechanics of Materials*, 35(12):1161–1176, December 2003.
- [47] K. Boomsma and D. Poulikakos. The Effects of Compression and Pore Size Variations on the Liquid Flow Characteristics in Metal Foams. *Journal of Fluids Engineering*, 124(1):263, 2002.
- [48] C.Y. Zhao. Review on thermal transport in high porosity cellular metal foams with open cells. *International Journal of Heat and Mass Transfer*, 55(13-14):3618–3632, June 2012.
- [49] L. Jin and K. Leong. Heat Transfer Performance of Metal Foam Heat Sinks Subjected to Oscillating Flow. *IEEE Transactions on Components and Packaging Technologies*, 29(4):856–863, December 2006.

- [50] H. Mahdi, P. Lopez, A. Fuentes, and R. Jones. Thermal performance of aluminium-foam CPU heat exchangers. *International Journal of Energy Research*, 30(11):851–860, September 2006.
- [51] W. H. Shih, W. H., Chiu, W. C., Hsieh. Height effect on heat-transfer characteristics of aluminium-foam heat sinks. *Heat Transfer Transactions of the ASME*, 128(6):530–537, 2006.
- [52] T Daxner, F G Rammerstorfer, and H J Bo. Adaptation of density distributions for optimising aluminium foam structures. *Material Science and Technology*, 16:935–939, 2000.
- [53] A. H. Brothers and D. C. Dunand. Density-Graded Cellular Aluminum. *Advanced Engineering Materials*, 8(9):805–809, September 2006.
- [54] A. Rabiei and A.T. O'Neill. A study on processing of a composite metal foam via casting. *Materials Science and Engineering: A*, 404(1-2):159–164, September 2005.
- [55] L. Vendra and A. Rabiei. A study on aluminumsteel composite metal foam processed by casting. *Materials Science and Engineering: A*, 465(1-2):59–67, September 2007.
- [56] C. Gaillard, J.F. Despois, and A. Mortensen. Processing of NaCl powders of controlled size and shape for the microstructural tailoring of aluminium foams. *Materials Science and Engineering: A*, 374(1-2):250–262, June 2004.
- [57] R. Jamshidi-Alashti and G. Roudini. Producing replicated open-cell aluminum foams by a novel method of melt squeezing procedure. *Materials Letters*, 76:233–236, June 2012.
- [58] R. Goodall and A. Mortensen. Microcellular Aluminium? Child’s Play! *Advanced Engineering Materials*, 9(11):951–954, November 2007.

- [59] Y. Conde, J.-F. Despois, R. Goodall, A. Marmottant, L. Salvo, C. San Marchi, and A. Mortensen. Replication Processing of Highly Porous Materials. *Advanced Engineering Materials*, 8(9):795–803, September 2006.
- [60] J Despois, A Marmottant, L Salvo, and A Mortensen. Influence of the infiltration pressure on the structure and properties of replicated aluminium foams. *Materials Science and Engineering: A*, 462(1-2):68–75, July 2007.
- [61] R. Goodall, J. Despois, A. Marmottant, L. Salvo, and A. Mortensen. The effect of preform processing on replicated aluminium foam structure and mechanical properties. *Scripta Materialia*, 54(12):2069–2073, June 2006.
- [62] M. Young, J. DeFouw, J. Frenzel, and D. Dunand. Cast-Replicated NiTiCu Foams with Superelastic Properties. *Metallurgical and Materials Transactions A*, 43(August):2939–2944, February 2012.
- [63] A Bansiddhi, T D Sargeant, S I Stupp, and D C Dunand. Porous NiTi for bone implants: a review. *Acta biomaterialia*, 4(4):773–82, July 2008.
- [64] J. Banhart. Aluminium Foams: On the Road to Real Application. *Materials Research Society*, (Bulletin):290–295, 2003.
- [65] R. L. Bhattacharya, Mahajan. Finned Metal Foam Heat Sinks for Electronics Cooling in Forced Convection. *Journal of Electronic Packaging*, 124(3):155–163, 2002.
- [66] J Baumeister, J Banhart, and M Weber. Aluminium foams for transport industry. *Materials and Design*, 18(4-6):217–220, December 1997.
- [67] J. Banhart. Aluminium foams for lighter vehicles. *International Journal of Vehicle Design*, 37(2/3):114 – 125, 2005.
- [68] S. Nesic, P. Schäffler, K. Unruh, W. Michels, and U. Krupp. Analysis of Cellular Metals as Energy-Absorbing Elements in Car Seats. *Advanced Engineering Materials*, 13(11):1056–1059, November 2011.

- [69] H Kavi, A Toksoy, and M Guden. Predicting energy absorption in a foam-filled thin-walled aluminum tube based on experimentally determined strengthening coefficient. *Materials & Design*, 27(4):263–269, 2006.
- [70] J. Banhart and J. Baumeister. Deformation characteristics of metal foams. *Journal of Materials Science*, 33:1431–1440, 1998.
- [71] C. Zhang, Y. Feng, and X. Zhang. Mechanical properties and energy absorption properties of aluminum foam-filled square tubes. *Transactions of Nonferrous Metals Society of China*, 20(8):1380–1386, August 2010.
- [72] I.W Hall, M Guden, and T.D Claar. Transverse and longitudinal crushing of aluminum-foam filled tubes. *Scripta Materialia*, 46(7):513–518, April 2002.
- [73] H Mata, R Natal Jorge, A A Fernandes, R A F Valente, and M P L Parente. FEM analysis of Sandwich Shells with Metallic Foam Cores. *Computational Mechanics*, pages 4–5, 2010.
- [74] Aluminium foam technology applied to automotive design. Technical report, Cymat Technologies Ltd., Ontario, Canada.
- [75] [http: www.metcomb.com](http://www.metcomb.com).
- [76] F. Simancik and W. Rajner. Alulight - Aluminum Foam for Lightweight Construction. Technical report, SAE 2000 World Congress, Detroit, Michigan, 2000.
- [77] C. Cingi, E. Niini, and J. Orkas. Foamed aluminum parts by investment casting. *Colloids and Surfaces A: Physicochemical and Engineering Aspects*, 344(1-3):113–117, July 2009.
- [78] D Leitlmeier, H Degischer, and H J Flankl. Development of a Foaming Process for Particulate Reinforced Aluminum Melts. *Advanced Engineering Materials*, (10):735–740, 2002.

- [79] A. Pollien, Y. Conde, L. Pambaguian, and A. Mortensen. Graded open-cell aluminium foam core sandwich beams. *Materials Science and Engineering: A*, 404(1-2):9–18, September 2005.
- [80] H.-W. Seeliger. Aluminium Foam Sandwich (AFS) Ready for Market Introduction. *Advanced Engineering Materials*, 6(6):448–451, June 2004.
- [81] J Banhart and H Seeliger. Recent Trends in Aluminium Foam Sandwich Technology Industrial Implementation of AFS Technology. *Advanced Engineering Materials-Euromat Montpellier*, pages 1–13, 2011.
- [82] T.J. Lu, A. Hess, and M.F. Ashby. Sound absorption in metallic foams. *Journal of Applied Physics*, 85(11):7528–7539, 1999.
- [83] T. Morimoto. Sound absorbing materials. Technical Report 5, Kansai Electronics Industry Promotion Center Ltd., Osaka, Japan, 1993.
- [84] N. Plesner. Designing for Quiet, Vibration-Free Operation. Technical report, Aero EAR Specialty Composites, Indianapolis.
- [85] U. Vaidya, S. Pillay, S. Bartus, C. Ulven, D. Grow, and B. Mathew. Impact and post-impact vibration response of protective metal foam composite sandwich plates. *Materials Science and Engineering: A*, 428(1-2):59–66, July 2006.
- [86] J Banhart, J Baurneister, and M Weber. Damping properties of aluminium foams. *Materials Science*, (95):221–228, 1996.
- [87] N. Glenn. Vibration Characteristics Determined for Stainless Steel Sandwich Panels With a Metal Foam Core for Lightweight Fan Blade Design. Technical report, National Aeronautics and Space Administration Glenn Research Center.
- [88] L.P. Lefebvre, J. Banhart, and D. C. Dunand. Porous Metals and Metallic Foams: Current Status and Recent Developments. *Advanced Engineering Materials*, 10(9):775–787, September 2008.

- [89] G. Walther, B. Klöden, T. Büttner, T. Weiß gärber, B. Kieback, A Böhm, D. Naumann, S. Saberi, and L. Timberg. A New Class of High Temperature and Corrosion Resistant Nickel-Based Open-Cell Foams. *Advanced Engineering Materials*, 10(9):803–811, September 2008.
- [90] B. Ozmat, B. Leyda, and B. Benson. Thermal Applications of Open-Cell Metal Foams. *Materials and Manufacturing Processes*, 19(5):839–862, October 2004.
- [91] [http: www.ergaerospace.com](http://www.ergaerospace.com).
- [92] D. Sabatino, S. Lane, W. Road, R David, and N. Street. High Temperature Heat Exchanger Development Office of Naval Research Under Contract Number : N00014-03-C-0444. 2005.
- [93] S. Satyapal, T. Filburn, J. Trela, and J. Strange. Performance and Properties of a Solid Amine Sorbent for Carbon Dioxide Removal in Space Life Support Applications. *Energy & Fuels*, 15(2):250–255, March 2001.
- [94] K Leong and L Jin. Effect of oscillatory frequency on heat transfer in metal foam heat sinks of various pore densities. *International Journal of Heat and Mass Transfer*, 49(3-4):671–681, February 2006.
- [95] B. Ozmat. Reticulated Metal Foams Build Better Heatsinks. *Power Electronics Technology*, pages 24–29, 2007.
- [96] L. Persheng, Y. Bing, H. Anmin, and L. Karming. Development in applications of porous metals. *Trans. Nonferrous Met. Soc. China*, 11(5):629–638, 2001.
- [97] H Wadley. Fabrication and structural performance of periodic cellular metal sandwich structures. *Composites Science and Technology*, 63(16):2331–2343, December 2003.
- [98] M. Eisenmann. *M. Eisenmann, in ASM Handbook Vol. 7, Metal Powder Technologies and Applications, ASM International, Materials Park (USA), p. 1031, volume 7. 1998.*

- [99] M. Kleiner, M. Geiger, and A. Klaus. Manufacturing of Lightweight Components by Metal Forming. *CIRP Annals - Manufacturing Technology*, 52(2):521–542, January 2003.
- [100] Z. Esen and S. Bor. Processing of titanium foams using magnesium spacer particles. *Scripta Materialia*, 56(5):341–344, March 2007.
- [101] Q. Tian and X Guo. Electro-deposition for foamed zinc material from zinc sulfate solution. *6th Pacific Rim International Conference on Advanced Materials and Processing*, 561-565(3):1669–1672, 2007.
- [102] T W Clyne, I O Golosnoy, J C Tan, and a E Markaki. Porous materials for thermal management under extreme conditions. *Philosophical transactions. Series A, Mathematical, physical, and engineering sciences*, 364(1838):125–46, January 2006.
- [103] W Hsieh, J Wu, W Shih, and W Chiu. Experimental investigation of heat-transfer characteristics of aluminum-foam heat sinks. *International Journal of Heat and Mass Transfer*, 47(23):5149–5157, November 2004.
- [104] R L Mahajan. Forced Convection in High Porosity Metal Foams. *Journal of Heat Transfer*, 122:557–565, 2000.
- [105] A. Bhattacharya and R. L. Mahajan. Metal Foam and Finned Metal Foam Heat Sinks for Electronics Cooling in Buoyancy-Induced Convection. *Journal of Electronic Packaging*, 128(3):259, 2006.
- [106] Z. Hashin and S. Shtrikman. A Variational Approach to the Theory of the Effective Magnetic Permeability of Multiphase Materials. *Journal of Applied Physics*, 33(10):3125, 1962.
- [107] P.G. Collishaw and J.R.G Evans. An assessment of expressions for the apparent thermal conductivity of cellular materials. *Journal Of Materials Science*, 29:486–498, 1994.

- [108] R. Goodall, L. Weber, and A. Mortensen. The electrical conductivity of micro-cellular metals. *Journal of Applied Physics*, 100(4):044912, 2006.
- [109] K.P. Dharmasena and H. N. G. Wadley. Electrical conductivity of open-cell metal foams. *Materials Research*, 17(3):625–631, 2002.
- [110] E Solorzano, J Reglero, M Rodriguezperez, D Lehmkus, M Wichmann, and J De-saja. An experimental study on the thermal conductivity of aluminium foams by using the transient plane source method. *International Journal of Heat and Mass Transfer*, 51(25-26):6259–6267, December 2008.
- [111] E. Solorzano, M. Rodriguez-perez, L. Jaime, and J. De Saja. Influence of Solid Phase Conductivity and Cellular Structure on the Heat Transfer Mechanisms of Cellular Materials : Diverse Case Studies **. *Advanced Engineering Materials*, 11(10):818–824, 2009.
- [112] R. Coquard, M. Loretz, and D. Baillis. Conductive Heat Transfer in Metallic/Ceramic Open-Cell Foams. *Advanced Engineering Materials*, 10(4):323–337, April 2008.
- [113] A Bhattacharya. Thermophysical properties of high porosity metal foams. *International Journal of Heat and Mass Transfer*, 45(5):1017–1031, February 2002.
- [114] J W Paek, B H Kang, S Y Kim, and J M Hyun. Effective Thermal Conductivity and Permeability of Aluminum Foam Materials. *International Journal of Thermophysics*, 21(2):453–464, 2000.
- [115] S. Mancin, C. Zilio, A. Cavallini, and L. Rossetto. Pressure drop during air flow in aluminum foams. *International Journal of Heat and Mass Transfer*, 53(15-16):3121–3130, July 2010.
- [116] P. Du Plessis, A. Montillet, and J. Legrand. Pressure drop prediction for flow through high porosity metallic foams. *Chemical Engineering Science*, 49(21):3545–3553, 1994.

- [117] J Despois and A Mortensen. Permeability of open-pore microcellular materials. *Acta Materialia*, 53(5):1381–1388, March 2005.
- [118] J G. Fourie and J P. Du Plessis. Pressure drop modelling in cellular metallic foams. *Chemical Engineering Science*, 57(14):2781–2789, July 2002.
- [119] J. Ahmed, C. Pham-huu, and D. Edouard. A predictive model based on tortuosity for pressure drop estimation in slim and fat foams. *Chemical Engineering Science*, 66(20):4771–4779, 2011.
- [120] W. Xu, H. Zhang, Z. Yang, and J. Zhang. Numerical investigation on the flow characteristics and permeability of three-dimensional reticulated foam materials. *Chemical Engineering Journal*, 140(1-3):562–569, July 2008.
- [121] M.S. Phanikumar and R.L. Mahajan. Non-Darcy natural convection in high porosity metal foams. *International Journal of Heat and Mass Transfer*, 45(18):3781–3793, August 2002.
- [122] C.Y. Zhao, T.J. Lu, H.P. Hodson, and J.D. Jackson. The temperature dependence of effective thermal conductivity of open-celled steel alloy foams. *Materials Science and Engineering: A*, 367(1-2):123–131, February 2004.
- [123] C.Y. Zhao, T.J. Lu, and H.P. Hodson. Natural convection in metal foams with open cells. *International Journal of Heat and Mass Transfer*, 48(12):2452–2463, June 2005.
- [124] G. Hetsroni, M. Gurevich, and R. Rozenblit. Natural convection in metal foam strips with internal heat generation. *Experimental Thermal and Fluid Science*, 32(8):1740–1747, September 2008.
- [125] S. Mancin, C. Zilio, A. Cavallini, and L. Rossetto. Heat transfer during air flow in aluminum foams. *International Journal of Heat and Mass Transfer*, 53(21-22):4976–4984, October 2010.

- [126] S. Mancin, C. Zilio, A. Diani, and L. Rossetto. Experimental air heat transfer and pressure drop through copper foams. *Experimental Thermal and Fluid Science*, 36:224–232, January 2012.
- [127] M.K. Chyu, Y. Hsing, V. Natarajan, J.S. Chiou, Effects of perpendicular flow entry on convective heat/mass transfer from pin-fin arrays. *Heat Transfer Transactions of the ASME*, 121:668–664, 1999.
- [128] J. Hwang and C. Lui. Detailed heat transfer characteristic comparison in straight and 90-deg turned trapezoidal ducts with pin-fin arrays. *International Journal of Heat and Mass Transfer*, 42:4005–4016, 1999.
- [129] S. Tzeng and T. Jeng. Convective heat transfer in porous channels with 90-deg turned flow. *International Journal of Heat and Mass Transfer*, 49(7-8):1452–1461, April 2006.
- [130] W Lu, C Zhao, and S Tassou. Thermal analysis on metal-foam filled heat exchangers. Part I: Metal-foam filled pipes. *International Journal of Heat and Mass Transfer*, 49(15-16):2751–2761, July 2006.
- [131] C Zhao, W Lu, and S Tassou. Thermal analysis on metal-foam filled heat exchangers. Part II: Tube heat exchangers. *International Journal of Heat and Mass Transfer*, 49(15-16):2762–2770, July 2006.
- [132] C. TJoen, P. De Jaeger, H. Huisseune, S. Van Herzeele, N. Vorst, and M. De Paepe. Thermo-hydraulic study of a single row heat exchanger consisting of metal foam covered round tubes. *International Journal of Heat and Mass Transfer*, 53(15-16):3262–3274, July 2010.
- [133] L. W. Jin K. C. Leong. Heat transfer of oscillating and steady flows in a channel filled with porous media. *International Journal of Heat and Mass Transfer*, 31(03):63–72, 2004.

- [134] T. Lu, H. Stone, and M. Ashby. Heat transfer in open-cell metal foams. *Acta Materialia*, 46(10):3619–3635, June 1998.
- [135] I Ghosh. Heat transfer correlation for high-porosity open-cell foam. *International Journal of Heat and Mass Transfer*, 52(5-6):1488–1494, February 2009.
- [136] M. Bai and J. Chung. Analytical and numerical prediction of heat transfer and pressure drop in open-cell metal foams. *International Journal of Thermal Sciences*, 50(6):869–880, June 2011.
- [137] K. Vafai and C.L. Tien. Boundary and inertia effects on flow and heat transfer in porous media. *International Journal of Heat and Mass Transfer*, 24:195–203, 1981.
- [138] R. Wirtz. A Semi-Empirical Model for Porous Media Heat Exchanger Design. *Proceedings, American society of Mechanical Engineering National Heat Transfer Conference, Baltimore, MD*, pages 1–8.
- [139] P. Jiang and Z. Ren. Numerical investigation of forced convection heat transfer in porous media using a thermal non-equilibrium model. *International Journal of Heat and Fluid Flow*, 22(1):102–110, February 2001.
- [140] A.V. Kuznetsov. Investigation of the effect of transverse thermal dispersion on forced convection in porous media. *Acta Mechanica*, 43:35–43, 2000.
- [141] S. Annapragada, J. Murthy, and S. Garimella. Permeability and Thermal Transport in Compressed Open-Celled Foams. *Numerical Heat Transfer, Part B: Fundamentals*, 54(1):1–22, June 2008.
- [142] M. Wang and N. Pan. Modeling and prediction of the effective thermal conductivity of random open-cell porous foams. *International Journal of Heat and Mass Transfer*, 51(5-6):1325–1331, March 2008.

- [143] L. Giani, G. Groppi, and E. Tronconi. Mass-Transfer Characterization of Metallic Foams as Supports for Structured Catalysts. *Industrial & Engineering Chemistry Research*, 44(14):4993–5002, July 2005.
- [144] L. Ma, Z. Song, and D. He. Cellular structure controllable aluminium foams produced by high pressure infiltration process. *Scripta Materialia*, 41(7):785–789, August 1999.
- [145] Q. Fabrizio, A. Boschetto, L. Rovatti, and L. Santo. Replication casting of open-cell AlSi7Mg0.3 foams. *Materials Letters*, 65(17-18):2558–2561, September 2011.
- [146] URL: [//www.saltinstitute.org](http://www.saltinstitute.org).
- [147] Rogers and Mayhew. Applications to Particular Fluids. In Longman, editor, *Engineering Thermodynamics Work and Heat Transfer*, chapter 9, page 165. Bath, second edition, 1967.
- [148] L. F. Mondolfo. Aluminum-Silicon system. In *Aluminum Alloys: Structure and properties*, chapter 2, pages 368–376. Butterworth & Co, first edition, 1979.
- [149] B. Gabriel. Energy-Dispersive Spectroscopy. In Carnes Publication Services, editor, *Sem: A User's Manual for Materials Science*, chapter 3, pages 53–74. 1985.
- [150] K. Heinrich. Qualitative Analysis. In Litton Educational, editor, *Electron Beam X-Ray Microanalysis*, chapter 7, pages 187–200. Van Nostrand Reinhold, 1 edition, 1981.
- [151] URL: [//www.macor.info](http://www.macor.info).
- [152] J.P. Holman. Steady-State Conduction-One Dimension. In *Heat Transfer*, chapter 2, pages 25–55. McGrawHill, London, ninth edition, 2002.
- [153] C. Steven and P. Sommer. Understanding Electrical Discharge Machining. In *The complete EDM Handbook*, pages 19–26. 2005.

- [154] URL: www.electrolube.com.
- [155] J. R. Taylor. Propagation of Uncertainties. In Ann McGuire, editor, *An Introduction to Error Analysis*, chapter 3, pages 45–79. Second edition, 1997.
- [156] K Boomsma. On the effective thermal conductivity of a three-dimensionally structured fluid-saturated metal foam. *International Journal of Heat and Mass Transfer*, 44(4):827–836, February 2001.
- [157] C. Hutter, D. Büchi, V. Zuber, and P. Rudolf von Rohr. Heat transfer in metal foams and designed porous media. *Chemical Engineering Science*, 66(17):3806–3814, September 2011.
- [158] C. Hutter, C. Allemann, S. Kuhn, and Ph. Rudolf von Rohr. Scalar transport in a milli-scale metal foam reactor. *Chemical Engineering Science*, 65(10):3169–3178, May 2010.
- [159] C. San Marchi, J.-F. Despois, and A. Mortensen. Uniaxial deformation of open-cell aluminum foam: the role of internal damage. *Acta Materialia*, 52(10):2895–2902, June 2004.
- [160] Gibson L. J. M.F. and Ashby. Cellular Solids Structure and Properties. pages 175–234. Cambridge, 2nd edition, 1997.
- [161] G. Incera Garrido, F. Patcas, S. Lang, and B. Kraushaar-Czarnetzki. Mass transfer and pressure drop in ceramic foams: A description for different pore sizes and porosities. *Chemical Engineering Science*, 63(21):5202–5217, November 2008.
- [162] T Ki and S Jeong. Pressure Drop Characteristics of Slit-Type Heat Exchanger. In Jr. S. D. Miller and R. G. Ross, editor, *International Cryocooler*, pages 201–210, Boulder, CO, 2011.
- [163] B Antohe. Numerical characterization of micro heat exchangers using experimentally tested porous aluminum layers. *International Journal of Heat and Fluid Flow*, 17(6):594–603, December 1996.

- [164] J.T Richardson, Y Peng, and D Remue. Properties of ceramic foam catalyst supports: pressure drop. *Applied Catalysis A: General*, 204(1):19–32, November 2000.
- [165] Air Flow Measurement in Electronic Systems. Technical report, Advanced Thermal Solutions, Norwood, MA.
- [166] L.J. Yang, X.Z. Du, and Y.P. Yang. Influences of wind-break wall configurations upon flow and heat transfer characteristics of air-cooled condensers in a power plant. *International Journal of Thermal Sciences*, 50(10):2050–2061, October 2011.
- [167] H. Badr, M. Habib, R. Ben-Mansour, S. Said, and S. Al-Anizi. Erosion in the tube entrance region of an air-cooled heat exchanger. *International Journal of Impact Engineering*, 32(9):1440–1463, September 2006.
- [168] G. Zaragoza and R. Goodall. Metal Foams with Graded Pore Size for Heat Transfer Applications. *Advanced Engineering Materials*, pages 1–6, August 2012.
- [169] Pradeep M. Kamath, C. Balaji, and S.P. Venkateshan. Convection heat transfer from aluminium and copper foams in a vertical channel An experimental study. *International Journal of Thermal Sciences*, 64:1–10, February 2013.

Appendix

The experimental heat transfer calculations were compared against a simplified scheme developed by Mancin et al [125] for overall foam-finned surface efficiency and the heat transfer coefficient calculations. The heat transfer coefficient can be calculated with the following equations:

$$h_{cCALC} = \alpha \cdot a \cdot H \cdot \left(\frac{1 + \Omega \cdot a \cdot H}{1 + a \cdot H} \right) \quad (11.1)$$

with

$$\Omega = \frac{\tanh(m \cdot L)}{m \cdot L} \quad (11.2)$$

and

$$m = \left(\frac{4\alpha}{\lambda_{ft}} \right)^{0.5} \quad (11.3)$$

For all the foams except the 5 PPI one:

$$\alpha = \frac{\lambda_{air}}{d_f} \cdot 0.02 \cdot Re^{0.9} Pr_{air}^{0.33} \quad (11.4)$$

and for the 5 PPI foam:

$$\alpha = \frac{\lambda_{air}}{d_f} \cdot 0.058 \cdot Re^{0.75} Pr_{air}^{0.33} \quad (11.5)$$

Where

$$Re = \frac{d_f \cdot G}{\mu_{air} \cdot \varepsilon} \quad (11.6)$$

and is referred to the fiber thickness t while L , equivalent fin length, was calculated as,

$$L = 6.6 \cdot H \cdot PPI^{0.99} \cdot (0.0254 - t \cdot PPI) \quad (11.7)$$

where d_f is the strut diameter that has been taken equal to fiber thickness t in the calculation.

Nomenclature

\mathbf{a} heat transfer area per unit volume (m^{-1})

d_f strut diameter (m)

G air mass velocity = \dot{m}_{air} / S ($kgm^{-2}s^{-1}$)

H specimen height (m)

h_{cALC} heat transfer coefficient defined by Eq. 11.1

l fiber length (m)

PPI number of pores per linear inches ($pores \text{ in}^{-1}$)

Pr_{air} air Prandtl number ($-$)

Re Reynolds number ($-$)

S cross-section of the empty channel (m^2)

t fiber thickness (m)

α interstitial heat transfer coefficient defined by equations 11.4 and 11.5 ($Wm^{-2}K^{-1}$)

ε porosity ($-$)

μ_{air} air dynamic viscosity ($Pa\ s$)

λ_{air} thermal conductivity of the air ($Wm^{-1}K^{-1}$)

λ_f thermal conductivity of the meta ($Wm^{-1}K^{-1}$)

Ω foam efficiency ($-$)